Mismatched Processing for Radar Interference Cancellation

By

Lumumba A. Harnett

Submitted to the graduate degree program in the Department of Electrical Engineering and Computer Science and the Graduate Faculty of the University of Kansas in fulfillment of the requirements for Doctor of Philosophy.

Shannon Blunt, Chairperson

James Stiles

Committee members

Christopher Allen

Erik Perrins

Richard Hale

Date defended: July 18, 2022

The Dissertation Committee for Lumumba A. Harnett certifies
that this is the approved version of the following dissertation

Mismatched Processing for Radar Interference Cancellation

Shannon Blunt, Chairperson

Date approved: July 18, 2022

To my mother and father

Abstract

Matched processing is a fundamental filtering operation within radar signal processing to estimate scattering in the radar scene based on the transmit signal. Although matched processing maximizes the signal-to-noise ratio (SNR), the filtering operation is ineffective when interference is captured in the receive measurement. Adaptive interference mitigation combined with matched processing has proven to mitigate interference and estimate the radar scene. A known caveat of matched processing is the resulting sidelobes that may mask other scatterers. The sidelobes can be efficiently addressed by windowing but this approach also comes with limited suppression capabilities, loss in resolution, and loss in SNR. The recent emergence of mismatch processing has shown to optimally reduce sidelobes while maintaining nominal resolution and signal estimation performance. Throughout this work, re-iterative minimum-mean square error (RMMSE) adaptive and least-squares (LS) optimal mismatch processing are proposed for enhanced signal estimation in unison with adaptive interference mitigation for various radar applications including random pulse repetition interval (PRI) staggering pulse-Doppler radar, airborne ground moving target indication, and radar & communication spectrum sharing. Mismatch processing and adaptive interference cancellation each can be computationally complex for practical implementation. Sub-optimal RMMSE and LS approaches are also introduced to address computational limitations. The efficacy of these algorithms is presented using various high-fidelity Monte Carlo simulations and open-air experimental datasets.

Acknowledgements

I would like to thank Dr. Shannon Blunt for his overarching mentorship and all-encompassing guidance. I would also like to thank the many talented students, faculty, and staff in the Radar Systems and Remote Sensing Laboratory, Kansas Applied Research Laboratory, and Department of Electrical Engineering and Computer Science at the University of Kansas which includes faculty: Dr. James Stiles, Dr. Christopher Allen, Dan Depardo, and Dr. Patrick McCormick; former and current students: Dr. Justin Metcalf, Dr. Cenk Sahin, John Jakabowsky, Audrey Seybert, Dr. Peng Tan San, Jonathan Owen, Brandon Ravenscroft, Dr. Charles Mohr, Alex Ramos, Christian Jones, and Daniel Herr; and staff: Roger Williams, Joy Grisafe-Gross, and Anna Paradis. Special thanks to Chancellor Bernadette Gray-Little for granting me an opportunity of a lifetime to attend the University of Kansas and Dr. Dan Scholnik of the Naval Research Laboratory for his mentorship. Last, but surely not least, special thanks to Dr. Otsebele Nare of Hampton University for seeing the talent in a motivated young man and inspiring me to go above and beyond. There's many more I could list but overall, the many fulfilling interactions at the University of Kansas, Naval Research Laboratory, and Hampton University has truly molded me into the engineer I am today. Thank you everyone!

Portions of this work was supported by the Office of Naval Research under Contracts Nos. N00014-16-C-2029 and N00014-20-C-1006, the University of Kansas Chancellor's Fellowship, the National Science Foundation Graduate Research Fellowship Program under Grant No. DGE-1451148.

Contents

List of Figures

List of Tables

Preface

The essence of radar systems is to characterize the information in a free-space environment using reflections from electromagnetic (EM) waves. One integral radar application is moving target indication (MTI) which extracts range, velocity, and angular location of moving targets, known in short as movers, from the radar scene. Radars operate within the radio spectrum of the EM spectrum. In this band of the EM spectrum, unavoidable sensitivity loss occurs due to thermal noise within the radio frequency (RF) receiver from signal amplification [1]. The radar receiver can encounter further loss from EM interference (EMI) during free-space propagation due to a separate emitting RF device [2] and phenomenological interference from reflections that have little to no velocity (known as clutter) [3]. Noise and interference each corrupt the radar measurements and limit the radar performance in characterizing illuminated scatterers.

Radar signal processing is tasked with regaining sensitivity loss from noise by using a filter coherent or "matched" to the transmit signal. However, such a filter is ineffective with interference. Instead, a filter with cancellation properties is necessary to mitigate the interference and regain sensitivity. The emergence of digital technologies has spawned a generation of algorithms that perform mismatch filtering for signal estimation and adaptive interference cancellation. This work explores the performance their combination provides. The mismatch algorithms provide improvement for signal estimation, but they come with a caveat: an increase in the computational resources necessary to compute them. Such an increase hinders real-time processing. Therefore, sub-optimal mismatch approaches are also explored.

In Chapter 1, an overview of radar fundamentals is presented. The chapter covers a wide range of topics such as pulse compression waveforms, open-air propagation of an EM waves, and signals models of collected radar returns. Information on side looking airborne radar and clutter is also presented. The chapter is meant to provide the radar knowledge necessary for subsequent chapters.

Chapter 2 explores a waveform diverse transmission approach known as random staggered pulse repetition interval (PRI) radar. Using matched processing on a random PRI staggering transmission introduces atypical sidelobes structures with higher-than-normal power. Clutter further exacerbates the problem. Adaptive processing using re-iterative minimum mean-square error (RMMSE) in conjunction adaptive clutter cancellation is proposed for enhanced signal estimation. A partial adaptive RMMSE approach is proposed for real-time application. The proposed methods are examined via high fidelity Monte Carlo simulations and ground-based pulse-Doppler radar measurements captured at the University of Kansas (KU).

Chapter 3 explores least-squares (LS) optimal and RMMSE adaptive processing for airborne ground MTI (GMTI) radar. Airborne radar succumbs to a coupling of velocity and angular location information making robust clutter cancellation difficult [4]. Space-time adaptive processing (STAP) is a proven adaptive cancellation approach that accounts for angle-Doppler coupling to facilitate the suppression of clutter. The chapter proposes mismatch processing and STAP together. STAP is well-known to be computationally expensive [4]. Therefore, partial adaptive STAP is combined with reduced rank LS and partial adaptive RMMSE. The proposed methods are also examined via high fidelity Monte Carlo simulations. The experimental analysis is performed on the synthetic aperture radar (SAR) GMTI GOTCHA dataset from the Air Force Research Laboratory (AFRL/RYA) [5].

Chapter 4 explores shared spectrum between radar and mobile communications. The chapter proposes a method to operate radar in the presence of interference from a mobile communication system by leveraging digital beamforming for signal separation and RMMSE via adaptive pulse compression (APC) for simultaneous estimation and cancellation. A suboptimal APC approach that performs over blocks of data instead of single samples is explored for improved computational efficiency. The proposed methods are examined using a synthetic dataset generated from the separate collections of long term evolution (LTE) wireless and ground-based pulse-Doppler radar transmissions on the same radar receiver. Each collection was performed at KU and later combined off-line. The radar signal processing within each chapter was performed

off-line. Conclusions and future work for each chapter is described in Chapter 5.

Two appendices accompany the chapters. The first appendix presents derivations for the maximum signal-to-noise ratio (SNR) and signal-to-interference-plus-noise ratio (SINR) filters. The second appendix presents a list of acronyms and mathematical notations. Below is a brief overview of some notations outlined in Appendix B. Scalar quantities are denoted in lowercase italic letter e.g., a. Uppercase italic letters likewise denote a scalar quantity to the describe "the number of" a quantity, or a set (when explicitly written). Vector quantities are denoted in lowercase bold letter e.g., $\mathbf{a}$. All vector quantities are column vectors unless otherwise specified. Uppercase bold letters represent a matrix quantity e.g., $\mathbf{A}$. The transposition, complex conjugation, and conjugate transposition (Hermitian) operations are denoted as superscripts, respectively, as $(\bullet)^T$, $(\bullet)^*$, and $(\bullet)^H$. A vector with N number of scalar quantities is represented as $\mathbf{a} = \begin{bmatrix} a_0 & a_1 & \cdots & a_{N-1} \end{bmatrix}^T$ with a dimension of $N \times 1$. A matrix with M number of $N \times 1$ vector quantities is $\mathbf{A} = \begin{bmatrix} \mathbf{a}_0 & \mathbf{a}_1 & \cdots & \mathbf{a}_{M-1} \end{bmatrix}$ with a of dimension $N \times M$ which can be expanded to

$$\mathbf{A} = \begin{bmatrix} a_{0,0} & a_{0,1} & \cdots & a_{0,M-1} \\ a_{1,0} & \ddots & \ddots & \vdots \\ \vdots & \ddots & \ddots & a_{N-2,M-1} \\ a_{N-1,0} & \cdots & a_{N-1,M-2} & a_{N-1,M-1} \end{bmatrix}.$$

In some instances, a vector or matrix quantity will have a subscript defining its dimension. For example, an identity matrix having a size of $N \times N$ is $\mathbf{I}_{N\times N}$. A bold number with a subscript defining its dimension is a quantity containing only that number e.g., $\mathbf{0}_{N\times 1}$. The element-wise (Hadamard) product operation is denoted with the symbol $\odot$. The Kronecker product operation is denoted with the symbol $\otimes$. The expected value operator of a quantity is denoted as $E\{\bullet\}$. The norm operation of a quantity is denoted as $\|\bullet\|$.

Chapter 1

Radar Background

Radar systems fundamental functions are search and detection, tracking, and imaging [2]. The focus of this work is on search and detection. Radars illuminate the environment using an electromagnetic (EM) wave from a transmit radar aperture. The scattering from the scene illumination is collected at a receive radar aperture. Desired scatterers are called targets. Unwanted scatterers that do not pertain to the radar application are called clutter [2].

Search radars scan a radar scene for potential targets. Moving target indication (MTI) is a radar application that detects moving targets, also known as movers, by discriminating their angular location and velocity from clutter. MTI has a myriad of applications such as airport surveillance and automotive collision avoidance to name a few. MTI considers clutter to be scatterers with zero velocity or a slow-moving velocity below a user-defined velocity threshold. Some examples of stationary clutter include the Earth's surface and man-made objects like buildings. Naturally moving environmental effects such as trees blowing in the wind or ocean waves are examples of non-stationary, slow-moving clutter. Non-stationary clutter is called internal clutter motion (ICM) and causes challenges in the detection of movers [6, 7].

Range, velocity, and angular location of scatterers are measured from reflected radar signals. Range is the distance between the radar and scatterer. Range measures the round-trip time delay from a radar pulse in fast-time signals. Velocity is obtained via the Doppler effect. The Doppler frequency is measured from a slow-time delay of multiple radar pulses. Angular location is obtained by measuring the direction-of-arrival (DOA) of an EM wave which corresponds to a spatial frequency. The spatial frequency is measured from the delay of the EM wave across a phased array of antenna elements also known as element-space signals. Fast-time, slow-time, and

element-space signals leverage the delay of the radar pulse but in different ways. Signal coherence is performed for each signal in receive processing to obtain an estimate of the desired information.

Interference limits the performance of estimating scatterer information. The primary interference source radar systems must combat is thermal noise. Radars operate in the radio frequency (RF) band of the EM spectrum. In RF, analog components in the radar receiver generates thermal noise [1]. Noise limits the radar dynamic range, decreases the radar sensitivity, and corrupts the receive radar signals. In addition to noise, a separate operating RF device overlapping in time and spectrum causes unintentional EM interference (EMI) to the radar. Lastly, in a radar scene there is an abundance of clutter measured relative to the number of movers. The aggregate of clutter will result in a high-power response that can mask slower movers with lower power. The unwanted clutter response poses a problem to the detection of other movers. Therefore, clutter is considered an interference source in MTI radar as well.

Receive signal processing can maximize the signal strength via signal coherence and minimize interference strength via attenuation. Filtering, whether it be low-pass, band-pass, band-stop and/or high-pass filtering, is used to fulfill receive signal processing objectives. In the following sections, signal coherence of fast-time, slow-time, and element-space signals in the presence of noise and interference is examined. After, an overview of clutter cancellation in side-looking airborne radar (SLAR) is presented. The background information on SLAR can be relaxed to ground-based and stationary radars.

1.1 Pulse Compression Waveforms

A complex-valued baseband representation of a pulse waveform is characterized by a time-varying amplitude $A(t)$ and phase $\Phi(t)$

$$s(t) = A(t)\, e^{j\Phi(t)} \tag{1.1}$$

for a time duration of $0 \leq t \leq \tau$ where τ is the pulse duration [8, 9]. Waveform modulation can be performed in amplitude and/or phase. The waveform is fed through a high-power amplifier (HPA) to increase the signal transmit power. Higher signal energy increases the energy on scatterers thereby increasing the probability of detection. The amplifier is driven into saturation to maximum output power. The relationship between input power and output power of a HPA is non-linear which will result in waveform distortion when performing amplitude modulation in a saturated HPA [10]. Accordingly, radar systems primarily avoid amplitude modulation by having a constant modulus amplitude of $A(t) = 1$.

A simple radar pulse is a rectangular function absent of phase modulation $\Phi(t) = 0$ and has a constant modulus amplitude. A fundamental phase modulation is linear frequency modulation (LFM) known as a chirp. A LFM waveform has time varying phase of

$$\Phi(t) = \pi \frac{B}{\tau} t^2 \tag{1.2}$$

where $B = |f_{\text{start}} - f_{\text{end}}|$ is a 3 dB swept bandwidth from a start frequency f_{start} to an end frequency f_{end}. Although the phase is parabolic, the LFM waveform get its name from the relationship between phase and frequency. Performing the time derivative of the phase produces the instantaneous frequency

$$f(t) = \frac{1}{2\pi} \frac{d}{dt} \Phi(t) = \frac{B}{\tau} t. \tag{1.3}$$

By observation, (1.3) is a linear function with a rate of change B/τ called the chirp rate [8]. The instantaneous frequency can be swept in a positive or negative manner. A positive chirp rate is called an up-chirp. Conversely, a negative chirp rate is called a down-chirp. Up- and down-chirps exhibit similar waveform properties.

Substituting (1.2) into (1.1) and considering constant modulus, the baseband representation of a chirp waveform is

$$s(t) = e^{j\pi(B/\tau)t^2} \tag{1.4}$$

[8, 9]. The radar waveform is upconverted to a RF carrier frequency f_{RF} for operation in the EM spectrum

$$s_{\mathrm{RF}}(t) = \mathrm{Re}\left\{ s(t) e^{j2\pi f_{\mathrm{RF}} t} \right\} \tag{1.5}$$

[8] where $\mathrm{Re}\{\bullet\}$ takes the real component of a complex-valued quantity. For example, the real-valued passband representation of a LFM waveform is $s_{\mathrm{RF}}(t) = \cos(2\pi f_{\mathrm{RF}} t + \pi(B/\tau)t^2)$. Figure 1.1 shows the relationship between instantaneous frequency and pulse duration for a simple pulse and up-chirp LFM with $f_{\mathrm{start}} = -0.5B$ and $f_{\mathrm{end}} = 0.5B$ [8]. The power spectral density of the waveforms is presented in Fig. 1.2.

A radar waveform determines range resolution and energy-on-target. Range resolution is the separability between two closely spaced scatterers. Being able to discern two scatterers increases the detection probability. Energy-on-target is the amount of signal energy on scatterers in a scene. The energy-on-target is directly related to scatterer signal strength sensed at the receiver. A shorter radar pulse duration provides higher range resolution. A longer radar pulse duration provides higher energy-on-target. A simple pulse must trade-off between range resolution and energy-on-target using the pulse duration. Frequency modulation waveforms provide range resolution of a shorter pulse while sustaining the energy-on-target of a longer pulse [8].

Waveform performance is characterized by the sidelobes of its normalized autocorrelation. The autocorrelation describes how rapidly a signal changes as a function of time [11]. The normalized autocorrelation is

$$r(t) = \frac{s^*(-t) * s(t)}{\int_0^\tau |s(t)|^2 dt} \tag{1.6}$$

where $(\bullet)^*$ denotes complex conjugation, $*$ denotes continuous convolution operation such that for casual functions $a(t) * b(t) = \int_0^t a(\tau) b(t-\tau) d\tau$ for $t \in [0, \infty)$, and the energy of a waveform is $E_{\mathrm{s}} = \langle s^*(t), s(t) \rangle = \int_0^\tau |s(t)|^2 dt$ [8] where $\langle a(t), b(t) \rangle$ denotes a continuous-time inner product between arbitrary continuous functions $a(t)$ and $b(t)$. Figure 1.3 depicts the autocorrelation of

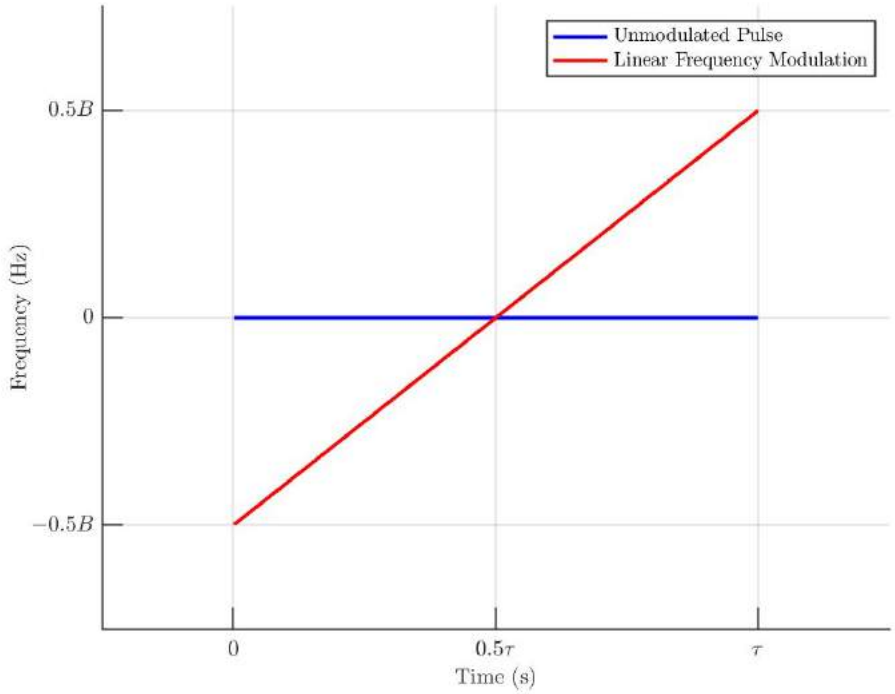

Fig. 1.1: Instantaneous frequency versus time for an unmodulated waveform (blue) and a LFM waveform (red)

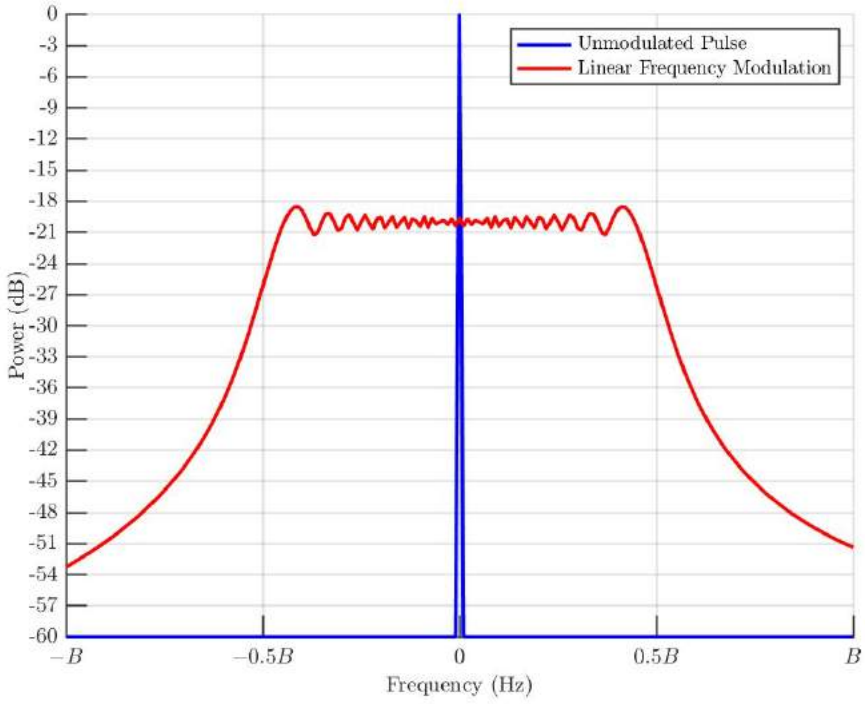

Fig. 1.2: Spectrum of an unmodulated waveform (blue) and a LFM waveform (red)

unmodulated and LFM waveforms. An unmodulated waveform produces a triangle function as its autocorrelation response. The autocorrelation for a LFM is

$$r_{\mathrm{LFM}}(t) = \mathrm{sinc}\left(\left(1 - \frac{|t|}{\tau}\right)\pi B\tau\right) \tag{1.7}$$

[8]. The time-bandwidth product $B\tau$ is a fundamental quantity of a radar waveform due to its direct relationship to fast-time signal coherence performance. The time-bandwidth product of a simple pulse is $B\tau = 1$ which also shows that the bandwidth and pulse duration are inversely proportional for a simple pulse. A LFM always has a time-bandwidth product greater than one. The time-bandwidth product of the LFM waveform depicted in Figure 1.3 is $B\tau = 100$. An ideal waveform would produce an impulse for its autocorrelation response which means energy does not spread over delay. An LFM produces a sinc response that approximates the impulse with increase time-bandwidth product. The autocorrelation response contains mainlobe and sidelobes responses. The mainlobe defines the range resolution. The sidelobes describe the energy spread in adjacent range

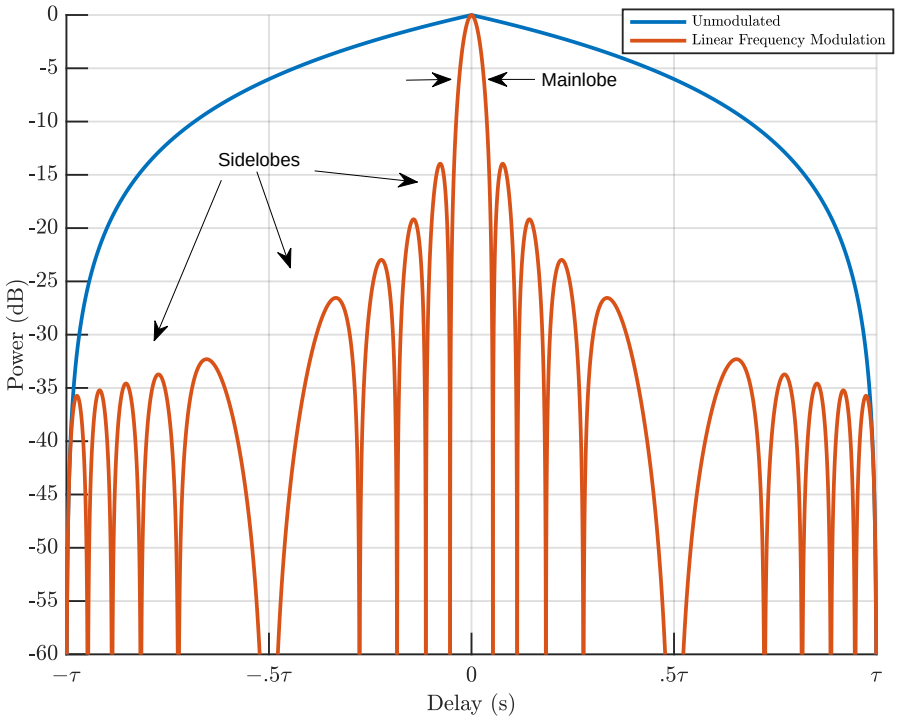

Fig. 1.3: Normalized autocorrelation of a unmodulated waveform (blue) and a LFM waveform (red)

samples.

Two popular range resolution metrics include the half-power and Rayleigh resolutions [8]. The half-power resolution, also referred to as 3 dB resolution, characterizes the 3 dB loss from the mainlobe peak power. The Rayleigh resolution, often referred to as null-to-null resolution, is the width of the first nulls on each side of the mainlobe. For a LFM waveform, the nulls occur approximately at $t \approx \pm 1/B$ when $B\tau > 10$ [8]. The Rayleigh resolution of a LFM waveform is

$$\delta R = \frac{c}{2B} \tag{1.8}$$

[8]. A lower resolution is desirable and improves with increasing bandwidth.

Relatively speaking, the LFM peak sidelobe level is considered high and problematic to radar detection. A LFM have a peak sidelobe power of approximately -13.2 dB below the mainlobe peak power. Radars require a high degree of sensitivity to detect radar reflections. In receive processing, sidelobes from one scatterer can mask mainlobes of other scatterers in nearby delay intervals. The sidelobes of a waveform autocorrelation response can be modified by changing the linearity of the instantaneous frequency. Phase-coded and non-linear FM waveforms can produce lower sidelobes. However, phase-coded waveforms cannot achieve the wide bandwidth possibilities of a LFM [12]. The disadvantage of implementing non-linear FM waveforms is there complexity to implement in hardware. The improvement in digital technology, such as arbitrary waveform generation, has led to a surge in waveform diversity [13]. Legacy radar systems would require hardware upgrades to facilitate advance technologies which can be costly.

The simplicity to implement a LFM in hardware is a trade-off that is often taken since the high sidelobes can be mitigated in receive processing. One of the most common receive processing methods to mitigate range sidelobes in receive processing is windowing. Windowing is an amplitude weighting of the receive filter and is computationally inexpensive to perform. A signal mismatch occurs with windowing causing a minor loss in signal strength. Windowing and mismatch loss is discussed further in Section 1.6. The use of LFM waveforms within legacy

systems are prevalent due to their simplicity to implement. Since a LFM waveform is a fundamental waveform, it is implemented within this work. Nonetheless, this work is generalized such that other phase modulations are applicable.

1.2 Radar Transmission, Scattering, and Reception

An overview of the free-space transmission of radar systems is presented. Consider a monostatic radar configuration where the transmit and receive antennas are colocated. The passband waveform is emitted from the transmit antenna into the radar scene as an EM wave. The emitted EM wave propagates into the environment at the speed of light and illuminates scatterers [2]. The EM wave in the far-field is assumed to be a plane wave and impinges on scatterers in the radar scene [2].

The emitted EM wave travels to a scatterer and encounters atmospheric refraction on the way. Atmospheric refraction from particles in the air (such as water vapor or oxygen) absorbs the radiated energy causing a carrier frequency dependent attenuation to the transmit signal. Scattering can be forward-scattering or backscattering [14]. For narrowband signal in the far field, movers have point reflectively and clutter has surface reflectively [14]. The roughness of a scatterer surfaces can be specular and/or diffuse [14]. Specular surfaces include roads or standing water. A diffuse surface includes corn fields or wooded areas. Two-way propagation from backscattering is collected at the receiver. There exist bi- and multi-static transmit/receive schemes in which forward-scattering must be considered as well.

For a simple pulse transmitted from a isotropic antenna, the transmitted power density of the EM plane wave is

$$Q_{\mathrm{Tx}} = \frac{P_{\mathrm{Tx}} A_{\mathrm{Tx}}}{\lambda_{\mathrm{RF}}^2 R^2} \tag{1.9}$$

[14] where P_{Tx} is the peak power of the radar transmitter, A_{Tx} is the effective aperture of the transmit antenna, $\lambda_{\mathrm{RF}} = c/f_{\mathrm{RF}}$ is the carrier wavelength at the speed of light c, and R is the range from the radar to a scatter in the radar environment. The transmit power density is typically seen with the antenna gain. The relationship between effective aperture and antenna gain is

$G_{\mathrm{Tx}} = 4\pi A_{\mathrm{Tx}} / \lambda_{\mathrm{RF}}^2$ [14].

The transmit power density incident on a scatterer interacts with the scatterer radar cross section (RCS) denoted σ_{RCS}. RCS incorporates the backscattering coefficient of the scatterer and is determined by the scatterer physical size and EM properties [14]. The power reflected from the illuminated scatterer has a power density of

$$Q_{\mathrm{refl}} = \frac{Q_{\mathrm{Tx}} \sigma_{\mathrm{RCS}}}{4\pi R^2}. \tag{1.10}$$

After reflection, the plane wave travels a distance R back to the receiver. Again, experiencing atmospheric refraction. The receive signal power of the emission is

$$P_{\mathrm{r}} = Q_{\mathrm{refl}} A_{\mathrm{Rx}} = \frac{P_{\mathrm{Tx}} A_{\mathrm{Tx}} A_{\mathrm{Rx}} \sigma_{\mathrm{RCS}}}{4\pi \lambda_{\mathrm{RF}}^2 R^4} \tag{1.11}$$

where A_{Rx} is the effective aperture of the receive antenna [14]. The signal is sent through an amplifier in the receiver, down-conversion from passband to baseband, in-phase/quadrature (IQ) sampling (also known as discretization), and quantization. At this point, the signal is ready for digital signal processing. After signal processing, the signal is sent for detection processing.

Ideally, the signal strength will be fully preserved from transmit to receive. However, loss is inherent in the propagation chain. The signal experiences a two-way path loss represented by $1/R^4$ in (1.11). The quantity illustrates that signal energy decreases with distance from the radar. Another factor to signal loss is thermal noise in the radar receiver. In the universe, any blackbody with a temperature above absolute zero generates random motion of charged particles known as thermal noise [10].

Thermal noise power of a radar receiver is

$$P_{\mathrm{v}} = k_{\mathrm{z}} T_0 F B_{\mathrm{Rx}} \tag{1.12}$$

where k_{z} is Boltzmann's constant, T_0 is the standard temperature (typically set to room

temperature of 290 K), F is the noise figure, and B_{Rx} is the instantaneous receiver bandwidth [14]. Assuming the instantaneous receiver bandwidth is driven by the waveform bandwidth, the noise power becomes dependent on the receiver noise figure. Thermal noise is attributed to active components in the receiver. For a device operating in the RF band, thermal noise dominates other noise sources such as atmospheric noise [1]. The amplifier is the primary active component that generates noise in the receiver. Low-noise amplifiers (LNAs) are readily used in the RF receiver to reduce the noise figure. The noise power can be obtained by determining the receiver noise figure. A key metric to analyze the effects of noise on the signal is signal-to-noise ratio (SNR)

$$\mathrm{SNR} = \frac{P_{\mathrm{r}}}{P_{\mathrm{v}}} \tag{1.13}$$

[14]. The probability of detection is a function of SNR [15]. The noise contribution can drop the SNR below a detection threshold.

Interference sources during open-air transmission can trump thermal noise in its detriment to the radar signal. The aggregate of clutter reflections from the radar transmission may overpower reflections for a desired mover. Also, EMI from a separate operating RF device, specifically a wireless communication transmission, can also overpower the transmitted radar signal. EMI constructively and destructively interferes with the radar signal effectively causing a decorrelation of the receive signal with the transmit radar waveform. Interference with higher power than thermal noise causes radar sensitivity to diminish effectively setting a higher "noise floor."

As an example, consider a wireless communication signal operating in-band with a radar. The communication device transmits with a peak power P_{c} on an isotropic antenna, an effective aperture A_{c}, and range R_{c} to the radar. The communication signal is a one-way transmission to the radar with a direct line-of-sight to the radar receive antenna. The power density of the EM wave propagating from the communication system is

$$Q_{\mathrm{c}} = \frac{P_{\mathrm{c}} A_{\mathrm{c}}}{\lambda_{\mathrm{RF}}^2 R_{\mathrm{c}}^2} \tag{1.14}$$

assuming the radar is in the far-field of the communication signal such that the signal power density

captured by the effective aperture of the radar receiver is a plane wave. The interference power captured by the radar receiver is

$$P_{\mathrm{i}} = Q_{\mathrm{c}} A_{\mathrm{Rx}} = \frac{P_{\mathrm{c}} A_{\mathrm{c}} A_{\mathrm{Rx}}}{\lambda_{\mathrm{RF}}^2 R_{\mathrm{c}}^2} \tag{1.15}$$

which is equivalent to Friis transmission equation [16].

Thermal noise and interference are additive in their impact on the radar signal as seen in Figure 1.4. Interference effect on the receive signal strength is analyzed via the signal-to-interference-plus-noise ratio (SINR). SINR considers the ratio of the receiver power relative to the linear combination of interfering sources

$$\mathrm{SINR} = \frac{P_{\mathrm{r}}}{P_{\mathrm{i}} + P_{\mathrm{v}}}. \tag{1.16}$$

The incorporation of the interference source makes the probability of detection a function of SINR [15]. Assuming the interference power is significantly larger than the noise power i.e., $P_{\mathrm{i}} >> P_{\mathrm{v}}$, then (1.16) can be approximated to signal-to-interference ratio (SIR)

$$\mathrm{SINR}|_{P_{\mathrm{i}} >> P_{\mathrm{v}}} \approx \mathrm{SIR} = \frac{P_{\mathrm{r}}}{P_{\mathrm{i}}}. \tag{1.17}$$

The interference power presented in (1.15) is only an example. Interference from a wireless communication is addressed in Chapter 5. Interference from clutter is addressed in Chapters 3 and 4.

A radar can improve SINR by increasing the transmit power, increasing the size of the effective aperture, and/or closing the distance to the scatterer when operating at a given carrier

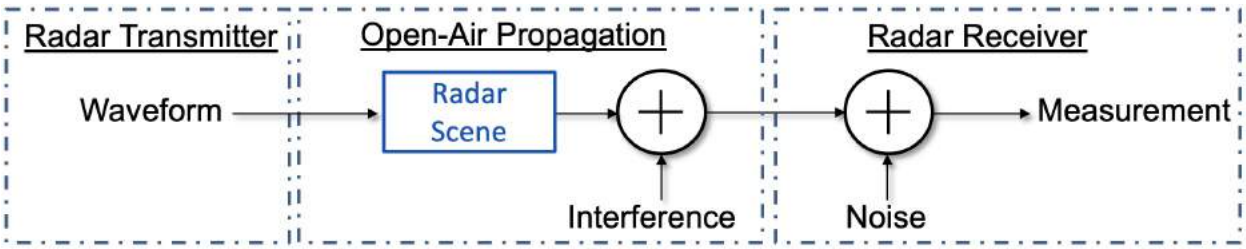

Fig. 1.4: General signal flow diagram

frequency. Transmit parameters are often optimized to achieve the best possible SINR. For example, the transmit power is maximized since the transmit amplifier is driven into saturation. The effective aperture is dependent on the physical array element whether it be a parabolic antenna, horn antenna, etc. [17]. Also, antenna size increases with increasing wavelength (in order words antenna size increases with decreasing carrier frequency) [17]. Lastly, the option to change the radar physical location is not always available. The next option to increase SINR is exploiting signal coherence in each signal dimension. Signal coherence increases signal strength in noise-limited and interference-limited environments to improve SNR and SINR. The improvement subsequently improves the probability of detection.

1.3 Fast-Time Signals

Consider the transmission of a pulse train, into the radar scene as depicted in Figure 1.5. The interval between start of pulses is the pulse repetition interval (PRI). The number of pulses emitted per second is the pulse repetition frequency (PRF). These quantities are inversely proportional

$$f_{\mathrm{r}} = \frac{1}{T_{\mathrm{r}}} \tag{1.18}$$

where f_{r} denotes PRF and T_{r} denotes PRI [2]. The PRI contains the transmit pulse and a receive time interval. The receive time interval is a "listening period" for scatterer reflections to be collected by the receiver. Fast-time signals considers the reflections captured from the start of the

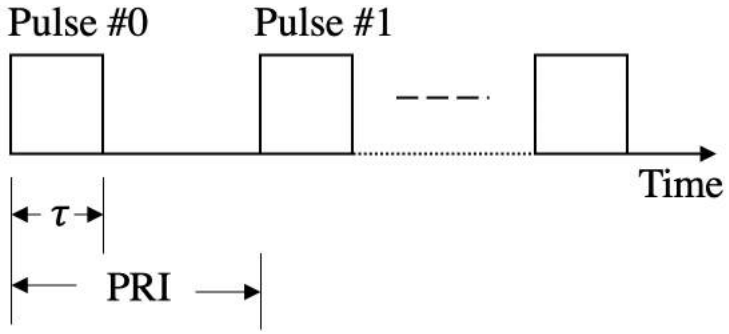

Fig. 1.5: Pulse train

transmission. If a radar transmits and receive from a single aperture, then the portion of the PRI corresponding to the pulse duration is a blind region. The ratio between pulse duration and PRI, τ/T_{r}, is called the duty cycle [8]. A FM waveform with a duty cycle of 100% is called a FM continuous-wave (FMCW) [9, 18]. MTI systems typically have low duty cycles below 30%.

Range is extracted from the fast-time interval collected at the receiver. Consider a pulse transmitting into an open-air environment with scatterers present. The time delay of the pulse from transmission to reception is the round-trip time delay denoted as T_{Δ}. Using the relationship between the speed of the EM wave in free space and delay, the range of a reflected pulse is

$$R = \frac{cT_{\Delta}}{2} \tag{1.19}$$

[2]. The same waveform is transmitted every pulse for coherent gain at the caveat of range ambiguities. The maximum unambiguous range

$$R_{\max} = \frac{cT_{\mathrm{r}}}{2} \tag{1.20}$$

is the distance the radar cannot disambiguate pulse returns [2]. Pulse agility is a waveform diversity method that avoids range ambiguities by transmitting a different waveform pulse-to-pulse [19, 20]. Pulse agile radar waveforms are not considered within this work.

Considering the transmission of a radar waveform $s(t)$ illuminating scatterers in a radar scene. The fast-time receive signal model detailing the response captured at the radar receiver after signal amplification is described using a linear model

$$y(t) = s(t) * x(t) + i(t) + v(t) \tag{1.21}$$

where $x(t)$ is complex scatterers in the radar range profile, $i(t)$ is interference captured by the radar during open-air propagation, and $v(t)$ is thermal noise from the radar receiver. The waveform $s(t)$ is deterministic since it is a known quantity. The range profile, noise (which is always present), and

EMI (which may or may not be present) are characterized statistically due to the unpredictability of illuminated scatterers in the scene, EMI source signal, and random nature of particles, respectively. Each are considered a continuous random process. The processes are assumed to be stationary in a wide sense since the mean of the signal is expected to remain constant over the time interval of collection [11]. Specifically, the signals are also assumed to be weakly ergodic with zero-mean. For long collection intervals (on the order of seconds) this assumption breaks down and must be accounted for. Typical PRI values of MTI systems allow for this assumption to hold.

Noise is characterized as a Gaussian process. Thermal noise contribution to the receive signal is also called additive white Gaussian noise (AWGN). "Additive" due to its linear combination with the desired signal and "white" based on the flat RF frequency response (in a nod to the color white in the optical region). The statistical distribution of the clutter within the range profile changes depending on terrain, material, and RCS [3, 4, 21]. The interference signal randomness depends on the type of waveform being transmitted. For example, commercial communications signals will be random due information modulation symbols being random. A separate radar transmitting in a similar nature as the one being presented will not be random. Subsumed into $i(t)$ is also a convolution operation since the interference waveform reflects off scatterers on the way to the radar receiver.

Pulse compression is the operation of passing the receive signal through a filter in fast-time to determine the impulse response of the open-air environment. The impulse response of the open-air environment corresponds to the range delay of scatterers. A well-known pulse compression filter is the band-pass, finite impulse response (FIR) filter matched to the radar waveform [8, 9]. The namely match filter is

$$u_{\mathrm{MF}}(t) = \frac{s^*(-t)}{\int_0^{\tau} |s(t)|^2 dt} \tag{1.22}$$

for $0 \leq t \leq \tau$ [9]. The match filter maximizes SNR in fast-time. The pulse compression response

from the application of the match filter to the receive signal is

$$\begin{aligned} z(t) &= u_{\mathrm{MF}}(t) * y(t) \\ &= \int_0^{T_{\mathrm{r}}} r(t-\zeta)\, x(\zeta) d\zeta + \bar{i}(t) + \bar{v}(t) \\ &= \bar{x}(t) + \bar{i}(t) + \bar{v}(t) \end{aligned} \tag{1.23}$$

where $\bar{x}(t) = \int_0^{T_{\mathrm{r}}} r(t-\zeta)\, x(\zeta) d\zeta$ contains the desired response $x(t)$ and range sidelobe contributions from nearby scattering, $\bar{i}(t) = u_{\mathrm{MF}}(t) * i(t)$ is filtered interference, and $\bar{v}(t) = u_{\mathrm{MF}}(t) * v(t)$ is filtered noise. The pulse compression response is passed through a detector to determine if any scattering is within the range profile [15]. The filter converts the receive signal from fast-time to time delay which is subsequently mapped to range using the relationship $t = 2R/c$. Note, the name "match filter" strictly describes a pulse compression filter. The term "matched" is used to describe any filter leveraging the transmit signal for the receive filter to maximize SNR. Matched filters are later used within the description of slow-time, element-space, and space-time signals.

The estimate of the range profile is equivalently stated as the pulse compression response $\hat{x}(t) = z(t)$ where $\hat{\bullet}$ denotes an estimate of a quantity. The distinction is made to avoid confusion later since receive processing to obtain velocity and angular location can be performed before or after pulse compression without the loss of generality. Pre-pulse compression processing uses $y(t)$ from (1.21) and post-pulse compression processing uses $z(t)$ from (1.23).

The pulse compression response represents the importance of waveform design relative to the autocorrelation response. When multiple scatterers are in the radar scene, the receive response is a superposition of autocorrelation responses (which for a LFM is a sinc-like response) scaled by the complex amplitude of the scattering. Sidelobes from other range delays contribute detrimentally to the range delay under test. Pulse compression improves SNR and SINR by the time-bandwidth of the waveform.

A discrete form of pulse compression is implemented after analog-to-digital conversion (ADC).

Define f_{s} as the receiver sampling frequency and $T_{\mathrm{s}} = 1/f_{\mathrm{s}}$ as the receiver sampling period. The number of samples to characterize a waveform with duration τ is

$$L_{\mathrm{s}} = f_{\mathrm{s}}\tau. \tag{1.24}$$

The discrete representation of the waveform is a $L_{\mathrm{s}} \times 1$ waveform vector is

$$\mathbf{s} = \begin{bmatrix} s[0] & s[1] & \cdots & s[L_{\mathrm{s}}-1] \end{bmatrix}^T \tag{1.25}$$

such that $s[\ell_{\mathrm{s}}] = s(\ell_{\mathrm{s}}T_{\mathrm{s}})$ for $\ell_{\mathrm{s}} = 0, 1, \ldots, (L_{\mathrm{s}}-1)$ and $(\bullet)^T$ denotes transposition. The number of fast-time samples is obtained using the PRI

$$L_{\mathrm{f}} = f_{\mathrm{s}}T_{\mathrm{r}}. \tag{1.26}$$

Collecting L_{f} fast-time samples of the receive signal from (1.21) forms

$$\mathbf{y}_{\mathrm{f}}(\ell) = \begin{bmatrix} y[\ell] & y[\ell+1] & \cdots & y[\ell+L_{\mathrm{f}}-1] \end{bmatrix}^T \tag{1.27}$$

where $\mathbf{y}_{\mathrm{f}}(\ell)$ is a $L_{\mathrm{f}} \times 1$ fast-time signal vector. The discrete representation of the receive signal model is

$$\mathbf{y}_{\mathrm{f}}(\ell) = \mathbf{S}\mathbf{x}_{\mathrm{R}}(\ell) + \mathbf{i}_{\mathrm{f}}(\ell) + \mathbf{v}_{\mathrm{f}}(\ell) \tag{1.28}$$

where $\mathbf{x}_{\mathrm{R}}(\ell) = \begin{bmatrix} x(\ell) & x(\ell+1) & \cdots & x(\ell+L_{\mathrm{R}}-1) \end{bmatrix}^T$ is a $L_{\mathrm{R}} \times 1$ discretized range profile with $L_{\mathrm{R}} = L_{\mathrm{f}} + L_{\mathrm{s}} - 1$ being the number of samples after discrete circular convolution, $\mathbf{i}_{\mathrm{f}}(\ell) = \begin{bmatrix} i_{\mathrm{f}}(\ell) & \cdots & i_{\mathrm{f}}(\ell+1) & \cdots & i_{\mathrm{f}}(\ell+L_{\mathrm{f}}-1) \end{bmatrix}^T$ is a $L_{\mathrm{f}} \times 1$ interference vector, $\mathbf{v}_{\mathrm{f}}(\ell) = \begin{bmatrix} v_{\mathrm{f}}(\ell) & \cdots & v_{\mathrm{f}}(\ell+1) & \cdots & v_{\mathrm{f}}(\ell+L_{\mathrm{f}}-1) \end{bmatrix}^T$ is a $L_{\mathrm{f}} \times 1$ noise vector, and

$\mathbf{S} = [\ \mathbf{s}_0 \quad \mathbf{s}_1 \quad \cdots \quad \mathbf{s}_{L_\mathrm{R}-1}\ ]$ is a $L_\mathrm{f} \times L_\mathrm{R}$ convolution matrix where the ℓ_R column is

$$\mathbf{s}_{\ell_\mathrm{R}} = \begin{cases} [\ s[L_\mathrm{s} - \ell_\mathrm{R}] \quad \cdots \quad s[L_\mathrm{s}] \quad \mathbf{0}_{1\times(L_\mathrm{f}-\ell_\mathrm{R}+1)}\ ]^T & 0 \le \ell_\mathrm{R} \le L_\mathrm{s} \\ [\ \mathbf{0}_{1\times(L_\mathrm{s}-\ell_\mathrm{R})} \quad \mathbf{s} \quad \mathbf{0}_{1\times(L_\mathrm{f}-\ell_\mathrm{R}+))}\ ]^T & L_\mathrm{s} < \ell_\mathrm{R} \le L_\mathrm{f} - L_\mathrm{R} \\ [\ \mathbf{0}_{1\times\ell_\mathrm{R}} \quad s[0] \quad \cdots \quad s[\ell_\mathrm{R} - (L - L_\mathrm{R})]\ ]^T & L_\mathrm{f} - L_\mathrm{R} < \ell_\mathrm{R} \le L_\mathrm{R}. \end{cases} \tag{1.29}$$

The complex scattering observed at $x[\ell]$ is an aggregate of the many scatterers located in that range bin. Each scatterer has a corresponding power since each may have a different RCS.

Each thermal noise sample in the noise vector is assumed to have a Gaussian distribution. The samples are also independent of each other $E\{v(i)v(j)\} = E\{v(i)\}E\{v(j)\}$. When considering the properties together, the noise samples fall under the criterion of independent and identically distributed (IID). Accordingly, the noise vector is a complex normal random vector with a mean vector $\mathbf{0}_{L_\mathrm{f}\times 1}$ and $L_\mathrm{f} \times L_\mathrm{f}$ covariance matrix $\mathbf{R}_{\mathrm{f,v}} = \sigma_\mathrm{v}^2 \mathbf{I}_{L_\mathrm{f}\times L_\mathrm{f}}$ where σ_v^2 is the variance (see Appendix A equation (A.2) for a formal definition of the covariance matrix). The variance is likewise noise power.

The discrete match filter is

$$\mathbf{U}_\mathrm{MF} = \frac{1}{\mathbf{s}^H \mathbf{s}} \mathbf{S} \tag{1.30}$$

where the energy of the discrete-time waveform (using a vector inner product) is $E_\mathrm{s} = \mathbf{s}^H \mathbf{s} = \|\mathbf{s}\|^2 = L_\mathrm{s}$. Implementation of discrete pulse compression response is

$$\mathbf{z}(\ell) = \hat{\mathbf{x}}_\mathrm{R}(\ell) = \mathbf{U}_\mathrm{MF}^H \mathbf{y}_\mathrm{f}(\ell) \tag{1.31}$$

where $\hat{\mathbf{x}}_\mathrm{R}(\ell)$ is a $L_\mathrm{R} \times 1$ estimate of range profile. A common response that occurs in pulse compression is range straddling which occurs when a scatterer mainlobe falls between sample points. Therefore, a given response cannot be fully match. Range straddling is reduced by increasing the range resolution. Also, contained within the application of the filter in (1.31) is the matrix inner product $\mathbf{S}^H \mathbf{S}/L_\mathrm{s}$. The inner product has basis vectors of time-shifted versions of the

discretized normalized autocorrelation. Pulse compression and ADC stages can be interchanged without the loss of generality.

1.4 Slow-Time Signals

Slow-time is formed from the collection of a pulse train by a pulse-Doppler radar. Multiple PRIs are oriented and aligned by their respective fast-time signals. Figure 1.6 depicts the formation of the slow-time dimension. A moving scatterer shifts the RF frequency of the radar EM wave impinging onto it. The amount of frequency shift caused by the mover is the Doppler frequency [2]. An estimate of Doppler spectrum is obtained by examining the spectral content of a slow-time signal. A scatterer with velocity v_{s} has a Doppler frequency of

$$f_{\mathrm{D}} = \frac{2v_{\mathrm{mov}}}{\lambda_{\mathrm{RF}}} \tag{1.32}$$

[2]. Only the radial velocity relative to the radar position can be observed [2]. Movers closing in on the radar have a positive Doppler frequency shift and movers traveling away have a negative shift.

A continuous slow-time signal model is presented to provide a general understanding of slow-time. The continuous model is not achievable as slow-time can only be in samples. The purpose is to provide a theoretical basis to the practical discrete slow-time signal model which effectively is slow-time sampling. The continuous slow-time model is

$$y\left(t_{\psi},t\right) = \mathrm{rect}\left(t_{\psi}\right) \int_{-\infty}^{\infty} \left[s\left(t\right) * x\left(f_{\mathrm{D}},t\right)\right] e^{j2\pi f_{\mathrm{D}} t_{\psi}} df_{\mathrm{D}} + i\left(t_{\psi},t\right) + v\left(t_{\psi},t\right) \tag{1.33}$$

where the slow-time duration is limited by the duration of the coherent processing interval (CPI) from $0 \leq t_{\psi} \leq T_{\mathrm{CPI}}$. The slow-time signal of interest corresponds to a time-limited complex sinusoid with Doppler frequency f_{D}. The application of the pulse compression filter to (1.33)

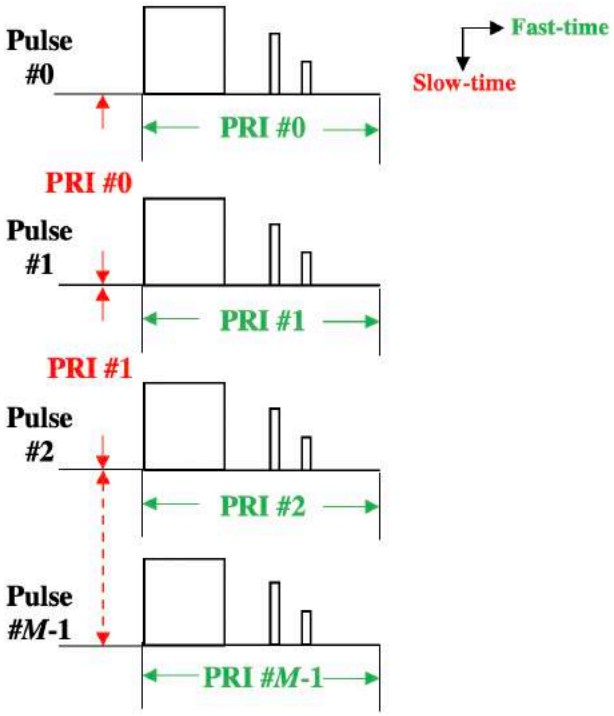

Fig. 1.6: Slow-time formation

obtains the range, slow-time response

$$\begin{aligned} z\left(t_\psi,t\right) &= h\left(t\right) * y\left(t_\psi,t\right) \\ &= \text{rect}\left(t_\psi\right) \int_{-\infty}^{\infty} \int_{0}^{T_\text{r}} r\left(t-\zeta\right) x\left(f_\text{D},\zeta\right) e^{j2\pi f_\text{D} t_\psi} d\zeta\, df_\text{D} + \bar{i}\left(t_\psi,t\right) + \bar{v}\left(t_\psi,t\right) \\ &= \text{rect}\left(t_\psi\right) \int_{-\infty}^{\infty} \bar{x}\left(f_\text{D},t\right) e^{j2\pi f_\text{D} t_\psi} df_\text{D} + \bar{i}\left(t_\psi,t\right) + \bar{v}\left(t_\psi,t\right) \end{aligned} \tag{1.34}$$

where $\bar{x}\left(f_\text{D},t\right) = \int_0^{T_\text{r}} r\left(t-\zeta\right) x\left(f_\text{D},\zeta\right) d\zeta$ subsumes the aggregate of range sidelobe contributions, $\bar{i}\left(t_\psi,t\right)$ is filtered interference in range, and $\bar{v}\left(t_\psi,t\right)$ is filtered noise in range. The Doppler spectrum is band-unlimited due to the time limitation on the signal. To put into context, this means infinite number of velocities are possible for examination. In the discrete model, uniform sampling restricts the unambiguous Doppler spectrum to a maximum frequency corresponding to the slow-time sampling frequency.

Doppler processing is a Doppler spectrum estimation technique performed using a normalized

Fourier transform (FT) since the slow-time signal is a complex sinusoid. The normalized FT is a collection of Doppler frequency shifted band-pass filters matched to the slow-time signal and hence maximizes SNR in the Doppler spectrum. Performing Doppler processing yields the range-Doppler response

$$\begin{aligned}\hat{x}\left(f_{\mathrm{D}},t\right) &= \frac{1}{E_{\mathrm{t}}}\int_{0}^{T_{\mathrm{CPI}}} z\left(t_{\psi},t\right)e^{-j2\pi f_{\mathrm{D}}t_{\psi}}dt_{\psi} \\ &= \frac{1}{T_{\mathrm{CPI}}}\int_{-\infty}^{\infty}\bar{x}\left(f_{q},t\right)\mathrm{sinc}\left(f_{\mathrm{q}}-f_{\mathrm{D}}\right)df_{\mathrm{q}}+\bar{i}\left(f_{\mathrm{D}},t\right)+\bar{v}\left(f_{\mathrm{D}},t\right) \\ &= \frac{1}{T_{\mathrm{CPI}}}\int_{-\infty}^{\infty}\int_{0}^{T_{r}}\mathrm{sinc}\left(f_{\mathrm{q}}-f_{\mathrm{D}}\right)x\left(f_{\mathrm{q}},\zeta\right)r\left(t-\zeta\right)d\zeta df_{\mathrm{q}}+\bar{i}\left(f_{\mathrm{D}},t\right)+_{\mathrm{t}}\left(f_{\mathrm{D}},t\right)\end{aligned} \tag{1.35}$$

where the energy is $E_t = \int_0^{T_{\mathrm{CPI}}}\left|e^{j2\pi f_{\mathrm{D}}t_{\psi}}\right|^2 dt_{\psi} = T_{\mathrm{CPI}}$, $\bar{i}\left(f_{\mathrm{D}},t\right)$ is filtered interference in range and Doppler, and $\bar{v}\left(f_{\mathrm{D}},t\right)$ is filtered noise in range and Doppler. The time-limitation of the slow-time signal response leads to a sinc response in Doppler. The range-Doppler response, also called a range-Doppler map, is an aggregate of a multivariate response (and will be a multivariate sinc response for an LFM waveform due to the waveform autocorrelation) scaled by the scatterer complex amplitude. Contained in each Doppler frequency bin are the desired response (at $f_{\mathrm{D}} = f_{\mathrm{q}}$), sidelobe responses from adjacent frequencies (at $f_{\mathrm{D}} \neq f_{\mathrm{q}}$), interference, and noise. Upon estimation of the spectrum, the Doppler frequencies are subsequently mapped to velocity using (1.32).

Next, the discrete slow-time model is presented. To reiterate, slow-time is obtained by orienting PRIs in parallel. Each PRI in the CPI is the start of a new slow-time sample. The slow-time sampling period and sampling frequency corresponds to PRI and PRF, respectively. Denote the ψth slow-time sample and its corresponding PRI $T_{\mathrm{r},\psi}$. Considering a transmission of Ψ pulses with corresponding Ψ PRIs, the receive signal model for the ψth PRI is

$$y\left(\psi,t\right) = \sum_{f_{\mathrm{D}}\in F_{\mathrm{D}}}\left[s\left(t\right)*x\left(f_{\mathrm{D}},t\right)\right]e^{j2\pi f_{\mathrm{D}}T_{\mathrm{acc},\psi}} + i\left(\psi,t\right)+v\left(\psi,t\right) \tag{1.36}$$

where $T_{\text{acc},\psi}$ is the accumulation time for ψ = 1, 2,..., Ψ PRIs. Define accumulation time as

$$T_{\text{acc},\psi} = \sum_{i=0}^{\psi-1} T_{\text{r},i} \tag{1.37}$$

where $T_{\text{r},0} = 0$ for mathematical convenience such that $T_{\text{acc},1}$ corresponds to the first pulse. The set F_{D} contains Doppler frequencies of all scatterers captured by the receiver. The number of scatterers is unknown. Consequently, the cardinality of F_{D} is unknown. Implementing pulse compression produces the following result

$$z(\psi,\ell) = \sum_{f_{\text{D}} \in F_{\text{D}}} \bar{x}(f_{\text{D}},\ell)\, e^{j2\pi f_{\text{D}} T_{\text{acc},\psi}} + \bar{i}(\psi,\ell) + \bar{v}(\psi,\ell). \tag{1.38}$$

The emission of multiple pulses from a PD radar can increase SINR as well. Coherent integration, also known as pre-summing, is an aggregate of slow-time samples. Define Γ as the number of slow-time samples to be integrated and M as the number of samples after pre-summing such that

$$M = \frac{\Psi}{\Gamma} \tag{1.39}$$

where Γ is an integer factor of Ψ. Using the signal model, pre-summing of slow-time samples is

$$z(m,t) = \frac{1}{\Gamma} \sum_{\gamma=0}^{\Gamma-1} z(\gamma + m\Gamma, t). \tag{1.40}$$

for $m = 0, 1, \ldots, M-1$ PRIs. Presumming exhibits a coherent gain of Γ. The technique exploits constructive and destructive interference. The signal component is coherent (constructive interference) while the interference and noise components are not (destructive interference).

The trade-off of pre-summing occurs in the Doppler spectrum. Presumming performs a Γ-tap FIR low-pass filter of the Doppler spectrum. Hence, the unambiguous Doppler frequency is reduced causing higher velocity scatterers that were not initially aliased to become aliased. When

considering pre-summing, the slow-time receive signal model becomes

$$z(m,t) = \sum_{f_{\mathrm{D}} \in F_{\mathrm{D}}} \bar{x}(f_{\mathrm{D}}, \ell)\, e^{j2\pi f_{\mathrm{D}} T_{\mathrm{acc},\psi}} + \bar{i}(m,t) + \bar{v}(m,t) \tag{1.41}$$

where the accumulation time is written in a similar manner as (1.37) by replacing ψ with m. Presumming can be performed after pulse compression as well.

The Doppler frequency is typically expressed in normalized terms. Explicitly define the duration of the CPI and average PRI, respectively, as

$$T_{\mathrm{CPI}} = \sum_{m=0}^{M-1} T_{\mathrm{r},m} \quad \text{and} \tag{1.42}$$

$$T_{\mathrm{r,avg}} = \frac{1}{M} T_{\mathrm{CPI}}. \tag{1.43}$$

The normalized Doppler frequency is the relationship between the Doppler frequency and the average PRI

$$\omega = f_{\mathrm{D}} T_{\mathrm{r,avg}}. \tag{1.44}$$

Next, define ε_m as a mth normalized PRI by average PRI

$$\varepsilon_{\mathrm{r},m} = \frac{T_{\mathrm{r},m}}{T_{\mathrm{r,avg}}}. \tag{1.45}$$

The normalized accumulation time is

$$\varepsilon_{\mathrm{acc},m} = \frac{T_{\mathrm{acc},m}}{T_{\mathrm{r,avg}}} = \sum_{i=0}^{m-1} \varepsilon_{\mathrm{r},i} \tag{1.46}$$

where similarly $\varepsilon_{\mathrm{r},0} = 0$ for convenience such that $\varepsilon_{\mathrm{acc},0} = 0$ corresponds to the first pulse. The relationship of Doppler frequency and accumulation time is

$$f_{\mathrm{D}} T_{\mathrm{acc},m} = \left(f_{\mathrm{D}} T_{\mathrm{r,avg}}\right) \frac{T_{\mathrm{acc},m}}{T_{\mathrm{r,avg}}} = \omega \varepsilon_{\mathrm{acc},m}. \tag{1.47}$$

For uniform PRI, the PRIs do not deviate from the average PRI meaning $\varepsilon_{\text{acc},m} = 1$ since $T_{\text{r,avg}} = T_{\text{r},m}$ for all M. The normalized accumulation time changes when changing the PRI from pulse to pulse known as staggering. The mth slow-time sample in normalized frequency terms after the implementation of ADC is

$$z[m,\ell] = \sum_{\omega\in\Omega} \bar{x}[\omega,\ell]\, e^{j2\pi\omega\varepsilon_{\text{acc},m}} + \bar{i}[m,\ell] + \bar{v}[m,\ell]. \tag{1.48}$$

where Ω is a set of normalized Doppler frequencies corresponding to the scattering within the radar scene. Contributions from range sidelobe responses are subsumed in a similar manner as (1.34).

Across slow-time samples, the scatterers have a linear phase progression. The phase progression is a result of a time-varying change in range and a pulse-to-pulse phase rotation [22]. The phase progression across slow-time samples for a scatterer is characterized by the $M \times 1$ temporal steering vector

$$\mathbf{c}_{\text{t}}(\omega) = \begin{bmatrix} 1 & e^{j2\pi\omega\varepsilon_{\text{acc},1}} & \cdots & e^{j2\pi\omega\varepsilon_{\text{acc},M-1}} \end{bmatrix}^T. \tag{1.49}$$

The temporal steering vector is in Vandermonde form and contains samples of a complex sinusoid with a normalized Doppler frequency ω [22]. The steering vector structure holds under the assumption that the scatterer acceleration is stationary within the CPI. The rate at which the phase progresses over slow-time corresponds to a Doppler frequency since frequency is the time derivative of phase. The collection of M PRIs in a CPI yields the $M \times 1$ temporal data vector

$$\begin{aligned} \mathbf{z}_{\text{t}}(\ell) &= \sum_{\omega\in\Omega} \bar{x}[\omega,\ell]\, \mathbf{c}_{\text{t}}(\omega) + \mathbf{i}_{\text{t}}(\ell) + \mathbf{v}_{\text{t}}(\ell) \\ &= \mathbf{C}_{\text{t}}\mathbf{x}_{\text{D}}(\ell) + \mathbf{i}_{\text{t}}(\ell) + \mathbf{v}_{\text{t}}(\ell) \end{aligned} \tag{1.50}$$

where $\mathbf{z}_{\text{t}}(\ell) = \begin{bmatrix} z[0,\ell] & z[1,\ell] & \cdots & z[M-1,\ell] \end{bmatrix}^T$ is the $M \times 1$ slow-time measurement vector, $\mathbf{i}_{\text{t}}(\ell) = \begin{bmatrix} \bar{i}[0,\ell] & \bar{i}[1,\ell] & \cdots & \bar{i}[M-1,\ell] \end{bmatrix}^{\mathbf{T}}$ is a $M \times 1$ slow-time interference vector, $\mathbf{v}_{\text{t}}(\ell) = \begin{bmatrix} \bar{v}[0,\ell] & \bar{v}[1,\ell] & \cdots & \bar{v}[M-1,\ell] \end{bmatrix}^{\mathbf{T}}$ is a $M \times 1$ slow-time noise vector, and $\mathbf{C}_{\text{t}}$ is a

$M \times \mathfrak{c}\{\Omega\}$ bank of temporal steering vectors, $\mathbf{x}_{\mathrm{D}}$ is a $\mathfrak{c}\{\Omega\} \times 1$ vector containing the illuminated scatterers in Doppler where $\mathfrak{c}\{\bullet\}$ denotes cardinality of a set.

Unavoidable model mismatch begins to occur for slow-time sampling for high dynamic range operation and higher radar sensitivity. Unknown errors can be a result of timing jitter due to hardware tolerances and finite granularity of the Doppler spectrum. The granularity is controllable to some degree by the oversampling amount [23]. Mismatch error effects can be modeled within the temporal steering vector by incorporating a mth timing error offset $T_{\mathrm{err},m}$ and Doppler frequency discretization error offset $f_{\mathrm{D,err}}$

$$\begin{aligned} \mathbf{c}(\omega;\boldsymbol{\eta}_{\mathrm{t}}) &= \left[\begin{array}{cccc} e^{j2\pi\omega\varepsilon_{\mathrm{acc},0}\eta_{\mathrm{t},0}} & e^{j2\pi\omega\varepsilon_{\mathrm{acc},1}\eta_{\mathrm{t},1}} & \cdots & e^{j2\pi\omega\varepsilon_{\mathrm{acc},M-1}\eta_{\mathrm{t},M-1}} \end{array} \right]^T \\ &= \mathbf{c}(\omega) \odot \mathbf{h}_{\mathrm{t}} \end{aligned} \tag{1.51}$$

where the $M \times 1$ slow-time error vector is $\mathbf{h}_{\mathrm{t}} = [e^{j2\pi\eta_{\mathrm{t},0}}\ e^{j2\pi\eta_{\mathrm{t},1}}\ \ldots\ e^{j2\pi\eta_{\mathrm{t},M-}}]^T$ which captures the mth mismatch error

$$\eta_{\mathrm{t},m} = \left(f_{\mathrm{D,err}} T_{\mathrm{r,avg}}\right) \frac{T_{\mathrm{err},m}}{T_{\mathrm{r,avg}}} \tag{1.52}$$

collected into a $M \times 1$ vector $\boldsymbol{\eta}_{\mathrm{t}} = [\eta_{\mathrm{t},0}\ \eta_{\mathrm{t},1}\ \ldots\ \eta_{\mathrm{t},M-1}]^T$ and $\odot$ is denotes the Hadamard (element-wise) product [23].

Since errors are unknown, they can be viewed as a form of calibration tolerance for hardware and processing fidelity [23]. Hence, the tolerance limit can only be quantified. Under the assumption that the the frequency discretization is uniform in the Doppler spectrum and jittering is invariant of Doppler, the slow-time signal model can be modified to include the modeling errors

$$\mathbf{z}_{\mathrm{t}}(\ell) = (\mathbf{C}_{\mathrm{t}}\mathbf{x}_{\mathrm{D}}(\ell)) \odot \mathbf{h}_{\mathrm{t}} + \mathbf{i}_{\mathrm{t}}(\ell) + \mathbf{v}_{\mathrm{t}}(\ell) = \mathbf{C}_{\mathrm{t}}\mathbf{x}_{\mathrm{D}}(\ell) + \mathbf{e}_{\mathrm{t}}(\ell) + \mathbf{i}_{\mathrm{t}}(\ell) + \mathbf{v}_{\mathrm{t}}(\ell) \tag{1.53}$$

where $\mathbf{e}_{\mathrm{t}}(\ell) = (\mathbf{C}_{\mathrm{t}}\mathbf{x}_{\mathrm{D}}(\ell)) \odot (\mathbf{h}_{\mathrm{t}} - \mathbf{1}_{M\times 1}) = [\xi(0,\ell)\ \xi(1,\ell)\ \ldots\ \xi(M-1,\ell)]^T$ is model mismatch error vector [23]. The modeling errors amplitude and phase distributions are statistically IID pulse-to-pulse with zero-mean. Also, modeling errors, source signals, and the additive noise are

all statistically independent [23]. These assumptions allow for mathematical tractability but emphasize that the error is unknown [23].

A PD radar transmitting the same PRI creates a uniform sampling in slow-time. A drawback of uniform slow-time sampling is its inability to disambiguate mover Doppler frequencies greater than the PRF. The maximum unambiguous Doppler frequency for a uniform PRI transmission is

$$\omega_{\max} = \frac{f_{\mathrm{r}} T_{\mathrm{r,avg}}}{2} \tag{1.54}$$

[24]. Aliasing occurs due to the inability to distinguish between two Doppler frequencies. Aliasing happens at integer multiples of the PRF since the samples of the complex sinusoid land on the same points temporally. All scatterers, aliased or not, fold in the first PRF regime between -PRF/2 and PRF/2. All others PRF regimes replicate the folding occurring in the first PRF regime. Having all scatterers in one regime is not desirable since movers with Doppler frequencies greater than the PRF will be detected at an incorrect velocity. Earlier, it was shown that range is limited by the duration of the PRI which is inversely proportional to PRF. The relationship between unambiguous range and unambiguous velocity is a well-known trade space and the basis of high, medium, and low PRF regimes that define radar applications [2].

Staggering the PRI pulse-to-pulse incurs a non-uniform sampling in slow-time. Figure 1.7 depicts an example of a slow-time sampling for an arbitrary Doppler frequency is shown. Non-uniform sampling increases the uniqueness of the sampling to a given sinusoid thus reducing aliasing and improving the unambiguous Doppler frequency (and velocity detection) of the radar

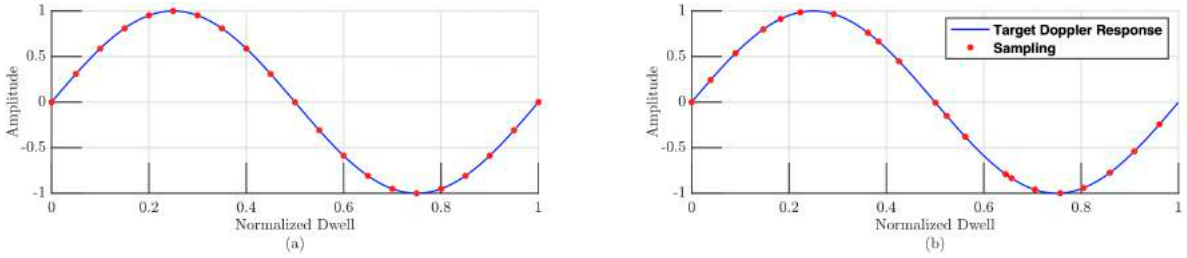

Fig. 1.7: Real part of an arbitrary Doppler response undergoing slow-time sampling based on a) uniform PRIs and b) randomly staggered PRIs

system. Staggering increases the extent of the unambiguous Doppler frequency to integer multiples of the least common multiple of the PRFs

$$\omega_{\max} = \frac{\zeta_{\text{ext}}}{2} = \frac{T_{\text{r,avg}} \text{LCM}\left\{\mathbf{f}_{\text{r}}\right\}}{2} \tag{1.55}$$

[21, 25] where $\zeta_{\text{ext}} = T_{\text{r,avg}}\text{LCM}\{\mathbf{f}_{\text{r}}\}$ is the Doppler extent, $\mathbf{f}_{\text{r}} = \begin{bmatrix} f_{\text{r},0} & f_{\text{r},1} & \cdots & f_{\text{r},M-1} \end{bmatrix}^T$ is a vector of the transmitted PRFs, and $\text{LCM}\{\bullet\}$ denotes the LCM operator. The Doppler extent could be quite large for some random staggering sequences. A maximum frequency is set to a practical value, denoted ζ_{mov}, within the parameters of the application to include all expected movers such that $\zeta_{\text{mov}} \leq \zeta_{\text{ext}}$.

The true Doppler frequencies of the mover and clutter are unknown. For this reason, the Doppler spectrum is estimated over a set of test frequencies. Using distinct frequency points to perform Doppler processing makes the estimate susceptible to Doppler straddling. Straddling occurs when a scatterer true Doppler frequency lands between discrete test frequencies. To compensate, the spectrum is oversampled beyond the Doppler resolution to increase the possibility of cohering to a signal.

Define the number of frequency points to the extent of the Doppler spectrum as

$$L_{\text{D}} = \zeta_{\text{mov}} K_{\text{D}} M \tag{1.56}$$

for an oversampling factor K_{D}. Define the Doppler resolution as

$$\delta f_{\text{D}} = \frac{1}{T_{\text{CPI}}} = \frac{1}{M T_{\text{r,avg}}} \tag{1.57}$$

[24] and normalized Doppler resolution using (1.44) as

$$\delta \omega = \frac{1}{M}. \tag{1.58}$$

The granularity of the oversampled spectrum is

$$\Delta\omega = \frac{\delta\omega}{K_{\mathrm{D}}} = \frac{1}{K_{\mathrm{D}}M}. \tag{1.59}$$

For staggering, the granularity of the spectrum is maintained. As a result, the number of frequency points L_{D} will increase proportionally with the additional spectrum beyond the first PRI regime.

After the collection of slow-time data, Doppler processing is performed using a normalized discrete Fourier transform (DFT). Each column in the matrix is essentially a Doppler filter. The DFT structure inherently considers evenly spaced temporal samples (in other words a uniform PRI transmission). Compensation of the FT is required to maximize signal coherence for non-uniform sampling, or staggered PRI transmission, using the non-uniform DFT [26]. The non-uniform DFT structure becomes a DFT when uniform sampling. The range-Doppler estimate is obtained by applying Doppler processing to pulse compressed fast-time data

$$\hat{x}\left[\omega,\ell\right] = \frac{1}{M}\sum_{m=0}^{M-1} z\left[m,\ell\right] e^{-j2\pi\omega\varepsilon_{\mathrm{acc},m}} = \mathbf{u}_{\mathrm{DP}}^{H}\left(\omega\right)\mathbf{z}_{\mathrm{t}}\left(\ell\right) \tag{1.60}$$

where the Doppler filter is

$$\mathbf{u}_{\mathrm{DP}}\left(\omega\right) = \frac{\mathbf{c}_{\mathrm{t}}\left(\omega\right)}{\mathbf{c}_{\mathrm{t}}^{H}\left(\omega\right)\mathbf{c}_{\mathrm{t}}\left(\omega\right)}. \tag{1.61}$$

The Doppler filter is a bandpass FIR filter centered at ω. A different filter is formed for each frequency examined hence the uniform or non-uniform DFT matrix. The energy in the temporal steering vector is $\mathbf{c}_{\mathrm{t}}^{H}\left(\omega\right)\mathbf{c}_{\mathrm{t}}\left(\omega\right) = ||\mathbf{c}_{\mathrm{t}}\left(\omega\right)||^2 = M$ for all ω [22]. When considering oversampling in Doppler, a $M \times L_{\mathrm{D}}$ bank of Doppler filters is formed

$$\mathbf{U}_{\mathrm{DP}} = \frac{1}{M}\mathbf{C}_{\mathrm{t}} \tag{1.62}$$

where $\mathbf{C}_{\mathrm{t}}$ is a $M \times L_{\mathrm{D}}$ bank of temporal steering vectors

$$\mathbf{C}_{\mathrm{t}} = \left[\ \mathbf{c}_{\mathrm{t}}\left(-\omega_{\max}\right) \quad \cdots \quad \mathbf{c}_{\mathrm{t}}\left(-\Delta\omega\right) \quad \mathbf{c}_{\mathrm{t}}\left(0\right) \quad \mathbf{c}_{\mathrm{t}}\left(\Delta\omega\right) \quad \cdots \quad \mathbf{c}_{\mathrm{t}}\left(\omega_{\max}\right)\ \right]. \tag{1.63}$$

Since (1.63) is known, the $M \times \mathfrak{c}\{\Omega\}$ bank of mover steering vectors presented in previous slow-time signal models is replaced by the $M \times L_{\mathrm{D}}$ bank of temporal steering vectors. The filters are applied to the slow-time receive vector to obtain the $L_{\mathrm{D}} \times 1$ estimate of the Doppler spectrum for the ℓth range sample

$$\hat{\mathbf{x}}_{\mathrm{D}}(\ell) = \mathbf{U}_{\mathrm{DP}}^{H} \mathbf{z}_{\mathrm{t}}(\ell). \tag{1.64}$$

Figure 1.8 presents a oversampled Doppler processing estimate for a uniform PRI transmission using a single point target at zero-Doppler and $M = 10$ pulses. The range-Doppler response is sent through a detector for either 1-D Doppler detection or 2-D range-Doppler detection.

The abundance of clutter can result in a Doppler sidelobe response that can potentially masks slower movers. Therefore, clutter is considered an interference source in MTI radar. The slow-time

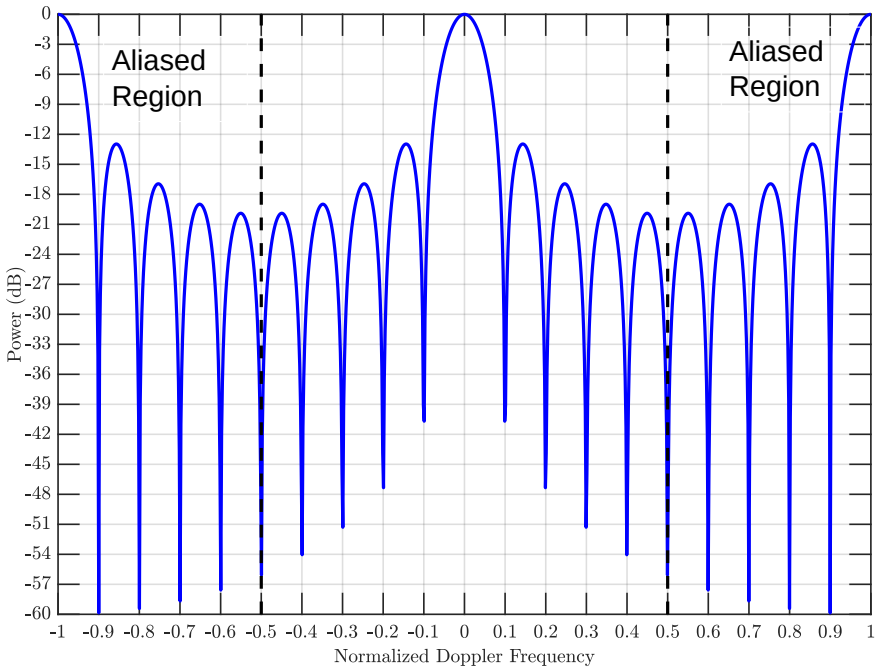

Fig. 1.8: Doppler processing of a single point target at zero-Doppler

signal model at the ℓth range sample when considering movers and clutter scatterers separately is

$$\begin{aligned}\mathbf{z}_{\mathrm{t}}(\ell) &= \sum_{\omega_{\mathrm{mov}}\in\Omega_{\mathrm{mov}}} \bar{x}[\omega_{\mathrm{mov}},\ell]\,\mathbf{c}_{\mathrm{t}}(\omega_{\mathrm{mov}}) + \sum_{\omega_{\mathrm{clu}}\in\Omega_{\mathrm{clu}}} \bar{x}[\omega_{\mathrm{clu}},\ell]\,\mathbf{c}_{\mathrm{t}}(\omega_{\mathrm{clu}}) + \mathbf{e}_{\mathrm{t}}(\ell) + \mathbf{v}_{\mathrm{t}}(\ell) \\ &= \mathbf{C}_{\mathrm{t,mov}}\mathbf{x}_{\mathrm{D,mov}}(\ell) + \mathbf{C}_{\mathrm{t,clu}}\mathbf{x}_{\mathrm{D,clu}}(\ell) + \mathbf{e}_{\mathrm{t}}(\ell) + \mathbf{v}_{\mathrm{t}}(\ell) \\ &= \mathbf{z}_{\mathrm{t,mov}}(\ell) + \mathbf{z}_{\mathrm{t,clu}}(\ell) + \mathbf{e}_{\mathrm{t}}(\ell) + \mathbf{v}_{\mathrm{t}}(\ell).\end{aligned} \tag{1.65}$$

where subscript "mov" denotes movers, subscript "clu" denotes clutter, $\Omega = [\ \Omega_{\mathrm{mov}} \quad \Omega_{\mathrm{clu}}\ ]$ is a set containing mover and clutter normalized Doppler frequencies, $\mathbf{C}_{\mathrm{t,mov}}$ is a $M \times \mathfrak{c}\{\Omega_{\mathrm{mov}}\}$ bank of temporal steering vectors corresponding to movers, $\mathbf{C}_{\mathrm{t,clu}}$ is a $M \times \mathfrak{c}\{\Omega_{\mathrm{clu}}\}$ bank of clutter temporal steering vectors, $\mathbf{z}_{\mathrm{t,mov}}$ is the mover receive data, and $\mathbf{z}_{\mathrm{t,clu}}$ is the clutter receive data.

The contribution of the interference sources in Doppler are likewise examined via SINR. Assume the signal is being estimated at Doppler cell-under-test (CUT) frequency ω, the application a Doppler filter to the signal model in (1.65) is

$$\begin{aligned}\hat{x}[\omega,\ell] &= \mathbf{u}_{\mathrm{DP}}^{H}(\omega)\,\mathbf{z}_{\mathrm{t,mov}}(\ell) + \mathbf{u}_{\mathrm{DP}}^{H}(\omega)\,\mathbf{z}_{\mathrm{t,clu}}(\ell) + \mathbf{u}_{\mathrm{DP}}^{H}(\omega)\,\mathbf{e}_{\mathrm{t}}(\ell) + \mathbf{u}_{\mathrm{DP}}^{H}(\omega)\,\mathbf{v}_{\mathrm{t}}(\ell) \\ &= \bar{x}(\omega)\,\mathbf{u}_{\mathrm{DP}}^{H}(\omega)\,\mathbf{c}_{\mathrm{t}}(\omega) + \sum_{\substack{\omega_{\kappa}\neq\omega \\ \omega_{\kappa}\in\Omega}} \bar{x}[\omega_{\kappa},\ell]\,\mathbf{u}_{\mathrm{DP}}^{H}(\omega)\,\mathbf{c}_{\mathrm{t}}(\omega_{\kappa}) + \mathbf{u}_{\mathrm{DP}}^{H}(\omega)\,\mathbf{e}_{\mathrm{t}}(\ell) + \mathbf{u}_{\mathrm{DP}}^{H}(\omega)\,\mathbf{v}_{\mathrm{t}}(\ell).\end{aligned} \tag{1.66}$$

Note, the following inner product is true $\mathbf{u}_{\mathrm{DP}}^{H}(\omega)\,\mathbf{c}_{\mathrm{t}}(\omega) = 1$. The interference within the CUT contains Doppler sidelobe responses from surrounding clutter and movers in the spectrum. The mitigation of clutter signals becomes an accompanying method to increase SINR since Doppler processing maximizes the signal strength.

The signal component of Doppler SINR is the average signal power

$$P_{\mathrm{r}}(\omega,\ell) = E\left\{\left|\bar{x}[\omega,\ell]\,\mathbf{u}_{\mathrm{DP}}^{H}(\omega)\,\mathbf{c}_{\mathrm{t}}(\omega)\right|^{2}\right\} = \rho[\omega,\ell]\left|\mathbf{u}_{\mathrm{DP}}^{H}(\omega)\,\mathbf{c}_{\mathrm{t}}(\omega)\right|^{2} \tag{1.67}$$

where $\rho[\omega,\ell] = E\{|\bar{x}[\omega,\ell]|^{2}\}$ is the power of the complex amplitude. The sources causing loss to

the signal strength consists of model mismatch error, clutter, and noise. The power of the mismatch error is

$$P_{\mathrm{e}}(\omega,\ell) = E\left\{\left|\mathbf{u}_{\mathrm{DP}}^{H}(\omega)\,\mathbf{e}_{\mathrm{t}}(\ell)\right|^{2}\right\} = \mathbf{u}_{\mathrm{DP}}^{H}(\omega)\,\mathbf{R}_{\mathrm{t,err}}(\ell)\,\mathbf{u}_{\mathrm{DP}}(\omega) \tag{1.68}$$

where the temporal error covariance matrix is

$$\mathbf{R}_{\mathrm{t,err}}(\ell) = \sigma_{\mathrm{t,err}}^{2}\mathbf{I}_{M\times M} \odot \sum_{\omega\in\Omega} \rho\left[\omega,\ell\right]\mathbf{c}_{\mathrm{t}}(\omega)\,\mathbf{c}_{\mathrm{t}}^{H}(\omega) \tag{1.69}$$

and $\sigma_{\mathrm{t,err}}^{2} = (1/M)E\{(\mathbf{h}_{\mathrm{t}} - \mathbf{1}_{M\times 1})^{H}(\mathbf{h}_{\mathrm{t}} - \mathbf{1}_{M\times 1})\}$ is the modeling error "noise" power [23]. The interference power contribution from clutter is

$$P_{\mathrm{i}}(\omega,\ell) = \sum_{\substack{\omega_{\kappa}\neq\omega \\ \omega_{\kappa}\in\Omega}} E\left\{\left|x\left[\omega_{\kappa},\ell\right]\mathbf{u}_{\mathrm{DP}}^{H}(\omega)\,\mathbf{c}_{\mathrm{t}}(\omega_{\kappa})\right|^{2}\right\} = \mathbf{u}_{\mathrm{DP}}^{H}(\omega)\,\mathbf{R}_{\mathrm{t,clu}}(\ell)\,\mathbf{u}_{\mathrm{DP}}(\omega) \tag{1.70}$$

where the temporal clutter covariance matrix is

$$\mathbf{R}_{\mathrm{t,clu}}(\ell) = \sum_{\substack{\omega_{\kappa}\neq\omega \\ \omega_{\kappa}\in\Omega_{\mathrm{clu}}}} \rho\left[\omega_{\kappa},\ell\right]\mathbf{c}_{\mathrm{t}}(\omega_{\kappa})\,\mathbf{c}_{\mathrm{t}}^{H}(\omega_{\kappa}). \tag{1.71}$$

Lastly, define the average noise power as

$$P_{\mathrm{v}}(\omega,\ell) = E\left\{\left|\mathbf{u}_{\mathrm{DP}}^{H}(\omega)\,\mathbf{v}_{\mathrm{t}}(\ell)\right|^{2}\right\} = \mathbf{u}_{\mathrm{DP}}^{H}(\omega)\,\mathbf{R}_{\mathrm{t,v}}(\ell)\,\mathbf{u}_{\mathrm{DP}}(\omega) \tag{1.72}$$

where the noise covariance matrix is

$$\mathbf{R}_{\mathrm{t,v}}(\ell) = E\left\{\mathbf{v}_{\mathrm{t}}(\ell)\,\mathbf{v}_{\mathrm{t}}^{H}(\ell)\right\} = \sigma_{\mathrm{v}}^{2}\mathbf{I}_{M\times M}. \tag{1.73}$$

The noise samples are temporally uncorrelated from pulse to pulse [4]. Consequently, the noise correlation between two pulses is $E\{v(i,\ell)v^{*}(j,\ell)\} = \sigma_{\mathrm{v}}^{2}\delta_{ij}$ where the Kronecker delta defined is

$\delta_{ij} = 1$ when $i = j$ and $\delta_{ij} = 0$ when $i \neq j$. The temporal noise sample is Gaussian distributed with zero-mean and noise power σ_{v}^2 and falls under the IID criterion. The optimal interference covariance matrix containing clutter noise, and modeling errors is

$$\mathbf{R}_{\mathrm{t,opt}}(\ell) = \mathbf{R}_{\mathrm{t,clu}}(\ell) + \mathbf{R}_{\mathrm{t,err}}(\ell) + \mathbf{R}_{\mathrm{t,v}}(\ell). \tag{1.74}$$

Define SINR as a function of range and Doppler

$$\mathrm{SINR}(\omega,\ell) = \frac{P_{\mathrm{r}}(\omega,\ell)}{P_{\mathrm{e}}(\omega,\ell) + P_{\mathrm{i}}(\omega,\ell) + P_{\mathrm{v}}(\omega,\ell)} = \frac{\rho[\omega,\ell]\left|\mathbf{u}_{\mathrm{DP}}^H(\omega)\,\mathbf{c}_{\mathrm{t}}(\omega)\right|^2}{\mathbf{u}_{\mathrm{DP}}^H(\omega)\,\mathbf{R}_{\mathrm{t,opt}}(\ell)\mathbf{u}_{\mathrm{DP}}(\omega)}. \tag{1.75}$$

1.5 Element-Space Signals

The angular location of scatterers is obtained by measuring the delay of reflected plane waves along a phased array of antenna elements. The rate of the delay along the elements can be mapped to the DOA of the wave. An element-space signal is formed from the collection of antenna elements. Each element corresponds to a new element-space sample. The time delay of a plane wave across the array corresponds to a linear phase progression and spatial frequency. Spatial frequency is mapped to the azimuth and elevation of scatterers within the scene.

Consider a linear array of N elements. The nth element has the Cartesian coordinate position

$$\mathbf{p}_n = \begin{bmatrix} p_{x_n} & p_{y_n} & p_{z_n} \end{bmatrix}^T. \tag{1.76}$$

A linear array with equally spaced elements in one-dimension is called a uniform linear array (ULA) [17, 27]. A ULA with elements along the y-axis, an interelement spacing of d meters for each element, and the nth antenna position is $\mathbf{p}_n = \begin{bmatrix} 0 & nd & 0 \end{bmatrix}^T$. A depiction of the array is presented in Figure 1.9. The length of the array is Nd and the phase center of the array is $Nd/2$. Only azimuth is obtainable for a ULA orientation depicted. The elevation can be obtained if the ULA is along the z-axis. Planar arrays provide an extra layer of fidelity in determining

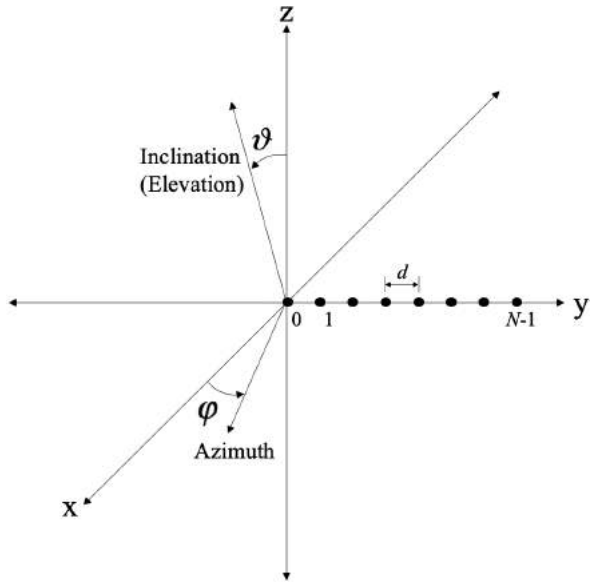

Fig. 1.9: Uniform linear array

both azimuth and elevation angles of illuminated scatterers [27]. For planar arrays, elements are positioned on the YZ-plane and can have different lattice structures [27].

Reflections from illuminated scatterers in the far-field impinge on a linear array as a plane wave. Define the unit vector of a plane wave as

$$\mathbf{a}(\vartheta,\varphi) = [\ \sin\vartheta\cos\varphi \quad \sin\vartheta\sin\varphi \quad \cos\vartheta\ ]^T \tag{1.77}$$

where ϑ is elevation and ϕ is azimuth of the plane wave relative to the array. The unit vector can likewise be written in UV-space using the following mappings: $u = \sin\vartheta\sin\varphi$ and $v = \cos\vartheta$ such that $\vartheta(u,v) = \cos^{-1}(\vartheta)$ and $\phi(u,v) = \sin^{-1}(u/\sqrt{1-v})$ [27]. By definition, $-1 \leq u \leq 1$, $-1 \leq v \leq 1$, and $u^2 + v^2 \leq 1$.

The time delay of the wave as it impinges on each element is

$$\begin{aligned}\tau_n(\vartheta(u,v),\varphi(u,v)) &= \frac{-\mathbf{a}^H(\vartheta(u,v),\varphi(u,v))\,\mathbf{p}_n}{c} \\ &= -\frac{nd}{c}\sin\vartheta\sin\varphi \\ &= -\frac{nd}{c}u\end{aligned} \tag{1.78}$$

[27]. Signals propagating away from the array are considered to be traveling in a positive direction [27]. The minus sign on $\mathbf{a}(\vartheta(u,v),\varphi(u,v))$ in (1.78) is due to reflections propagating toward the array [27]. A plane wave in a homogeneous medium has a wavenumber

$$\mathbf{k}\left(\vartheta(u,v),\varphi(u,v)\right)=\frac{2\pi f_{\mathrm{RF}}}{c}\mathbf{a}\left(\vartheta(u,v),\varphi(u,v)\right) \tag{1.79}$$

[27]. Leveraging these definitions, the phase of the plane wave on the nth element in the ULA is

$$\begin{aligned}\phi_n&=\mathbf{k}^H\left(\vartheta(u,v),\varphi(u,v)\right)\mathbf{p}_n\\&=2\pi f_{\mathrm{RF}}\tau_n\left(\vartheta(u,v),\varphi(u,v)\right)\\&=2\pi n\theta\end{aligned} \tag{1.80}$$

where the spatial frequency of the plane wave is

$$\theta(\vartheta(u,v),\varphi(u,v))=\frac{d}{\lambda_{\mathrm{RF}}}\sin\vartheta\sin\varphi=\frac{d}{\lambda_{\mathrm{RF}}}u \tag{1.81}$$

noting that wavelength is $\lambda_{\mathrm{RF}}=c/f_{\mathrm{RF}}$ [27]. The spectrum contains visible and virtual regions [27]. The beampattern of the array is only defined over the visible region. To prevent grating lobes from the virtual region being present in the visible space simultaneously, the interelement spacing for a ULA is set to $d=\lambda_{\mathrm{RF}}/2$ and is called a standard linear array [27]. Substituting the standard array element spacing and considering the extent of $u=\pm1$ into (1.81), the maximum spatial frequency is

$$\theta_{\max}=\left(\frac{\lambda_{\mathrm{RF}}}{2}\right)\left(\frac{1}{\lambda_{\mathrm{RF}}}\right)=\frac{1}{2} \tag{1.82}$$

where the spatial spectrum spans $-\theta_{\max}\leq\theta\leq\theta_{\max}$. A standard array is considered going forward. The spatial frequency $\theta(\vartheta(u,v),\varphi(u,v))$ will become denoted as θ thereby subsuming azimuth, elevation, u, and v.

A general diagram of a linear array and plane wave is presented in Figure 1.10. A reflecting

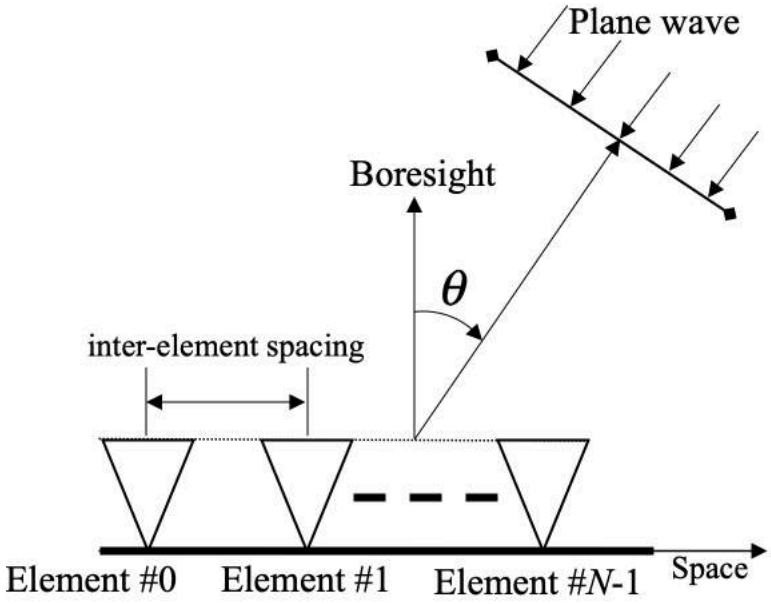

Fig. 1.10: Plane wave impinging on a uniform linear array

plane wave at boresight has a zero spatial frequency. Plane waves with a positive spatial frequency are to the right of radar boresight and vice versa. Plane waves from multiple illuminated scatterers are collected along the array. The plane perpendicular to boresight is called endfire. Considering a transmission of a waveform and the illumination of multiple scatterers for a single PRI, the element-space receive signal model at the nth antenna element is

$$y(n,t) = \sum_{\theta \in \Theta} [s(t) * x(\theta,t)] e^{j2\pi n\theta} + i(n,t) + v(n,t). \tag{1.83}$$

where Θ is a set of spatial frequencies for mover and clutter scatterers, $i(n,t)$ is interference and $v(n,t)$ is thermal noise for time duration $0 \leq t \leq T_{\mathrm{r}}$. The number of spatial frequencies from scatterers in the set Θ is unknown. Following pulse compression and ADC, the receive spatial signal model becomes

$$z[n,\ell] = \sum_{\theta \in \Theta} \bar{x}[\theta,\ell] e^{j2\pi n\theta} + \bar{i}[n,\ell] + \bar{v}[n,\ell] \tag{1.84}$$

where range sidelobes are subsumed into $\bar{x}[\theta,\ell]$, $\bar{i}[\theta,\ell]$, and $\bar{v}[\theta,\ell]$. Considering the collection of

illuminated scatterers at the phased array, the $N \times 1$ spatial data vector is

$$\begin{aligned} \mathbf{z}_{\mathrm{s}}(\ell) &= \sum_{\theta \in \Theta} \bar{x}[\theta, \ell]\, \mathbf{c}_{\mathrm{s}}(\theta) + \mathbf{i}_{\mathrm{s}}(\ell) + \mathbf{v}_{\mathrm{s}}(\ell) \\ &= \mathbf{C}_{\mathrm{s}} \mathbf{x}_{\mathrm{A}}(\ell) + \mathbf{i}_{\mathrm{s}}(\ell) + \mathbf{v}_{\mathrm{s}}(\ell) \end{aligned} \tag{1.85}$$

where the spatial steering vector is

$$\mathbf{c}_{\mathrm{s}}(\theta) = \begin{bmatrix} 1 & e^{j2\pi\theta} & \cdots & e^{j2\pi(N-1)\theta} \end{bmatrix}^T, \tag{1.86}$$

$\mathbf{C}_{\mathrm{s}}$ is a $N \times \mathfrak{c}\{\Theta\}$ bank of spatial steering vectors, and $\mathbf{x}_{\mathrm{A}}$ is a $\mathfrak{c}\{\Theta\} \times 1$ vector containing the illuminated scatterers in angle [22].

Model mismatch likewise occurs for spatial signals due to element location uncertainty, calibration tolerance, and mutual coupling effects between elements [23]. The effects can be modeled within the spatial steering vector by incorporating a nth element error offset $d_{\mathrm{err},n}$

$$\begin{aligned} \mathbf{c}(\theta; \boldsymbol{\eta}_{\mathrm{s}}) &= \begin{bmatrix} e^{j2\pi\theta\varepsilon_{\mathrm{acc},0}\eta_{\mathrm{s},0}} & e^{j2\pi\theta\varepsilon_{\mathrm{acc},1}\eta_{\mathrm{s},1}} & \cdots & e^{j2\pi\theta\varepsilon_{\mathrm{acc},M-1}\eta_{\mathrm{s},M-1}} \end{bmatrix}^T \\ &= \mathbf{c}(\theta) \odot \mathbf{h}_{\mathrm{s}} \end{aligned} \tag{1.87}$$

where the spatial error vector is $\mathbf{h}_{\mathrm{s}} = \begin{bmatrix} e^{j2\pi\eta_{\mathrm{s},0}} & e^{j2\pi\eta_{\mathrm{s},1}} & \cdots & e^{j2\pi\eta_{\mathrm{s},M-1}} \end{bmatrix}^T$ which captures the mismatch error effects

$$\eta_{\mathrm{t},n} = \frac{d_{\mathrm{err},n}}{\lambda_{\mathrm{RF}}} \sin\vartheta \sin\varphi, \tag{1.88}$$

and collected into a $N \times 1$ vector $\boldsymbol{\eta}_{\mathrm{s}} = [\eta_{\mathrm{s},0}\ \eta_{\mathrm{s},1}\ \ldots\ \eta_{\mathrm{s},N-1}]^T$. The model mismatch interference is assumed to be a stationary and zero-mean [23]. The element-space signal model is modified to account for the modeling error

$$\begin{aligned} \mathbf{z}_{\mathrm{s}}(\ell) &= (\mathbf{C}_{\mathrm{s}} \mathbf{x}_{\mathrm{A}}(\ell)) \odot \mathbf{h}_{\mathrm{s}} + \mathbf{i}_{\mathrm{s}}(\ell) + \mathbf{v}_{\mathrm{s}}(\ell) \\ &= \mathbf{C}_{\mathrm{s}} \mathbf{x}_{\mathrm{A}}(\ell) + \mathbf{e}_{\mathrm{s}}(\ell) + \mathbf{i}_{\mathrm{s}}(\ell) + \mathbf{v}_{\mathrm{s}}(\ell) \end{aligned} \tag{1.89}$$

where $\mathbf{e}_{\mathrm{s}}(\ell) = (\mathbf{C}_{\mathrm{s}}\mathbf{x}_{\mathrm{A}}(\ell)) \odot (\mathbf{h}_{\mathrm{s}} - \mathbf{1}_{N\times 1}) = [\xi(0,\ell)\ \xi(1,\ell)\ ...\ \xi(N-1,\ell)]^T$ [23].

The spatial spectrum is obtained by performing spatial filtering called receive beamforming. The beamformer is a spatial filter applied to element-space samples to estimate the DOA of reflected waves. Beamforming can be performed in analog or digital. The beam can be steered in two ways: electrical and mechanically. Mechanically steering is a physical direction change of the array. Electrical steering of the array beam is performed by implementing phase delays to each array element. Electrical steered digital beamforming from a fully digital array is considered. The spectral estimate of beamspace is

$$\hat{x}[\theta,\ell] = \frac{1}{N}\sum_{n=0}^{N-1} z[n,\ell]\, e^{-j2\pi n\theta} = \mathbf{u}_{\mathrm{BF}}^{H}(\theta)\,\mathbf{z}_{\mathrm{s}}(\ell) \tag{1.90}$$

where the $N \times 1$ maximum SNR beamformer is

$$\mathbf{u}_{\mathrm{BF}}(\theta) = \frac{\mathbf{c}_{\mathrm{s}}(\theta)}{\mathbf{c}_{\mathrm{s}}^{H}(\theta)\,\mathbf{c}_{\mathrm{s}}(\theta)}. \tag{1.91}$$

The energy across array elements is $\mathbf{c}_{\mathrm{s}}^{H}(\theta)\,\mathbf{c}_{\mathrm{s}}(\theta) = \|\mathbf{c}_{\mathrm{s}}(\theta)\|^2 = N$. The beamformer is a band-pass FIR beamformer steered to θ. Unlike Doppler processing, receive beamforming typically considers one beam direction at a time. Often in the same direction of the transmit beam. Reflections by clutter scatterers in MTI span the spatial spectrum. When observing the spatial spectrum alone, movers are masked by the clutter. In MTI, Doppler and spatial signals are examined simultaneously since a mover is distinguishable in Doppler. The Rayleigh resolution beamwidth of a ULA array is

$$\delta\theta = \frac{a_{\mathrm{s}}\lambda_{\mathrm{RF}}}{Nd} \tag{1.92}$$

where a_{s} is the beam-boarding factor [22]. An estimation of the spatial spectrum is presented in Figure 1.11. The maximum SNR beamformer produces a sinc-like response as well.

SINR is likewise a metric of performance in beamspace. The signal structure for temporal and spatial signals are similar in that they are complex sinusoids. Although, slow-time and element-

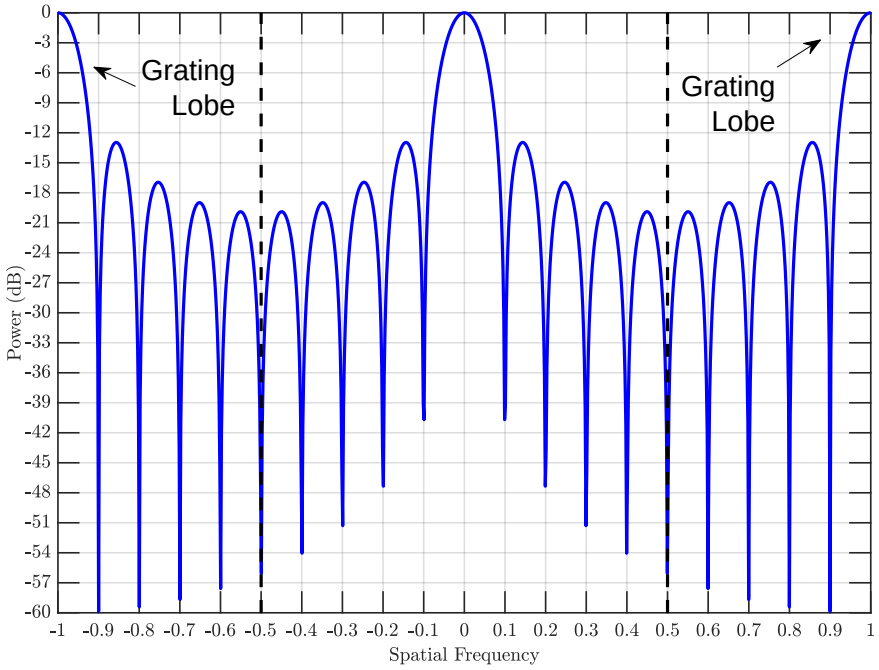

Fig. 1.11: Beampattern of receive beamformer electronically steered to boresight

space signals are obtained by different physical means. Beamspace SINR is straightforward to obtain using the estimate in (1.90) and a similar procedure from (1.67 - 1.75) from the previous section

$$\text{SINR}(\theta,\ell) = \frac{P_{\text{r}}(\theta,\ell)}{P_{\text{i}}(\theta,\ell)+P_{\text{v}}(\theta,\ell)} = \frac{\rho[\theta,\ell]\left|\mathbf{u}_{\text{BF}}^{H}(\theta)\,\mathbf{c}_{\text{s}}(\theta)\right|^{2}}{\mathbf{u}_{\text{BF}}^{H}(\theta)\,\mathbf{R}_{\text{s,opt}}(\ell)\,\mathbf{u}_{\text{BF}}(\theta)}. \tag{1.93}$$

where the signal power is $\rho[\theta,\ell] = E\{|\bar{x}[\theta,\ell]|^2\}$ [22]. The optimal spatial interference covariance matrix is

$$\mathbf{R}_{\text{s,opt}}(\ell) = \mathbf{R}_{\text{s,int}}(\ell) + \mathbf{R}_{\text{s,err}}(\ell) + \mathbf{R}_{\text{s,v}}(\ell). \tag{1.94}$$

where the spatial interference covariance matrix is $\mathbf{R}_{\text{s,int}}(\ell) = E\{\mathbf{i}_{\text{s}}(\ell)\mathbf{i}_{\text{s}}^{H}(\ell)\}$. The spatial error covariance matrix is

$$\mathbf{R}_{\text{s,err}}(\ell) = \sigma_{\text{s,err}}^{2}\mathbf{I}_{N\times N} \odot \sum_{\theta\in\Theta} \sigma^{2}[\theta,\ell]\,\mathbf{c}_{\text{s}}(\theta)\,\mathbf{c}_{\text{s}}^{H}(\theta) \tag{1.95}$$

where $\sigma^2_{\text{s,err}} = (1/N)E\{(\mathbf{h}_\text{s} - \mathbf{1}_{N\times 1})^H(\mathbf{h}_\text{s} - \mathbf{1}_{N\times 1})\}$ [23]. Lastly, the noise covariance matrix is

$$\mathbf{R}_{\text{s,v}}(\ell) = E\left\{\mathbf{v}_\text{s}(\ell)\,\mathbf{v}_\text{s}^H(\ell)\right\} = \sigma_\text{v}^2\mathbf{I}_{N\times N}. \tag{1.96}$$

The noise covariance assume array elements are IID and mutually uncorrelated such that the noise correlation element to element is $E\{v(i,\ell)v^*(j,\ell)\} = \sigma_\text{v}^2\delta_{ij}$ [4].

1.6 Windowing

Recall that the match filter is synonymous with the maximum SNR filter for pulse compression in fast-time signals. The Doppler filter and beamformer presented in the previous sections are likewise matched filters since they maximize SNR in their respective dimensions. Estimation of the Doppler and spatial spectrums result in a sinc response like in range delay with a LFM waveform. Accordingly, the primary drawback of matched processing in general is high power sidelobes relative to the peak power of the mainlobe.

Mismatch signal estimation is a class of receive processing techniques to reduce the sidelobe response and improve radar sensitivity. Mismatch filtering explores amplitude and/or phase modulation to the filters to modify the mainlobe and sidelobe response. One of the early and most common forms to mitigate sidelobes is windowing [8]. Windowing is an amplitude-only weighting of the filter taps which taper the transition regions of the filter. Windowing can be leveraged in fast-time, slow-time, and/or element-space to deviate from a sinc sidelobe response.

Windowing is a popular technique due to its low computation and simplicity to implement. There are a couple of drawbacks to windowing. First, there is an increase in the mainlobe resolution due to weighting inherently increases the spectral bandwidth. Second, a loss in SNR occurs due to processing mismatch. Caveats of windowing are acceptable since they come at the significant benefit of lower sidelobes. Examples of window functions include a Hamming, Taylor, or Chebyshev [8].

Windowing will be applied to slow-time signals to show the efficacy of the approach.

Translating windowing to other dimensions is straight forward using different steering vectors. A weighting is performed on the temporal steering vector

$$\mathbf{u}_{\mathrm{WDP}}(\omega) = \frac{\mathbf{c}_{\mathrm{t}}(\omega) \odot \mathbf{b}_{\mathrm{t}}}{(\mathbf{c}_{\mathrm{t}}(\omega) \odot \mathbf{b}_{\mathrm{t}})^{H} \mathbf{c}_{\mathrm{t}}(\omega)} \tag{1.97}$$

where $\mathbf{b}_{\mathrm{t}}$ denotes a $M \times 1$ temporal window. Although mismatch loss from the weighting is unavoidable, the form presented in (1.97) ensures $\mathbf{u}_{\mathrm{WDP}}(\omega)^{H} \mathbf{c}_{\mathrm{t}}(\omega) = 1$ to maintain signal strength. The filter is applied to the receive data

$$\hat{x}[\omega, \ell] = \mathbf{u}_{\mathrm{WDP}}^{H}(\omega) \mathbf{z}_{\mathrm{t}}(\ell). \tag{1.98}$$

Figure 1.12 presents an example of a Taylor window with five nearly constant sidelobe levels and a -40 dB peak sidelobe level being applied to a zero-Doppler slow-time signal. The benefit windowing has on sidelobes is apparent. However, Taylor weighting parameters exhibit widening of the mainlobe subsequently decreasing Doppler resolution. In subsequent chapters, optimal and

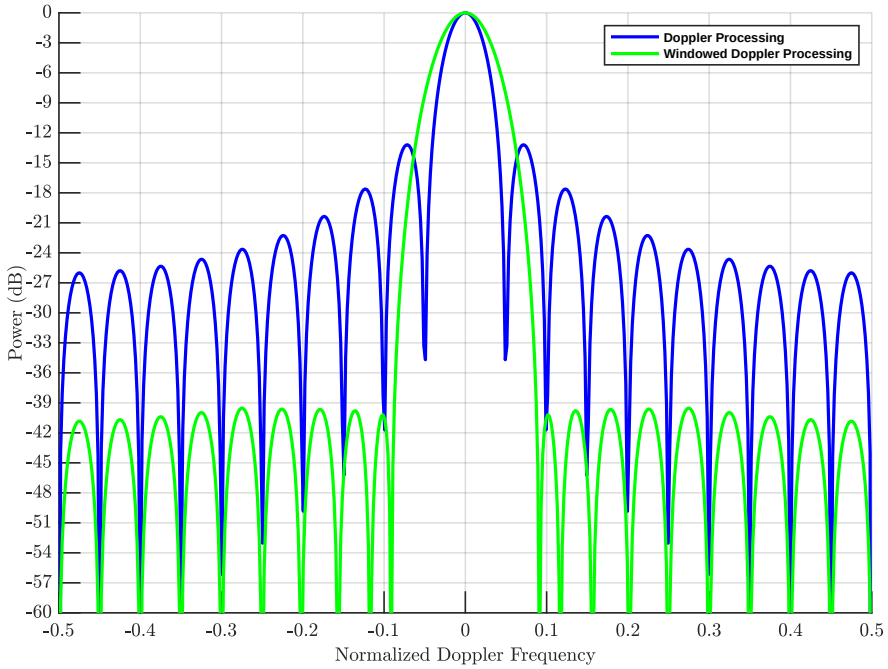

Fig. 1.12: Estimate of Doppler spectrum using Doppler filter (blue) and Taylor window (green)

adaptive mismatch processing methods, such as least-squares (LS) and re-iterative minimum-mean square error (RMMSE), are presented that can suppress sidelobes at a reduced mismatch loss and without sacrificing mainlobe width. These techniques leverage phase in addition to amplitude for their filter weights.

1.7 Space-Time Signals

The radar datacube presented in Figure 1.13 comprises of measurements from fast-time, slow-time, and element-space signals [28, 29]. Pulse compression is a 1-D convolution in fast-time to obtain range. Doppler processing is a 1-D spectral estimation of slow-time signals to obtain velocity. Receive beamforming is a 1-D spatial filtering across antenna elements to obtain angular location. Coupling dimensions provides improved fidelity in processing. A prime example is space-time adaptive processing (STAP) which is an angle-Doppler sequential clutter cancellation and spectral estimation technique for space-time signals. A space-time signal is a coupling of slow-time and element-space signals. The space-time signal model is presented as a precursor to the overview of STAP in the succeeding section.

Consider the reflections from a PD radar being collected on multiple antenna elements. Define M pulses in a CPI and N elements in a ULA. The receive signal for the mth PRI and nth element is

$$y(m,n,t) = \sum_{\omega\in\Omega}\sum_{\theta\in\Theta}\left[s(t) * x(\omega,\theta,t)\right] e^{j2\pi(\varepsilon_{\text{acc},m}\omega + n\theta)} + i(m,n,t) + v(m,n,t) \tag{1.99}$$

where $x(\omega,\theta,t)$ is the illuminated complex scatterers with a Doppler frequency ω and spatial frequency θ, $i[m,n,\ell]$ is the interference contribution, and $v[m,n,\ell]$ is the thermal noise contribution. The sets Ω and Θ contains the Doppler and spatial frequencies of all scatterers captured by the receiver. The cardinality of the sets are equal but their quantities are unknown. The receive space-time signal model after ADC and pulse compression as well as incorporating

model mismatch error is

$$z[m,n,\ell] = \sum_{\omega\in\Omega}\sum_{\theta\in\Theta} \bar{x}[\omega,\theta,\ell]\, e^{j2\pi(\varepsilon_{\text{acc},m}\omega+n\theta)} + \xi[m,n,\ell] + \bar{i}[m,n,\ell] + \bar{v}[m,n,\ell] \tag{1.100}$$

where $\bar{x}[\omega,\theta,\ell]$ is the complex amplitude with range sidelobes subsumed, $\xi[m,n,\ell]$ is the model mismatch error, $\bar{i}[m,n,\ell]$ is the interference post pulse compression, and $\bar{v}[m,n,\ell]$ is the thermal noise post pulse compression. For space-time signals, interference is substituted for clutter going forward in this chapter. A range sample of the radar datacube is a $M \times N$ space-time matrix

$$\mathbf{Z}_{\text{st}}(\ell) = \begin{bmatrix} z(0,0,\ell) & \cdots & z(0,N-1,\ell) \\ \vdots & \ddots & \vdots \\ z(M-1,0,\ell) & \cdots & z(M-1,N-1,\ell) \end{bmatrix} \tag{1.101}$$

The matrix is oriented into a $MN \times 1$ space-time data vector via vectorization

$$\mathbf{z}_{\text{st}}(\ell) = \text{vec}\{\mathbf{Z}_{\text{st}}(\ell)\} \tag{1.102}$$

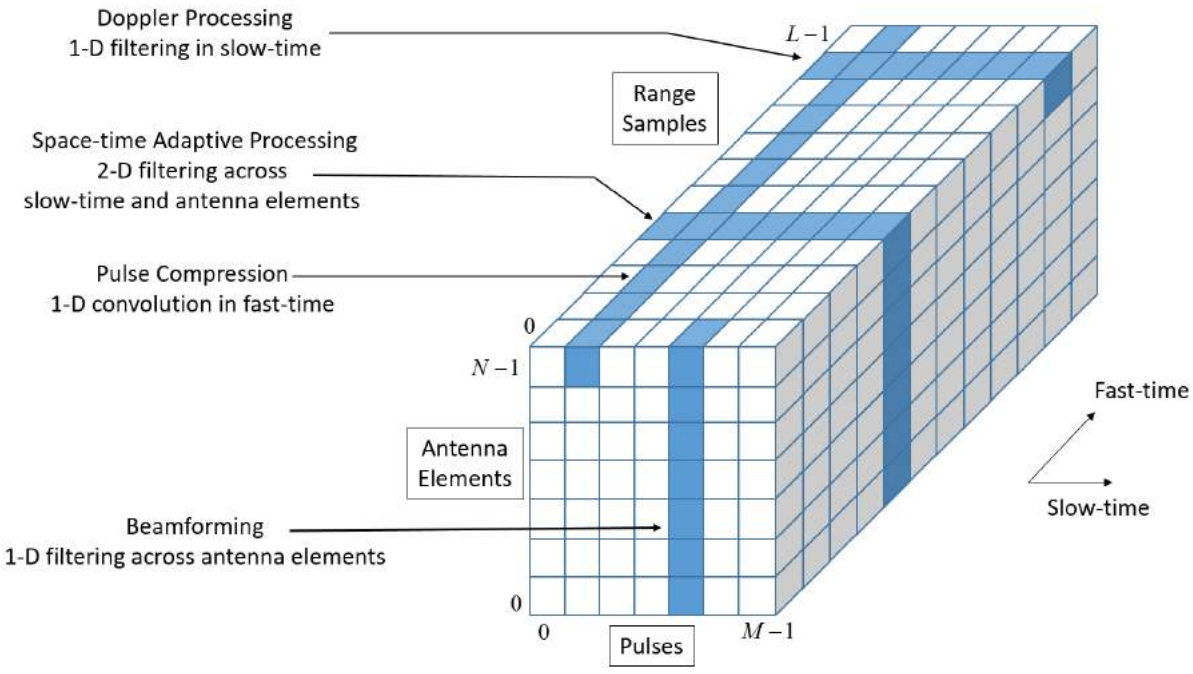

Fig. 1.13: Radar datacube

where vec$\{\bullet\}$ is the vectorization operation of a matrix [4]. Within the space-time data vector contains the familiar components of movers, clutter, model mismatch, and thermal noise

$$\begin{aligned}\mathbf{z}_{\text{st}}(\ell) = &\sum_{\omega_{\text{mov}}\in\Omega_{\text{mov}}}\sum_{\theta_{\text{mov}}\in\Theta_{\text{mov}}} x[\omega_{\text{mov}},\theta_{\text{mov}},\ell]\,\mathbf{c}_{\text{st}}(\omega_{\text{mov}},\theta_{\text{mov}}) \\ &+\sum_{\omega_{\text{clu}}\in\Omega_{\text{clu}}}\sum_{\theta_{\text{clu}}\in\Theta_{\text{clu}}} x[\omega_{\text{clu}},\theta_{\text{clu}},\ell]\,\mathbf{c}_{\text{st}}(\omega_{\text{clu}},\theta_{\text{clu}}) + \mathbf{e}_{\text{st}}(\ell) + \mathbf{v}_{\text{st}}(\ell).\end{aligned} \tag{1.103}$$

where the $MN\times 1$ space-time steering vector

$$\mathbf{c}_{\text{st}}(\omega,\theta) = \mathbf{c}_{\text{t}}(\omega)\otimes\mathbf{c}_{\text{s}}(\theta) \tag{1.104}$$

is a coupling of the temporal and spatial steering vectors with $\otimes$ denoting the Kronecker product, the $MN\times 1$ space-time error vector is $\mathbf{e}_{\text{st}}(\ell) = \mathbf{e}_{\text{t}}(\ell)\otimes\mathbf{e}_{\text{s}}(\ell)$, and the $MN\times 1$ thermal noise vector is $\mathbf{v}_{\text{st}}(\ell) = \mathbf{v}_{\text{t}}(\ell)\otimes\mathbf{v}_{\text{s}}(\ell)$. The space-time data vector is alternatively expressed as

$$\begin{aligned}\mathbf{z}_{\text{st}}(\ell) &= \mathbf{C}_{\text{st,mov}}\mathbf{x}_{\text{AD,mov}}(\ell) + \mathbf{C}_{\text{st,clu}}\mathbf{x}_{\text{AD,clu}}(\ell) + \mathbf{e}_{\text{st}}(\ell) + \mathbf{v}_{\text{st}}(\ell) \\ &= \mathbf{z}_{\text{st,mov}}(\ell) + \mathbf{z}_{\text{st,clu}}(\ell) + \mathbf{e}_{\text{st}}(\ell) + \mathbf{v}_{\text{st}}(\ell).\end{aligned} \tag{1.105}$$

where $\mathbf{C}_{\text{st,mov}}$ represents a $MN\times\mathfrak{c}\{\Omega_{\text{mov}}\}$ bank of space-time steering vectors corresponding to movers and $\mathbf{C}_{\text{st,clu}}$ represents the $MN\times\mathfrak{c}\{\Omega_{\text{clu}}\}$ bank of space-time steering vectors corresponding to clutter. Sets Ω and Θ are interchangeable here since they contain the same number of elements.

Receive processing of a space-time signal is performed via angle-Doppler filtering by coupling Doppler processing and receive beamforming

$$\hat{x}[\omega,\theta,\ell] = \frac{1}{MN}\sum_{m=0}^{M-1}\sum_{n=0}^{N-1} z[m,n,\ell]\,e^{-j2\pi(\varepsilon_{\text{acc},m}\omega+n\theta)} = \mathbf{u}_{\text{AD}}^{H}(\omega,\theta)\,\mathbf{z}_{\text{st}}(\ell) \tag{1.106}$$

where the the $MN\times 1$ angle-Doppler filter is

$$\mathbf{u}_{\text{AD}}(\omega,\theta) = \mathbf{u}_{\text{DP}}(\omega)\otimes\mathbf{u}_{\text{BF}}(\theta) = \frac{\mathbf{c}_{\text{st}}(\omega,\theta)}{\mathbf{c}_{\text{st}}^{H}(\omega,\theta)\,\mathbf{c}_{\text{st}}(\omega,\theta)} \tag{1.107}$$

Recall the Doppler spectrum is oversampled using a $M \times L_{\mathrm{D}}$ bank of Doppler filters. Spatial signals consider a single $N \times 1$ spatial steering vector a time. Coupling the bank of Doppler filters and beamformer forms a $MN \times L_{\mathrm{D}}$ bank of angle-Doppler filters for each spatial frequency

$$\mathbf{U}_{\mathrm{D}}(\theta) = \mathbf{U}_{\mathrm{DP}} \otimes \mathbf{u}_{\mathrm{BF}}(\theta). \tag{1.108}$$

The $L_{\mathrm{D}} \times 1$ Doppler spectrum estimate for each spatial frequency is

$$\hat{\mathbf{x}}_{\mathrm{D}}(\theta, \ell) = \mathbf{U}_{\mathrm{D}}^{H}(\theta)\, \mathbf{z}_{\mathrm{st}}(\ell). \tag{1.109}$$

The response is a Doppler spectrum for a single spatial frequency and range sample.

A SLAR observes clutter "moving" relative to the velocity of the platform. The platform motion induces a spectral spread in the clutter Doppler bandwidth and a clutter Doppler offset [6, 24]. Illuminated clutter scatterers are observed at all spatial frequencies. The relationship between Doppler frequency and spatial frequency for a radar on a moving platform is

$$\omega_{\mathrm{clu}} = \frac{2 v_{\mathrm{p}} T_{\mathrm{r}}}{d} \theta_{\mathrm{clu}} = \beta\, \theta_{\mathrm{clu}} \tag{1.110}$$

where v_{p} is the radar platform velocity and $\beta = 2 v_{\mathrm{p}} T_{\mathrm{r,avg}} / d$ is the interelement-spacing transversed in a single PRI [4]. The relaxation to a stationary platform is done by setting $v_{\mathrm{p}} = 0$ m/s. A radar mounted tangentially pointing left of the flight path (think right-handed coordinate system) senses clutter to be moving toward the radar and have a positive spatial frequency. Clutter moving away has a negative spatial frequency. In Figure 1.14, an example of 3-element array moving at $\beta = 1$ for 3 pulses is presented [4]. The figure considers a uniform PRI transmission and ULA. In Fig 1.15, a 2-D power spectral density of clutter for multiple β values is presented [4, 29]. When $\beta = 1$, the Doppler and spatial frequencies are unambiguous. When $0 < \beta < 1$, the data is spatially ambiguous. When $\beta > 1$, the data is Doppler ambiguous [4]. Longer ranges correspond to smaller cone angles leading to wider clutter bandwidths and vice versa [7]. Airborne affects, such as crab

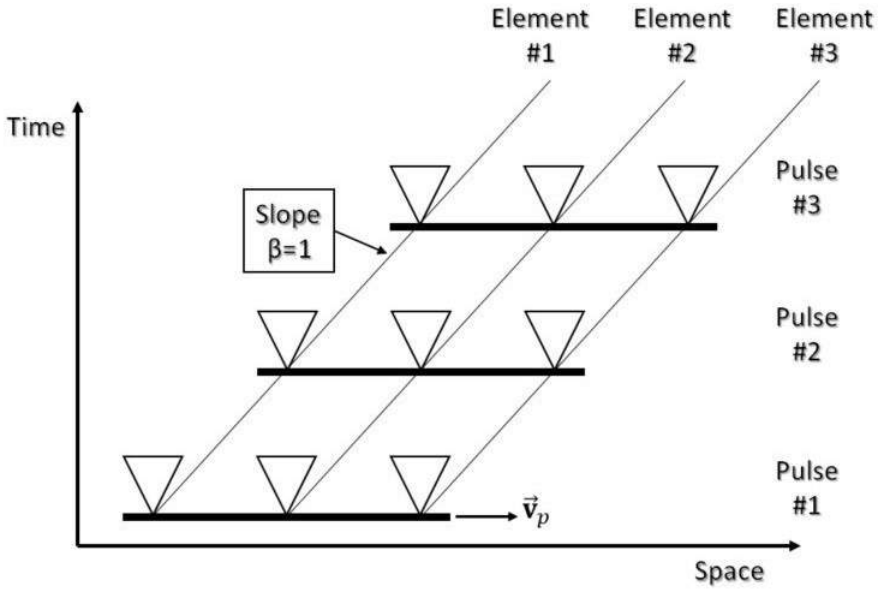

Fig. 1.14: A 3-element ULA traveling for 3 pulses in a CPI on moving platform for $\beta = 1$

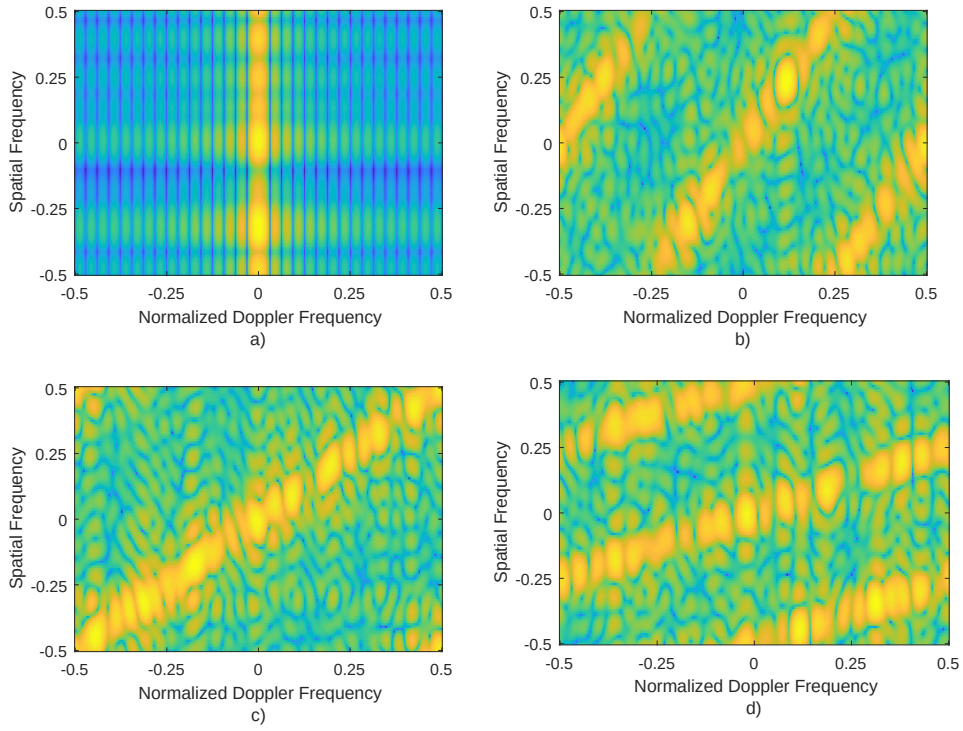

Fig. 1.15: Clutter ridges for $\beta = 0$ stationary platform, $\beta = 0.5$ moving platform (spatial ambiguity), $\beta = 1$ moving platform (no ambiguity), and $\beta = 2$ moving platform (Doppler ambiguity) [4, 29]

angle, play a role in the coupling as well [4].

Clutter scatterers being illuminated by a SLAR can be divided into range and angle clutter patches. A clutter patch is an aggregate of complex, coherent reflections from smaller scatterers [22]. Figure 1.16 depicts clutter patches in a scene [22, 29]. The scattering in the scene at the ℓth range bin is

$$\mathbf{z}_{\text{st,clu}}(\ell) = \sum_{i=0}^{N_{\text{cp}}-1} \sum_{j=0}^{N_{\text{a}}-1} \mathbf{a}_{ij}(\ell) \odot \mathbf{c}_{\text{st}}\left(\omega_{ij}, \theta_{ij}\right) \tag{1.111}$$

where N_{cp} is statistically independent clutter patches and N_{a} is the number of ambiguous ranges [22]. The clutter covariance matrix is

$$\mathbf{R}_{\text{st,clu}}(\ell) = \sum_{i=0}^{N_{\text{cp}}-1} \sum_{j=0}^{N_{\text{a}}-1} \mathbf{A}_{ij}(\ell) \odot \mathbf{c}_{\text{st}}\left(\omega_{ij}, \theta_{ij}\right) \mathbf{c}_{\text{st}}^{H}\left(\omega_{ij}, \theta_{ij}\right) \tag{1.112}$$

[22]. If the amplitudes are correlated from pulse-to-pulse and channel-to-channel, then $\mathbf{A}_{ij}(\ell) = \sigma_{\text{clu},ij}^{2}(\ell)\mathbf{1}_{MN\times MN}$ [22]. The rank of the clutter covariance matrix can be characterized by Brennan's Rule $r_{\text{st,clu}} = \text{rank}\{\mathbf{R}_{\text{st,clu}}(\ell)\} \approx \lfloor N + (M-1)\beta \rfloor$ [4, 30] where rank$\{\bullet\}$ denotes the rank of a matrix and $\lfloor \bullet \rfloor$ is a rounding operation to the next integer closet to $-\infty$.

The angle-Doppler SINR is determined using a similar process that was performed to determine

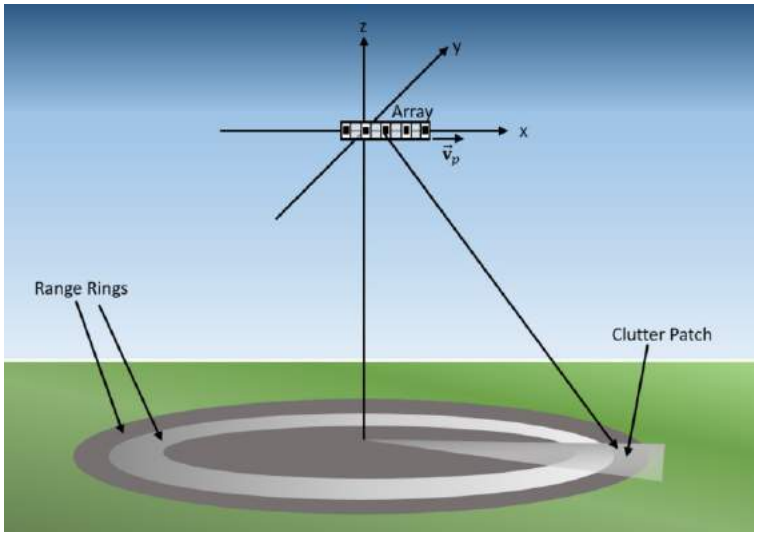

Fig. 1.16: Clutter patch in a radar scene

the Doppler SINR in (1.67 - 1.75)

$$\text{SINR}(\omega,\theta,\ell) = \frac{\rho[\omega,\theta,\ell]\left|\mathbf{u}_{\text{AD}}^{H}(\omega,\theta)\,\mathbf{c}_{\text{st}}(\omega,\theta)\right|^{2}}{\mathbf{u}_{\text{AD}}^{H}(\omega,\theta)\,\mathbf{R}_{\text{st,opt}}(\ell)\,\mathbf{u}_{\text{AD}}(\omega,\theta)} \tag{1.113}$$

[4, 22]. The optimal space-time interference covariance matrix is

$$\mathbf{R}_{\text{st,opt}}(\ell) = \mathbf{R}_{\text{st,clu}}(\ell) + \mathbf{R}_{\text{st,err}}(\ell) + \mathbf{R}_{\text{st,v}}(\ell). \tag{1.114}$$

The space-time error covariance matrix is

$$\mathbf{R}_{\text{st,err}}(\ell) = \mathbf{R}_{\text{t,err}}(\ell) \otimes \mathbf{R}_{\text{s,err}}(\ell) \tag{1.115}$$

using the temporal and spatial error covariance matrices from (1.69) and (1.95) respectively. Lastly, the noise covariance matrix is

$$\mathbf{R}_{\text{st,v}}(\ell) = \mathbf{R}_{\text{t,v}}(\ell) \otimes \mathbf{R}_{\text{s,v}}(\ell) = \sigma_{\text{v}}^{2}\mathbf{I}_{MN\times MN}. \tag{1.116}$$

1.8 Clutter Cancellation and Space-Time Adaptive Processing

Prior to this subsection, the maximization of signal strength has been explored. Maximum SNR filters in fast-time (match filter), slow-time (Doppler filter), and space (receive beamformer) are best for noise-limited environments and do not account for open-air interference. When performing GMTI, degradation to SINR by clutter is unavoidable. Clutter attenuation is a necessary step to unmask slower movers and increase SINR. Clutter has a center frequency at zero-Doppler and some Doppler bandwidth due to ICM. A high-pass Doppler filter known as a MTI filter is implemented to remove the clutter reflections since clutter is localized at zero Doppler frequency. For airborne radar, a Doppler frequency shifted band-stop filter is needed to account for the motion of the airborne platform. Typically, MTI filtering is performed prior to angle-Doppler processing for a sequential cancellation-then-estimation filtering procedure. There

are two methods to generate a MTI filter: data-independent and data-dependent. The dependence is based on the filter taps formation.

One fundamental data-independent method is a pulse canceller [24]. Pulse cancellers are kept at a low-order (around 3) [24]. The low-order FIR filter is computationally pleasing. Interestingly, the coefficients of the N-pulse canceler ($N-1$ filter order) [24] follows the Nth row of a Cholesky factorized Pascal's Triangle [31] normalized by N. A method for SLAR to compensate for the Doppler shift of clutter away from zero-Doppler is displaced phase center antenna (DPCA) processing [4]. In DPCA, delay between elements caused by platform motion is compensated for. A disadvantage to DPCA is that it requires $\beta = 1$, known as the DPCA condition, to be satisfied for operation [4].

Adaptive MTI filters are data-dependent approaches which use clutter statistics extracted from receive data to modify the MTI filter stopband frequencies. One method is a clutter projection that uses a singular value decomposition on the receive (i.e. a slow-time, fast-time data matrix). The highest singular value will correspond to the clutter due to its abundance. The corresponding slow-time singular vector is used to form a projection matrix to project away from the clutter subspace. For airborne radars, clutter spreads over multiple singular values due to the increased rank. Thus, a clutter projection on airborne data is difficult to implement without an estimation of the model order.

Space-time adaptive processing is a method to adaptively cancel clutter reflections for a SLAR. STAP attenuates clutter signals using a maximum SINR angle-Doppler filter. Below is a brief synopsis of the maximum SINR filter widely used for space-time signals [4, 7, 22, 32, 33]. Here, the error mismatch vector is incorporated into the maximum SINR filter since it resides in the optimal covariance matrix. Consider the following binary detection problem

$$\begin{aligned} &\text{Target Absent}-H_0 : \mathbf{z}_{H_0}(\ell) = \mathbf{z}_{\text{st,clu}}(\ell) + \mathbf{e}_{\text{st}}(\ell) + \mathbf{v}_{\text{st}}(\ell) \\ &\text{Target Present}-H_1 : \mathbf{z}_{H_1}(\ell) = \mathbf{z}_{\text{st,mov}}(\ell) + \mathbf{z}_{\text{st,clu}}(\ell) + \mathbf{e}_{\text{st}}(\ell) + \mathbf{v}_{\text{st}}(\ell). \end{aligned} \tag{1.117}$$

The target absent hypothesis characterizes the interfering sources. The optimal covariance matrix

leverages the target absent hypothesis

$$\mathbf{R}_{\text{st,opt}}(\ell) = E\left\{\mathbf{z}_{H_0}(\ell)\,\mathbf{z}_{H_0}^{H}(\ell)\right\} \tag{1.118}$$

[4, 22]. When expanded, the matrix in (1.118) becomes optimal covariance matrix in (1.114). The optimal covariance matrix fully characterizes the second order statistics of interference sources in the recieved signal. It can be shown that the optimal filter to maximize SINR is

$$\mathbf{w}_{\text{AD}}(\omega,\theta,\ell) = \psi\mathbf{R}_{\text{st,opt}}^{-1}(\ell)\,\mathbf{c}_{\text{st}}(\omega,\theta) \tag{1.119}$$

where ψ is a scalar term for normalization [4, 22]. Readers should review Appendix A for a detailed derivation of the maximum SNR and SINR filters.

A cancellation matrix is formed by scaling the optimal covariance matrix by the noise power

$$\mathbf{R}_{\text{st,canc}}(\ell) = \frac{1}{\sigma_{\text{v}}^2}\mathbf{R}_{\text{st,opt}}(\ell) \tag{1.120}$$

[34]. The cancellation matrix projects the signal component onto the orthogonal complement of the clutter subspace while preserving the full-rank noise [34]. Considering cancellation transform and matched filter normalizing terms together such that $\psi = 1/(\|\mathbf{c}_{\text{st}}(\omega,\theta)\|^2\sigma_{\text{v}}^2)$, the filter in (1.119) is modified to

$$\mathbf{w}_{\text{AD}}(\omega,\theta,\ell) = \mathbf{R}_{\text{st,canc}}^{-1}(\ell)\,\mathbf{u}_{\text{AD}}(\omega,\theta). \tag{1.121}$$

The form of (1.121) facilitates the replacement of the matched angle-Doppler filter by other mismatch processing techniques. The optimal filter contains the cancellation matrix to perform clutter cancellation and the angle-Doppler filtering for estimation. The

cancellation-then-estimation procedure is apparent in the application of the filter

$$\begin{aligned}\hat{x}(\omega,\theta,\ell) &= \mathbf{w}_{\mathrm{AD}}^{H}(\omega,\theta,\ell)\,\mathbf{z}_{\mathrm{st}}(\ell) \\ &= \mathbf{u}_{\mathrm{AD}}^{H}(\omega,\theta)\,\mathbf{R}_{\mathrm{st,canc}}^{-1}(\ell)\,\mathbf{z}_{\mathrm{st}}(\ell) \\ &= \mathbf{u}_{\mathrm{AD}}^{H}(\omega,\theta)\,\widehat{\mathbf{z}}_{\mathrm{st}}(\ell)\,.\end{aligned} \tag{1.122}$$

where the application of the cancellation transform matrix to the space-time receive data produces

$$\widehat{\mathbf{z}}_{\mathrm{st}}(\ell) = \mathbf{R}_{\mathrm{st,canc}}^{-1}(\ell)\,\mathbf{z}_{\mathrm{st}}(\ell) = \mathbf{z}_{\mathrm{st,mov}}(\ell) + \mathbf{e}_{\mathrm{st,mov}}(\ell) + \mathbf{v}_{\mathrm{st}}(\ell)\,. \tag{1.123}$$

Substituting the optimal filter from (1.121) into (1.113) results in the maximum SINR response

$$\begin{aligned}\mathrm{SINR}_{\mathrm{opt}}(\omega,\theta,\ell) &= \mathbf{u}_{\mathrm{AD}}^{H}(\omega,\theta)\,\mathbf{R}_{\mathrm{st,canc}}^{-1}(\ell)\,\mathbf{c}_{\mathrm{st}}(\omega,\theta) \\ &= \frac{\mathbf{c}_{\mathrm{st}}^{H}(\omega,\theta)\,\mathbf{R}_{\mathrm{st,canc}}^{-1}(\ell)\,\mathbf{c}_{\mathrm{st}}(\omega,\theta)}{\mathbf{c}_{\mathrm{st}}^{H}(\omega,\theta)\,\mathbf{c}_{\mathrm{st}}(\omega,\theta)}\end{aligned} \tag{1.124}$$

Knowledge of the cancellation covariance matrix is not possible since clutter is unknown a priori. Since the clutter is unknown, the cancellation matrix is estimated in receive processing. A common method to estimate the covariance matrix is using a maximum likelihood estimate method called the sample covariance matrix (SaCM) [4]. For a given data matrix (in this case space-time and range samples), a single range CUT is examined for its clutter characteristics. The target absent hypothesis is the primary response observed in the range cells. Therefore, multiple adjacent range cells to the CUT are used to train the SaCM. Using the CUT within the calculation leads to self-cancellation of the mover. Adjacent cells nearest to the CUT called guard cells will contain sidelobes of the mover. As a result, guard cells are also removed to avoid self-cancellation [4, 29, 35]. Taking self-cancellation into consideration, estimation of the clutter covariance matrix is

$$\hat{\mathbf{R}}_{\mathrm{st,canc}}(\ell) = \frac{1}{\mathfrak{c}\left\{L_{\mathrm{p}}\right\}\sigma_{\mathrm{v}}^{2}} \sum_{\substack{\iota \neq \ell \\ \iota \in L_{\mathrm{p}}}} \mathbf{z}_{\mathrm{st}}(\iota)\,\mathbf{z}_{\mathrm{st}}^{H}(\iota) + \sigma_{\mathrm{v}}^{2}\mathbf{I}_{MN\times MN} \tag{1.125}$$

where L_{p} is the set of range samples remaining after the CUT and guard cells are removed [4, 35].

The Reed, Mallett, and Brennan (RMB) rule defined in [36] states that $\mathfrak{c}\{L_{\mathrm{p}}\} = 2MN - 3$ homogeneous samples are necessary to be within 3 dB of the optimal covariance matrix. In general, the homogeneous assumption implies the covariance matrix is the same for every range sample

$$\mathbf{R}_{\mathrm{opt}} = \mathbf{R}_{\mathrm{opt}}(\ell) \ \ \forall \ell \tag{1.126}$$

[35]. As mentioned earlier, the clutter environment is often heterogeneous. Furthermore, due to a finite time interval being collected and processed, only a limited numbers of samples are available for training the covariance matrix. For this reason, achieving the IID assumption is difficult. The estimation stage will contain some unavoidable residual error due to its imperfection. Nevertheless, the assumption is useful to provide a baseline for performance.

The covariance matrix would need to be estimated and inverted for every range CUT for maximum performance. Performing these matrix operation multiple times can be computationally expensive. Estimation of the optimal covariance matrix requires a computation of $O\left\{\mathfrak{c}\left\{L_{\mathrm{p}}\right\}M^2N^2\right\}$ [37]. The computation becomes approximately $O\left\{2M^3N^3\right\}$ assuming sample support is available to satisfy RMB rule. The computation cost for matrix inversion is $O\left\{M^3N^3\right\}$ [37]. For a space-time signal, the number of pulses is the primary culprit to increase computation since more energy-on-target and higher Doppler resolution is desirable. To mitigate computation complexity, reduced-rank techniques are utilized [4, 32, 33].

Reduced-rank techniques employ a linear transformation to obtain a solution in a lower rank subspace. Assuming the optimal covariance matrix is available, reduced-rank processing performance can be no better than full-rank processing [38]. Reduce-rank techniques are useful for practical application of high dimension covariance matrices in adaptive processing. When using an estimated covariance matrix, reduce rank processing outperforms full-rank processing by suppressing estimation errors [38]. Reduce-rank processing reduces the amount of samples needed to satisfy the RMB rule for a covariance matrix from $\mathfrak{c}\{L_{\mathrm{p}}\} \approx 2MN$ to $\mathfrak{c}\{L_{\mathrm{p}}\} \approx 2r_{\mathrm{st,clu}}$

covariance matrix [38]. The clutter covariance matrix is known to be low rank [4, 7]. The diagonal loading term seen in the cancellation matrix ensures the noise subspace is at the measured noise floor. The loading term also improves the condition number and ensures the matrix is full rank.

Denote D_{t} as the desired rank of the slow-time dimension, which is also the number of pulses in a sub-CPI, and a $M \times D_{\mathrm{t}}$ Doppler transformation matrix $\mathbf{T}_{\mathrm{t}}$. Likewise denote D_{s} as the desired rank of the element-space dimension, which is number of elements in a sub-array, and a $N \times D_{\mathrm{s}}$ spatial transformation matrix $\mathbf{T}_{\mathrm{s}}$. A $MN \times D_{\mathrm{t}} D_{\mathrm{s}}$ space-time transformation matrix is formed by coupling the matrices

$$\mathbf{T}_{\mathrm{st}} = \mathbf{T}_{\mathrm{t}} \otimes \mathbf{T}_{\mathrm{s}} \tag{1.127}$$

[4]. Figure 1.17 presents the multiple reduction configurations [4, 29]. The reduction of the slow-time samples can be performed pre- or post-Doppler processing. There is an equivalent duel for reduction of element-space samples in element- and beamspace. There are data-dependent and fixed methods of forming the transformation matrix [38–44]. One common fixed transformation method is based on the steering vectors of the signals is used. For angle and Doppler processing, steering vectors is equivalent to using a DFT matrix. The advantage of a fixed transformation is the computational efficiency needed to employ reduce dimension techniques is less than the

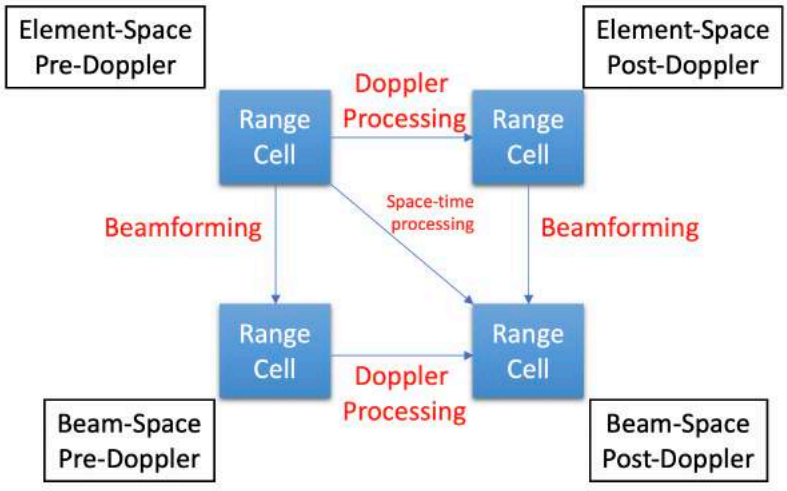

Fig. 1.17: Reduced dimension configurations

data-dependent methods [38]. The formation of the transformation matrix depends on the type of processing to be performed.

The transformation matrix is applied to the receive space-time data vector to form a $D_{\mathrm{t}}D_{\mathrm{s}} \times 1$ reduce dimension data vector

$$\tilde{\mathbf{z}}_{\mathrm{st}}(\ell) = \mathbf{T}_{\mathrm{st}}^{H}\mathbf{z}_{\mathrm{st}}(\ell) \tag{1.128}$$

where $\tilde{\bullet}$ denotes a reduced rank quantity, [4]. Leveraging the application of the transformation matrix in (1.128) into the binary detection problem in (1.117), a $D_{\mathrm{t}}D_{\mathrm{s}} \times D_{\mathrm{t}}D_{\mathrm{s}}$ cancellation covariance matrix can be formed

$$\tilde{\mathbf{R}}_{\mathrm{st,canc}}(\ell) = \mathbf{T}_{\mathrm{st}}^{H}\mathbf{R}_{\mathrm{st,canc}}(\ell)\mathbf{T}_{\mathrm{st}} \tag{1.129}$$

[4]. Utilizing a maximum SINR filter formulation, it can be shown that the partially adaptive maximum SINR filter is

$$\tilde{\mathbf{w}}_{\mathrm{AD}}(\omega,\theta,\ell) = \tilde{\mathbf{R}}_{\mathrm{st,canc}}^{-1}(\ell)\,\tilde{\mathbf{u}}_{\mathrm{AD}}(\omega,\theta) \tag{1.130}$$

where the reduced rank space-time steering vector is

$$\tilde{\mathbf{c}}_{\mathrm{st}}(\omega,\theta) = \mathbf{T}_{\mathrm{st}}^{H}\mathbf{c}_{\mathrm{st}}(\omega,\theta) \tag{1.131}$$

leading to the reduce rank filter $\tilde{\mathbf{u}}_{\mathrm{AD}}(\omega,\theta)$. The lower rank filter is mapped to the full-rank filter. Thus, the equivalent maximum SINR filter utilizing a rank-reduction is

$$\begin{aligned}\mathbf{w}_{\mathrm{AD}}(\omega,\theta,\ell) &= \mathbf{T}_{\mathrm{st}}\tilde{\mathbf{w}}_{\mathrm{AD}}(\ell,\omega,\theta)\\ &= \mathbf{T}_{\mathrm{st}}\left(\mathbf{T}_{\mathrm{st}}^{H}\mathbf{R}_{\mathrm{st,canc}}\mathbf{T}_{\mathrm{st}}\right)^{-1}\mathbf{T}_{\mathrm{st}}^{H}\mathbf{u}_{\mathrm{AD}}(\omega,\theta).\end{aligned} \tag{1.132}$$

Reduced dimension processing reduces the computation complexity of matrix inversion via rank-reduction is $O\left(L_{\mathrm{D}}L_{\mathrm{S}}D_{\mathrm{t}}^{3}D_{\mathrm{s}}^{3}\right)$. Estimation of the optimal covariance matrix requires a computation of $O\left(\mathfrak{c}\left\{L_{\mathrm{p}}\right\}L_{\mathrm{D}}L_{\mathrm{S}}D_{\mathrm{t}}^{3}D_{\mathrm{s}}^{3}\right)$ such that $\mathfrak{c}\left\{L_{\mathrm{p}}\right\} = 2D_{\mathrm{t}}D_{\mathrm{s}}$. Subsumed into the transformation is a normalization that ensures the main diagonal of $\mathbf{T}_{\mathrm{st}}\mathbf{T}_{\mathrm{st}}^{H}$ are ones and the

off-diagonal terms are scaled appropriately. For an oversampled spectrum, the off-diagonal terms deviate from the ideal case of zeros. The deviation leads to a mismatch error within the transformation. Post-Doppler processing (in element-space and beamspace) simultaneously reduces the rank and performs Doppler processing within the same matrix. In [4], multi-window post-Doppler STAP applies different Doppler filters to each reflection received on each antenna element.

This work considers a element-space post-Doppler formulation only due to the small amount of array elements used within simulation and experimental results. The element-space post-Doppler STAP processing utilizes the match filter bank for rank reduction. The number of the slow-time samples are reduced from M to D_{t} such that $D_{\mathrm{t}} << M$. In [45], a form called adjacent-bin was introduced for the multi-window post-Doppler transformation matrix. Leveraging the bank of temporal steering vectors, the adjacent-bin temporal transformation matrix is

$$\mathbf{T}_{\mathrm{t}}(\omega) = \frac{1}{\sqrt{L_D}}[\ \mathbf{c}_{\mathrm{t}}(\omega - A_{\mathrm{t}}\Delta\omega) \quad \cdots \quad \mathbf{c}_{\mathrm{t}}(\omega - \Delta\omega) \quad \mathbf{c}_{\mathrm{t}}(\omega) \quad \mathbf{c}_{\mathrm{t}}(\omega + \Delta\omega) \quad \cdots \quad \mathbf{c}_{\mathrm{t}}(\omega + A_{\mathrm{t}}\Delta\omega)\ ] \tag{1.133}$$

where $A_{\mathrm{t}} = (D_{\mathrm{t}} - 1)/2$ is the surrounding temporal steering vectors on each side of the Doppler frequency of interest [4, 45]. The post-Doppler implementation is a reduction of the oversampling from L_{D} to D_{t} and not M to D_{t}. There is nothing withstanding $D_{\mathrm{t}} \geq M$. For a computationally benefit, its intuitive to make $D_{\mathrm{t}} << M$. Element-space reduction will not be performed. Since reduction is not being performed, no manipulation of the beamformer occurs. Therefore, the spatial transformation matrix is simply

$$\mathbf{T}_{\mathrm{s}}(\theta) = \mathbf{I}_{N \times N} \tag{1.134}$$

meaning $D_{\mathrm{s}} = N$ [4]. Coupling the two dimensions using (1.127) produces the space-time transformation matrix

$$\mathbf{T}_{\mathrm{st}}(\omega, \theta) = \mathbf{T}_{\mathrm{t}}(\omega) \otimes \mathbf{I}_{N \times N} \tag{1.135}$$

making the transformation of function of Doppler frequency and independent of spatial frequency

[4]. The benefit of the smaller covariance matrix for inversion comes at the price of having to perform the inverse multiple times.

Chapter 2

Adaptive Mismatch Doppler Processing for Uniform and Staggered Pulse Repetition Interval Radar

Illumination of a radar scene at a uniform pulse repetition interval (PRI) generates a uniform sampling in slow-time. Uniform sampling is favorable when using a Fourier transform (FT) to obtain the Doppler spectrum. Uniform PRI transmission also introduces a well-known trade-space between unambiguous range and unambiguous velocity/Doppler that is dictated by the PRI and pulse repetition frequency (PRF), respectively. In the Doppler spectrum, frequencies above the PRF, which is also the slow-time sampling frequency, alias into the interval $[-\text{PRF}/2, \text{PRF}/2]$. The aliasing in the spectrum makes Doppler frequencies above and below the PRF indistinguishable in integer multiples of the PRF. Furthermore, implementation of a moving target indication (MTI) filter for clutter cancellation causes blind speeds in the Doppler spectrum at intervals of the PRF [6, 24, 25]. MTI filtering is designed as a high-pass filter which becomes a comb filter due to aliasing. Lastly, performing a oversampled discrete FT (DFT) to obtain the Doppler spectrum incurs a undesirable sinc roll-off in the Doppler spectrum due to the temporal limitation of the receive slow-time signal. Clutter sidelobe responses from the sinc roll-off may mask other low-power, slow traveling movers. Typically, windowing the slow-time data provides adequate sidelobe suppression at the penalty of a widen mainlobe and mismatch loss.

PRI staggering is a pulse diversity scheme to increase unambiguous velocity, eliminate aliasing, and remove blind speeds in a pulse-Doppler radar [24, 25]. Staggering varies the PRI pulse-to-pulse resulting in a non-uniform slow-time sampling (see Figure 1.7 in Chapter 1 on slow-time signals for an example). PRI staggering uniquely samples a complex sinusoid corresponding to

a Doppler shift to diminish aliasing and expand the Doppler spectrum. The Doppler spectrum is obtained by compensating for non-uniform sampling in the temporal component of the FT (see (1.60)). Staggering is known to be effective in increasing the maximum detectable velocity. In junction with MTI filtering, staggering provides greater clutter suppression and has a smaller effect on mover energy being attenuated [46].

Staggering by a random selection of PRIs comes at the penalty of degraded sidelobe roll-off [47]. Figure 2.1 illustrates an example of Doppler processing for uniform and staggered PRI transmissions with and without windowing. The example uses a Taylor window [48] with a -40 dB peak sidelobe and five nearly constant sidelobes. For the selection of staggers utilized in the example, the non-uniform PRI peak sidelobe is higher than uniform PRI. The sidelobe benefits of windowing is lost once staggering is implemented. As mentioned, staggering does provide a unambiguous response of the true target. However, having an unambiguous Doppler response with low sidelobes relative to the peak of the mover mainlobe is ideal.

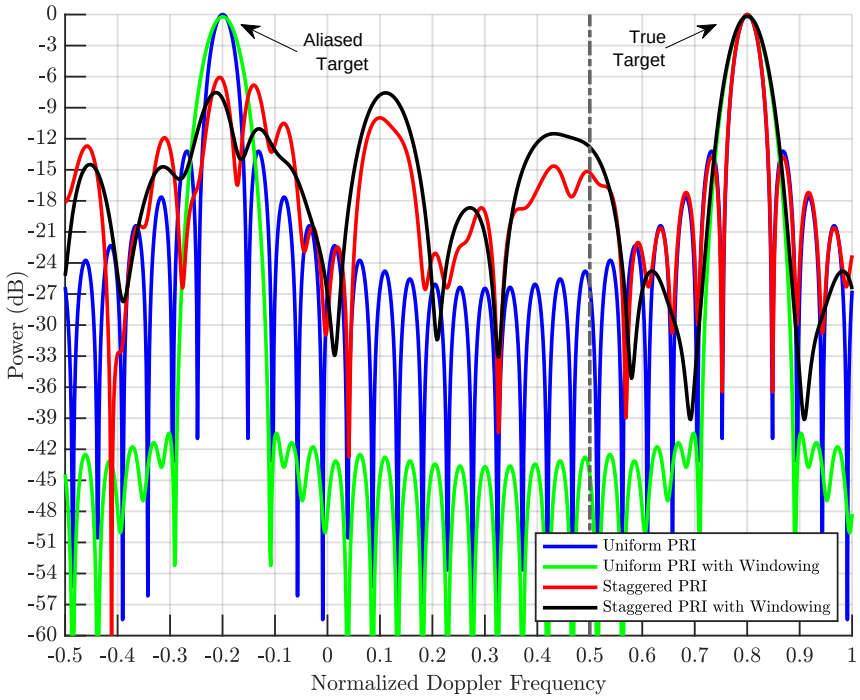

Fig. 2.1: Normalized Doppler response for a noise-free signal at +0.8 when applying Doppler processing and windowed Doppler processing (to reduce sidelobes) to a uniform PRI and a randomly staggered PRI

Non-uniform sampling arises in a variety of applications. Astronomers encounter non-uniform observations of space signals due to many environmental factors such as time of day and weather (e.g. [49, 50]), prompting the development of least-squares (LS) approaches for the generation of a periodogram [51–53]. Spectral analysis of non-uniform sampling has also received broader interest in the signal processing community. A myriad of publications addresses non-uniform sampling using Capon method, multiple-signal characterization method (MUSIC), root-MUSIC, and estimation of signal parameters via rotational invariance technique (ESPRIT) [54–59]. One major drawback of these algorithms is that they require the number of signal sources in the data to be known. In [60], the authors introduced a non-parametric iterative weighted LS approach called real-valued iterative adaptive approach (RIAA). The algorithm was shown to provide a performance benefit over previous proposed LS periodogram approaches. RIAA method was likewise leveraged for missing samples in uniform data (another form a non-uniform sampling) and shown to provide separation of targets [61–63].

In the radar community, the effects of non-uniform slow-time sampling via PRI staggering were first examined for Doppler processing and MTI filtering in [46, 64, 65]. Later, [66] specifically examined the effects of random staggers on MTI filtering showing that blind speeds can be mitigated via random staggering. LS approaches have been proposed for a uniform PRI system implementing Doppler processing in [67, 68]. A super resolution approach for pulse-to-pulse staggering was introduced in [69] using an all-pole/autoregressive spectral analysis. Additionally, the authors provided a method for real-time application using an iterative search algorithm. In [70], clutter suppression for phase-coded waveforms for fixed PRI, non-uniform PRI, and coherent-on-receive radar was presented. The filters were generated based on second-order cone programming and minimum variance distortion-less response (MVDR) optimization approaches. The latter includes implementing an iterative approach akin to re-iterative minimum mean-squared error (RMMSE) for coherent-on-receive processing. A drawback, highlighted in [70], is the high computation cost to generate the adaptive filters. Implementing the RMMSE filter on-line is difficult because of the computational liability.

To address the deleterious sidelobe effects of PRI staggering, a form of RMMSE called adaptive mismatch Doppler processing (AMMDP) is proposed. Adaptive Doppler processing using RMMSE was first proposed in [19] for time-range adaptive processing (TRAP) as a joint 2-D range-Doppler adaptive filter with adaptive pulse compression (APC), a RMMSE approach for fast-time signals [71, 72], to mitigate range sidelobe modulation and interference in pulse-agile systems. A joint range-angle filter called space-range adaptive processing (SRAP) was similarly proposed in [20] for pulse-agile systems. AMMDP is a slow-time dual to re-iterative super-resolution (RISR), a spectral estimation technique originally proposed for adaptive direction-of-arrival (DOA) estimation for element-space signals [23]. More recently, practical implementation of RISR for DOA estimation were presented in [73, 74]. RISR was also examined for DOA estimation of non-uniform spatial samples in sparse co-prime arrays [75, 76]. The authors leveraged RISR for estimation of a virtual array manifold then subsequently perform MUSIC for spatial smoothing. A RMMSE transform to a DFT implementation was presented for stretch processing in [77]. Since stretch processing likewise uses a DFT matrix, the transform can also be leveraged in Doppler processing. More recently, forms of RISR for Doppler processing in unison with MTI filtering called baseline supplementary loading (BaSL) and baselines supplementary cancellation (BaSC) were proposed in [34] for joint and sequential clutter cancellation with spectral estimation, respectively. When AMMDP is combined with adaptive cancellation, it becomes a subset of the BaSC formulation. RMMSE has shown to be effective in addressing fast-time Doppler [78–80], mutual coupling calibration [81], and brain imaging [82] as well.

The computation complexity of implementing RISR is a result of inverting a high dimensional covariance matrix for every adaptive iteration and range sample. Rank reduction techniques have been proposed to address the computational complexity of RMMSE. One proposed computationally efficient method considered a rank-3 update that leverages the matrix inversion lemma [72]. In [83–85], fast APC (FAPC) reduced computation by performing a decomposition method (effectively a pre-pulse compression rank reduction) of the mean-square error (MSE) cost

function prior to filter generation. However, FAPC occasionally suppressed small targets in dense scattering. To mitigate these effects, a gain constrained version of APC, based on a MVDR framework, was used to minimize the mismatch loss and preserve the gain on lower power scatterers [86]. FAPC was later expanded to TRAP to show its viability on Doppler processing [87]. In [88], a gradient descent approach was proposed for RMMSE as an alternative to the matrix inverse for APC to mitigate computation for waveforms with large time-bandwidth products. In [89], match filter RMMSE (MF-RMMSE) exploits match filter outputs within the MSE framework. The technique minimized the MSE cost function post-pulse compression allowing for a smaller processing window while reducing sidelobe power. Overall, the computation of RMMSE has shown to be problematic to processing and research has been conducted to significantly reduce its effects.

A reduce rank form of RISR, known as reduced dimension RISR (RD-RISR), was presented in [90] for DOA estimation in multiple-input multiple-output (MIMO) radar. The authors present a data transformation approach to reduce the dimension of the data vector. However, the reduction in computation was a byproduct of an assumption of the MIMO transmission scheme and not a modification to the RISR cost function. Relaxing the transmission scheme to a single-input multiple-output (SIMO) scenario i.e., a single antenna transmission being collected at multiple receivers, the rank of the receive data vector would remain the same. The proposed RD-RISR algorithm then becomes the RISR algorithm and consequently cannot be utilized. Likewise, if the MIMO assumption made to reduce the rank of the algorithm is not satisfied, the proposed technique is not viable.

Within the space-time adaptive processing (STAP) radar community rank reduction using linear transformations of space-time signals is prevalent due to a similar problem of estimating and inverting a high dimensional covariance matrix and lack of sample support to train a covariance matrix. To facilitate real-time application, a computationally efficient approach called partial adaptive mismatch Doppler processing (PAMMDP) is introduced that leverages similar transformations. To summarize, RMMSE is proposed to address sidelobe degradation caused by

random PRI staggering. The proposed adaptive Doppler filter solution is combined with an adaptive MTI filter for a sequential cancellation-then-estimation procedure. Lastly, rank reduction techniques are explored to address the computationally complexity of the RMMSE procedure. The proposed techniques are examined via a Monte Carlo simulation and open-air experimentation captured at the University of Kansas Radar Systems and Remote Sensing Laboratory. Conclusions and future work are presented in Chapter 5. Portions of this work were presented in [91].

2.1 Slow-Time Signal Model and Clutter Cancellation

Brief synopses of the slow-time signal model and clutter cancellation utilized within this chapter are presented. Readers should refer to Sections 1.4 and 1.8, respectively, for detailed overviews. Consider a pulse-Doppler radar on a stationary platform transmitting radar waveform $s(t)$ for M PRIs. Denote $T_{\mathrm{r},m}$ as the mth PRI and $T_{\mathrm{r,avg}} = E\{T_{\mathrm{r},m}\} = (1/M)\sum_{m=0}^{M-1} T_{\mathrm{r},m}$ as the average PRI such that the mth normalized PRI is their ratio $\varepsilon_{\mathrm{r},m} = T_{\mathrm{r},m}/T_{\mathrm{r,avg}}$ for $m = 0,1,...,M-1$. The mth normalized accumulation time is a cumulative sum of normalized PRIs $\varepsilon_{\mathrm{acc},m} = \sum_{i=0}^{m-1} \varepsilon_{\mathrm{r},i}$. The illuminated scatterers captured on receive for the mth PRI is described in the following signal model

$$y(m,t) = \sum_{\omega} \left[s(t) * x(\omega,t) \right] e^{j2\pi\omega\varepsilon_{\mathrm{acc},m}} + v(m,t) \tag{2.1}$$

where ω is the normalized Doppler frequency. The receive signal is discretized in fast-time and pulse compressed to form range delay, slow-time samples

$$z[m,\ell] = \sum_{\omega} \bar{x}[\omega,\ell]\, e^{j2\pi\omega\varepsilon_{\mathrm{acc},m}} + \bar{v}[m,\ell] + \xi[m,\ell] \tag{2.2}$$

where, for the ℓth range sample, $\bar{x}[\omega,\ell]$ is the complex scattering recieved in the range-Doppler bin (including range sidelobe contributions from nearby scattering), $\bar{v}[m,\ell]$ is filtered thermal noise from pulse compression, and $\xi[m,\ell]$ is the model mismatch error.

A slow-time receive signal model is formed from the collection of illuminated scatterers for M pulses in a coherent processing interval (CPI) to form a $M \times 1$ slow-time data vector

$$\mathbf{z}_{\mathrm{t}}(\ell) = \sum_{\omega} \bar{x}[\omega, \ell]\, \mathbf{c}_{\mathrm{t}}(\omega) + \mathbf{e}_{\mathrm{t}}(\ell) + \mathbf{v}_{\mathrm{t}}(\ell) = \mathbf{C}_{\mathrm{t}} \mathbf{x}_{\mathrm{D}}(\ell) + \mathbf{e}_{\mathrm{t}}(\ell) + \mathbf{v}_{\mathrm{t}}(\ell) \tag{2.3}$$

where $\mathbf{c}_{\mathrm{t}}(\omega) = \begin{bmatrix} 1 & e^{j2\pi\omega\varepsilon_{\mathrm{acc},1}} & \cdots & e^{j2\pi\omega\varepsilon_{\mathrm{acc},M-1}} \end{bmatrix}^T$ is a $M \times 1$ temporal steering vector, $\mathbf{v}_{\mathrm{t}}(\ell)$ is a $M \times 1$ noise vector in slow-time, $\mathbf{e}_{\mathrm{t}}(\ell) = (\mathbf{C}_{\mathrm{t}} \mathbf{x}_{\mathrm{D}}(\ell)) \odot (\mathbf{h}_{\mathrm{t}} - \mathbf{1}_{M\times 1})$ is a $M \times 1$ model mismatch error vector, $\mathbf{h}_{\mathrm{t}} = \begin{bmatrix} e^{j2\pi\eta_{\mathrm{t},0}} & e^{j2\pi\eta_{\mathrm{t},1}} & \ldots & e^{j2\pi\eta_{\mathrm{t},M-}} \end{bmatrix}^T$ is a $M \times 1$ slow-time error vector the mth mismatch error $\eta_{\mathrm{t},m} = f_{\mathrm{D,err}} T_{\mathrm{err},m}$, $\mathbf{C}_{\mathrm{t}}$ is a $M \times L_{\mathrm{D}}$ bank of temporal steering vectors, and $\mathbf{x}_{\mathrm{D}}(\ell) = \begin{bmatrix} \bar{x}(-\omega_{\max}, \ell) & \cdots & \bar{x}(0, \ell) & \cdots & \bar{x}(\omega_{\max}, \ell) \end{bmatrix}^T$ is a $L_{\mathrm{D}} \times 1$ of Doppler frequency points in the Doppler spectrum at the ℓth range sample. The number of points in the Doppler spectrum is $L_{\mathrm{D}} = K_{\mathrm{D}} M$ where K_{D} is an oversampling factor. The signal component of the data vector can be decomposed into clutter and non-clutter components

$$\mathbf{z}_{\mathrm{t}}(\ell) = \mathbf{C}_{\mathrm{t,clu}} \mathbf{x}_{\mathrm{D,clu}}(\ell) + \mathbf{C}_{\mathrm{t,rem}} \mathbf{x}_{\mathrm{D,rem}}(\ell) + \mathbf{e}_{\mathrm{t,clu}}(\ell) + \mathbf{e}_{\mathrm{t,rem}}(\ell) + \mathbf{v}_{\mathrm{t}}(\ell). \tag{2.4}$$

The remaining components consist of movers and other target-absent portions of the spectrum. See Figure 2.2 for an example of information contained within radar scene.

Clutter reflections are attenuated using a high-pass Doppler filter. The high-pass filter can be characterized from clutter and noise covariance matrices. Combining the covariance matrices and normalizing by the noise power forms a $M \times M$ cancellation transform matrix

$$\mathbf{R}_{\mathrm{t,canc}}(\ell) = \frac{1}{\sigma_{\mathrm{v}}^2} \left(\mathbf{R}_{\mathrm{t,clu}}(\ell) + \mathbf{R}_{\mathrm{t,v}} \right) \tag{2.5}$$

where $\mathbf{R}_{\mathrm{t,clu}}(\ell)$ is the clutter covariance matrix and $\mathbf{R}_{\mathrm{t,v}} = E\{\mathbf{v}_{\mathrm{t}}(\ell)\, \mathbf{v}_{\mathrm{t}}^H(\ell)\} = \sigma_{\mathrm{v}}^2 \mathbf{I}_{M\times M}$ is the noise covariance matrix with noise power σ_{v}^2 [34]. When cancellation is not used, the cancellation transform is set to an identity matrix $\mathbf{R}_{\mathrm{t,canc}}(\ell) = \mathbf{I}_{M\times M}$. The clutter covariance matrix is estimated

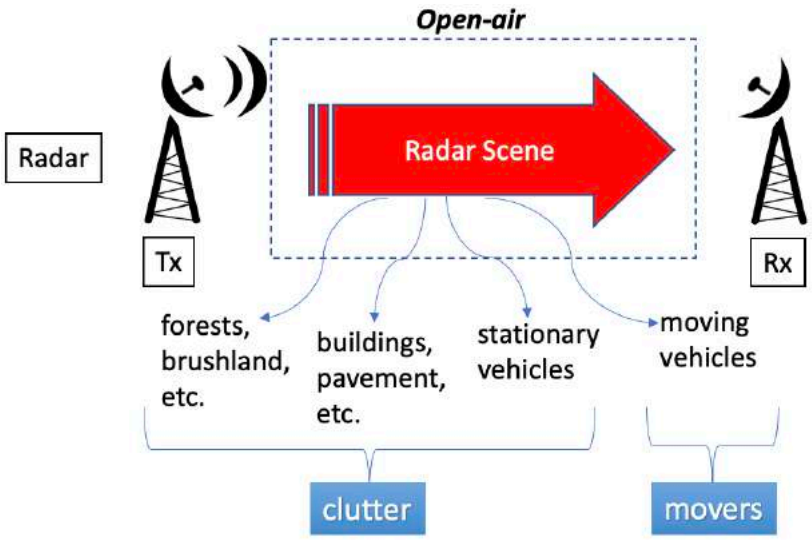

Fig. 2.2: Information contained within radar receive data

on receive using a sample covariance matrix (SaCM)

$$\hat{\mathbf{R}}_{\mathrm{t,clu}}(\ell) = \frac{1}{\mathfrak{c}\{L_{\mathrm{p}}\}} \sum_{\substack{\kappa \neq \ell \\ \kappa \in L_{\mathrm{p}}}} \mathbf{z}_{\mathrm{t}}(\kappa)\, \mathbf{z}_{\mathrm{t}}^{H}(\kappa) \tag{2.6}$$

where L_{p} is the set of range samples remaining after the range cell-under-test (CUT) and guard cells are removed to avoid self-cancellation [4]. The estimation of the clutter covariance matrix using receive data makes the high-pass Doppler filter adaptive. The adaptive filter is trained over range samples. The estimated clutter and noise covariance matrices are inserted into (2.5) to form an estimate of the cancellation matrix.

The optimal cancellation filter would be a brick wall high-pass filter that ensures clutter is fully suppressed while preserving signal strength in other Doppler frequencies. In the transition regions lies a minimum detectable velocity which is typically set to 3 dB loss from the filter peak. Additionally, mismatch and estimation loss from the cancellation transform is inevitable. Range sample support constraints and heterogeneous range samples tend to hinder the SaCM from satisfying Reed, Mallett, and Brennan (RMB) rule and the adaptive MTI filter frequency response from being within 3 dB of the optimal MTI filter frequency response. Overall, the adaptive filter inherently incurs loss and a frequency response away from the ideal filter. However, leveraging

the clutter statistics for cancellation has shown to provide the best "match" to the signal model of the clutter.

Utilizing the cancellation matrix on the signal vector results in the removal of the clutter components

$$\widehat{\mathbf{z}}_{\mathrm{t}}(\ell) = \mathbf{R}_{\mathrm{t,canc}}^{-1}(\ell)\,\mathbf{z}_{\mathrm{t}}(\ell) = \mathbf{C}_{\mathrm{t,rem}}\mathbf{x}_{\mathrm{D,rem}}(\ell) + \mathbf{e}_{\mathrm{t,rem}}(\ell) + \mathbf{v}_{\mathrm{t}}(\ell). \tag{2.7}$$

The maximum SNR Doppler filter $\mathbf{u}_{\mathrm{DP}}(\omega) = \mathbf{c}_{\mathrm{t}}(\omega)/M$ is applied to (2.7) obtain the maximum SINR estimate of at each Doppler frequency

$$\hat{x}_{\mathrm{DP}}[\omega,\ell] = \mathbf{u}_{\mathrm{DP}}^{H}(\omega)\,\widehat{\mathbf{z}}_{\mathrm{t}}(\ell) = \mathbf{u}_{\mathrm{DP}}^{H}(\omega)\,\mathbf{R}_{\mathrm{t,canc}}^{-1}(\ell)\mathbf{z}_{\mathrm{t}}(\ell) = \mathbf{w}_{\mathrm{DP}}^{H}(\omega,\ell)\mathbf{z}_{\mathrm{t}}(\ell) \tag{2.8}$$

where the maximum SINR Doppler filter is $\mathbf{w}_{\mathrm{DP}}(\omega,\ell) = \mathbf{R}_{\mathrm{t,canc}}^{-1}(\ell)\mathbf{u}_{\mathrm{DP}}(\omega)$. Windowing is incorporated into the formulation by replacing $\mathbf{u}_{\mathrm{DP}}(\omega)$ with

$$\mathbf{u}_{\mathrm{WDP}}(\omega) = \frac{\mathbf{c}_{\mathrm{t}}(\omega)\odot\mathbf{b}_{\mathrm{t}}}{(\mathbf{c}_{\mathrm{t}}(\omega)\odot\mathbf{b}_{\mathrm{t}})^{H}\mathbf{c}_{\mathrm{t}}(\omega)} \tag{2.9}$$

where $\mathbf{b}_{\mathrm{t}}$ is a $M\times 1$ slow-time taper. The windowed filter with cancellation is expressed as

$$\mathbf{w}_{\mathrm{WDP}}(\omega,\ell) = \mathbf{R}_{\mathrm{st,canc}}^{-1}(\ell)\,\mathbf{u}_{\mathrm{WDP}}(\omega). \tag{2.10}$$

The estimate after windowing is obtained similar to (2.8).

2.2 Adaptive Mismatch Doppler Processing

The estimate of the Doppler response at ω can be decomposed into the desired response and error sources corrupting the desired response

$$\hat{x}_{\mathrm{DP}}[\omega,\ell] = g[\omega,\omega,\ell]\bar{x}[\omega,\ell] + \sum_{\gamma\neq\omega} g[\omega,\gamma,\ell]\bar{x}[\gamma,\ell] + \hat{v}[\omega,\ell] \tag{2.11}$$

where the coefficient

$$g\left[\omega_i,\omega_j,\ell\right] = \frac{\mathbf{c}_{\mathrm{t}}^H(\omega_i)\mathbf{R}_{\mathrm{t,canc}}^{-1}(\ell)\mathbf{c}_{\mathrm{t}}(\omega_j)}{M} \tag{2.12}$$

corresponds to the frequency response of the clutter cancellation filter. The desired range-Doppler response is $d_{\mathrm{opt}} = g[\omega,\omega,\ell]\bar{x}[\omega,\ell]$. The error deviating the estimate from the desired response is $d_{\mathrm{err}} = \sum_{\gamma\neq\omega} g[\omega,\gamma,\ell]\bar{x}[\gamma,\ell] + \hat{v}[\omega,\ell]$. The ideal filter would ensure that $g\left[\omega_i,\omega_j,\ell\right] \triangleq 0$ for clutter frequencies when $\omega_i = \omega_{\mathrm{clu}}$ or $\omega_j = \omega_{\mathrm{clu}}$ and $g\left[\omega_i,\omega_j,\ell\right] \triangleq 1$ otherwise in the spectrum. When MTI filtering is not employed, the frequency response is $g[\omega,\omega,\ell] \triangleq 1$ for all ω. A general estimate of the desired response is obtained by applying a weight vector to the post-cancellation receive data $d_{\mathrm{est}} = \hat{x}[\omega,\ell] = \mathbf{u}^H(\omega,\ell)\,\widehat{\mathbf{z}}_{\mathrm{t}}(\ell)$ similar to (2.8). The desired and estimated responses are related by $d_{\mathrm{est}} = d_{\mathrm{opt}} + d_{\mathrm{err}}$. A MSE cost function is formed using d_{err}

$$J_{\mathrm{MSE}}(\omega,\ell) = E\left\{|d_{\mathrm{err}}|^2\right\} = E\left\{|d_{\mathrm{opt}} - d_{\mathrm{est}}|^2\right\} = E\left\{\left|g[\omega,\omega,\ell]\bar{x}[\omega,\ell] - \mathbf{u}^H(\omega,\ell)\,\widehat{\mathbf{z}}_{\mathrm{t}}(\ell)\right|^2\right\}. \tag{2.13}$$

The cost function is parabolic with absolute minimum located at $d_{\mathrm{err}} = 0$. When the error is minimized, $|d_{\mathrm{opt}}|^2 = |d_{\mathrm{est}}|^2$. An optimization is performed on the cost function to obtain the optimal filter. The MSE cost function in (2.13) is similar to the MSE cost function presented in [23, 71, 72]. Using the post-cancellation data vector modifies the MSE cost function to include the impact of the MTI filter on the estimated and desired responses. The cost function from [23, 71, 72] and (2.13) are equivalent when cancellation is not used. Therefore, the MSE cost function in (2.13) is a general form that includes a linear transformation which in this case is adaptive cancellation.

The minimum of the cost function is obtained by determining its slope at zero. The slope

is determined by taking the first order derivative using a complex gradient operation with real and imaginary partial derivatives. Consider an arbitrary $M \times 1$ vector $\mathbf{a} = [\ a_0 \quad a_1 \quad \cdots \quad a_{M-1}\ ]^T$ where the real and imaginary components of mth element is $a_m = p_m + jq_m$. The mth partial derivatives with respect to a_m using Wirtinger derivatives are

$$\begin{aligned} \frac{\partial}{\partial a_m} &= \frac{1}{2}\left(\frac{\partial}{\partial p_m} - j\frac{\partial}{\partial q_m}\right) \\ \frac{\partial}{\partial a_m^*} &= \frac{1}{2}\left(\frac{\partial}{\partial p_m} + j\frac{\partial}{\partial q_m}\right). \end{aligned} \tag{2.14}$$

The corresponding $M \times 1$ gradient vector operations with respect to $\mathbf{a}$ and $\mathbf{a}^*$ are $\nabla_{\mathbf{a}} = [\ \frac{\partial}{\partial a_0} \quad \frac{\partial}{\partial a_1} \quad \cdots \quad \frac{\partial}{\partial a_{M-1}}\ ]^T$ and $\nabla_{\mathbf{a}^*} = [\ \frac{\partial}{\partial a_0^*} \quad \frac{\partial}{\partial a_1^*} \quad \cdots \quad \frac{\partial}{\partial a_{M-1}^*}\ ]^T$, respectively [92]. Applying the operator to the MSE cost function with respect to $\mathbf{u}^*(\omega,\ell)$ results in

$$\nabla_{\mathbf{u}^*} J_{\text{MSE}}(\omega,\ell) = -E\{g^*[\omega,\omega,\ell]\bar{x}^*[\omega,\ell]\,\widehat{\mathbf{z}}(\ell)\} + E\{\widehat{\mathbf{z}}(\ell)\widehat{\mathbf{z}}^H(\ell)\}\mathbf{u}(\omega,\ell). \tag{2.15}$$

The dependence on ω and ℓ is subsumed on the gradient for notational convenience. Setting $\nabla_{\mathbf{u}^*} J_{\text{MSE}}(\ell) \triangleq 0$ and solving for $\mathbf{u}(\omega,\ell)$ produces the minimum mean-square error (MMSE) Doppler filter

$$\mathbf{u}_{\text{MMSE}}(\omega,\ell) = (E\{\widehat{\mathbf{z}}_{\text{t}}(\ell)\,\widehat{\mathbf{z}}_{\text{t}}^H(\ell)\})^{-1} E\{g^*[\omega,\omega,\ell]\bar{x}^*[\omega,\ell]\,\widehat{\mathbf{z}}(\ell)\} \tag{2.16}$$

where $E\{\widehat{\mathbf{z}}_{\text{t}}(\ell)\,\widehat{\mathbf{z}}_{\text{t}}^H(\ell)\}$ is a $M \times M$ auto-covariance matrix of the received data and $E\{g^*[\omega,\omega,\ell]\bar{x}^*(\omega,\ell)\,\widehat{\mathbf{z}}_{\text{t}}(\ell)\}$ is a $M \times 1$ cross-correlation vector between the receive data and desired Doppler spectrum.

The signal model from (2.7) is substituted into the data covariance matrix assuming all signal components and noise are uncorrelated to noise

$$E\{\widehat{\mathbf{z}}_{\text{t}}(\ell)\,\widehat{\mathbf{z}}_{\text{t}}^H(\ell)\} = \mathbf{C}_{\text{t,rem}}\mathbf{P}_{\text{D,rem}}(\ell)\,\mathbf{C}_{\text{t,rem}}^H + \mathbf{R}_{\text{t,err,rem}}(\ell) + \mathbf{R}_{\text{t,v}} \tag{2.17}$$

where $\mathbf{P}_{\mathrm{D,rem}}(\ell) = E\{\mathbf{x}_{\mathrm{D,rem}}(\ell)\,\mathbf{x}_{\mathrm{D,rem}}^{H}(\ell)\}$ is the $L_{\mathrm{D}} \times L_{\mathrm{D}}$ Doppler power distribution matrix and $\mathbf{R}_{\mathrm{t,err,rem}}(\ell) = E\{\mathbf{e}_{\mathrm{t,rem}}(\ell)\,\mathbf{e}_{\mathrm{t,rem}}^{H}(\ell)\}$ is the $M \times M$ error covariance matrix. The remaining steering vectors are unknown for an adaptive cancellation filter. The steering vectors can be approximated using the cancellation transform

$$\mathbf{R}_{\mathrm{t,canc}}^{-1}(\ell)\,\mathbf{C}_{\mathrm{t}} = \mathbf{R}_{\mathrm{t,canc}}^{-1}(\ell)\,[\mathbf{C}_{\mathrm{t,clu}}\ \mathbf{C}_{\mathrm{t,rem}}] \stackrel{\Delta}{=} [\mathbf{0}_{M\times L_{\mathrm{D,clu}}}\ \mathbf{C}_{\mathrm{t,rem}}] \tag{2.18}$$

where $L_{\mathrm{D,clu}} = \mathfrak{c}\{\Omega_{\mathrm{clu}}\}$ is the number of steering vectors corresponding to clutter which is equal to the cardinality of the set Ω_{clu}. Note, $L_{\mathrm{D}} = L_{\mathrm{D,clu}} + L_{\mathrm{D,rem}}$ where $L_{\mathrm{D,rem}} = \mathfrak{c}\{\Omega_{\mathrm{rem}}\}$ corresponds to the number of remaining steering vectors. The result is approximate since the cancellation matrix is estimated in practice.

The Doppler power distribution matrix is a covariance matrix of the Doppler spectrum. The diagonal is the power spectral density and the off-diagonals are the cross-correlation between frequencies. Define the elements of the distribution matrix as $\widehat{\rho}\left[\omega_i, \omega_j, \ell\right]$ where ω_i corresponds to rows and ω_j corresponds to columns. The complex scattering is assumed to be statistically independent in the Doppler spectrum [23]. Thus, terms in the power distribution matrix becomes

$$\widehat{\rho}\left[\omega_i, \omega_j, \ell\right] = \begin{cases} E\left\{|\bar{x}[\omega_i, \ell]|^2\right\}|g[\omega_i, \omega_i, \ell]|^2 & i = j \\ 0 & i \neq j \end{cases} \tag{2.19}$$

forming a diagonal matrix. The frequencies terms for the diagonal components are subsumed such that $\widehat{\rho}[\omega_i, \omega_i, \ell]$ is written as $\widehat{\rho}[\omega_i, \ell]$. The power distribution matrix after incorporating the statistically independence becomes

$$\mathbf{P}_{\mathrm{D,rem}}(\ell) \approx \widehat{\mathbf{P}}_{\mathrm{D}}(\ell) = E\left\{\mathbf{x}_{\mathrm{D}}(\ell)\,\mathbf{x}_{\mathrm{D}}^{H}(\ell)\right\} \odot \mathbf{g}_{\mathrm{D}}(\ell)\,\mathbf{g}_{\mathrm{D}}^{H}(\ell) \odot \mathbf{I}_{L_{\mathrm{D}}\times L_{\mathrm{D}}} \tag{2.20}$$

where the frequency response of the MTI filter is $\mathbf{g}_{\mathrm{D}}(\ell) = [\ g(-\omega_{\max}, -\omega_{\max}, \ell) \ \cdots\ g(0,0,\ell) \ \cdots\ g(\omega_{\max}, \omega_{\max}, \ell)\ ]^T$ corresponding to the

diagonal terms of the distribution matrix. The error covariance matrix is

$$\begin{aligned}\mathbf{R}_{\mathrm{t,err,rem}}(\ell) &= \sigma_{\mathrm{err}}^2\mathbf{I}_{M\times M}\odot\mathbf{C}_{\mathrm{t,rem}}\mathbf{P}_{\mathrm{D,rem}}(\ell)\,\mathbf{C}_{\mathrm{t,rem}}^H \\ &\approx \mathbf{R}_{\mathrm{t,err}}(\ell) \\ &= \sigma_{\mathrm{err}}^2\mathbf{I}_{M\times M}\odot\mathbf{R}_{\mathrm{t,canc}}^{-1}(\ell)\,\mathbf{C}_{\mathrm{t}}\widehat{\mathbf{P}}_{\mathrm{D}}(\ell)\,\mathbf{C}_{\mathrm{t}}^H\mathbf{R}_{\mathrm{t,canc}}^{-1}(\ell)\end{aligned} \tag{2.21}$$

after including assumptions made for the power distribution matrix and remaining steering vectors. The noise covariance matrix is the same as presented in (2.5). Substituting the data vector in (2.7) into the cross-correlation vector from (2.16) forms

$$E\{g^*[\omega,\omega,\ell]\,\bar{x}^*[\omega,\ell]\,\widehat{\mathbf{z}}(\ell)\} = \rho[\omega_{\mathrm{rem}},\ell]\,\mathbf{c}_{\mathrm{t}}(\omega_{\mathrm{rem}}) \approx \widehat{\rho}[\omega,\ell]\,\mathbf{R}_{\mathrm{t,canc}}^{-1}(\ell)\mathbf{c}_{\mathrm{t}}(\omega) \tag{2.22}$$

where $\rho_{\mathrm{rem}}[\omega,\ell] \approx \widehat{\rho}[\omega,\ell]$ using (2.19). The modifications to the data covariance matrix and cross-correlation vector are incorporated into the MMSE filter in (2.16) to produce a structured based MMSE Doppler filter

$$\mathbf{u}_{\mathrm{MMSE}}(\omega,\ell) = \widehat{\rho}[\omega,\ell]\,\mathbf{Q}_{\mathrm{t}}^{-1}(\ell)\,\mathbf{R}_{\mathrm{t,canc}}^{-1}(\ell)\mathbf{c}_{\mathrm{t}}(\omega) \tag{2.23}$$

where the structure covariance matrix (StCM) is

$$\begin{aligned}\mathbf{Q}_{\mathrm{t}}(\ell) &= \mathbf{R}_{\mathrm{t,canc}}^{-1}(\ell)\,\mathbf{C}_{\mathrm{t}}\widehat{\mathbf{P}}_{\mathrm{D}}(\ell)\,\mathbf{C}_{\mathrm{t}}^H\mathbf{R}_{\mathrm{t,canc}}^{-1}(\ell) + \sigma_{\mathrm{err}}^2\mathbf{I}_{M\times M}\odot\mathbf{R}_{\mathrm{t,canc}}^{-1}(\ell)\,\mathbf{C}_{\mathrm{t}}\widehat{\mathbf{P}}_{\mathrm{D}}(\ell)\,\mathbf{C}_{\mathrm{t}}^H\mathbf{R}_{\mathrm{t,canc}}^{-1}(\ell) + \sigma_{\mathrm{v}}^2\mathbf{I}_{M\times M} \\ &= \mathbf{R}_{\mathrm{t,canc}}^{-1}(\ell)\,\mathbf{C}_{\mathrm{t}}\widehat{\mathbf{P}}_{\mathrm{D}}(\ell)\,\mathbf{C}_{\mathrm{t}}^H\mathbf{R}_{\mathrm{t,canc}}^{-1}(\ell)\odot\left(\sigma_{\mathrm{err}}^2\mathbf{I}_{M\times M}+\mathbf{1}_{M\times M}\right)+\sigma_{\mathrm{v}}^2\mathbf{I}_{M\times M}\end{aligned} \tag{2.24}$$

and $\mathbf{1}_{M\times M}$ is a $M\times M$ matrix of all ones.

The multiple loading terms in StCM offer different benefits to the solution. The model error covariance matrix is a signal-dependent loading term which establishes a dynamic range of the estimates [23]. The term prevents the presence of spurious signals in the Doppler spectrum that would otherwise arise from modeling mismatch. The error power σ_{err}^2 is determined through

empirical analysis of the timing jitter imperfections. High fidelity components will allow for the error noise power to be much less than the noise floor. The noise covariance matrix is an inherent regularization that ensures the eigenvalues are no less than the noise power. The result lowers the condition number of the matrix which avoids inaccuracies in the final solution after implementing a matrix inversion.

The MMSE Doppler filter is applied to the receive data to obtain a MMSE estimate

$$\begin{aligned}\hat{x}_{\text{MMSE}}[\omega,\ell] &= \mathbf{u}^{H}_{\text{MMSE}}(\omega,\ell)\,\widehat{\mathbf{z}}_{\text{t}}(\ell)\\ &= \mathbf{w}^{H}_{\text{MMSE}}(\omega,\ell)\mathbf{z}_{\text{t}}(\ell)\\ &= \widehat{\rho}[\omega,\ell]\mathbf{c}^{H}_{\text{t}}(\omega)\mathbf{R}^{-1}_{\text{t,canc}}(\ell)\mathbf{Q}^{-1}(\ell)\mathbf{R}^{-1}_{\text{t,canc}}(\ell)\mathbf{z}(\ell)\end{aligned} \tag{2.25}$$

where the combination of the MTI filter for cancellation and MMSE Doppler filter for spectral estimation is

$$\mathbf{w}_{\text{MMSE}}(\omega,\ell) = \mathbf{R}^{-1}_{\text{t,canc}}(\ell)\mathbf{u}_{\text{MMSE}}(\omega,\ell) = \widehat{\rho}\,[\omega,\ell]\,\mathbf{R}^{-1}_{\text{t,canc}}(\ell)\mathbf{Q}^{-1}(\ell)\mathbf{R}^{-1}_{\text{t,canc}}\mathbf{c}_{\text{t}}(\omega). \tag{2.26}$$

A $M \times L_{\text{D}}$ bank of MMSE Doppler filters is formed by expanding the filter to multiple Doppler frequencies

$$\begin{aligned}\mathbf{U}_{\text{MMSE}}(\ell) &= \mathbf{Q}^{-1}(\ell)\mathbf{R}^{-1}_{\text{t,canc}}\mathbf{C}_{\text{t}}\widehat{\mathbf{P}}_{\text{D}}(\ell)\\ &= [\ \mathbf{u}_{\text{MMSE}}(-\omega_{\max},\ell)\ \ \cdots\ \ \mathbf{u}_{\text{MMSE}}(0,\ell)\ \ \cdots\ \ \mathbf{u}_{\text{MMSE}}(\omega_{\max},\ell)\ ].\end{aligned} \tag{2.27}$$

Note that the StCM is independent of Doppler frequency. Application of the filter bank results in the MMSE estimate of the Doppler spectrum

$$\hat{\mathbf{x}}_{\text{MMSE}}(\ell) = \mathbf{U}^{H}_{\text{MMSE}}(\ell)\,\widehat{\mathbf{z}}_{\text{t}}(\ell). \tag{2.28}$$

Consider the MMSE filter structure obtained in (2.26) and the original MMSE solution in [23]. Aside from the obvious distinction between the different dimensions in which they are applied

(slow-time and element-space, respectively), the difference in the solutions lie in the modification of the power distribution matrix to explicitly include filtering beforehand. The power distribution matrix presented here incorporates the frequency response of the cancellation into the cost function. For slow-time signals, it is appropriate to high-pass filter the signal for clutter cancellation. In this chapter specifically an adaptive high-pass filter is implemented. Although pulse cancellers is sufficient for stationary platforms, the approach is ineffective for random PRI staggering. Since the MSE cost function is generalized, the filter can also be a band-pass, low-pass, or band-stop filter. Other filters would be appropriate for interference cancellation. Chapter 3, for example, explores a 2-D band-stop filter with MMSE for space-time signals in airborne ground MTI radar.

The power distribution matrix requires the known desired Doppler spectrum to form the MMSE filter. The spectrum is of course unknown a priori. If the spectrum was known, the procedure to estimate it would be unnecessary. This "chicken or the egg" dilemma for MMSE is resolved by forming an estimate of the spectrum and using the response to form the MMSE filter. The RMMSE algorithm, presented in [23, 71, 72], took the substitution stage a step further by updating the power distribution matrix from a previous estimate using a iterative procedure. Each iteration gets closer to the desired response by minimizing the residual error. RMMSE is efficient in suppressing sidelobes and resolving signals. AMMDP implements RMMSE for slow-time signals.

The algorithm can suppress sidelobes beyond the noise floor. Additionally, a super resolution effect beyond the nominal resolution results in a mismatch loss. To maintain stability, a linear constraint is incorporated for RMMSE. The constrained version of RMMSE was introduced for fast-time signals [86]. The constraint was translated to RISR in [93] which also contained the introduction of a partial constrained version of RMMSE for low SNR spatial signals.

A linearly constrained minimum-variance (LCMV) framework [92] is considered for AMMDP. LCMV minimizes the average output power of the linear filter while the response is constrained to a complex amplitude. The complex amplitude constraint for AMMDP when considering clutter cancellation is Doppler frequency dependent because the cancellation response incurs distortion at clutter frequencies and is distortionless at remaining frequencies. The noise normalization being

applied to the cancellation matrix allows for the frequency response in (2.12) to be used as the gain constraint $\mathbf{u}^H(\omega,\ell)\mathbf{R}^{-1}_{\mathrm{t,canc}}(\ell)\mathbf{c}_{\mathrm{t}}(\omega) = g[\omega,\omega,\ell]$ to maintain the distortion at a given Doppler frequency. The gain constraint is adaptive since it is a function of the adaptive cancellation.

Figure 2.3 presents an example of the adaptive constraints using the frequency response and ideal constraints considering a known location of clutter. In portions of the spectrum where clutter is present, the adaptive constraint approaches a null constraint. In portions of the spectrum where clutter is not present, the constraint approaches a MVDR solution. When cancellation is not being employed i.e., $\mathbf{R}^{-1}_{\mathrm{t,canc}}(\ell) = \mathbf{I}_{M\times M}$, the constraint becomes a MVDR solution $\mathbf{u}^H(\omega,\ell)\mathbf{c}_{\mathrm{t}}(\omega) = 1$ since $g[\omega,\omega,\ell] = 1$ for all ω. A MVDR constraint was considered for RMMSE in [86, 93]. A similar procedure is presented here.

The constrained MSE cost function using a Lagrange multiplier λ_{L} is

$$\begin{aligned} J_{\mathrm{MSE}}(\omega,\ell) = E\{|g[\omega,\omega,\ell]\bar{x}[\omega,\ell] - \mathbf{u}^H(\omega,\ell)\widehat{\mathbf{z}}_{\mathrm{t}}(\ell)|^2\} \\ + \mathrm{Re}\{\lambda^*_{\mathrm{L}}\left(\mathbf{u}^H(\omega,\ell)\mathbf{R}^{-1}_{\mathrm{t,canc}}(\ell)\mathbf{c}_{\mathrm{t}}(\omega) - g[\omega,\omega,\ell]\right)\}. \end{aligned} \tag{2.29}$$

The adaptive filter is obtained by minimizing the cost function and incorporating the expanded

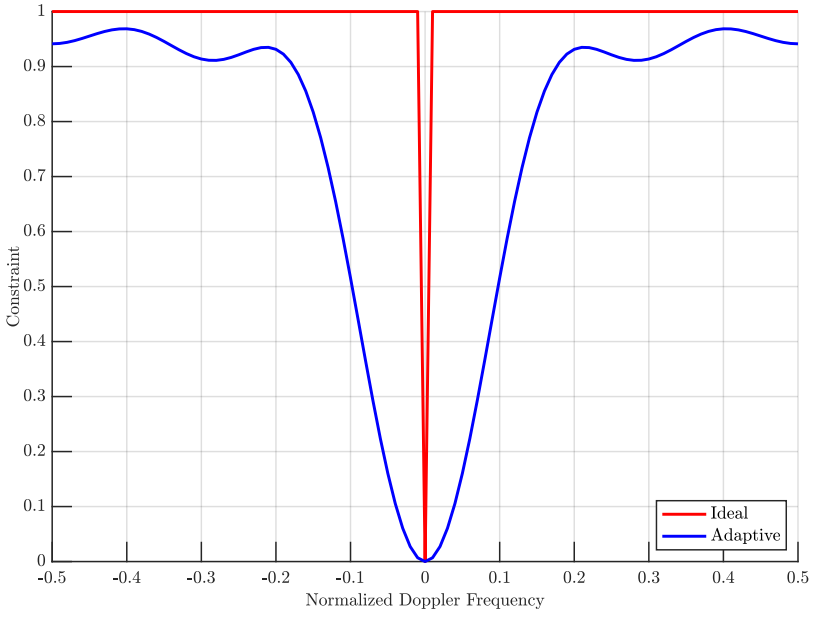

Fig. 2.3: Example of LCMV constraints for RMMSE with ideal and adaptive cancellation

expectations

$$\begin{aligned}\mathbf{u}_{\text{MMSE,con}}(\omega,\ell) &= \left(E\{\widehat{\mathbf{z}}_{\text{t}}(\ell)\widehat{\mathbf{z}}_{\text{t}}^{H}(\ell)\}\right)^{-1}\left(E\{g^{*}[\omega,\omega,\ell]\vec{x}^{*}[\omega,\ell]\widehat{\mathbf{z}}_{\text{t}}(\ell)\} - \frac{\lambda_{\text{L}}}{2}\mathbf{R}_{\text{t,canc}}^{-1}(\ell)\mathbf{c}_{\text{t}}(\omega)\right)\\ &= \left(\widehat{\rho}[\omega,\ell] - \frac{\lambda_{\text{L}}}{2}\right)\mathbf{Q}_{\text{t}}^{-1}(\ell)\mathbf{R}_{\text{t,canc}}^{-1}(\ell)\mathbf{c}_{\text{t}}(\omega).\end{aligned} \tag{2.30}$$

The constraint is evaluated using the inner product between the steering vector and filter

$$\begin{aligned}\mathbf{u}_{\text{MMSE,con}}^{H}(\omega,\ell)\,\mathbf{R}_{\text{t,canc}}^{-1}(\ell)\mathbf{c}_{\text{t}}(\omega) &= \left(\rho[\omega,\ell] - \frac{\lambda_{\text{L}}}{2}\right)\mathbf{c}_{\text{t}}^{H}(\omega)\mathbf{R}_{\text{t,canc}}^{-1}(\ell)\mathbf{Q}_{\text{t}}^{-1}(\ell)\mathbf{R}_{\text{t,canc}}^{-1}(\ell)\mathbf{c}_{\text{t}}(\omega)\\ &= g[\omega,\omega,\ell].\end{aligned} \tag{2.31}$$

The inner product is then solved for the Lagrange multiplier

$$\frac{\lambda_{\text{L}}}{2} = \rho[\omega,\ell] - \frac{g[\omega,\omega,\ell]}{\mathbf{c}_{\text{t}}^{H}(\omega)\mathbf{R}_{\text{t,canc}}^{-1}(\ell)\mathbf{Q}_{\text{t}}^{-1}(\ell)\mathbf{R}_{\text{t,canc}}^{-1}(\ell)\mathbf{c}_{\text{t}}(\omega)}. \tag{2.32}$$

Substituting the Lagrange multiplier into (2.30) produces the constrained MMSE filter

$$\mathbf{u}_{\text{MMSE,con}}(\omega,\ell) = \frac{g[\omega,\omega,\ell]\mathbf{Q}_{\text{t}}^{-1}(\ell)\mathbf{R}_{\text{t,canc}}^{-1}(\ell)\mathbf{c}_{\text{t}}(\omega)}{\mathbf{c}_{\text{t}}^{H}(\omega)\mathbf{R}_{\text{t,canc}}^{-1}(\ell)\mathbf{Q}_{\text{t}}^{-1}(\ell)\mathbf{R}_{\text{t,canc}}^{-1}(\ell)\mathbf{c}_{\text{t}}(\omega)}. \tag{2.33}$$

The MMSE filter presented in (2.16) and (2.23) is redefined as a unconstrained MMSE filter. The application of the constrained filter to the receive data is

$$\begin{aligned}\hat{x}_{\text{MMSE,con}}[\omega,\ell] &= \mathbf{u}_{\text{MMSE,con}}^{H}(\omega,\ell)\,\widehat{\mathbf{z}}_{\text{t}}(\ell)\\ &= \frac{g^{*}[\omega,\omega,\ell]\mathbf{c}_{\text{t}}^{H}(\omega)\mathbf{R}_{\text{t,canc}}^{-1}(\ell)\mathbf{Q}_{\text{t}}^{-1}(\ell)\mathbf{R}_{\text{t,canc}}^{-1}(\ell)\mathbf{z}_{\text{t}}(\ell)}{\mathbf{c}_{\text{t}}^{H}(\omega)\mathbf{R}_{\text{t,canc}}^{-1}(\ell)\mathbf{Q}_{\text{t}}^{-1}(\ell)\mathbf{R}_{\text{t,canc}}^{-1}(\ell)\mathbf{c}_{\text{t}}(\omega)}.\end{aligned} \tag{2.34}$$

The constrained solution suppresses sidelobes to the post coherent gain noise floor (which is set when filtering noise using standard Doppler processing). Therefore, for sidelobe energy to be suppressed, the sidelobe energy must be above the noise floor. the gain constrained RMMSE is

great for unmasking mover reflections obscured by sidelobes not noise

Oversampling beyond the nominal resolution to account for straddling makes RMMSE susceptible to mismatch loss. Beamspoiling was proposed for RMMSE in [94] for continuous waveforms to maintain the nominal resolution and overcome performance degradation from straddling. The waveforms in [94] were oversampled beyond the 3 dB range resolution. The spectrum can similarly be oversampled beyond the 3 dB Doppler resolution for Doppler processing to addresses straddling in the domain.

Beamspoiling was initially incorporated into the MSE cost function by modifying the bank of steering vectors in fast-time prior to the gain constraint [94]. Similar processing for slow-time is ineffective since the basis functions within signal matrix differ. The basis functions for fast-time signals are time-shifted versions of the waveform represented as a convolution matrix. Slow-time signals on the other hand use a bank of complex sinusoids represented by a oversampled DFT matrix. Accordingly, a new form of beamspoiling for Doppler processing is proposed. The MMSE Doppler with beamspoiling is

$$\mathbf{u}_{\text{MMSE,beam}}(\omega,\ell) = \frac{\sqrt{K_{\text{D}}}\sum\limits_{k_{\text{D}}=-K_{\text{D}}}^{K_{\text{D}}} \mathbf{u}_{\text{MMSE,con}}(\omega+k_{\text{D}}\Delta\omega,\ell)\,\mathbf{c}_{\text{t}}^{H}(\omega+k_{\text{D}}\Delta\omega)\,\mathbf{c}_{\text{t}}(\omega)}{\sum\limits_{k_{\text{D}}=-K_{\text{D}}}^{K_{\text{D}}} \mathbf{c}_{\text{t}}^{H}(\omega+k_{\text{D}}\Delta\omega)\,\mathbf{c}_{\text{t}}(\omega)}. \tag{2.35}$$

The beamspoiling formulation incorporates the adjacent filters to the extent of the mainlobe response in turn widening the mainlobe.

The AMMDP initializes by applying the maximum SINR Doppler filter to the receive data

$$\hat{\mathbf{x}}_{\text{AMMDP},0}(\ell) = \mathbf{U}_{\text{DP}}^{H}\hat{\mathbf{R}}_{\text{t,canc}}^{-1}(\ell)\,\mathbf{z}_{\text{t}}(\ell). \tag{2.36}$$

The first stage of the procedure estimates the ith power distribution matrix using the previous Doppler estimate

$$\hat{\mathbf{P}}_{\text{AMMDP},i}(\ell) = \hat{\mathbf{x}}_{\text{AMMDP},i-1}(\ell)\,\hat{\mathbf{x}}_{\text{AMMDP},i-1}^{H}(\ell) \odot \mathbf{I}_{L_{\text{D}}\times L_{\text{D}}}. \tag{2.37}$$

Note the term $\mathbf{g}_{\mathrm{D}}(\ell)$ as seen in (2.20) is subsumed into (2.37) due to the cancellation in the previous estimate (shown in (2.36) and (2.41)). Next, the StCM is formed using the power distribution matrix, noise power, and error power

$$\hat{\mathbf{Q}}_{\mathrm{AMMDP},i}(\ell) = \hat{\mathbf{R}}^{-1}_{\mathrm{t,canc}}(\ell)\,\mathbf{C}_{\mathrm{t}}\hat{\mathbf{P}}_{\mathrm{AMMDP},i}(\ell)\,\mathbf{C}_{\mathrm{t}}^{H}\hat{\mathbf{R}}^{-1}_{\mathrm{t,canc}}(\ell) \odot \left(\mathbf{1}_{M\times M} + \sigma^2_{\mathrm{err}}\mathbf{I}_{M\times M}\right) + \sigma^2_{\mathrm{v}}\mathbf{I}_{M\times M}. \tag{2.38}$$

The constrained filter is then formed using the StCM

$$\hat{\mathbf{u}}_{\mathrm{AMMDP,con},i}(\omega,\ell) = \frac{\hat{g}[\omega,\omega,\ell]\hat{\mathbf{Q}}^{-1}_{\mathrm{AMMDP},i}(\ell)\,\hat{\mathbf{R}}^{-1}_{\mathrm{t,canc}}(\ell)\,\mathbf{c}_{\mathrm{t}}(\omega)}{\mathbf{c}_{\mathrm{t}}^{H}(\omega)\,\hat{\mathbf{R}}^{-1}_{\mathrm{t,canc}}(\ell)\,\hat{\mathbf{Q}}^{-1}_{\mathrm{AMMDP},i}(\ell)\,\hat{\mathbf{R}}^{-1}_{\mathrm{t,canc}}(\ell)\,\mathbf{c}_{\mathrm{t}}(\omega)} \tag{2.39}$$

where $\hat{g}[\omega,\omega,\ell]$ is formed using (2.12) and the estimated cancellation matrix. Beamspoiling is then conducted for each range-Doppler bin,

$$\hat{\mathbf{u}}_{\mathrm{AMMDP,beam},i}(\omega,\ell) = \frac{\sqrt{K_{\mathrm{D}}}\sum\limits_{k_{\mathrm{D}}=-K_{\mathrm{D}}}^{K_{\mathrm{D}}}\hat{\mathbf{u}}_{\mathrm{AMMDP,con}}(\omega+k_{\mathrm{D}}\Delta\omega,\ell)\,\mathbf{c}_{\mathrm{t}}^{H}(\omega+k_{\mathrm{D}}\Delta\omega)\,\mathbf{c}_{\mathrm{t}}(\omega)}{\sum\limits_{k_{\mathrm{D}}=-K_{\mathrm{D}}}^{K_{\mathrm{D}}}\mathbf{c}_{\mathrm{t}}^{H}(\omega+k_{\mathrm{D}}\Delta\omega)\,\mathbf{c}_{\mathrm{t}}(\omega)}. \tag{2.40}$$

A bank of beamspoiled filters is generated similar to (2.27) and subsequently applied to the receive data to obtain the updated estimate of the spectrum

$$\hat{\mathbf{x}}_{\mathrm{AMMDP},i}(\ell) = \hat{\mathbf{U}}^{H}_{\mathrm{AMMDP,beam},i}(\ell)\,\hat{\mathbf{R}}^{-1}_{\mathrm{t,canc}}(\ell)\,\mathbf{z}_{\mathrm{t}}(\ell). \tag{2.41}$$

The procedure returns to (2.37) and concludes after a user-defined number of iterations.

A comparison of Doppler processing, unconstrained AMMDP, constrained AMMDP, and beamspoiled AMMDP after five iterations is illustrated in Figure 2.4. A mover is placed at a normalized Doppler frequency of 0.3. The constrained solution sets a noise floor for the sidelobes to reach. Beamspoiling reverts to nominal resolution but does have a single sidelobe on each side of the mainlobe. The peak sidelobe power is approximately down to -33 dB from -13 dB and the sidelobe width spans a small subset of Doppler frequencies. Each AMMDP solution is effective

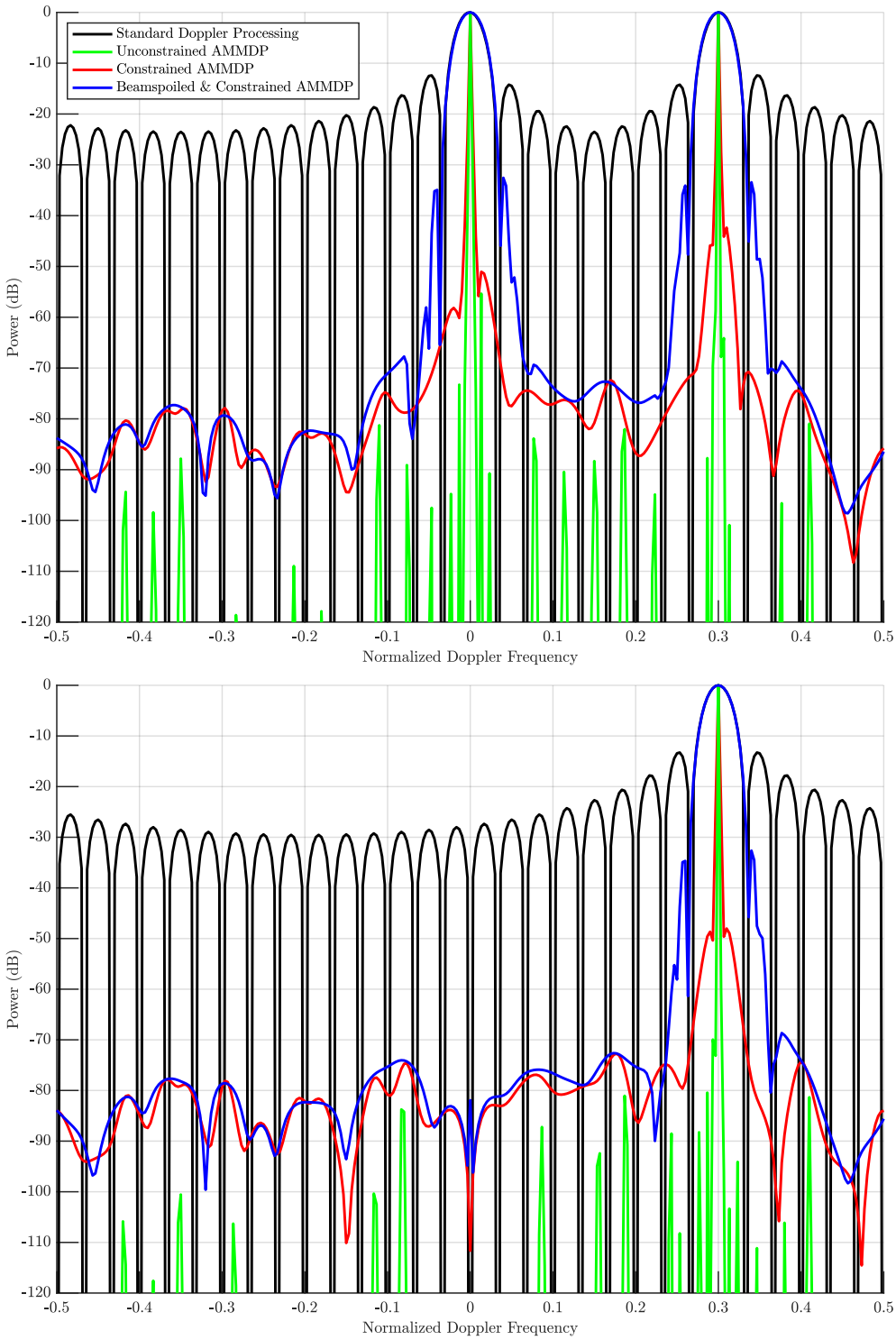

Fig. 2.4: Normalized Doppler response for Doppler processing (black), unconstrained AMMDP (green), constrained AMMDP (red), and beamspoiled & constrained AMMDP (blue) without cancellation (top) and with cancellation (bottom)

in sidelobe suppression without and with cancellation. Cancellation notch depth is affected by beamspoiling. The benefits of the gain constraint and beamspoiling is well investigated for RMMSE. The combined constrained and beamspoiled version will be the standard solution going forward.

2.3 Partial Adaptive Mismatch Doppler Processing

The reduce rank MSE cost function leverages the adjacent-bin multi-window post-Doppler framework utilized for reduced dimension STAP [4, 45]. The rank reduction of RMMSE is for computational complexity reduction only unlike STAP which uses the transformation matrix to lower sample support requirements and reduce computational complexity. Denote D_{t} as the number of pulses in a sub-CPI. The denotation likewise refers to the desired reduce rank and size of the StCM being inverted. The transformation enables L_{D} number of $D_{\mathrm{t}} \times D_{\mathrm{t}}$ matrix inversions for a bank of filters. The computational complexity reduces from $O\{M^3\}$ to $O\{L_{\mathrm{D}} D_{\mathrm{t}}^3\}$ per range bin. The implementation of a transformation matrix allows the matrix inverse size to be controlled and parallelized in the receive processor. One option to exploit the computation reduction is increasing the number of slow-time samples while maintaining the matrix inverse size. To have a computation benefit with the proposed approach, without parallelization, the rank must be reduced such that $D_{\mathrm{t}} < M/\sqrt[3]{L_{\mathrm{D}}}$ and, when considering oversampling, $D_{\mathrm{t}} < \sqrt[3]{M^2/K_{\mathrm{D}}}$. Effectively for a fixed number of pulses, the computational benefit of reduced dimension processing decreases as the oversampling factor increases.

Consider a $M \times D_{\mathrm{t}}$ Doppler transformation matrix formed in the adjacent-bin format $\mathbf{T}_{\mathrm{t}}(\omega) = (1/\sqrt{L_{\mathrm{D}}})[\ \mathbf{c}_{\mathrm{t}}(\omega - A_{\mathrm{t}}\Delta\omega) \ \cdots \ \mathbf{c}_{\mathrm{t}}(\omega) \ \cdots \ \mathbf{c}_{\mathrm{t}}(\omega + A_{\mathrm{t}}\Delta\omega)\ ]$ where $A_{\mathrm{t}} = (D_{\mathrm{t}} - 1)/2$. The adjacent-bin form requires D_{t} to be an greater than three. The transformation maps slow-time samples (full dimension) to a subset of the Doppler spectrum (reduced dimension). The relationship between the $M \times 1$ fully dimension filter $\mathbf{u}(\omega, \ell)$ and $D_{\mathrm{t}} \times 1$ reduced dimension filter $\tilde{\mathbf{u}}(\omega, \ell)$ is

$$\mathbf{u}(\omega, \ell) = \mathbf{T}_{\mathrm{t}}(\omega)\, \tilde{\mathbf{u}}(\omega, \ell) \tag{2.42}$$

[4]. As a result of the transformation, the implementation of the MMSE performs the optimization in the Doppler spectrum. The RMMSE approach then can be viewed as a direct update to the estimate. Substituting (2.42) into the MSE cost function from (2.13) results in

$$\begin{aligned}\tilde{J}_{\text{MSE}}(\omega,\ell) &= E\left\{\left|g[\omega,\omega,\ell]\bar{x}[\omega,\ell]-(\mathbf{T}_{\text{t}}(\omega)\tilde{\mathbf{u}}(\omega,\ell))^{H}\widehat{\mathbf{z}}_{\text{t}}(\ell)\right|^{2}\right\}\\ &= E\left\{\left|g[\omega,\omega,\ell]\bar{x}[\omega,\ell]-\tilde{\mathbf{u}}^{H}(\omega,\ell)\tilde{\mathbf{z}}_{\text{t}}(\omega,\ell)\right|^{2}\right\}.\end{aligned} \tag{2.43}$$

where the estimate of the desired response becomes $d_{\text{est}} = \tilde{\mathbf{u}}^{H}(\omega,\ell)\tilde{\mathbf{z}}_{\text{t}}(\ell)$. The desired response does not change. The data vector is transformed twice, first by clutter cancellation then by Doppler transformation matrix

$$\tilde{\mathbf{z}}_{\text{t}}(\omega,\ell) = \mathbf{T}_{\text{t}}^{H}(\omega)\,\widehat{\mathbf{z}}_{\text{t}}(\ell) = \mathbf{T}_{\text{t}}^{H}(\omega)\,\mathbf{R}_{\text{t,canc}}^{-1}(\ell)\mathbf{z}_{\text{t}}(\ell). \tag{2.44}$$

Applying the $D_{\text{t}} \times 1$ gradient vector with respect to the reduced rank filter, minimizing the cost function such that $\nabla_{\tilde{\mathbf{u}}^{*}}\tilde{J}_{\text{MSE}}(\omega,\ell) = 0$, and solving for $\tilde{\mathbf{u}}(\omega,\ell)$ yields the reduced dimension MMSE (RD-MMSE) Doppler filter formulation

$$\tilde{\mathbf{u}}_{\text{RD-MMSE}}(\omega,\ell) = \left(E\left\{\tilde{\mathbf{z}}_{\text{t}}(\omega,\ell)\tilde{\mathbf{z}}_{\text{t}}^{H}(\omega,\ell)\right\}\right)^{-1}E\{g^{*}[\omega,\omega,\ell]\bar{x}^{*}[\omega,\ell]\tilde{\mathbf{z}}_{\text{t}}(\omega,\ell)\}. \tag{2.45}$$

Using the signal model from (2.7) within the auto-covariance matrix and cross-correlation vector in 2.45, similar to (2.16-2.24), results in the unconstrained filter

$$\tilde{\mathbf{u}}_{\text{RD-MMSE}}(\omega,\ell) = \widehat{\rho}[\omega,\ell]\,\tilde{\mathbf{Q}}_{\text{t}}^{-1}(\omega,\ell)\,\mathbf{T}_{\text{t}}^{H}(\omega)\,\mathbf{R}_{\text{t,canc}}^{-1}(\ell)\,\mathbf{c}_{\text{t}}(\omega) \tag{2.46}$$

where reduce rank StCM is

$$\tilde{\mathbf{Q}}_{\text{t}}(\omega,\ell) = \mathbf{T}_{\text{t}}^{H}(\omega)\,\mathbf{R}_{\text{t,canc}}^{-1}(\ell)\,\mathbf{C}_{\text{t}}\widehat{\mathbf{P}}_{\text{D}}(\ell)\,\mathbf{C}_{\text{t}}^{H}\mathbf{R}_{\text{t,canc}}^{-1}(\ell)\,\mathbf{T}_{\text{t}}(\omega)\odot\left(\sigma_{\text{err}}^{2}\mathbf{I}_{D_{\text{t}}\times D_{\text{t}}}+\mathbf{1}_{D_{\text{t}}\times D_{\text{t}}}\right)+\sigma_{\text{v}}^{2}\mathbf{I}_{D_{\text{t}}\times D_{\text{t}}}. \tag{2.47}$$

Mapping the reduced dimension filter to the full dimension space using (2.42) results in

$$\begin{aligned}\mathbf{u}_{\text{RD-MMSE}}(\omega,\ell) &= \mathbf{T}_{\text{t}}(\omega)\,\tilde{\mathbf{u}}_{\text{RD-MMSE}}(\omega,\ell) \\ &= \widehat{\rho}\,[\omega,\ell]\,\mathbf{T}_{\text{t}}(\omega)\,\tilde{\mathbf{Q}}_{\text{t}}^{-1}(\omega,\ell)\,\mathbf{T}_{\text{t}}^{H}(\omega)\,\mathbf{R}_{\text{t,canc}}^{-1}(\ell)\,\mathbf{c}_{\text{t}}(\omega).\end{aligned} \tag{2.48}$$

Application of the RD-MMSE filter to the receive data is

$$\begin{aligned}\hat{x}_{\text{RD-MMSE}}(\omega,\ell) &= \mathbf{u}_{\text{RD-MMSE}}^{H}(\omega,\ell)\,\widehat{\mathbf{z}}_{\text{t}}(\ell) \\ &= \mathbf{w}_{\text{RD-MMSE}}^{H}(\omega,\ell)\,\mathbf{z}_{\text{t}}(\ell) \\ &= \widehat{\rho}\,[\omega,\ell]\mathbf{c}_{\text{t}}^{H}(\omega)\mathbf{T}_{\text{t}}(\omega)\,\tilde{\mathbf{Q}}_{\text{t}}^{-1}(\omega,\ell)\,\mathbf{T}_{\text{t}}^{H}(\omega)\,\mathbf{R}_{\text{t,canc}}^{-1}(\ell)\,\mathbf{z}(\ell)\end{aligned} \tag{2.49}$$

where the combination of the MTI filter for cancellation and RD-MMSE Doppler filter for spectral estimation is

$$\begin{aligned}\mathbf{w}_{\text{RD-MMSE}}(\omega,\ell) &= \mathbf{R}_{\text{t,canc}}^{-1}(\ell)\,\mathbf{u}_{\text{RD-MMSE}}(\omega,\ell) \\ &= \widehat{\rho}\,[\omega,\ell]\,\mathbf{R}_{\text{t,canc}}^{-1}(\ell)\,\mathbf{T}_{\text{t}}(\omega)\,\tilde{\mathbf{Q}}_{\text{t}}^{-1}(\omega,\ell)\,\mathbf{T}_{\text{t}}^{H}(\omega)\,\mathbf{R}_{\text{t,canc}}^{-1}(\ell)\,\mathbf{c}_{\text{t}}(\omega).\end{aligned} \tag{2.50}$$

The $M \times L_{\text{D}}$ bank of RD-MMSE Doppler filters is

$$\mathbf{U}_{\text{RD-MMSE}}(\ell) = [\ \mathbf{u}_{\text{RD-MMSE}}(-\omega_{\max},\ell)\ \ \cdots\ \ \mathbf{u}_{\text{RD-MMSE}}(0,\ell)\ \ \cdots\ \ \mathbf{u}_{\text{RD-MMSE}}(\omega_{\max},\ell)\ ]. \tag{2.51}$$

Applying the filter bank forms the RD-MMSE Doppler estimate of the spectrum

$$\hat{\mathbf{x}}_{\text{RD-MMSE}}(\ell) = \mathbf{U}_{\text{RD-MMSE}}^{H}(\ell)\,\widehat{\mathbf{z}}_{\text{t}}(\ell). \tag{2.52}$$

The incorporation of the gain constraint is similar to the previous section. The gain constrained

MSE cost function incorporates the reduced dimension filter

$$J_{\text{MSE}}(\omega,\ell) = E\{|g[\omega,\omega,\ell]\bar{x}[\omega,\ell] - \tilde{\mathbf{u}}^H(\omega,\ell)\tilde{\mathbf{z}}_{\text{t}}(\ell)|^2\} + \text{Re}\{\lambda_{\text{L}}^*\left(\tilde{\mathbf{u}}^H(\omega,\ell)\mathbf{T}_{\text{t}}^H(\omega)\mathbf{R}_{\text{t,canc}}^{-1}(\ell)\mathbf{c}_{\text{t}}(\omega) - g[\omega,\omega,\ell]\right)\}. \tag{2.53}$$

Optimizing the cost function for the reduce dimension filter and mapping back to full rank yields

$$\mathbf{u}_{\text{RD-MMSE,con}}(\omega,\ell) = \frac{g[\omega,\omega,\ell]\mathbf{T}_{\text{t}}(\omega)\tilde{\mathbf{Q}}_{\text{t}}^{-1}(\omega,\ell)\mathbf{T}_{\text{t}}^H(\omega)\mathbf{R}_{\text{t,canc}}^{-1}(\ell)\mathbf{c}_{\text{t}}(\omega)}{\mathbf{c}_{\text{t}}^H(\omega)\mathbf{R}_{\text{t,canc}}^{-1}(\ell)\mathbf{T}_{\text{t}}(\omega)\tilde{\mathbf{Q}}_{\text{t}}^{-1}(\omega,\ell)\mathbf{T}_{\text{t}}^H(\omega)\mathbf{R}_{\text{t,canc}}^{-1}(\ell)\mathbf{c}_{\text{t}}(\omega)} \tag{2.54}$$

which is straightforward to obtained using a similar procedure in the previous section. Beamspoiling is performed using the same formulation as (2.35)

$$\mathbf{u}_{\text{RD-MMSE,beam}}(\omega,\ell) = \frac{\sqrt{K_{\text{D}}}\sum_{k_{\text{D}}=-K_{\text{D}}}^{K_{\text{D}}}\mathbf{u}_{\text{RD-MMSE,con}}(\omega+k_{\text{D}}\Delta\omega,\ell)\,\mathbf{c}_{\text{t}}^H(\omega+k_{\text{D}}\Delta\omega)\,\mathbf{c}_{\text{t}}(\omega)}{\sum_{k_{\text{D}}=-K_{\text{D}}}^{K_{\text{D}}}\mathbf{c}_{\text{t}}^H(\omega+k_{\text{D}}\Delta\omega)\,\mathbf{c}_{\text{t}}(\omega)}. \tag{2.55}$$

The iterative procedure of PAMMDP closely follows the AMMDP procedure. The procedure initializes similarly with the maximum SNR Doppler filter response after clutter cancellation

$$\hat{\mathbf{x}}_{\text{PAMMDP},0}(\ell) = \mathbf{U}_{\text{DP}}^H\hat{\mathbf{R}}_{\text{t,canc}}^{-1}(\ell)\,\mathbf{z}_{\text{t}}(\ell). \tag{2.56}$$

The first stage of the procedure estimates the ith power distribution matrix using the previous Doppler estimate

$$\hat{\mathbf{P}}_{\text{PAMMDP},i}(\ell) = \hat{\mathbf{x}}_{\text{PAMMDP},i-1}(\ell)\,\hat{\mathbf{x}}_{\text{PAMMDP},i-1}^H(\ell) \odot \mathbf{I}_{L_{\text{D}}\times L_{\text{D}}}. \tag{2.57}$$

Next, the StCM is formed using the power distribution matrix, noise power, and error power

$$\hat{\mathbf{Q}}_{\text{PAMMDP},i}(\omega,\ell) = \mathbf{T}_{\text{t}}^{H}(\omega)\,\hat{\mathbf{R}}_{\text{t,canc}}^{-1}(\ell)\,\mathbf{C}_{\text{t}}\hat{\mathbf{P}}_{\text{PAMMDP},i}(\ell)\,\mathbf{C}_{\text{t}}^{H}\hat{\mathbf{R}}_{\text{t,canc}}^{-1}(\ell)\,\mathbf{T}_{\text{t}}(\omega)\odot\left(\mathbf{1}_{D_{\text{t}}\times D_{\text{t}}}+\ \sigma_{\text{err}}^{2}\mathbf{I}_{D_{\text{t}}\times D_{\text{t}}}\right) + \sigma_{\text{v}}^{2}\mathbf{I}_{D_{\text{t}}\times D_{\text{t}}}. \tag{2.58}$$

The StCM is mapped to each Doppler frequency. The constrained filter is then formed using the StCM

$$\hat{\mathbf{u}}_{\text{PAMMDP,con},i}(\omega,\ell) = \frac{\hat{g}[\omega,\omega,\ell]\mathbf{T}_{\text{t}}(\omega)\,\hat{\mathbf{Q}}_{\text{PAMMDP},i}^{-1}(\omega,\ell)\,\mathbf{T}_{\text{t}}^{H}(\omega)\,\hat{\mathbf{R}}_{\text{t,canc}}^{-1}(\ell)\,\mathbf{c}_{\text{t}}(\omega)}{\mathbf{c}_{\text{t}}^{H}(\omega)\,\hat{\mathbf{R}}_{\text{t,canc}}^{-1}(\ell)\,\mathbf{T}_{\text{t}}(\omega)\,\hat{\mathbf{Q}}_{\text{PAMMDP},i}^{-1}(\omega,\ell)\,\mathbf{T}_{\text{t}}^{H}(\omega)\,\hat{\mathbf{R}}_{\text{t,canc}}^{-1}(\ell)\,\mathbf{c}_{\text{t}}(\omega)} \tag{2.59}$$

where $\hat{g}[\omega,\omega,\ell]$ is formed using (2.12) and the estimated StCM. Beamspoiling is then conducted for each range-Doppler bin,

$$\hat{\mathbf{u}}_{\text{PAMMDP,beam},i}(\omega,\ell) = \frac{\sqrt{K_{\text{D}}}\sum\limits_{k_{\text{D}}=-K_{\text{D}}}^{K_{\text{D}}}\hat{\mathbf{u}}_{\text{PAMMDP,con}}(\omega+k_{\text{D}}\Delta\omega,\ell)\,\mathbf{c}_{\text{t}}^{H}(\omega+k_{\text{D}}\Delta\omega)\,\mathbf{c}_{\text{t}}(\omega)}{\sum\limits_{k_{\text{D}}=-K_{\text{D}}}^{K_{\text{D}}}\mathbf{c}_{\text{t}}^{H}(\omega+k_{\text{D}}\Delta\omega)\,\mathbf{c}_{\text{t}}(\omega)} \tag{2.60}$$

A bank of beamspoiled filters is generated and subsequently applied to the receive data to obtain the updated estimate of the spectrum

$$\hat{\mathbf{x}}_{\text{PAMMDP},i}(\ell) = \hat{\mathbf{U}}_{\text{PAMMDP,beam},i}^{H}(\ell)\,\hat{\mathbf{R}}_{\text{t,canc}}^{-1}(\ell)\,\mathbf{z}_{\text{t}}(\ell). \tag{2.61}$$

The procedure returns to (2.57) to update the power distribution matrix and concludes after a user-defined number of iterations.

In [38], the authors showed that reduced-rank adaptive processing performance is less than or equal to full-rank performance for fixed transformations. The trade space between performance and computation for PAMMDP is based on this premise. The StCM used in the RMMSE formulation is a full-rank matrix and sufficiently trained due to the oversampling of the spectrum.

Even for a critically sampled spectrum (which is equivalent to a DFT matrix) the rank of StCM is full. The performance of implementing a Doppler transformation matrix for the proposed PAMMDP is less than or equal to the full-rank AMMDP formulation. The simulation and experimental results will show a trade-off exists between sidelobe suppression and computation for practical application of RMMSE in random PRI staggering radar.

2.4 Simulation Results

The proposed Doppler processing formulations were examined over Monte Carlo simulations for 1000 trials. A chirp waveform is generated with $B\tau = 150$ for $M = 48$ pulses. The mth PRI is formed by multiplying a desired average PRI by a normalized PRI such that $T_m = \varepsilon_m T_{\text{r,avg}}$. The normalized PRI is a random variable with a uniform distribution. See Table 2.1 for more details about the distribution. The mean is set to $E[\varepsilon_m] = 1$ such that $E[T_m] = T_{\text{r,avg}}$. Next, an interval length of ε_m, denoted as W, is set to limit the temporal extent of the random PRI staggers. The interval length is varied from 0 to 1 by values of 0.1. When $W = 0$, the PRIs are uniform. The lower and upper bounds of ε_m, denoted as a and b respectively, were calculated thereafter. The average PRI for the analyses is set to $T_{\text{r,avg}} = 20\ \mu s$ which corresponds to a PRF of 50 kHz for a sampling rate of 200 MHz.

The randomness of the average PRI changes the slow-time sampling of the temporal steering vector. The standard deviation of the normalized PRI is denoted σ_ε. The temporal steering vectors denotation are change from $\mathbf{c}_{\text{t}}(\omega)$ to $\mathbf{c}_{\text{t}}(\omega;\sigma_\varepsilon)$ to include the dependence on the randomness. Doppler filters have a similar modification. Table 2.2 presents the numerical values for the distribution for varying interval lengths. Each standard deviation in Table 2.2 is examined for Doppler processing, window Doppler processing, AMMDP, and PAMMDP with and without clutter cancellation. Throughout the various analyses, a Taylor window with -50 dB peak sidelobe and five nearly constant sidelobes is employed. Also, five iterations of AMMDP and PAMMDP is performed. PAMMDP is examined at the minimum reduction of $D_{\text{t}} = 3$ (best-case computationally) to a maximum reduction (relative to the number of pulses) of $D_{\text{t}} = 47$

(worst-case computationally). The spectrum is examined with an oversampling factor of $K_{\mathrm{D}} = 5$. The efficacies of the formulations are examined under the following metrics: average sidelobe response, average loss factor, and total residual sidelobe response.

Table 2.1: Distribution parameters of PRI staggering

Parameter	ε_m	$T_m = \varepsilon_m T_{\mathrm{r,avg}}$
Distribution	$\varepsilon_m \sim U(a,b)$	$T_m \sim U(a_T, b_T)$
Mean (User Defined)	$\mu_\varepsilon = E[\varepsilon_m] = \frac{a+b}{2} = 1$	$\mu_T = E[T_m] = T_{\mathrm{r,avg}}$
Interval Length (User Defined)	$W = b - a$	$W_T = (b-a)\,T_{\mathrm{r,avg}}$
Upper Bound (Calculated)	$a = \mu_\varepsilon - \frac{W}{2}$	$a_T = \left(\mu_\varepsilon - \frac{W}{2}\right) T_{\mathrm{r,avg}}$
Lower Bound (Calculated)	$b = \mu_\varepsilon + \frac{W}{2}$	$b_T = \left(\mu_\varepsilon + \frac{W}{2}\right) T_{\mathrm{r,avg}}$
Variance (Calculated)	$\sigma_\varepsilon^2 = \frac{(b-a)^2}{12} = \frac{W^2}{12}$	$\sigma_T^2 = \frac{(b-a)^2}{12} T_{\mathrm{r,avg}}^2 = \frac{W^2}{12} T_{\mathrm{r,avg}}^2$
Standard Deviation (Calculated)	$\sigma_\varepsilon = \frac{b-a}{\sqrt{12}} = \frac{W}{\sqrt{12}}$	$\sigma_T = \frac{b-a}{\sqrt{12}} T_{\mathrm{r,avg}} = \frac{W}{\sqrt{12}} T_{\mathrm{r,avg}}$

Table 2.2: Numerical values of distribution parameters for $T_{\mathrm{r,avg}} = 20\mu s$

ε_m						T_m					
μ_ε	W	a	b	σ_ε^2	σ_ε	$\mu_T\ (\mu s)$	$W_T\ (\mu s)$	$a_T\ (\mu s)$	$b_T\ (\mu s)$	$\sigma_T^2\ (\mu s)$	$\sigma_T\ (\mu s)$
1.00	0.00	1.00	1.00	0.0000	0.0000	20.00	0.00	20.00	20.00	0.0000	0.0000
1.00	0.10	0.95	1.05	0.0008	0.0289	20.00	2.00	19.00	21.00	0.3333	0.5774
1.00	0.20	0.90	1.10	0.0033	0.0577	20.00	4.00	18.00	22.00	1.3333	1.1547
1.00	0.30	0.85	1.15	0.0075	0.0866	20.00	6.00	17.00	23.00	3.0000	1.7321
1.00	0.40	0.80	1.20	0.0133	0.1155	20.00	8.00	16.00	24.00	5.3333	2.3094
1.00	0.50	0.75	1.25	0.0208	0.1444	20.00	10.00	15.00	25.00	8.3333	2.8868
1.00	0.60	0.70	1.30	0.0300	0.1732	20.00	12.00	14.00	26.00	12.0000	3.4641
1.00	0.70	0.65	1.35	0.0408	0.2021	20.00	14.00	13.00	27.00	16.3333	4.0415
1.00	0.80	0.60	1.40	0.0533	0.2310	20.00	16.00	12.00	28.00	21.3333	4.61880
1.00	0.90	0.55	1.45	0.0675	0.2598	20.00	18.00	11.00	29.00	27.0000	5.1962
1.00	1.00	0.50	1.50	0.0834	0.2887	20.00	20.00	10.00	30.00	33.3333	5.7735

2.4.1 Average sidelobe response

Average sidelobe response (ASR) considers the average power spectral density of the Doppler spectrum. The analysis examines the suppression capabilities of the Doppler processing techniques. Consider the following signal vector after pulse compression

$$\mathbf{z}_{\mathrm{t}}(\ell;\sigma_\varepsilon) = \bar{x}[\omega_{\mathrm{mov}},\ell]\,\mathbf{c}_{\mathrm{t}}(\omega_{\mathrm{mov}};\sigma_\varepsilon) + \mathbf{v}_{\mathrm{t}}(\ell), \tag{2.62}$$

which contains a single point scatterer at zero-Doppler with unit amplitude i.e., $|\bar{x}[\omega_{\mathrm{mov}},\ell]|^2 = 1$ and $\omega_{\mathrm{mov}} = 0$. The noise floor is approximately -85 dB after pulse compression gain. The high SNR will show the sidelobe suppression capabilities relative to the noise floor. The ASR is the expectation of the estimate of the power spectrum over Monte Carlo trials

$$\mathrm{ASR}_p(\omega,\ell;\sigma_\varepsilon) = E\left\{\left|\mathbf{u}_p^H(\omega;\sigma_\varepsilon)\,\mathbf{z}_{\mathrm{t}}(\ell;\sigma_\varepsilon)\right|^2\right\} \tag{2.63}$$

where $p \in$ [DP, WDP, AMMDP, PAMMDP] for Doppler processing, windowed Doppler processing, AMMDP, and PAMMDP, respectively. Each Monte Carlo trial generates a different noise instantiation. The final responses are peak-normalized for a one-to-one comparison. Mismatch loss is examined in the succeeding section.

In Figure 2.5, ASR is presented for uniform PRI. Included in Fig 2.5 is a zoomed-in version of the spectrum on the mainlobe response to distinguish between techniques. Doppler processing results in a typical sinc response. Windowing provides the well-known benefit of sidelobe suppression. For a single point target, the AMMDP and PAMMDP formulations are robust in the suppression of sidelobes. A low rank implementation of PAMMDP affirms a robust response can be obtained for uniform PRI with minimal computation. The results are a baseline for the staggered PRI cases.

Figure 2.6 presents ASR with minor staggering for $\sigma_\varepsilon = 0.0289$. Sidelobes and aliasing are unchanged for Doppler processing. Sidelobes for windowing have increased above -50 dB. For

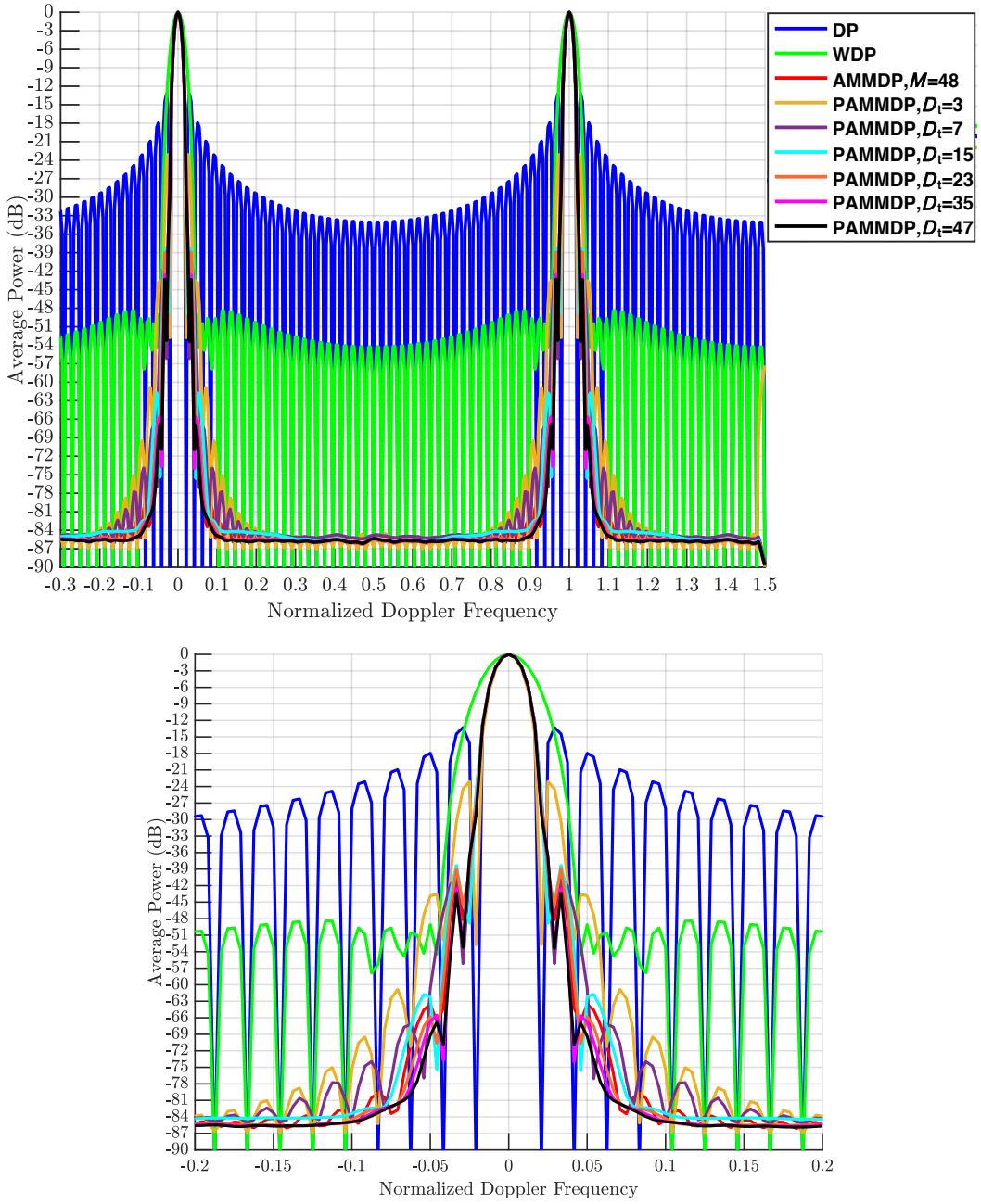

Fig. 2.5: Average sidelobe response for uniform PRI with $\sigma_\varepsilon = 0$ (top) and zoomed in between $\omega = -0.2$ and $\omega = 0.2$ (bottom)

both, aliasing is still prevalent. AMMDP can leverage the minor dithering of the PRI to suppress the aliased response at $\omega = 1$ by 60 dB. The differences between Figs. 2.5 and 2.6 are profound for PAMMDP. The trade-space between performance and computation begins to show with the slight dithering of the PRI. At $D_{\mathrm{t}} = 3$, PAMMDP sidelobes are below Doppler processing but above windowing closer toward the true target velocity. Also, PAMMDP is unable to suppress the aliased response. As D_{t} increases, the sidelobes are suppressed and the ability to suppress the aliased response improves. The suppression comes to a head at $D_{\mathrm{t}} = 47$, where performance is similar to AMMDP. Even performing better in some instances. Therefore, if, for example, $\tilde{M}$ out of M PRIs are varied within a CPI, $\tilde{M}$ number of adaptive degrees-of-freedom are required to suppress the deleterious sidelobes caused by staggering. This is observed throughout the PAMMDP results where D_{t} adaptive degrees-of-freedom are available while all M PRIs within the CPI are staggered. As D_{t} increases toward M, PAMMDP sidelobe cancellation performance also improves. This implies that for a uniform PRI, the adaptive degrees-of-freedom required is one which is shown by the robustness of PAMMDP $D_{\mathrm{t}} = 3$ in Fig. 2.5.

When performing AMMDP and PAMMDP an "edge effect" of the Doppler response occurs (seen at $\omega = 1.5$). The effect is a byproduct of the region of the spectrum that is examined. The spectrum is examined for a normalized Doppler frequencies between $\omega = -0.5$ to $\omega = 1.5$. One solution would be overlapping the regions to overcome the edge effect. A second option, presented here where the performance is presented for normalized Doppler frequencies between -0.3 to 1.5, is examining beyond the intended region.

In Figures 2.7-15, the different processing techniques are presented with each figure having a different standard deviation. The sidelobe performance of Doppler processing, windowing, AMMDP, and PAMMDP are similar within these figures. Overall, as standard deviation increases, aliasing diminishes and the sidelobes begin to "flatten" to a "sidelobe floor." The response is a result of a spread of the energy from the alias response into the rest of the spectrum. In some instances throughout these results, PAMMDP at $D_{\mathrm{t}} = 47$ performs better than AMMDP. Since PAMMDP is post-Doppler approach, the Doppler transformation matrix makes the formulation

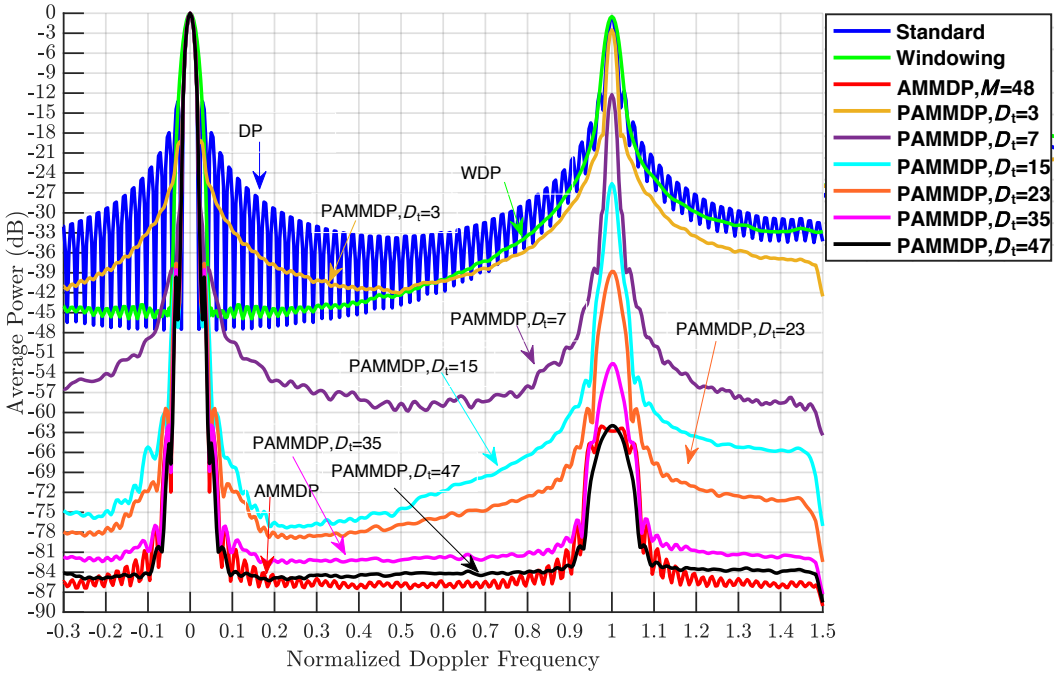

Fig. 2.6: Average sidelobe response for staggered PRI with $\sigma_\varepsilon = 0.0289$

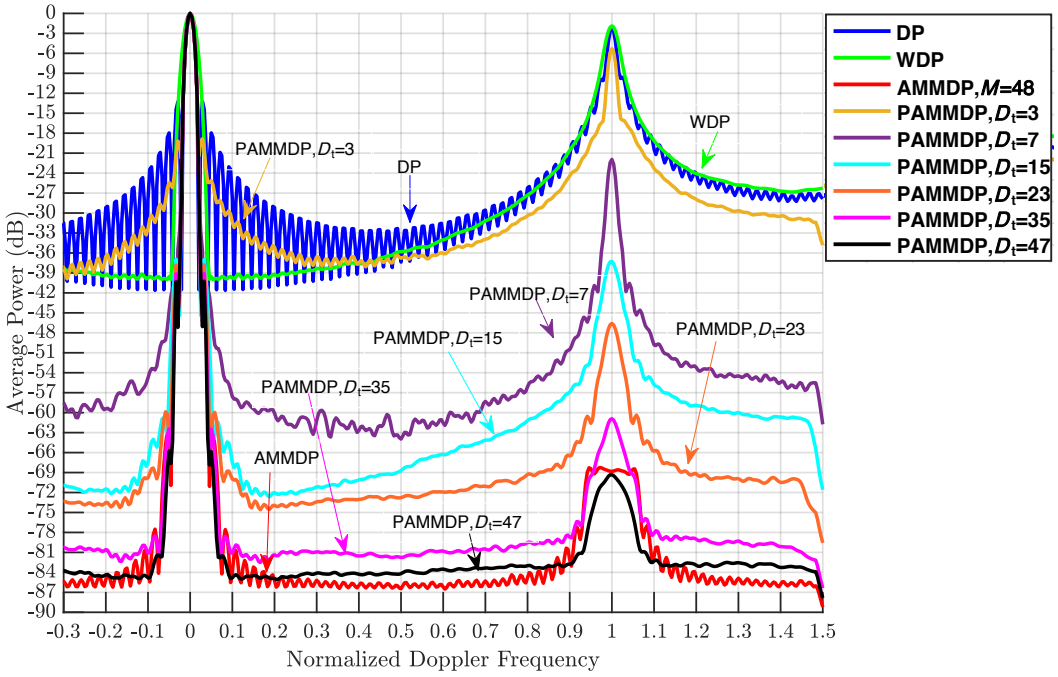

Fig. 2.7: Average sidelobe response for staggered PRI with $\sigma_\varepsilon = 0.0577$

structurally different. PAMMDP accounts for sidelobes post-processing thereby leveraging the coherence that was performed beforehand. The response is observed in Fig. 2.7. For the aliased target at Doppler frequency of 1, AMMDP has of a "square" response of while PAMMDP is "rounded." Also, looking at the sidelobes from normalized Doppler of 0.1 to 0.8, AMMDP displays a slight sinc lobing structure while PAMMDP is fairly flat although higher in power.

To accompany the figures, tables of the ASR values from the results are presented. Table 2.3 presents the ASR at $\omega = 1$ where aliasing would occur for uniform PRI. Lower power responses are desirable. As staggering is introduced, the suppression of the aliasing begins. The aliased response reduces with an increase in the standard deviation of the staggering. In these trials, the results had a benefit of -16.40 dB at $W = 1$. PAMMDP can reach a similar reduction at $W = 0.70$ with -16.80 dB at a low rank of 3. As the rank increases for PAMMDP, the less requirement for staggering is necessary. Table 2.4 presents the ASR from the 0.3 to 1.3 band of normalized Doppler frequencies omitting the edge effect. Highlighted in yellow is differences from Table 2.3. As staggering is introduced, the suppression of the aliasing begins. These tables show that AMMDP significantly benefits from the small dithering of the PRI. AMMDP is more consistent in the spread of the energy from the alias response into the rest of the spectrum.

The results presented consider a single point target with high SNR. Practically, multiple movers may be present and SNR can be lower. The open-air experiments presented in Section 2.5 are indicative of a radar scene. Readers should take into consideration the simulation results show the possibilities of AMMDP. Overall, AMMDP and PAMMDP provides a robust solution to sidelobe suppression of staggered PRI transmission. PAMMDP is viable method between performance and computation.

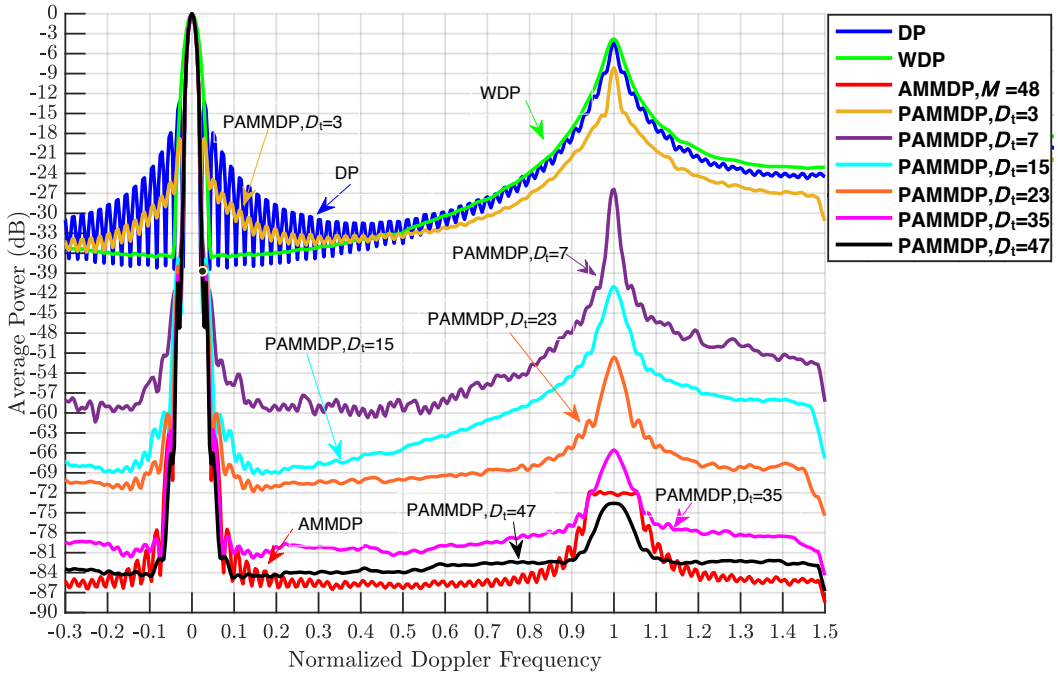

Fig. 2.8: Average sidelobe response for staggered PRI with $\sigma_\varepsilon = 0.0866$

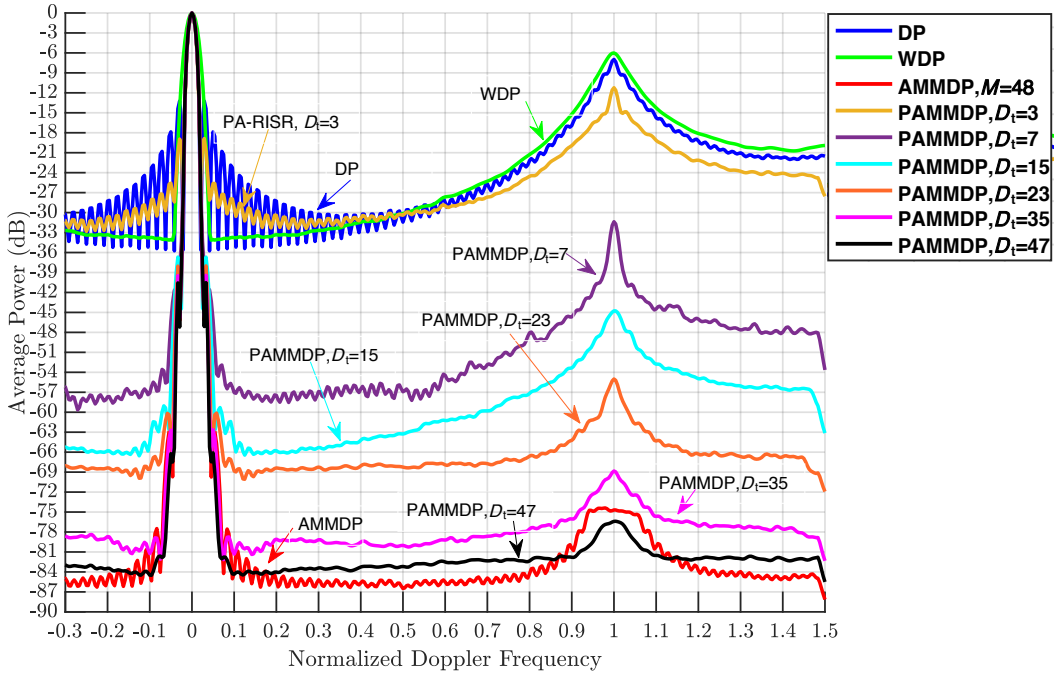

Fig. 2.9: Average sidelobe response for staggered PRI with $\sigma_\varepsilon = 0.1155$

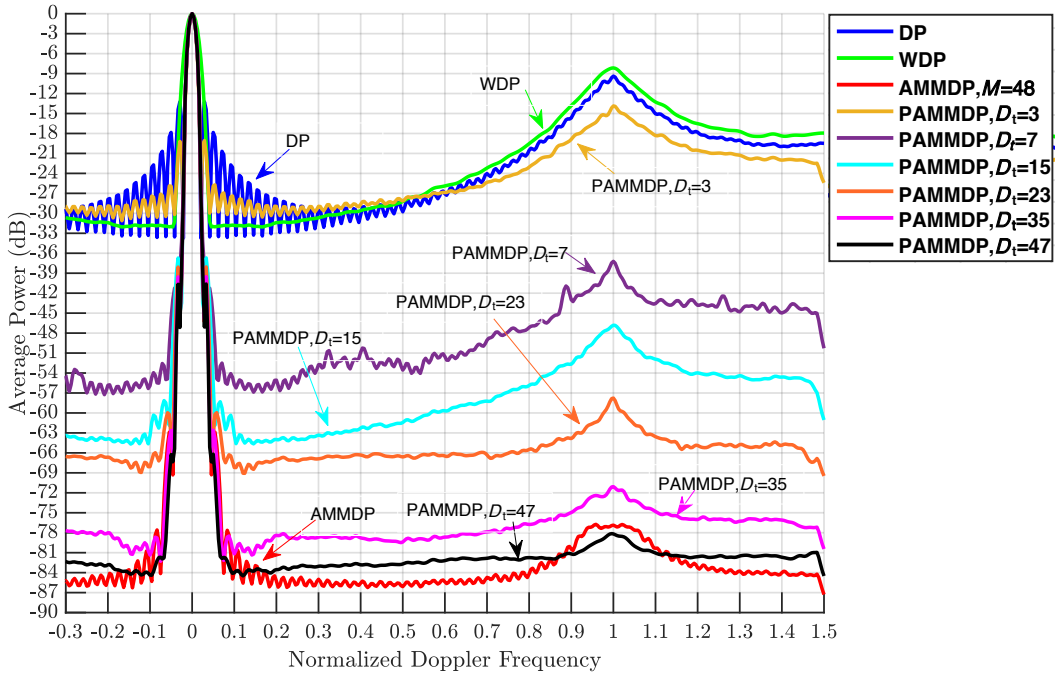

Fig. 2.10: Average sidelobe response for staggered PRI with $\sigma_\varepsilon = 0.1444$

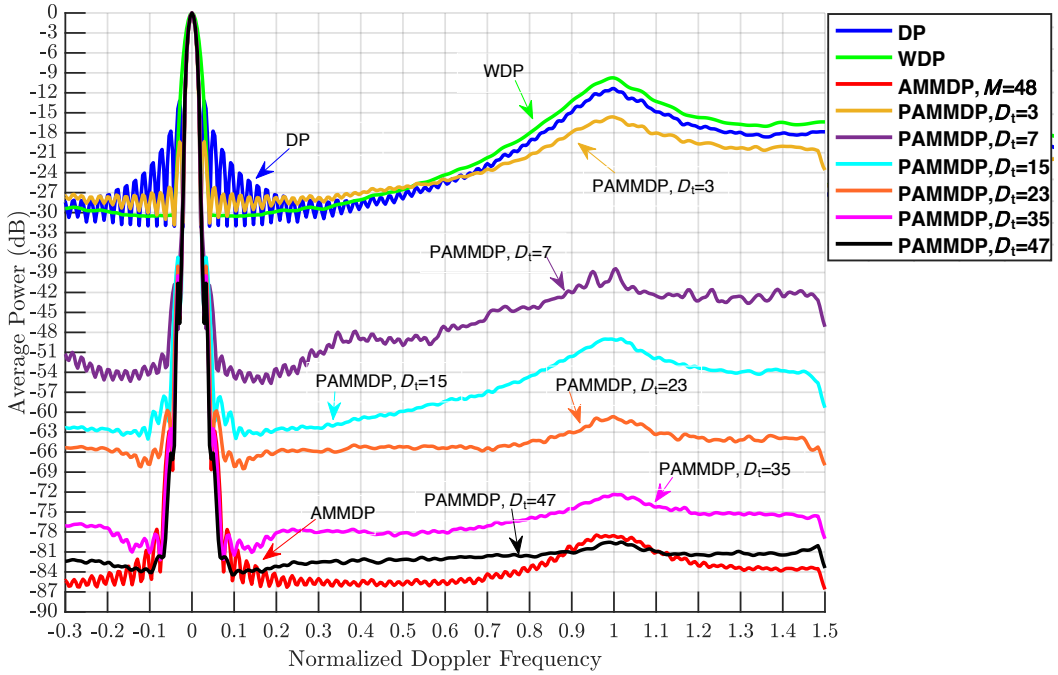

Fig. 2.11: Average sidelobe response for staggered PRI with $\sigma_\varepsilon = 0.1732$

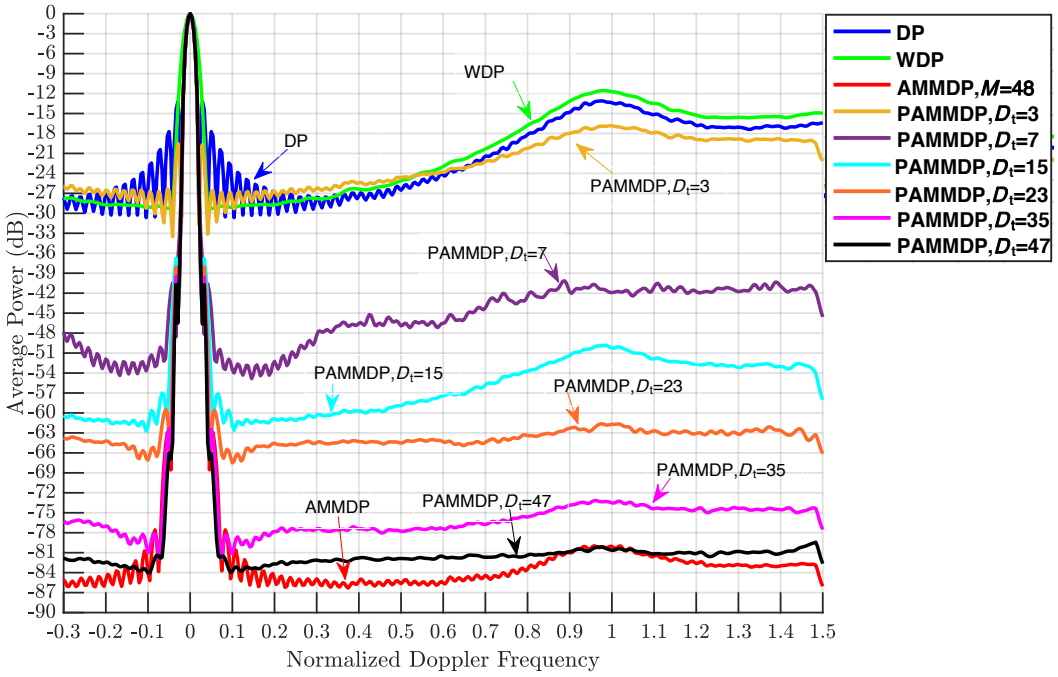

Fig. 2.12: Average sidelobe response for staggered PRI with $\sigma_\varepsilon = 0.2021$

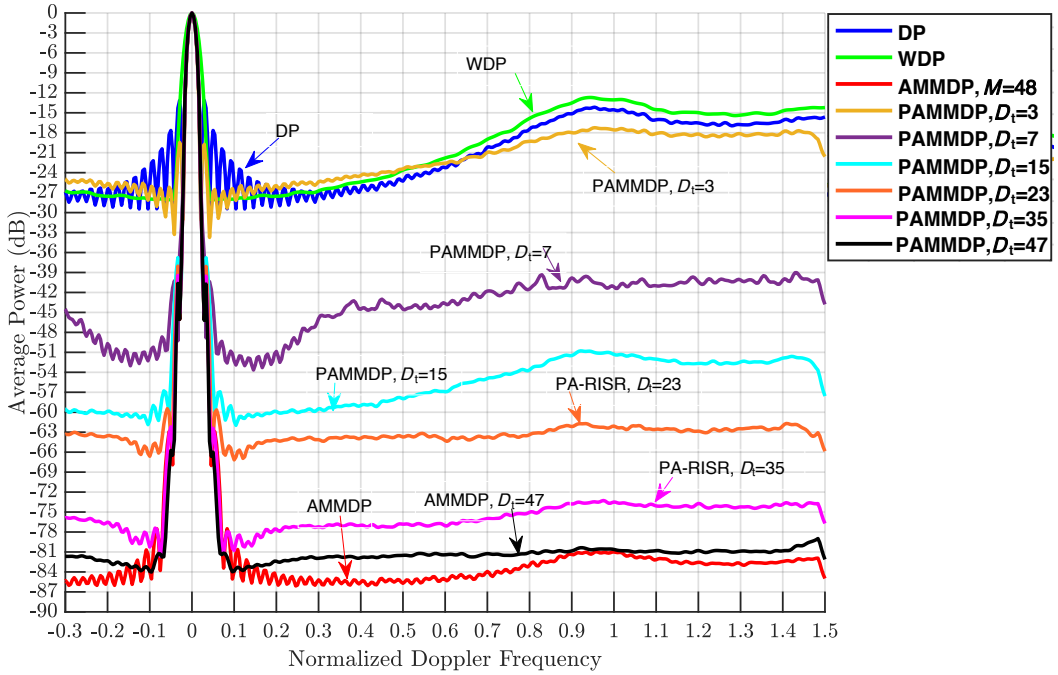

Fig. 2.13: Average sidelobe response for staggered PRI with $\sigma_\varepsilon = 0.2310$

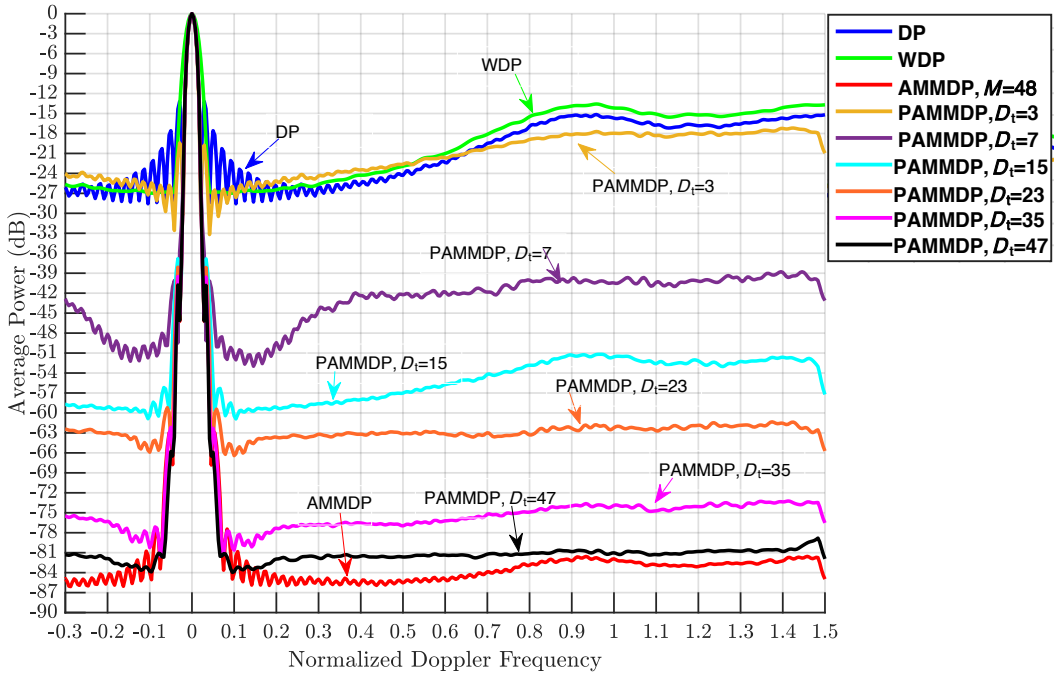

Fig. 2.14: Average sidelobe response for staggered PRI with $\sigma_\varepsilon = 0.2598$

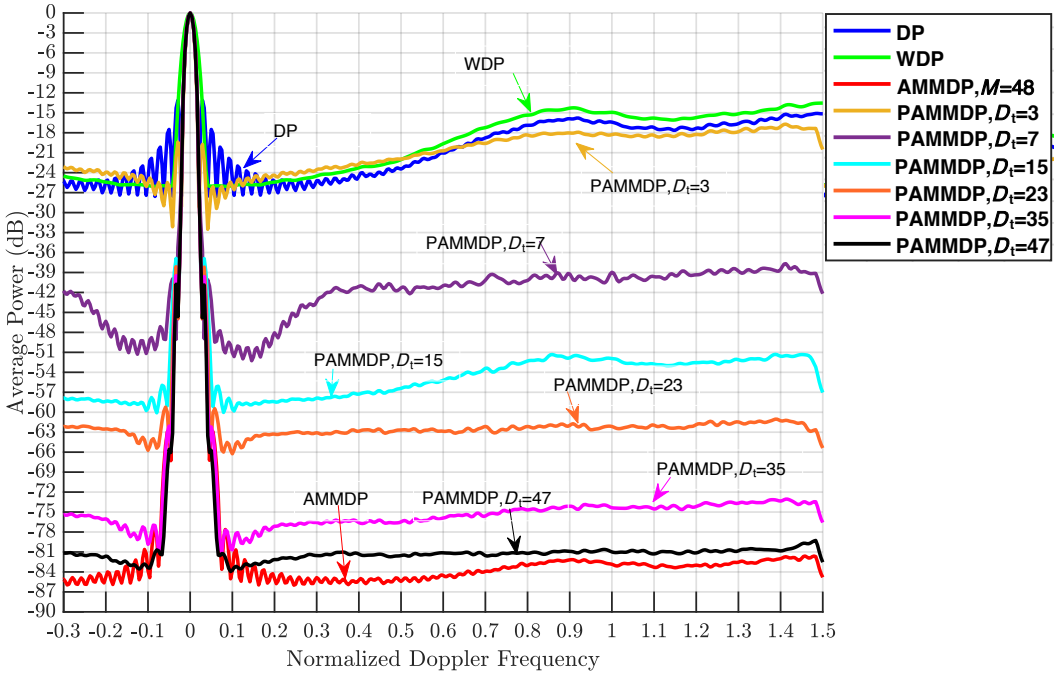

Fig. 2.15: Average sidelobe response for staggered PRI with $\sigma_\varepsilon = 0.2887$

Table 2.3: Average sidelobe response of aliased response at $\omega = 1$

W	σ_ε	σ_T (μs)	DP (dB)	WDP (dB)	AMMDP (dB)	PAMMDP (dB)					
						$D_t = 3$	$D_t = 7$	$D_t = 15$	$D_t = 23$	$D_t = 35$	$D_t = 47$
0.00	0.0000	0.0000	0.00	0.00	0.00	0.00	0.00	0.00	0.00	0.00	0.00
0.10	0.0289	0.5774	-0.57	-0.49	-62.79	-2.49	-12.23	-25.60	-38.80	-52.67	-61.97
0.20	0.0577	1.1547	-2.17	-1.88	-68.82	-5.29	-21.95	-37.26	-46.60	-60.91	-69.31
0.30	0.0866	1.7321	-4.39	-3.80	-72.12	-8.12	- 26.40	-41.00	-51.63	-65.57	-73.59
0.40	0.1155	2.3094	-6.98	-6.02	-74.68	-11.23	-31.37	-44.76	-55.01	-68.83	-76.40
0.50	0.1444	2.8868	-9.38	-8.15	-76.86	-13.87	-37.22	-46.82	-57.77	-71.07	-78.18
0.60	0.1732	3.4641	-11.35	-9.76	-78.55	-15.64	-38.56	-49.09	-60.67	-72.35	-79.72
0.70	0.2021	4.0415	-13.38	-11.71	-80.05	-16.85	-41.91	-50.26	-61.71	-73.51	-80.64
0.80	0.2310	4.61880	-14.55	-13.05	-81.00	-17.58	-41.16	-51.32	-62.09	-73.49	-80.62
0.90	0.2598	5.1962	-15.70	-14.17	-81.92	-17.97	-40.46	-51.56	-62.22	-73.89	-81.02
1.00	0.2887	5.7735	-16.40	-14.93	-82.85	-18.28	-38.97	-51.94	-62.14	-74.35	-80.99

Table 2.4: Maximum average sidelobe response over normalized Doppler bandwidth 0.3 to 1.3

W	σ_ε	σ_T (μs)	DP (dB)	WDP (dB)	AMMDP (dB)	PAMMDP (dB)					
						$D_t = 3$	$D_t = 7$	$D_t = 15$	$D_t = 23$	$D_t = 35$	$D_t = 47$
0.00	0.0000	0.0000	0.00	0.00	0.00	0.00	0.00	0.00	0.00	0.00	0.00
0.10	0.0289	0.5774	-0.57	-0.49	-62.05	-2.49	-12.23	-25.60	-38.80	-52.67	-61.97
0.20	0.0577	1.1547	-2.17	-1.88	-68.24	-5.29	-21.95	-37.26	-46.60	-60.91	-69.31
0.30	0.0866	1.7321	-4.39	-3.80	-71.72	-8.12	- 26.40	-41.00	-51.63	-65.57	-73.59
0.40	0.1155	2.3094	-6.98	-6.02	-74.38	-11.23	-31.37	-44.76	-55.01	-68.83	-76.39
0.50	0.1444	2.8868	-9.38	-8.15	-76.74	-13.87	-37.22	-46.82	-57.77	-71.07	-78.14
0.60	0.1732	3.4641	-11.35	-9.74	-78.45	-15.61	-38.43	-48.96	-60.67	-72.35	-79.51
0.70	0.2021	4.0415	-13.11	-11.56	-79.96	-16.84	-40.13	-49.86	-61.63	-73.16	-80.14
0.80	0.2310	4.61880	-14.16	-12.70	-80.95	-17.24	-39.34	-50.78	-61.71	-73.27	-80.36
0.90	0.2598	5.1962	-15.15	-13.57	-81.56	-17.71	-39.35	-51.18	-61.47	-73.49	-80.63
1.00	0.2887	5.7735	-15.79	-14.25	-82.16	-17.60	-38.42	-51.33	-61.36	-73.51	-80.62

2.4.2 Average Loss Factor

The SNR-normalized SINR metric from [32] examines the detriment caused by interference independent of the signal. The metric is a loss factor with the interference being the driving factor to the loss. The receive signal model considers homogeneous clutter. To mimic clutter, multiple point scatterers are generated. One hundred clutter scatterers are uniformly distributed over a normalized bandwidth of 0.01 centered at zero-Doppler with an average clutter-to-noise (CNR)

set to 80 dB. The signal vector used for the metric is

$$\mathbf{z}_{\mathrm{t}}(\ell;\sigma_{\varepsilon}) = \sum_{\omega_{\mathrm{clu}}} \bar{x}(\omega_{\mathrm{clu}},\ell)\,\mathbf{c}_{\mathrm{t}}(\omega_{\mathrm{clu}};\sigma_{\varepsilon}) + \mathbf{v}_{\mathrm{t}}(\ell). \tag{2.64}$$

To have a high-fidelity representation of the clutter, the samples used to generate the clutter in a given bin is preserved for formation of the optimal cancellation matrix. Ultimately, the analysis details how the sidelobe suppression affects the clutter cancellation.

When considering variations in staggering, the cancellation matrix becomes $\mathbf{R}_{\mathrm{t,canc}}(\ell;\sigma_{\varepsilon}) = (1/\sigma_{\mathrm{v}}^2)E\left\{\mathbf{z}_{\mathrm{t}}(\ell;\sigma_{\varepsilon})\,\mathbf{z}_{\mathrm{t}}^H(\ell;\sigma_{\varepsilon})\right\}$. SINR of the estimate is

$$\mathrm{SINR}_p(\omega,\ell;\sigma_{\varepsilon}) = \frac{\widehat{\rho}\,[\omega,\ell]\left|\mathbf{w}_p^H(\omega,\ell;\sigma_{\varepsilon})\,\mathbf{c}_{\mathrm{t}}(\omega;\sigma_{\varepsilon})\right|^2}{\mathbf{w}_p^H(\omega,\ell;\sigma_{\varepsilon})\,\mathbf{R}_{\mathrm{t,canc}}(\ell;\sigma_{\varepsilon})\,\mathbf{w}_p(\omega,\ell;\sigma_{\varepsilon})} \tag{2.65}$$

where $\mathbf{w}_p(\omega,\ell;\sigma_{\varepsilon}) = \mathbf{R}_{\mathrm{t,canc}}^{-1}(\ell;\sigma_{\varepsilon})\,\mathbf{u}_p(\omega,\ell;\sigma_{\varepsilon})$ denotes the multiple formulations $p \in$ [DP, WDP, AMMDP, PAMMDP] with cancellation. SNR is expressed as

$$\begin{aligned}\mathrm{SNR}_p(\omega,\ell;\sigma_{\varepsilon}) &= \frac{\widehat{\rho}\,[\omega,\ell]\left|\mathbf{w}_p^H(\omega,\ell;\sigma_{\varepsilon})\,\mathbf{c}_{\mathrm{t}}(\omega;\sigma_{\varepsilon})\right|^2}{\mathbf{w}_p^H(\omega,\ell;\sigma_{\varepsilon})\,\mathbf{R}_{\mathrm{t,v}}\mathbf{w}_p(\omega,\ell;\sigma_{\varepsilon})} \\ &= \frac{\widehat{\rho}\,[\omega,\ell]\left|\mathbf{w}_p^H(\omega,\ell;\sigma_{\varepsilon})\,\mathbf{c}_{\mathrm{t}}(\omega;\sigma_{\varepsilon})\right|^2}{\sigma_{\mathrm{v}}^2\left\|\mathbf{w}_p(\omega,\ell;\sigma_{\varepsilon})\right\|^2}.\end{aligned} \tag{2.66}$$

The loss factor is the ratio between SINR and SNR

$$\begin{aligned}\eta_p(\omega,\ell;\sigma_{\varepsilon}) &= \frac{\mathrm{SINR}_p(\omega,\ell;\sigma_{\varepsilon})}{\mathrm{SNR}_p(\omega,\ell;\sigma_{\varepsilon})} \\ &= \frac{\sigma_{\mathrm{v}}^2\left\|\mathbf{w}_p(\omega,\ell;\sigma_{\varepsilon})\right\|^2}{\mathbf{w}_p^H(\omega,\ell;\sigma_{\varepsilon})\,\mathbf{R}_{\mathrm{t,canc}}(\ell;\sigma_{\varepsilon})\,\mathbf{w}_p(\omega,\ell;\sigma_{\varepsilon})} \\ &= \frac{\sigma_{\mathrm{v}}^2\left\|\mathbf{R}_{\mathrm{t,canc}}^{-1}(\ell;\sigma_{\varepsilon})\,\mathbf{u}_p(\omega,\ell;\sigma_{\varepsilon})\right\|^2}{\mathbf{u}_p^H(\omega,\ell;\sigma_{\varepsilon})\,\mathbf{R}_{\mathrm{t,canc}}^{-1}(\ell;\sigma_{\varepsilon})\,\mathbf{u}_p(\omega,\ell;\sigma_{\varepsilon})}.\end{aligned} \tag{2.67}$$

The average loss factor (ALF) is the expectation over Monte Carlo trials

$$\mathrm{ALF}_p(\omega,\ell;\sigma_{\varepsilon}) = E\left\{\eta_p(\omega,\ell;\sigma_{\varepsilon})\right\}. \tag{2.68}$$

Mismatch loss is shown outside the clutter notch when ALF is less than 0 dB. Within the clutter notch, the ALF presents expected MDD. The metric describes the closest Doppler frequency to zero that can be attained before a predetermined SINR loss γ_{MDD} in the clutter notch. Define Ω_L as a set of normalized Doppler frequencies from -0.5 to 0 and Ω_U as a set of frequencies from 0 to 0.5. The MDD leveraging ALF is

$$\text{MDD}_p(\ell;\sigma_\varepsilon) = \frac{1}{2}\left(\underset{\omega_U}{\text{argmin}}\{|\text{ALF}_p(\omega_U,\ell;\sigma_\varepsilon)-\gamma_{\text{MDD}}|^2\} - \underset{\omega_L}{\text{argmin}}\{|\text{ALF}_p(\omega_L,\ell;\sigma_\varepsilon)-\gamma_{\text{MDD}}|^2\}\right) \tag{2.69}$$

where the operation $\underset{x}{\text{argmin}}\{f(x)\}$ is the value of x where $f(x)$ is minimized, $\omega_U \in \Omega_U$, and $\omega_L \in \Omega_L$. An example of MDD at $10\log_{10}(\gamma_{\text{MDD}}) = -3$ dB for an arbitrary optimal SINR is presented in Figure 2.16. The metric is typically set to -3 dB since that is where half the power is lost.

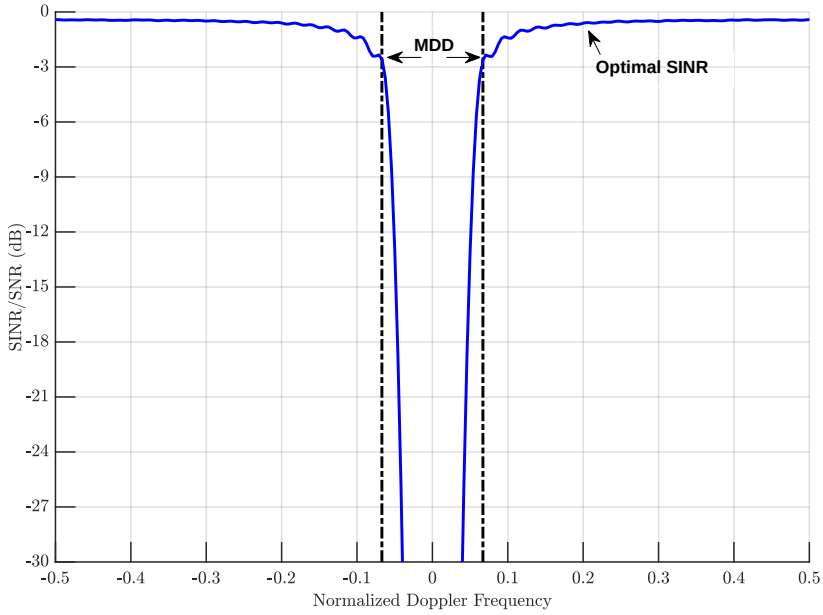

Fig. 2.16: Example of minimum detectable Doppler frequency for an SINR/SNR response

Figure 2.17 presents the loss factor for a uniform PRI. The ALF figures presented in this subsection contain two plots. The left plot presents the notch depth of the high-pass filter and the aliased notch. The right plot presents ALF above -6 dB to depict the mismatch loss. The left plot

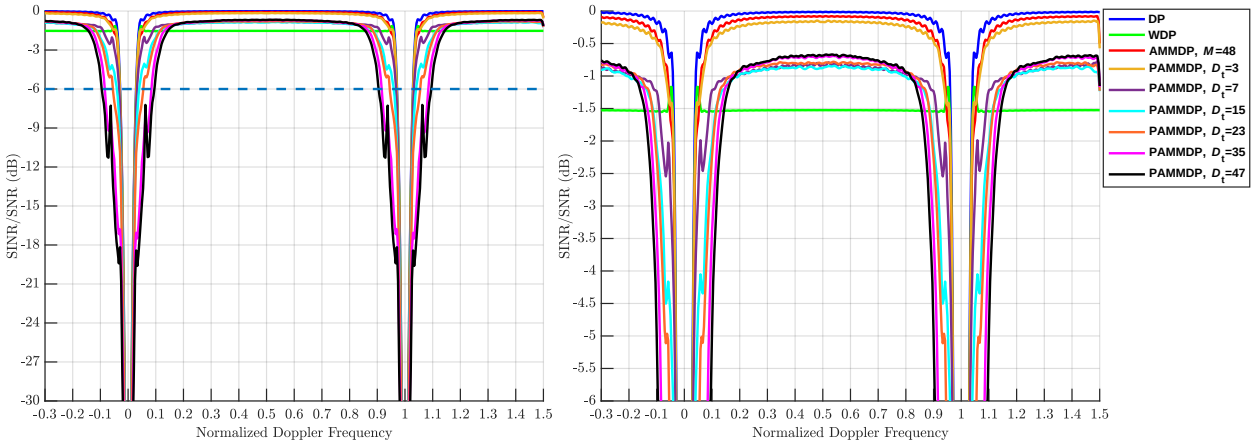

Fig. 2.17: Average loss factor for uniform PRI; Zoomed out (left) and zoomed in above -6 dB (right)

includes a dotted line at -6 dB. The undesirable comb filter from uniform transmission, which leads to blind speeds, is seen with an aliased null at normalized Doppler frequency of 1. Each formulation exhibits the same aliasing effect. AMMDP has the least amount of mismatch loss since it is the closet response to the optimal SINR. In the previous analysis, AMMDP was shown provide best sidelobe suppression (see Fig. 2.5). Thus, AMMDP provides minimal loss with maximal sidelobe suppression. For PAMMDP, the different reductions mainly have minor loss of roughly 0.8 dB. At $D_{\mathrm{t}} = 3$, the loss is closest to AMMDP because the D_{t} is less than the oversampling rate of 5 being used in these results. Consequently, beamspoiling causes PAMMDP to have a fractional loss for the benefit of nominal resolution. The MDD increases proportionally with D_{t}. Windowing provides the worst-case loss in comparison to adaptive formulations.

Figures 2.18-27 present ALF for with increasing standard deviation. These figures show as the standard deviation increases, staggering decreases the depth of the loss at $\omega = 1$ and MDD of each approach decreases. Also, throughout the results AMMDP performs efficiently by having a minor mismatch loss of a fraction of a dB. In Fig. 2.18 staggering for $\sigma_{\varepsilon} = 0.0289$ is presented. AMMDP and PAMMDP at $D_{\mathrm{t}} = 3$ remain the next two closest responses to the optimal SINR. As the reduced-rank decreases, the mismatch loss and MDD improves. In some instances, such as $D_{\mathrm{t}} = 35$ and $D_{\mathrm{t}} = 47$, the mismatch loss falls below windowing. These reductions would be high for a computational benefit.

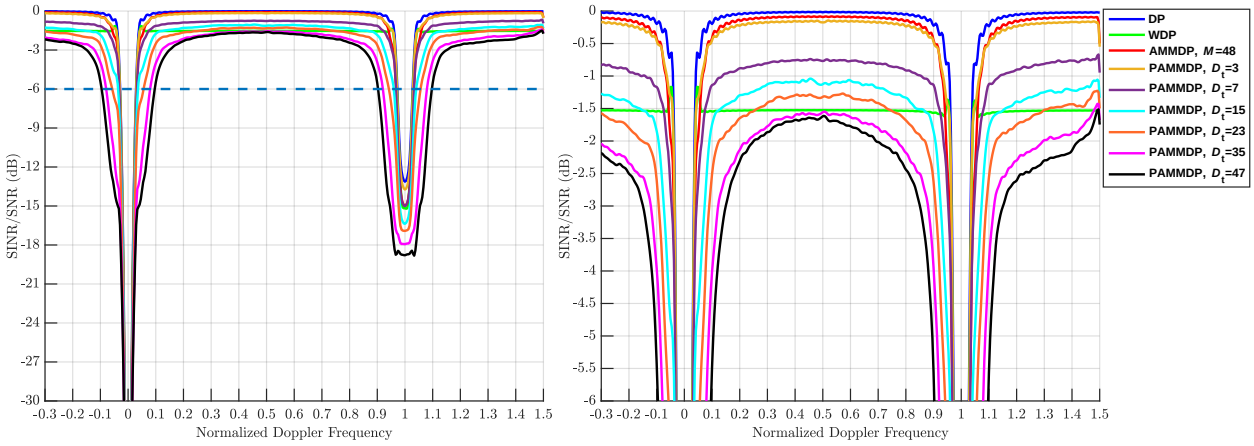

Fig. 2.18: Average loss factor for staggered PRI with $\sigma_\varepsilon = 0.0289$; Zoomed out (left) and zoomed in above -6 dB (right)

The performance of windowing, AMMDP, and PAMMDP observed in Figure 2.18 remains fairly consistent for Figs 2.18-27. Fig. 2.27 demonstrates the overall trade-space for PAMMDP performance. At higher rank reductions, PAMMDP is more susceptible to mismatch loss. Considering the results from the previous section, a lower rank has the lowest computation, worst-case sidelobes, and best-case mismatch loss. For a high deviation in the pulse-to-pulse staggering, a higher rank reduction has the highest computation, best-case sidelobes, and worst-case loss. Therefore, a lower reduced rank suffers less mismatch loss and have better MDD at the penalty of degraded sidelobe suppression performance. Also, the edge effect from performing AMMDP and PAMMDP likewise affects the loss. Solution presented in the previous section should be implemented to maximize the adaptive filters performance. It is worth mentioning that AMMDP and PAMMDP maintain a great notch at zero-Doppler and do not hinder performance.

Tables 2.5 and 2.6 are presented to accompany the responses show in the figures. Table 2.5 presents the average loss factor at the aliased target response of $\omega = 1$. Table 2.6 presents the ALF at over the 0.3 to 1.3 band of normalized Doppler frequencies omitting the edge effect. Highlighted in yellow is differences from Table 2.5. For uniform PRI in the first row presents the depth of the clutter notch. Since aliasing is undesirable, a lower power in the alias notch is undesirable. The table better represents the PAMMDP trade space showing that as rank increases,

performance decreases. In some cases, PAMMDP ability to compensate for aliasing is less than windowing. It should be emphasized that most of the performance benefit seen in Tables 2.5 and 2.6 is a result of staggering. The results show how performance is varied for each staggering scenario. The performance differences are a fraction of a dB so overall the performance difference results are small. However, the stability of the algorithms as a function of staggering is seen. Doppler processing, windowing, and AMMDP remain stable. PAMMDP stability across staggering decreases with increasing D_{t}.

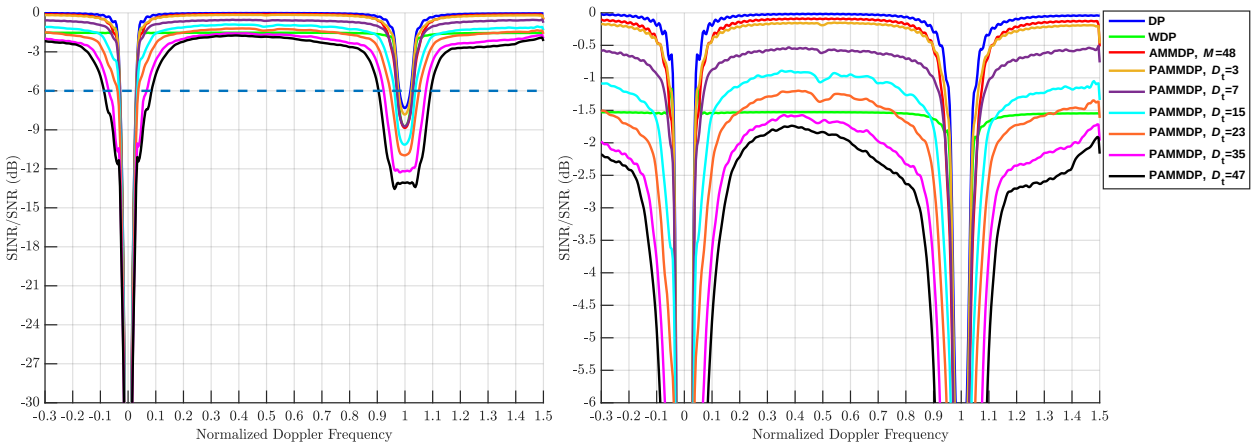

Fig. 2.19: Average loss factor for staggered PRI with $\sigma_{\varepsilon} = 0.0577$; Zoomed out (left) and zoomed in above -6 dB (right)

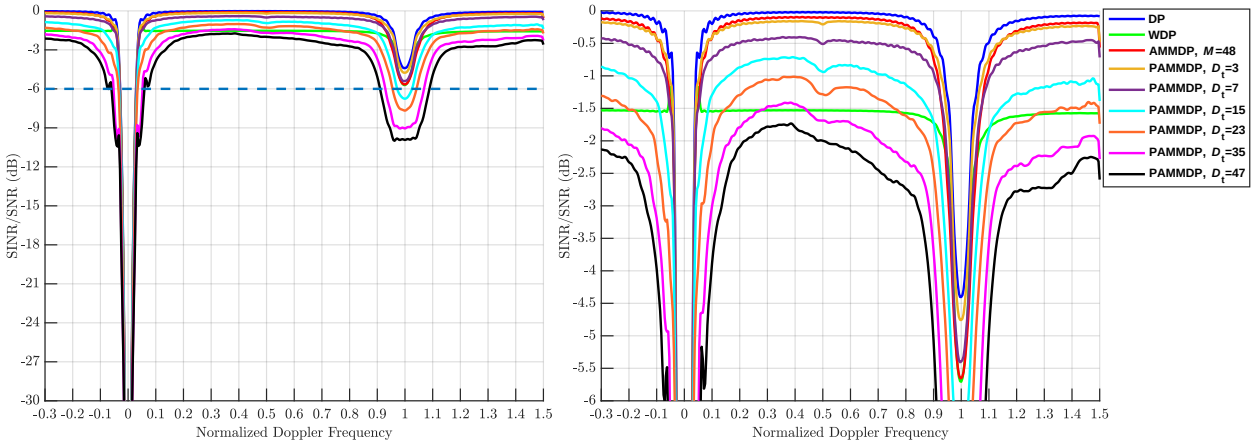

Fig. 2.20: Average loss factor for staggered PRI with $\sigma_{\varepsilon} = 0.0866$; Zoomed out (left) and zoomed in above -6 dB (right)

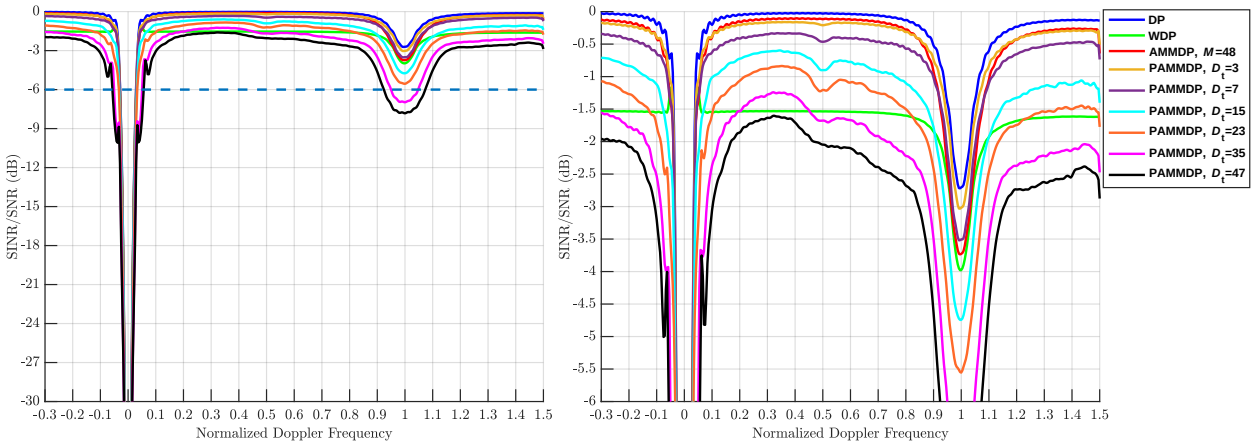

Fig. 2.21: Average loss factor for staggered PRI with $\sigma_\varepsilon = 0.1155$; Zoomed out (left) and zoomed in above -6 dB (right)

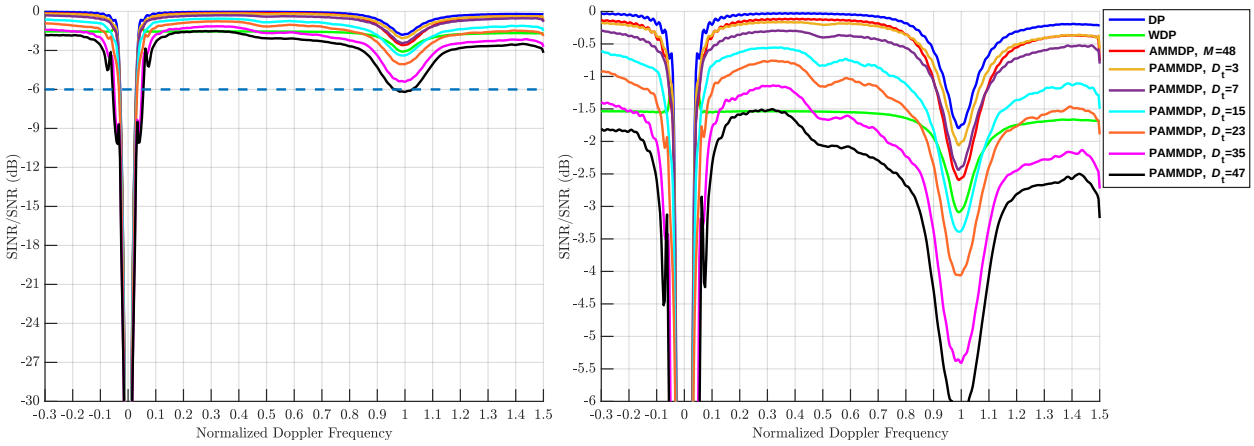

Fig. 2.22: Average loss factor for staggered PRI with $\sigma_\varepsilon = 0.1444$; Zoomed out (left) and zoomed in above -6 dB (right)

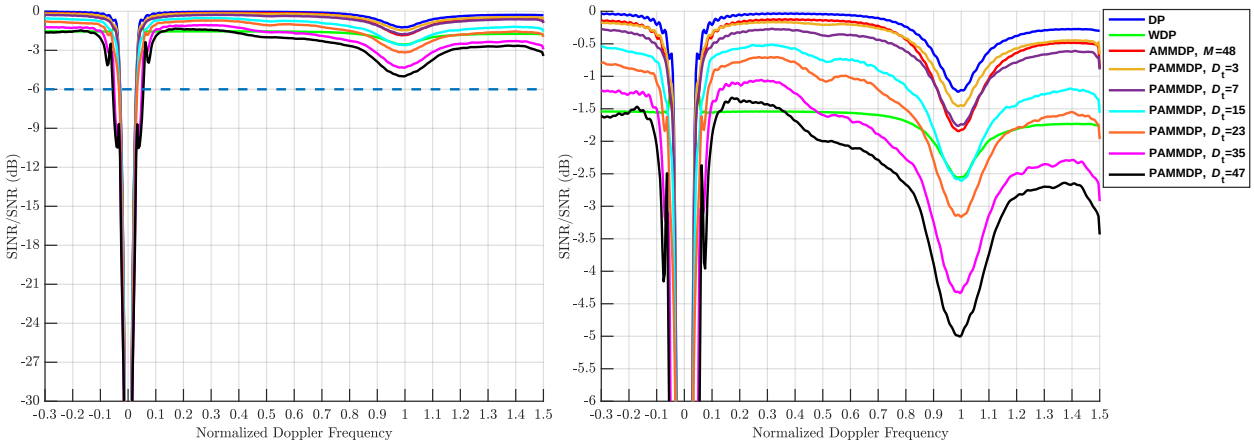

Fig. 2.23: Average loss factor for staggered PRI with $\sigma_\varepsilon = 0.1732$; Zoomed out (left) and zoomed in above -6 dB (right)

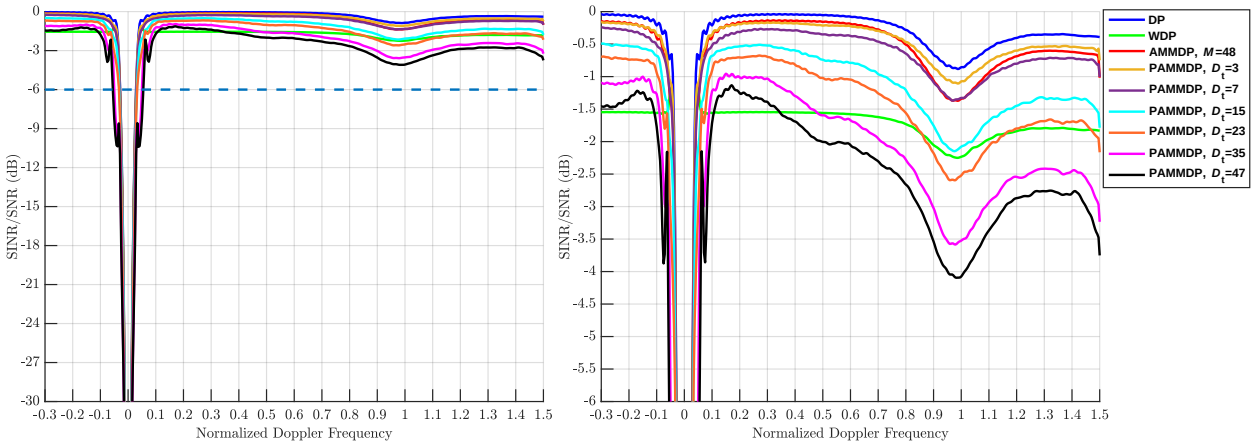

Fig. 2.24: Average loss factor for staggered PRI with $\sigma_\varepsilon = 0.2021$; Zoomed out (left) and zoomed in above -6 dB (right)

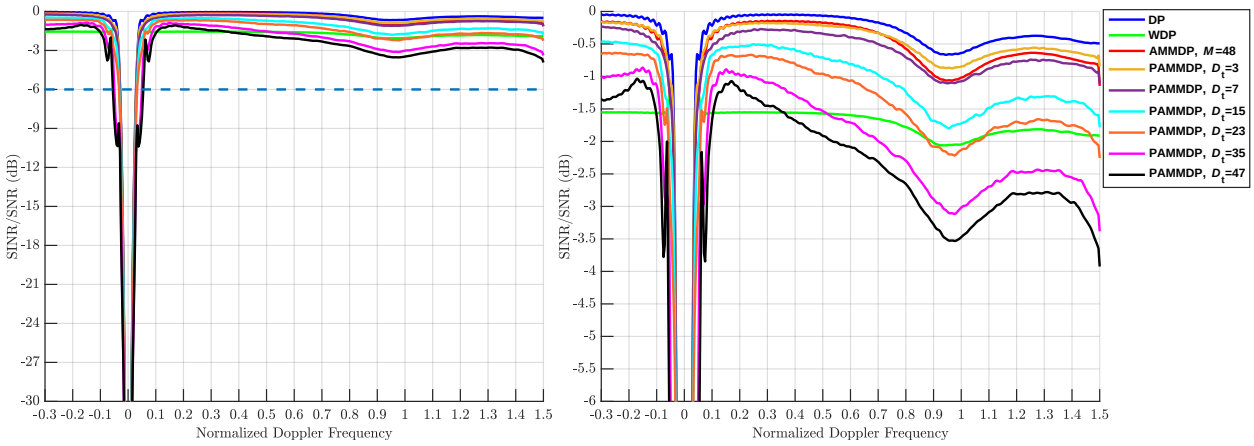

Fig. 2.25: Average loss factor for staggered PRI with $\sigma_\varepsilon = 0.2310$; Zoomed out (left) and zoomed in above -6 dB (right)

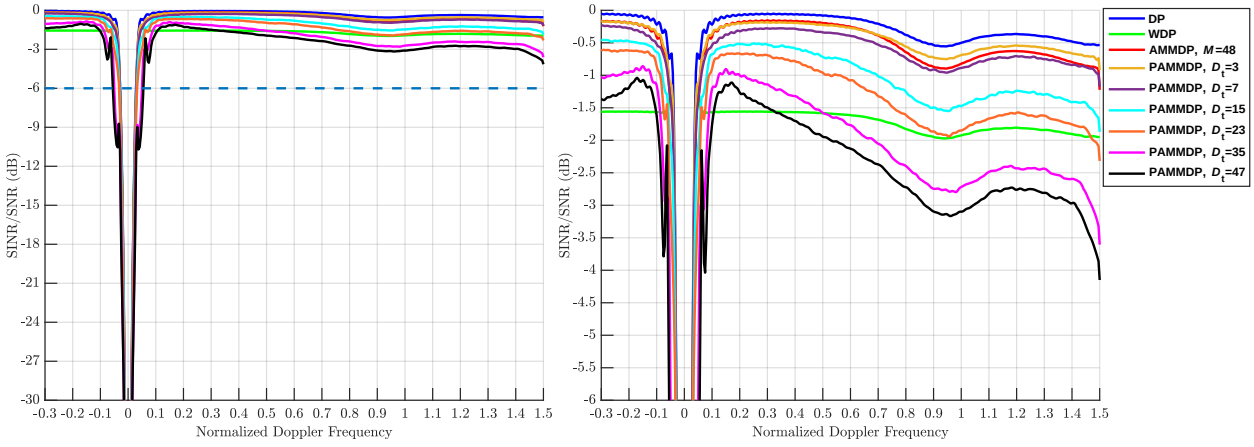

Fig. 2.26: Average loss factor for staggered PRI with $\sigma_\varepsilon = 0.2598$; Zoomed out (left) and zoomed in above -6 dB (right)

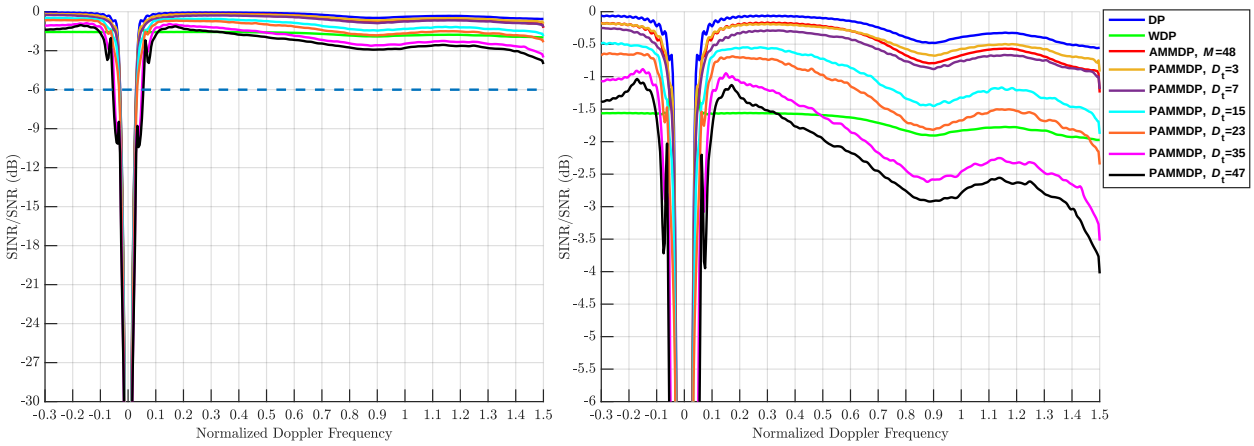

Fig. 2.27: Average loss factor for staggered PRI with $\sigma_\varepsilon = 0.2887$; Zoomed out (left) and zoomed in above -6 dB (right)

Table 2.5: Average loss factor at $\omega = 1$

W	σ_ε	σ_T (μs)	DP (dB)	WDP (dB)	AMMDP (dB)	PAMMDP (dB)					
						$D_t = 3$	$D_t = 7$	$D_t = 15$	$D_t = 23$	$D_t = 35$	$D_t = 47$
0.00	0.0000	0.0000	-69.31	-82.9	-84.54	-90.71	-79.51	-83.21	-81.10	-78.06	-79.08
0.10	0.0289	0.5774	-13.13	-15.16	-14.98	-13.73	-15.01	-16.37	-16.91	-17.93	-18.79
0.20	0.0577	1.1547	-7.33	-8.75	-8.85	-7.83	-8.73	-10.14	-10.96	-12.20	-13.09
0.30	0.0866	1.7321	-4.40	-5.71	-5.65	-4.76	-5.40	-6.76	-7.67	-9.05	-9.93
0.40	0.1155	2.3094	-2.70	-3.98	-3.73	-3.02	-3.51	-4.74	-5.55	-6.97	-7.82
0.50	0.1444	2.8868	-1.74	-3.06	-2.56	-2.01	-2.39	-3.38	-4.05	-5.41	-6.19
0.60	0.1732	3.4641	-1.21	-2.55	-1.82	-1.44	-1.74	-2.61	-3.16	-4.32	-4.99
0.70	0.2021	4.0415	-0.86	-2.23	-1.34	-1.07	-1.33	-2.08	-2.52	-3.52	-4.08
0.80	0.2310	4.61880	-0.64	-2.05	-1.02	-0.85	-1.07	-1.72	-2.13	-3.02	-3.47
0.90	0.2598	5.1962	-0.50	-1.92	-0.82	-0.69	-0.89	-1.47	-1.85	-2.72	-3.10
1.00	0.2887	5.7735	-0.39	-1.83	-0.67	-0.57	-0.75	-1.32	-1.67	-2.46	-2.79

Table 2.6: Average loss factor over normalized Doppler bandwidth 0.3 to 1.3

W	σ_ε	σ_T (μs)	DP (dB)	WDP (dB)	AMMDP (dB)	PAMMDP (dB)					
						$D_t = 3$	$D_t = 7$	$D_t = 15$	$D_t = 23$	$D_t = 35$	$D_t = 47$
0.00	0.0000	0.0000	-69.31	-95.18	-90.84	-90.71	-79.51	-83.21	-81.10	-78.06	-79.08
0.10	0.0289	0.5774	-13.13	-15.21	-14.98	-13.73	-15.01	-16.37	-16.91	-17.93	-18.82
0.20	0.0577	1.1547	-7.33	-8.75	-8.85	-7.83	-8.73	-10.14	-10.96	-12.28	-13.55
0.30	0.0866	1.7321	-4.40	-5.71	-5.65	-4.76	-5.41	-6.76	-7.67	-9.05	-9.99
0.40	0.1155	2.3094	-2.72	-3.98	-3.74	-3.03	-3.52	-4.74	-5.55	-6.97	-7.82
0.50	0.1444	2.8868	-1.80	-3.09	-2.59	-2.06	-2.44	-3.39	-4.06	-5.41	-6.19
0.60	0.1732	3.4641	-1.24	-2.56	-1.84	-1.46	-1.76	-2.61	-3.16	-4.34	-5.00
0.70	0.2021	4.0415	-0.88	-2.25	-1.37	-1.11	-1.37	-2.15	-2.60	-3.58	-4.10
0.80	0.2310	4.61880	-0.67	-2.06	-1.06	-0.88	-1.11	-1.80	-2.22	-3.12	-3.53
0.90	0.2598	5.1962	-0.55	-1.97	-0.90	-0.75	-0.96	-1.55	-1.94	-2.80	-3.17
1.00	0.2887	5.7735	-0.48	-1.91	-0.79	-0.68	-0.88	-1.45	-1.82	-2.62	-2.92

2.4.3 Total Residual Sidelobe Response

Total residual sidelobe response (TRSR) examines the aggregate sidelobe energy after processing. The metric examines the sidelobe suppression performance of the various Doppler processing algorithms. The analysis considers the following receive signal

$$\mathbf{z}_t(\ell;\sigma_\varepsilon) = \begin{cases} \bar{x}[\omega_{\text{mov}},\ell_{\text{mov}}]\,\mathbf{c}_t(\omega_{\text{mov}};\sigma_\varepsilon) + \sum\limits_{\omega_{\text{clu}}\in\Omega_{\text{clu}}} \bar{x}[\omega_{\text{clu}},\ell_{\text{clu}}]\,\mathbf{c}_t(\omega_{\text{clu}};\sigma_\varepsilon) + \mathbf{v}_t(\ell;\sigma_\varepsilon) & \text{for } \ell_{\text{mov}} = \ell \\ \sum\limits_{\omega_{\text{clu}}\in\Omega_{\text{clu}}} \bar{x}[\omega_{\text{clu}},\ell_{\text{clu}}]\,\mathbf{c}_t(\omega_{\text{clu}};\sigma_\varepsilon) + \mathbf{v}_t(\ell;\sigma_\varepsilon) & \text{otherwise,} \end{cases} \tag{2.70}$$

with a single target at $\omega_{\text{mov}} = 0.8$ placed in the center range bin of the data with SNR = 50 dB and 100 clutter scatterers containing normalized Doppler frequencies uniformly distribution over a normalized Doppler bandwidth of 0.01 centered at zero Doppler and an average CNR = 50 dB. Clutter is generated separately for each range bin and Monte Carlo run. The TRSR metric without cancellation is

$$\text{TRSR}_p(\ell;\sigma_\varepsilon) = \frac{\sum\limits_{\omega\in\Omega} \left|\mathbf{u}_p^H(\omega;\sigma_\varepsilon)\,\mathbf{z}_t(\ell;\sigma_\varepsilon)\right|^2}{\max\limits_{\omega} \left\{\left|\mathbf{u}_{\text{DP}}^H(\omega;\sigma_\varepsilon)\,\mathbf{z}_t(\ell;\sigma_\varepsilon)\right|^2\right\}} \tag{2.71}$$

where $p \in$ [DP, WDP, AMMDP, PAMMDP] to denote the different processing techniques. When cancellation is performed, $\mathbf{z}_{\mathrm{t}}(\ell;\sigma_\varepsilon)$ is replaced by $\widehat{\mathbf{z}}_{\mathrm{t}}(\ell;\sigma_\varepsilon)$. The set Ω contains the oversampled normalized Doppler spectrum from $\omega = -1$ to $\omega = 1$ but omits frequencies corresponding to the nominal mainlobe resolution of the mover mainlobe and clutter bandwidth. Hence, only the sidelobes are examined. The normalization term in each TRSR is approximately one. In some instances, it may be slightly above one due to the clutter. When clutter cancellation is performed, the normalization is always below one. The formation of the SaCM satisfies the RMB rule with guard cells removed to avoid self-cancellation.

In Figure 2.28, TRSR is presented without clutter cancellation as a function of standard deviation. Without staggering, the AMMDP formulation outperforms Doppler processing and window Doppler processing. When modest staggering is incorporated at $\sigma_\varepsilon = 0.0289$, AMMDP ability to suppress sidelobes significantly improves by roughly 20 dB. PAMMDP follows suit for higher values of D_{t}. Performance diminishes as D_{t} decreases. Even at $D_{\mathrm{t}} = 3$ for $\sigma_\varepsilon = 0.0289$, PAMMDP performs better than typical processing techniques. For the PAMMDP results, as standard deviation increases, it presents a valley then a monotonic increase. The loss in performance as a function of standard deviation shows that the lower reduced-rank filters do not have the degrees-of-freedoms necessary to combat the rising sidelobes. AMMDP can maintain its performance as standard deviation increases. Overall, staggering is an asset to AMMDP to improve the formulation sidelobe performance. In Figure 2.29, TRSR is presented with clutter cancellation. Without staggering, the Doppler processing, windowing, and adaptive mismatch processing techniques improve by approximately 3 dB in comparison to Figure 2.27. The gains in PAMMDP for lower ranks are higher with some improvements greater than 6 dB (see $D_{\mathrm{t}} = 7$ and $D_{\mathrm{t}} = 15$). As D_{t} increases, the effect of MTI filtering to boost performance decreases. Utilizing MTI filtering with AMMDP and PAMMDP provide a performance improvement to Doppler processing. Combining clutter cancellation and PAMMDP is a necessity to maximize the performance of the sidelobe suppression. Sidelobe suppression performance significantly improves for AMMDP and PAMMDP (at medium to high rank reductions) when PRI staggering

is incorporated. Lastly, an interesting result is the valley at $\sigma_\epsilon = 0.0577$ for the PAMMDP results which shows the responses having a maximum staggering performance at this variance.

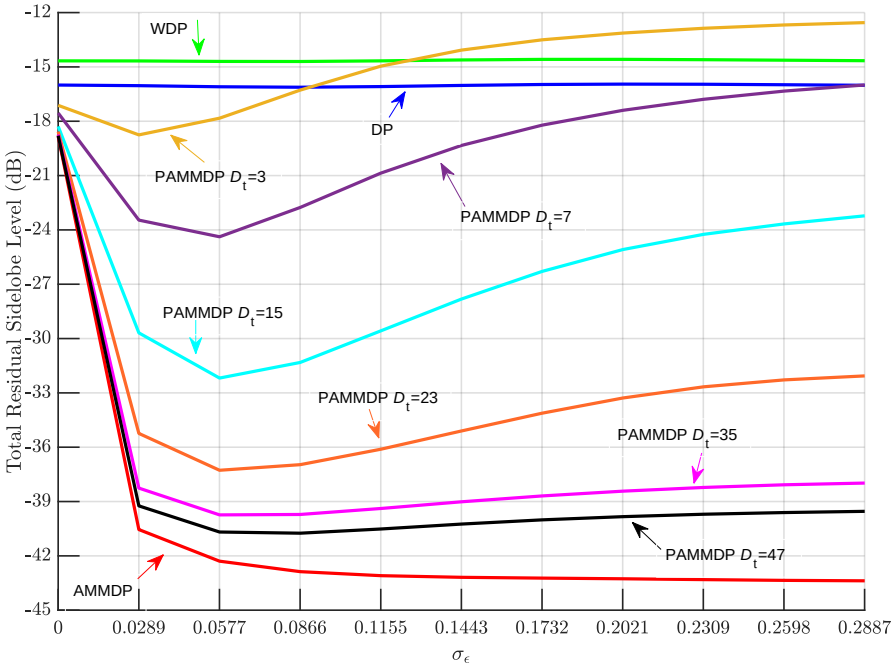

Fig. 2.28: Total residual sidelobe response for uniform and random staggered PRI without clutter cancellation

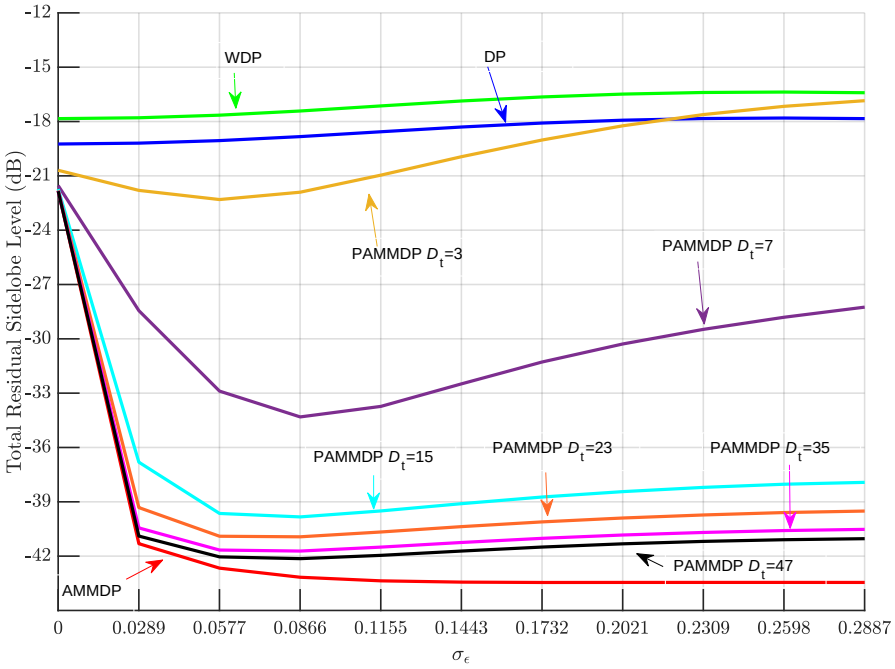

Fig. 2.29: Total residual sidelobe response for uniform and random staggered PRI with clutter cancellation

2.5 Ground-Based Open-Air Experimental Results

Open-air experimental testing was performed at the University of Kansas to further examine the proposed techniques. A monostatic, ground based, pulse-Doppler radar operating at S-band carrier frequency of 3.55 GHz with simultaneous transmit and receive capabilities was utilized. Figure 2.30 presents the experimentation set-up and scene field of view. The transmit and receive antennas are steered towards a nearby busy intersection. The radar scene included forestry and buildings in addition to moving vehicles. A transmit LFM waveform with a time bandwidth of $B\tau = 150$ was generated via an arbitrary waveform generator. The receive data was IQ sampled using a real-time spectrum analyzer. The IQ data was later processed off-line. The receiver sampling rate is f_s = 200 MHz. The noise floor is estimated to be -65 dBm. The noise floor decreases to approximately -104 dBm following coherent gains from pulse compression and Doppler processing. The error power is determined empirically and was set to 10 dB below the noise floor.

The uniform and staggered PRI datasets were collected in different runs. Consequently, the radar scenes in each collection differ. For continuity between the runs, a synthetic target is place at $\omega = 0.8$ in range cuts of interest that contain a target. The PRIs were staggered CPI-to-CPI for 48 CPIs. Each CPI contained a uniform PRI of 50 pulses. In total, 2400 pulses were transmitted. The random staggered PRI is selected over a PRF range of 30 kHz and 100 kHz. The selected staggers had an average PRF of 50 kHz. The random selection of PRI significantly increased the unambiguous Doppler frequency. Based on the PRI parameters, movers within the radar scene fell within the first PRI regime. However, the deleterious sidelobe effects of staggering still will be present in receive processing.

Presumming is performed on each CPI, improving the SNR by approximately 16 dB. Accordingly, the pulse-Doppler system transitioned to a pulse-to-pulse stagger with single CPI of $M = 48$ pulses. The averaging likewise changes the system PRF range to 600 Hz and 2 kHz with average PRF of 1 kHz for staggering. A second collection is obtained without PRI staggering where 2400 pulses were transmitted with a PRF of 50 kHz. After pre-summing, the uniform PRI collection contained $M = 48$ pulses and had a PRF of 1 kHz.

After discrete pulse compression, the range profile is 2000 range samples. The intersection being examined is contained within $L_{\mathrm{f}} = 400$ range samples. The Doppler spectrum is examined over a normalized Doppler region of -0.5 and 1. The spectrum was oversampled by a factor of $K_{\mathrm{D}} = 5$ for a total of $L_{\mathrm{D}} = 375$ Doppler frequencies. Windowing was performed using a Taylor window with a -50 dBm peak sidelobe and five nearly constant sidelobes. The iterative procedure of AMMDP and PAMMDP concluded after 5 iterations. PAMMDP was set to $D_{\mathrm{t}} = 17$.

2.5.1 Uniform PRI

In Figure 2.31, the Doppler spectrum at a range of 1035 m for a uniform PRI with and without MTI filtering for the different processing techniques. The first PRF regime is from $\omega = -0.5$ to $\omega = 0.5$. Any responses beyond $\omega = 0.5$ are aliased. By observation, movers are present at $\omega = -0.2$

Fig. 2.30: Hardware instrumentation setup (left) and annotated field of view (right, courtesy of Google Maps) for measured results. The radar and intersection are depicted with a yellow star and yellow ellipse, respectively

and approximately $\omega = -0.05$. The sidelobe suppression benefits of windowing, AMMDP, and PAMMDP over Doppler processing are shown. For AMMDP and PAMMDP, the reduction of power from the peak on movers and clutter is not fully a mismatch or signal loss. Rather the contributions from adjacent sidelobes are being suppressed thereby reducing the response to its "true" power. PAMMDP robustness from simulation results is observed here. In Fig. 2.31b, which has MTI filtering, each technique can efficiently suppress the clutter response at zero-Doppler while maintaining their estimation performance.

Range-Doppler maps of the collected data is presented for each processed technique with Doppler processing in Figure 2.32, windowing in Fig. 2.33, AMMDP in Fig. 2.34, and PAMMDP in Fig. 2.35. Aliased regions are highlighted by the pink dotted lines. Comparing maps containing clutter, the Doppler sidelobes for Doppler processing is only prevalent. Other techniques have the Doppler sidelobes suppressed. Windowing in Fig 2.33 presents the wider Doppler footprint of the targets due to the mainlobe width widening. The AMMDP and PAMMDP maps are almost identical and provides the mainlobe width of Doppler processing and sidelobe suppression of windowing. Each map presented can leverage MTI filtering to suppress the clutter.

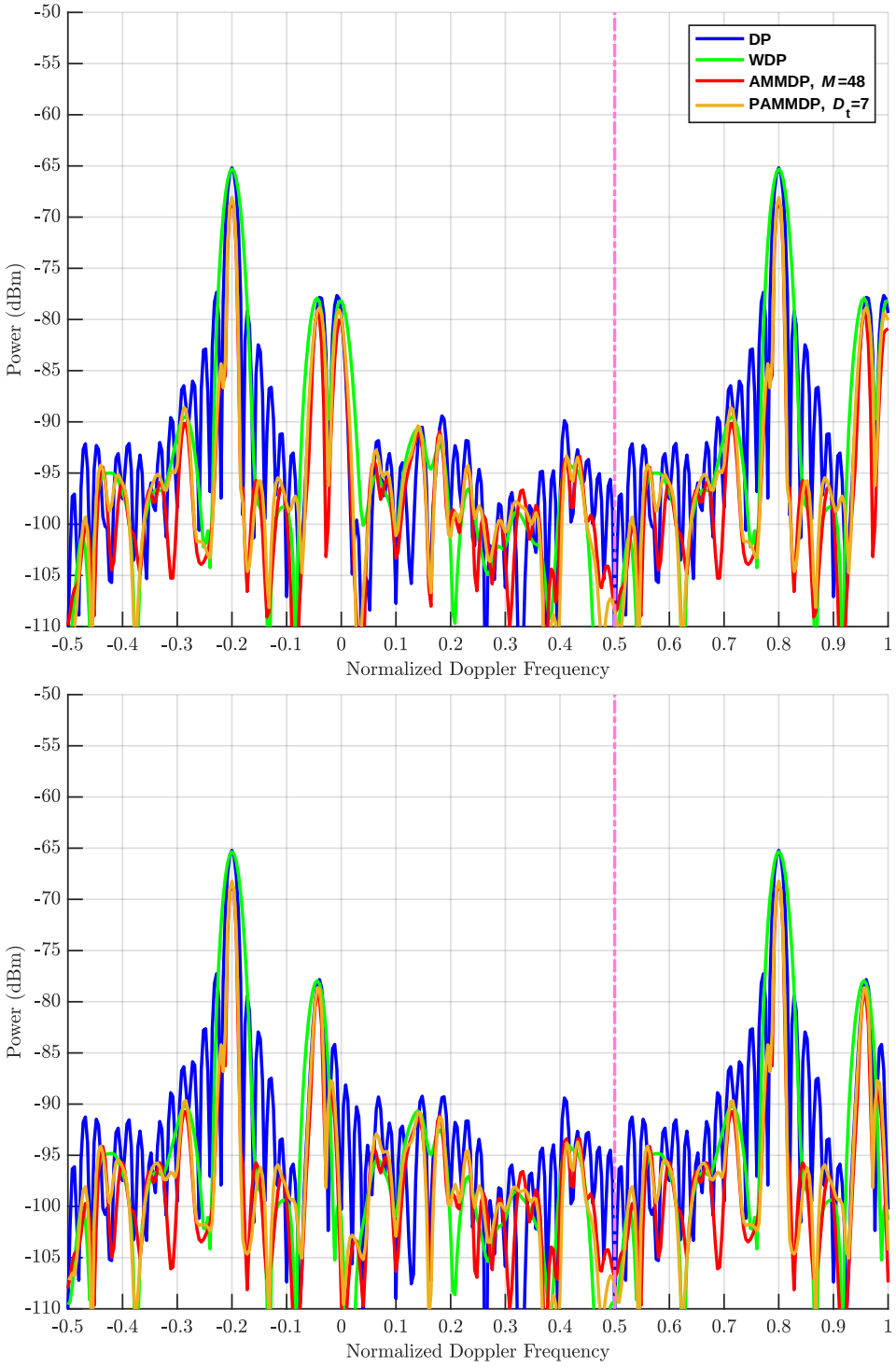

Fig. 2.31: Doppler spectrum at range CUT 1150 m for a staggered PRI (top) with clutter and (bottom) MTI filtering

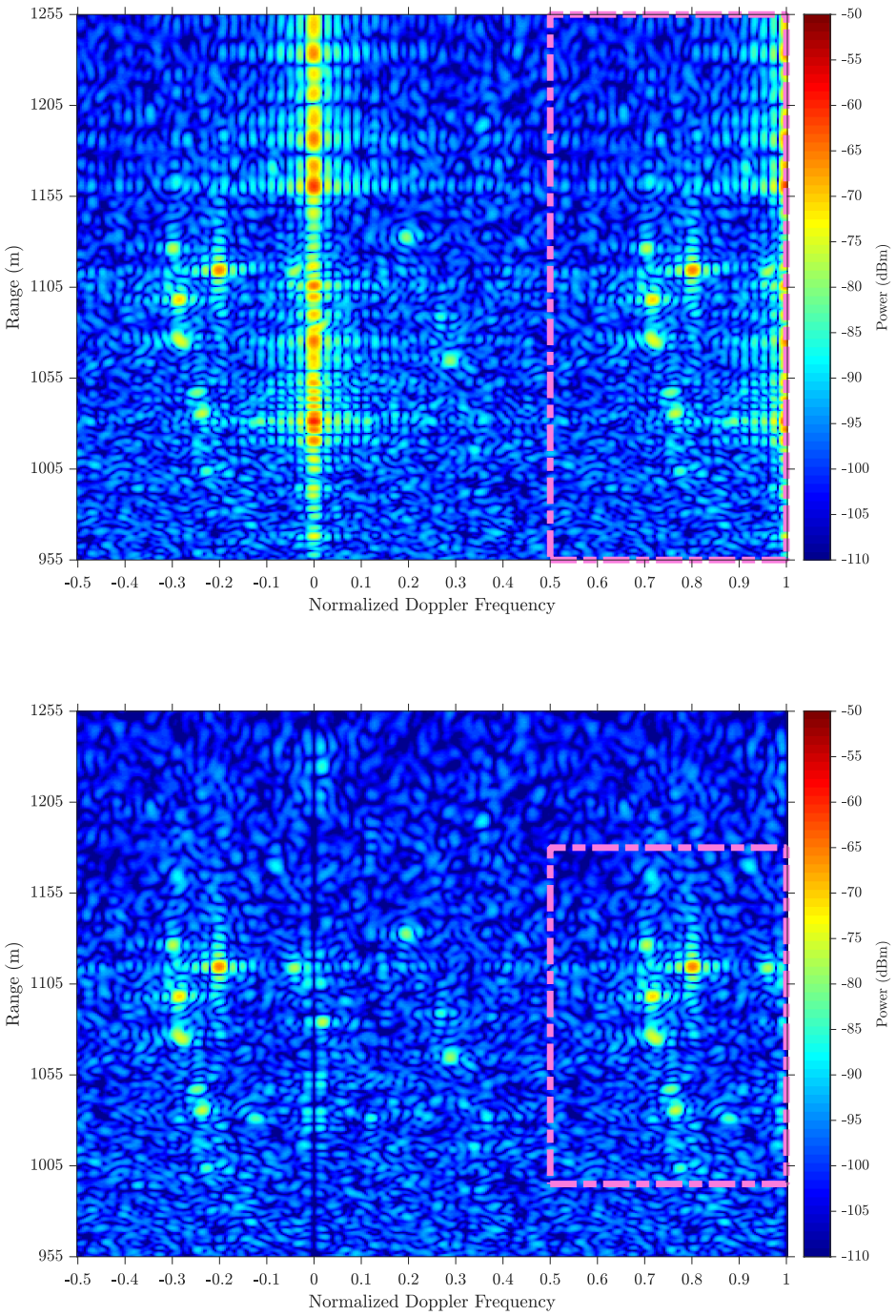

Fig. 2.32: Range-Doppler map of Doppler processing for a uniform PRI (top) with clutter and (bottom) MTI filtering

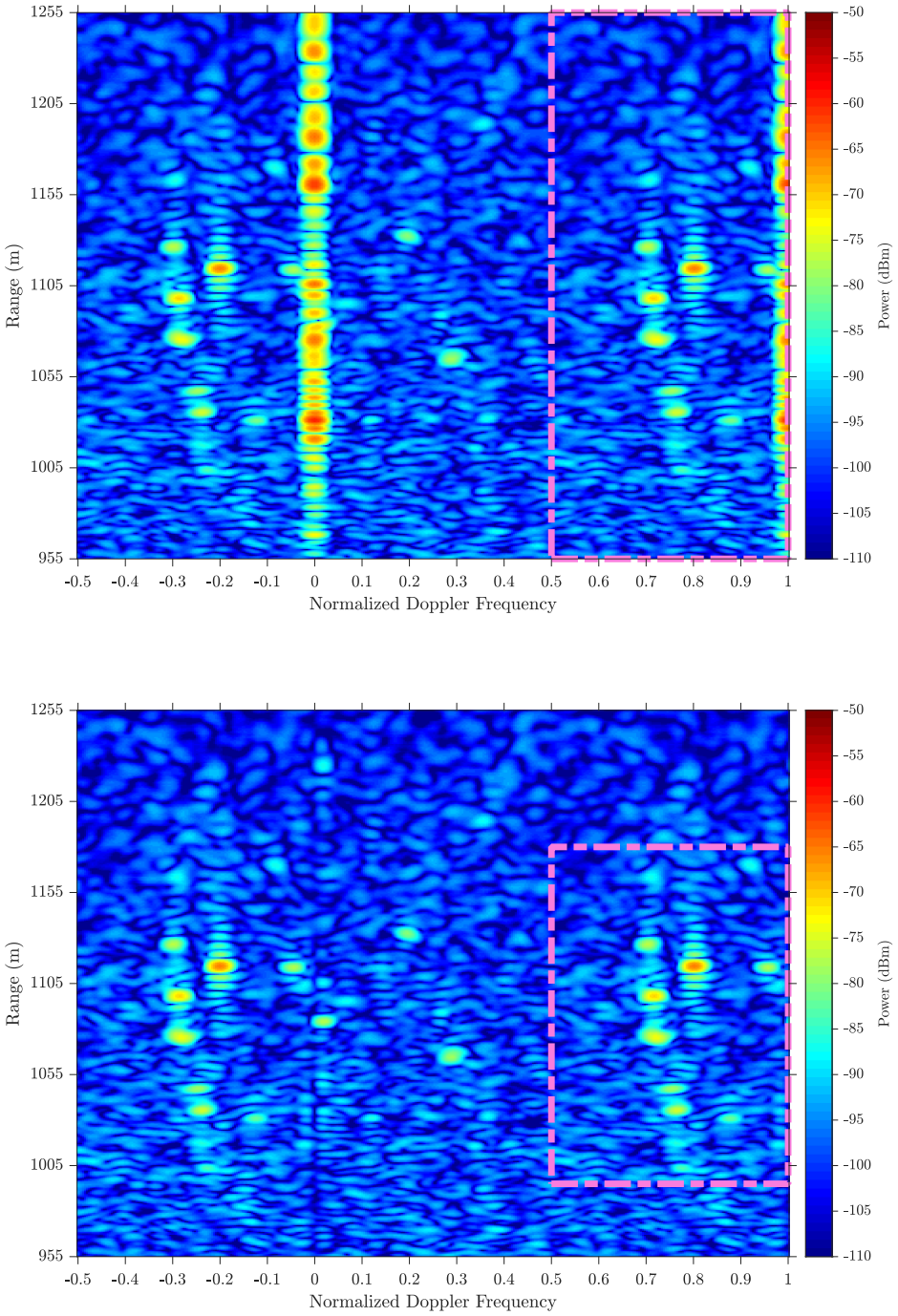

Fig. 2.33: Range-Doppler map of window Doppler processing for a uniform PRI (top) with clutter and (bottom) MTI filtering

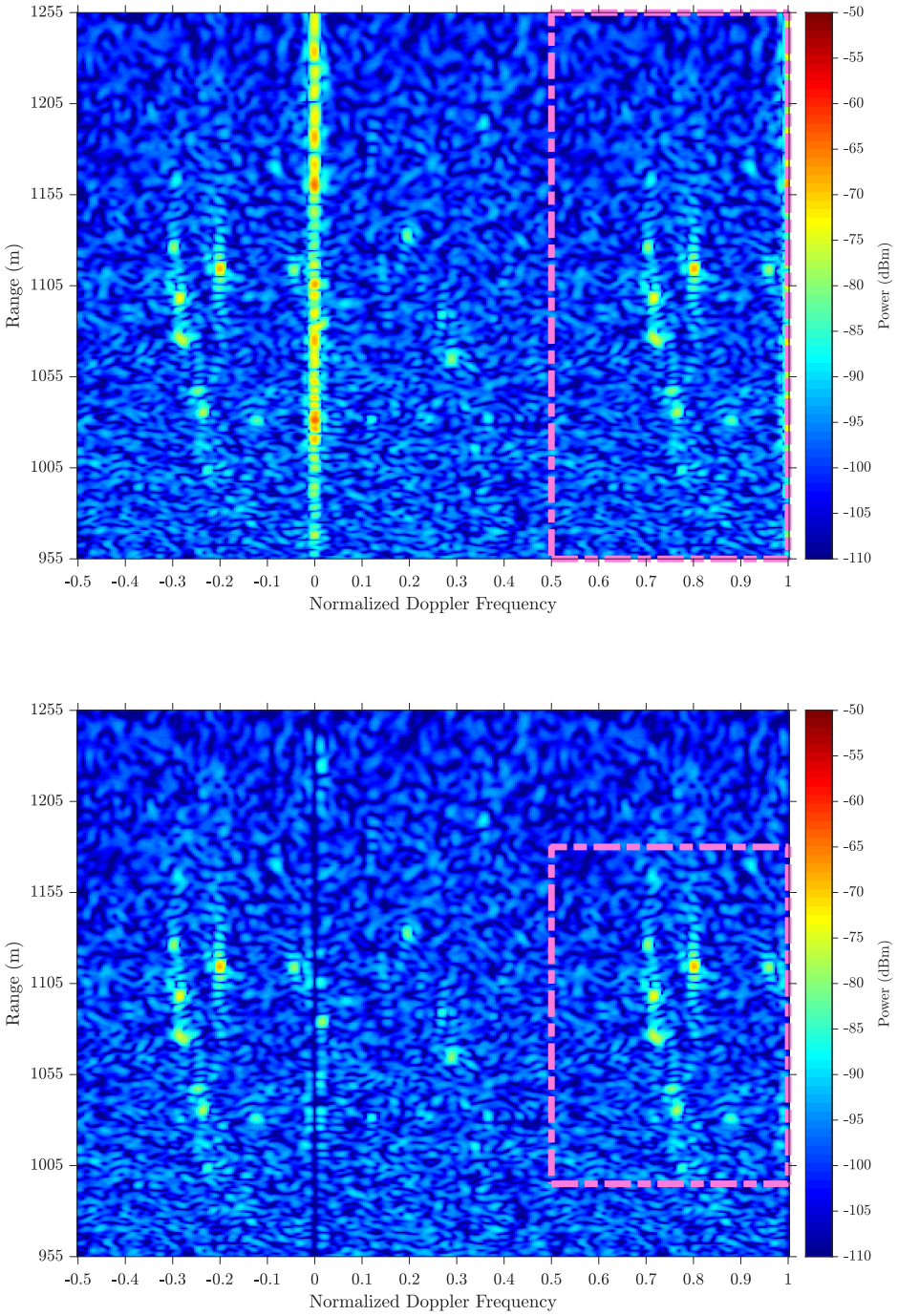

Fig. 2.34: Range-Doppler map of AMMDP for a uniform PRI (top) with clutter and (bottom) MTI filtering

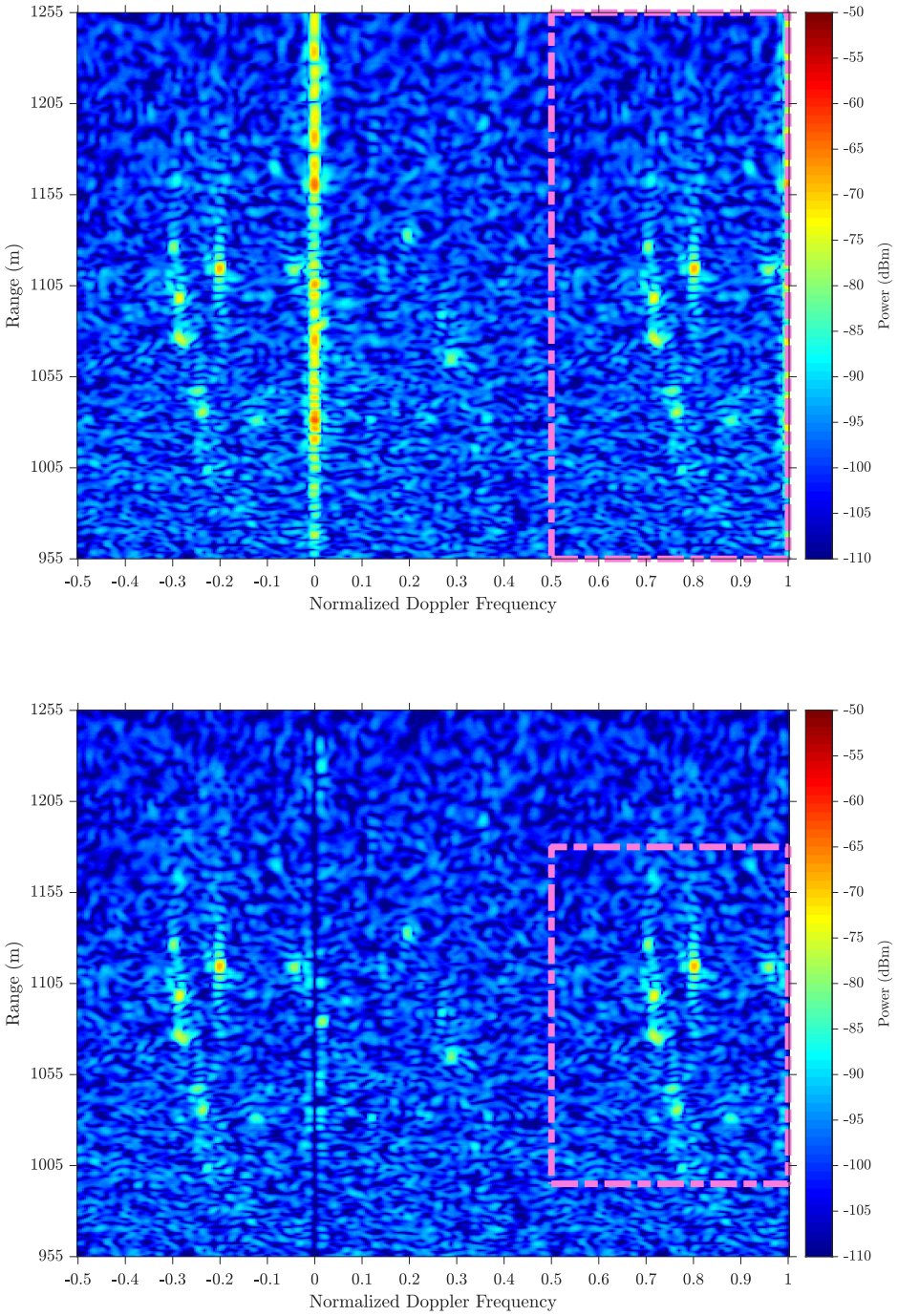

Fig. 2.35: Range-Doppler map of PAMMDP for a uniform PRI (top) with clutter and (bottom) MTI filtering

2.5.2 Staggered PRI

The following dataset was captured from a separate collection during the same test. Figure 2.36 presents the Doppler spectrum at range sample 1150 m. By observation, movers exist at $\omega = -0.3$, $\omega = 0.15$, and $\omega = 0.8$. Without MTI filtering in Fig. 2.36a, the sidelobe structure of Doppler processing and windowing masks the mover at 0.8. As expected, windowing sidelobe benefits diminish. AMMDP and PAMMDP can unmask this mover. Unlike for uniform PRI in the previous section, AMMDP and PAMMDP have differing sidelobe structures. AMMDP provides better nulls in some velocities (see normalized Doppler of $\omega = -0.32$ and $\omega = -0.11$). Incorporating MTI filtering as shown in Fig. 2.36b benefits each formulation. However, Doppler processing and windowing sidelobe floor is higher than AMMDP and PAMMDP. At zero-Doppler, Doppler processing presents a distinct null. Windowing likewise places a null yet not as deep. The AMMDP and PAMMDP formulation instead shows energy located in the Doppler bin.

The analysis continues to examine the range-Doppler maps of Doppler processing in Figure 2.37, windowing in Fig. 2.38, AMMDP in Fig. 2.39, and PAMMDP in Fig. 2.40. In Figs. 2.37a and 2.38a for Doppler processing and windowing, respectively, the spectral spread in Doppler due to staggering observed. Performing MTI filtering, shown in Figs. 2.36b and 2.37b, helps tremendously. However, in range bins where movers are located, there is a spread of energy in Doppler. AMMDP and PAMMDP, shown in Fig 2.38a and Fig. 2.39a, are able to efficiently suppress the sidelobes and unmask scattering independent of MTI filtering. With MTI filtering, each formulation leverages clutter cancellation to unmask slower movers closer to zero-Doppler. The adaptive mismatch techniques perform better to resolve movers in comparison to traditional techniques. Overall, PAMMDP at $D_{\mathrm{t}} = 17$ provided a computational improvement by a factor of approximately 3 and performs on par with AMMDP. Accordingly, the method can provide performance and computation benefit simultaneous.

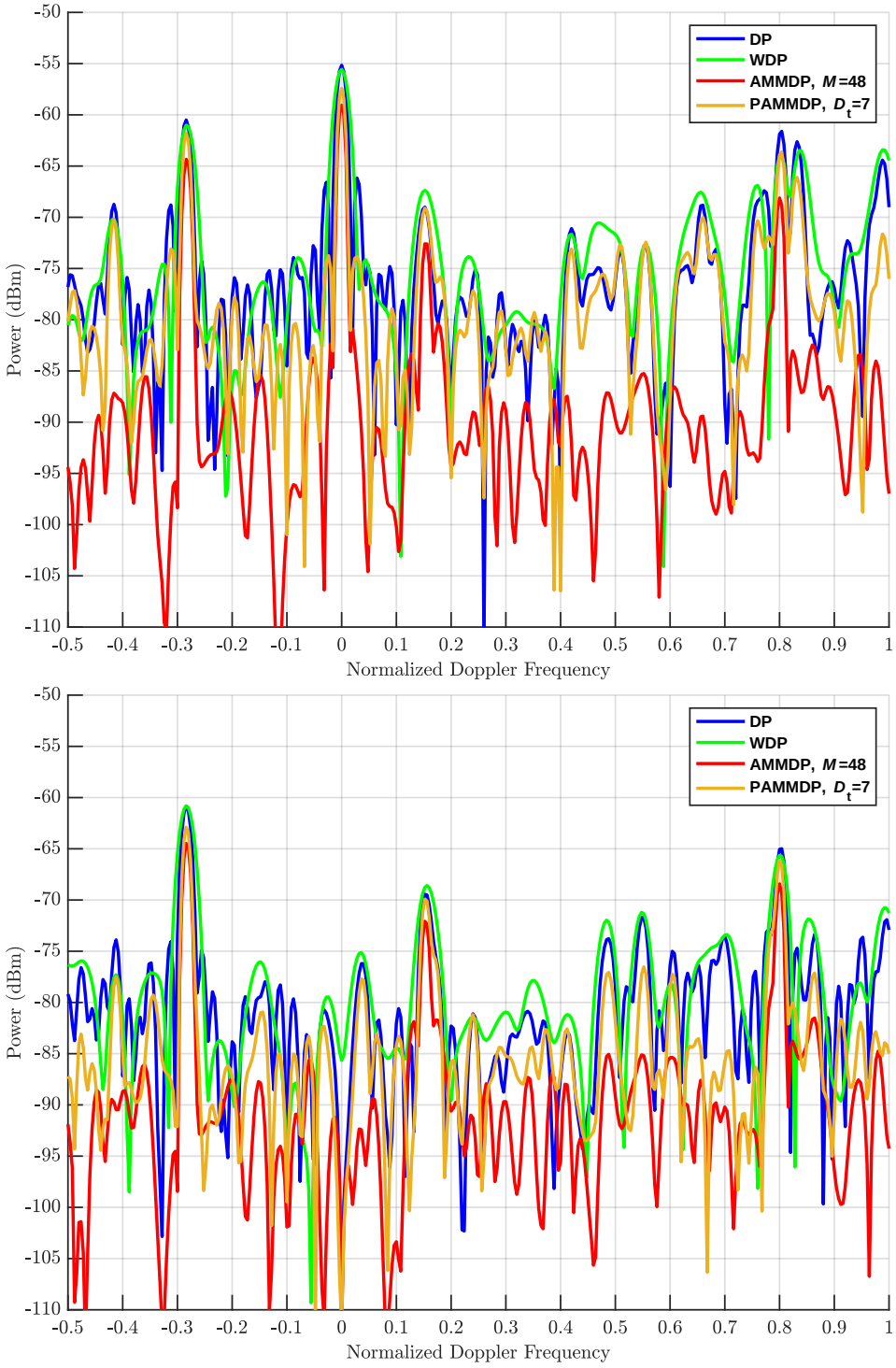

Fig. 2.36: Doppler spectrum at range CUT 1150 m for a staggered PRI (top) with clutter and (bottom) MTI filtering

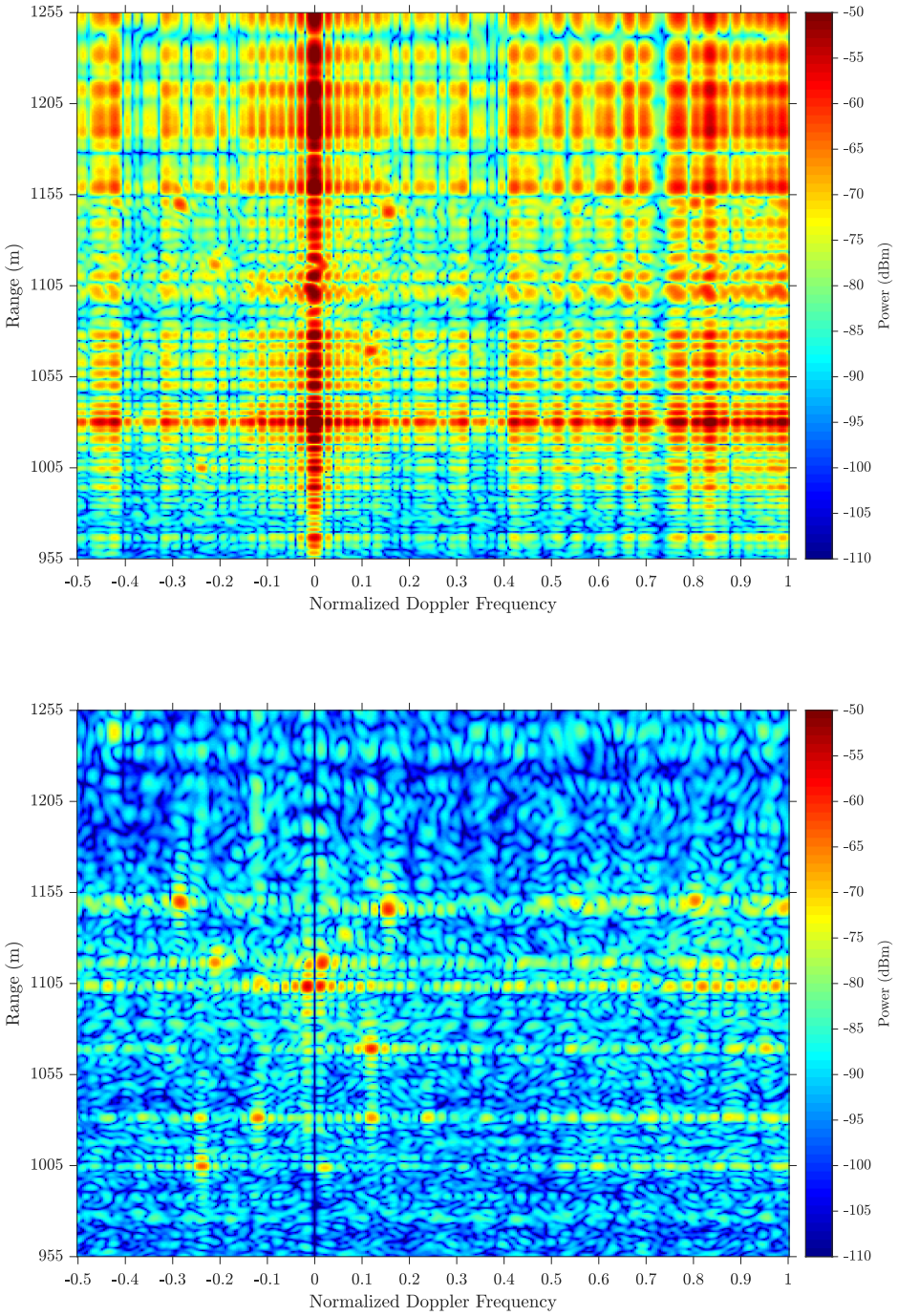

Fig. 2.37: Range-Doppler map of Doppler processing for a staggered PRI (top) with clutter and (bottom) MTI filtering

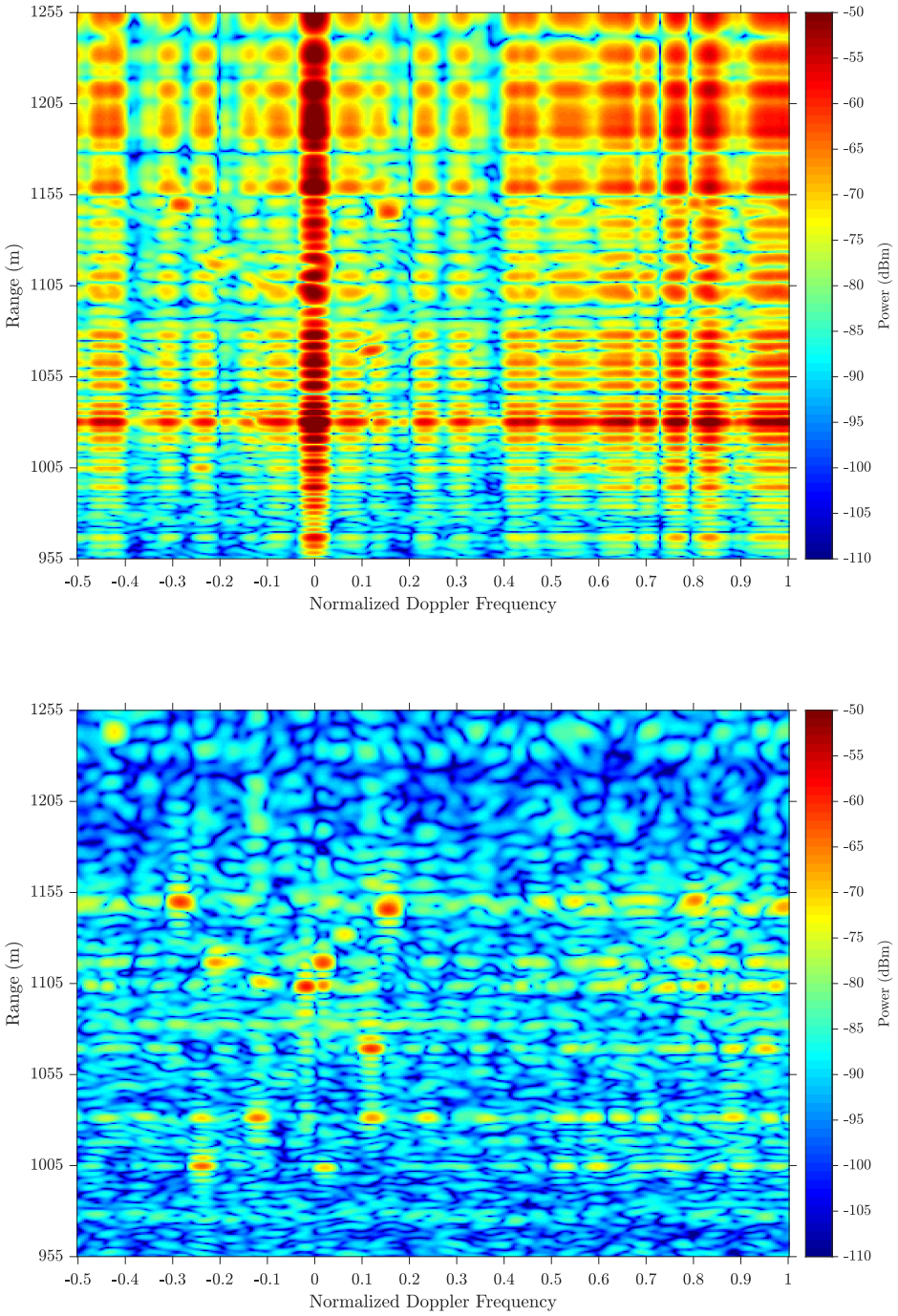

Fig. 2.38: Range-Doppler map of window Doppler processing for a staggered PRI (top) with clutter and (bottom) MTI filtering

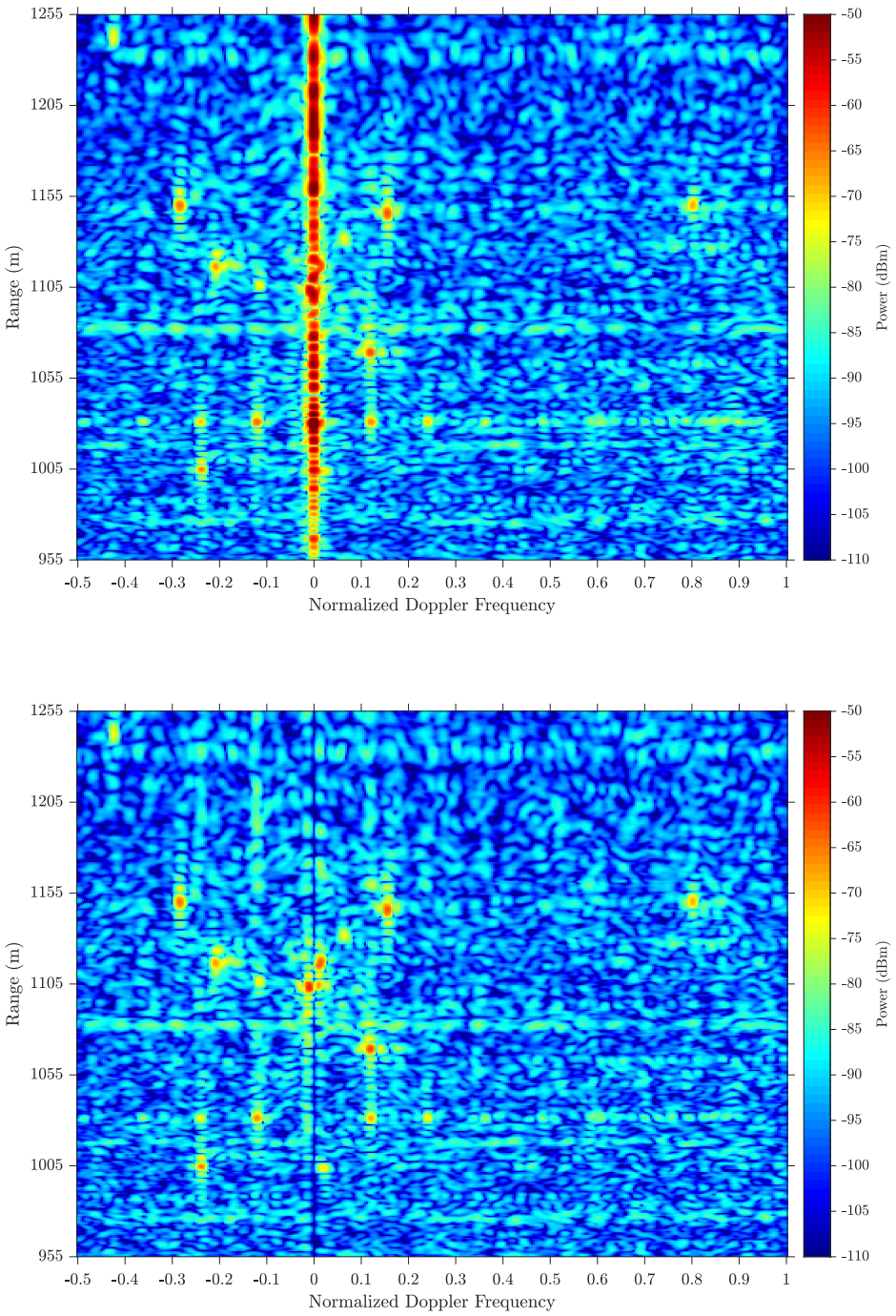

Fig. 2.39: Range-Doppler map of AMMDP for a staggered PRI (top) with clutter and (bottom) MTI filtering

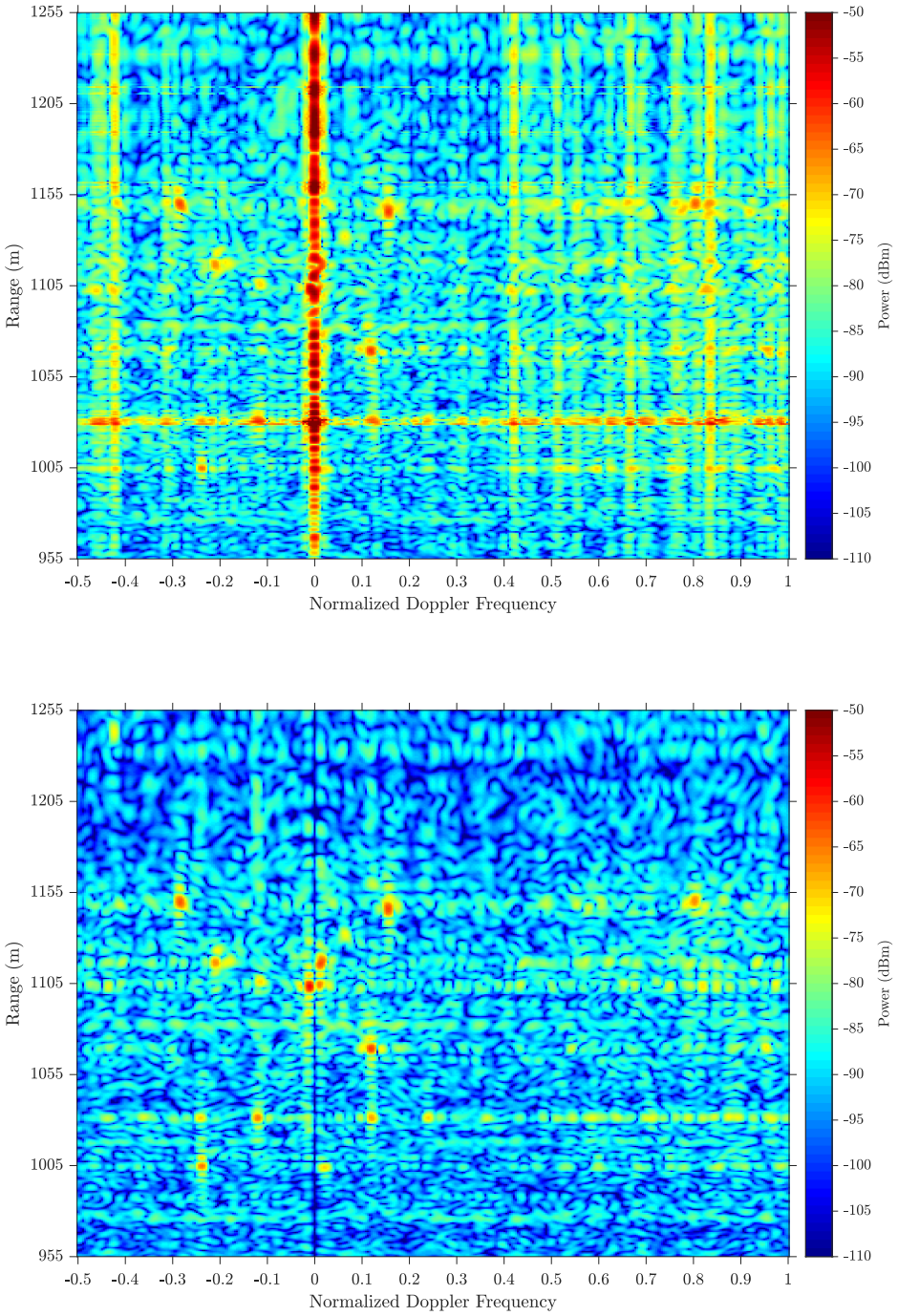

Fig. 2.40: Range-Doppler map of PAMMDP for a staggered PRI (top) with clutter and (bottom) MTI filtering

Chapter 3

Optimal and Adaptive Mismatch Angle-Doppler Processing for Airborne Radar

A side-looking airborne radar (SLAR) performing ground moving target indication (GMTI) uses a pulse-Doppler radar and a receive phase array to estimate the Doppler and angular location of movers from space-time measurements. Due to the platform motion of the radar, a coupling occurs between spatial angle and Doppler frequency. The coupling causes an angle induced Doppler shift of clutter in the Doppler spectrum. The receive response from clutter is high due to the abundance of clutter within a radar scene. Clutter sidelobes in angle and Doppler can mask slow-movers and hinder detection performance. Therefore, clutter cancellation is a staple in moving target indication (MTI) radar for improvement in mover estimation and detection. Instead of a high-pass Doppler filter, which is typical for clutter cancellation in the Doppler spectrum, airborne GMTI uses a band-stop Doppler filter that is Doppler frequency shifted based on the angle-Doppler coupling. Implementing such a filter is difficult since parameters of the aircraft, such as velocity and rotation about its principal axes, must be compensated for in the filter.

Space-time adaptive processing (STAP) is a novel technique to cancel clutter for airborne GMTI. STAP is an adaptive angle-Doppler filter that performs clutter cancellation by using receive data to adaptively account for angle-Doppler coupling. STAP is inherently a cascading of cancellation and estimation angle-Doppler filters and can be viewed as a sequential cancellation-then-estimation procedure. The cancellation stage is a data-dependent band-stop filter formed from assessing the clutter statistics of the radar scene and generating a filter with the stopband located at the clutter angle-Doppler frequency. The estimation stage subsequently

maximizes signal-to-noise (SNR) on the residual response using a bank of data-independent band-pass filters with each filter steered to a different angle-Doppler frequency.

A common method to perform the cancellation stage is sample matrix inversion [4]. The technique is computationally expensive since it requires an estimation and inversion of a sample covariance matrix (SaCM) every range sample. The dimension of the matrix scales with the number of pulses in a coherent processing interval (CPI) and number of elements in a phased array. Advancements have been made to overcome computational challenges of this first stage for practical application [4, 7, 33]. The well-known method of rank reduction of a covariance matrix will be explored in this work [4, 7, 33]. Reduced-rank processing decreases the matrix dimension and reduces the number of training samples needed to satisfy Reed, Mallett, and Brennan (RMB) [38]. The estimation of the covariance matrix containing clutter is expected to be low-rank [4]. STAP research focuses on modifications to the first stage to maximize cancellation performance which in turn improves detection performance.

The estimation stage contains sidelobes due to a 2-D sinc response from using matched angle-Doppler filters that maximum SNR. Variants of the estimation stage include a space-time autoregressive model [95], adaptive displaced phase center antenna (DPCA) [96], multi-stage Wiener filtering [97–101], and data-driven least-squares approaches [7, 102, 103]. Each of these methods propose modifications to both stages simultaneously. In this chapter, optimal and adaptive mismatch processing is proposed to replace the estimation stage in STAP. The mismatch processing approaches seek to maximum signal-to-interference-plus-noise ratio (SINR) by considering sidelobes as interference and mitigating them.

Optimal mismatch processing is a model-based least-squares (LS) approach. LS was introduced to suppress pulse compression range sidelobes for phase codes [104]. The formulation accounted for constant phase changes over chip intervals. The formulation was later modified for frequency modulation waveforms [94, 105]. The subsequent success of the LS formulation led to its implementation in stretch processing where the Fourier transform (FT) stage is replaced by a LS transform [77]. Since Doppler processing is a FT based approach, the LS transform was

explored for slow-time signals and included the incorporation of a covariance matrix to perform clutter cancellation [68]. The LS transform can maintain nominal resolution, incurs little mismatch loss, and provides adequate sidelobe suppression in comparison to traditional processing using a FT and windowing [68]. There is a natural progression to the implementation of LS on airborne GMTI radar since the difference from [68] is the implementation on 2-D space-time signals instead of 1-D slow-time signals.

Adaptive mismatch processing is a re-iterative minimum mean square error (RMMSE) approach introduced for adaptive beamforming and direction-of-arrival estimation for spatial signals as re-iterative super resolution (RISR) [23]. Practical implementation of RMMSE optimally reduces sidelobes with little mismatch loss by constraining the optimization and maintaining nominal resolution. RMMSE for spectral estimation has been explored further in adaptive beamforming [73–76, 93], multidimensional processing with pulse agile waveforms [19, 20], stretch processing [77], Doppler processing (which incorporated a covariance matrix to perform clutter cancellation) [34], fast-time Doppler [78–80], mutual coupling [81], and brain imaging [82]. Since the RMMSE formulation has shown to be applicable with Doppler processing and beamforming, implementing the technique for angle-Doppler processing is also a natural progression.

The downside to the proposed mismatch estimation techniques is the requirement to estimate and invert a structure covariance matrix (StCM) within the mismatch angle-Doppler filter. Incorporating the estimation StCM with the cancellation SaCM requires a matrix inversion at each stage in the cancellation-then-estimation procedure. To enable the use of mismatch processing in the estimation stage, reduce-rank LS and partial adaptive MMSE (introduced in the previous chapter) are proposed for computationally efficiency. Both approaches are optimized in a reduce rank subspace by leveraging reduce rank approaches.

The chapter begins with an overview of the space-time signal model and clutter cancellation for SLAR. After, a derivation of the cancellation-then-estimation filtering considering sidelobe interference is presented. Subsequent sections detail the proposed optimal and adaptive mismatch

processing algorithms and their reduce rank approaches. An analysis follows that explores the angle-Doppler response, cancellation preservation, sidelobe suppression of the various algorithms. Lastly, the efficacy of the algorithms are explored on open-air experimental data using the Air Force Research Laboratory (AFRL) GOTCHA dataset. Conclusions and future work are located in Chapter 5.

3.1 Space-Time Signal Model and Clutter Cancellation

Denote M as the number of pulses in a CPI, N as the number of elements in a uniform linear array (ULA), and L as the number of range samples. Consider a pulse-Doppler radar uniformly transmitting waveform $s(t)$ on M PRIs and receiving illuminated reflections on N antenna elements in a ULA. The receive response from illuminated scatterers for the mth pulse and nth antenna element is

$$y(m,n,t) = \sum_{\omega}\sum_{\theta}\left[s(t) * x(\omega,\theta,t)\right] e^{j2\pi(\varepsilon_{\text{acc},m}\omega + n\theta)} + v(m,n,t) \tag{3.1}$$

over the duration $0 \leq t \leq T_{\text{r}}$ where T_{r} is the PRI, ω is normalized Doppler frequency, θ is spatial frequency, $\varepsilon_{\text{acc},m}$ is the mth accumulation time, $x(\omega,\theta,t)$ is a reflected illuminated scatterer, and $v(m,n,t)$ is thermal noise. For a uniform PRI transmission, the accumulation time is $\varepsilon_{\text{acc},m} = m$. The receive signal after pulse compression and digitization is

$$z[m,n,\ell] = \sum_{\omega\in\Omega}\sum_{\theta\in\Theta} \bar{x}[\omega,\theta,\ell]\, e^{j2\pi(m\omega+n\theta)} + \xi[m,n,\ell] + \bar{v}[m,n,\ell] \tag{3.2}$$

where $\bar{x}(\omega,\theta,\ell)$ contains contributions from adjacent range sidelobes and $\bar{v}(m,n,\ell)$ is filtered noise. Both are a result of the application of a pulse compression filter. Model mismatch from underlining hardware effects and calibration errors is accounted for in $\xi[m,n,\ell]$. The platform motion of the SLAR results in a coupling of spatial and Doppler frequencies

$$\omega = \beta\theta \tag{3.3}$$

where $\beta = 2v_{\mathrm{p}}T_{\mathrm{r}}/d$ is the interelement spacing transvered in a single PRI for a platform velocity of v_{p} and interelement spacing d.

A $M \times 1$ temporal steering vector $\mathbf{c}_{\mathrm{t}}(\omega) = [\ 1 \quad e^{j2\pi\omega} \quad \cdots \quad e^{j2\pi(M-1)\omega}\ ]^T$ and $N \times 1$ spatial steering vector $\mathbf{c}_{\mathrm{s}}(\theta) = [\ 1 \quad e^{j2\pi\theta} \quad \cdots \quad e^{j2\pi(N-1)\theta}\ ]^T$ are coupled to form a $MN \times 1$ space-time steering vector $\mathbf{c}_{\mathrm{st}}(\omega,\theta) = \mathbf{c}_{\mathrm{t}}(\omega) \otimes \mathbf{c}_{\mathrm{s}}(\theta)$. A $M \times L_{\mathrm{D}}$ bank of temporal steering vectors

$$\mathbf{C}_{\mathrm{t}} = [\ \mathbf{c}_{\mathrm{t}}(-\omega_{\max}) \quad \cdots \quad \mathbf{c}_{\mathrm{t}}(-\Delta\omega) \quad \mathbf{c}_{\mathrm{t}}(0) \quad \mathbf{c}_{\mathrm{t}}(\Delta\omega) \quad \cdots \quad \mathbf{c}_{\mathrm{t}}(\omega_{\max})\ ] \tag{3.4}$$

with a granularity of $\Delta\omega = 1/L_{\mathrm{D}}$, maximum normalized Doppler frequency $\omega_{\max} = 1/2$ (because the transmission is uniform), and $L_{\mathrm{D}} = MK_{\mathrm{D}}$ Doppler frequency points oversampled by K_{D}. Typically, a single beam direction is examined at a time for spectrum of Doppler frequencies. The mismatch filtering being presented takes advantage of beams outside the transmit look direction. To span the spatial spectrum, denote $\theta_{\max}$ as the maximum spatial frequency, $L_{\mathrm{A}} = NK_{\mathrm{A}}$ as the number of beams in the spatial spectrum for an oversampling factor K_{A}, and $\Delta\theta = 1/L_{\mathrm{A}}$ as the granularity of spatial spectrum. The $N \times L_{\mathrm{A}}$ bank of spatial steering vectors is

$$\mathbf{C}_{\mathrm{s}} = [\ \mathbf{c}_{\mathrm{s}}(-\theta_{\max}) \quad \cdots \quad \mathbf{c}_{\mathrm{s}}(-\Delta\theta) \quad \mathbf{c}_{\mathrm{s}}(0) \quad \mathbf{c}_{\mathrm{s}}(\Delta\theta) \quad \cdots \quad \mathbf{c}_{\mathrm{s}}(\theta_{\max})\ ]. \tag{3.5}$$

The coupling of the bank of temporal steering vectors and bank of spatial steering vectors form the following $MN \times L_{\mathrm{A}}L_{\mathrm{D}}$ matrix

$$\mathbf{C}_{\mathrm{st}} = \mathbf{C}_{\mathrm{t}} \otimes \mathbf{C}_{\mathrm{s}}. \tag{3.6}$$

A radar datacube is formed via the collection of M pulses, N elements, and L ranges samples using (3.2). The ℓth range sample of the datacube is a $M \times N$ space-time data matrix $\mathbf{Z}_{\mathrm{st}}(\ell)$. Vectorizing the data matrix forms a $MN \times 1$ space-time receive signal model

$$\begin{aligned} \mathbf{z}_{\mathrm{st}}(\ell) &= \sum_{\omega}\sum_{\theta} \bar{x}[\omega,\theta,\ell]\,\mathbf{c}_{\mathrm{st}}(\omega,\theta) + \mathbf{e}_{\mathrm{st}}(\ell) + \mathbf{v}_{\mathrm{st}}(\ell) \\ &= \mathbf{C}_{\mathrm{st}}\mathbf{x}_{\mathrm{AD}}(\ell) + \mathbf{e}_{\mathrm{st}}(\ell) + \mathbf{v}_{\mathrm{st}}(\ell) \end{aligned} \tag{3.7}$$

where $\mathbf{v}_{\text{st}}(\ell)$ and $\mathbf{e}_{\text{st}}(\ell)$ are $MN \times 1$ noise and mismatch error vectors, respectively. The term $\mathbf{x}_{\text{AD}}(\ell)$ is a $L_{\text{A}}L_{\text{D}} \times 1$ vector corresponding to the frequency points in the angle-Doppler spectrum.

A cancellation transform is used to implement clutter cancellation in space-time signals. Consider the decomposition of the space-time signal model into clutter and remaining components

$$\mathbf{z}_{\text{st}}(\ell) = \mathbf{C}_{\text{st,clu}}\mathbf{x}_{\text{AD,clu}}(\ell) + \mathbf{C}_{\text{st,rem}}\mathbf{x}_{\text{AD,rem}}(\ell) + \mathbf{e}_{\text{st,clu}}(\ell) + \mathbf{e}_{\text{st,rem}}(\ell) + \mathbf{v}_{\text{st}}(\ell). \tag{3.8}$$

The $MN \times MM$ space-time cancellation matrix is

$$\mathbf{R}_{\text{st,canc}}(\ell) = \frac{1}{\sigma_{\text{v}}^2}\left(\mathbf{R}_{\text{st,clu}}(\ell) + \mathbf{R}_{\text{st,v}}\right) \tag{3.9}$$

where $\mathbf{R}_{\text{st,clu}}(\ell)$ is the space-time clutter covariance matrix and $\mathbf{R}_{\text{st,v}} = \sigma_{\text{v}}^2\mathbf{I}_{MN\times MN}$ is the space-time noise covariance matrix [34]. The noise assumes the space-time elements are uncorrelated pulse-to-pulse and element-to-element. Additionally, each space-time element is a Gaussian distributed random variable with zero mean and noise power σ_{v}^2. Residual errors will be present due to the statistical mismatch between the estimation and optimal cancellation matrix. The cancellation matrix is applied to the data to remove the clutter components

$$\widehat{\mathbf{z}}_{\text{st}}(\ell) = \mathbf{R}_{\text{st,canc}}^{-1}(\ell)\,\mathbf{z}_{\text{st}}(\ell) = \mathbf{C}_{\text{st,rem}}\mathbf{x}_{\text{AD,rem}}(\ell) + \mathbf{e}_{\text{st,rem}}(\ell) + \mathbf{v}_{\text{st}}(\ell). \tag{3.10}$$

The clutter covariance matrix is estimated as a SaCM

$$\hat{\mathbf{R}}_{\text{st,clu}}(\ell) = \frac{1}{\mathfrak{c}\left\{L_{\text{p}}\right\}} \sum_{\substack{\kappa\neq\ell \\ \kappa\in L_{\text{p}}}} \mathbf{z}_{\text{st}}(\kappa)\,\mathbf{z}_{\text{st}}^{H}(\kappa) \tag{3.11}$$

where L_{p} is the set of range samples remaining after the range CUT and guard cells are removed to avoid self-cancellation [4]. The summation effectively estimates the clutter on receive. According to the RMB rule [36], to be within 3 dB of the optimal clutter covariance matrix the

number of range samples needs to be approximately double the number of space-time samples. The RMB rules assumes the samples are homogeneous. Homogeneous samples implies they are independent and identically distributed (IID). Heterogeneous clutter, clutter discretes in the cell-under-test (CUT), and/or movers in the training samples diminish the ability to achieve the amount of homogeneous training samples needed satisfy the RMB rule. The lack of homogeneous training samples leads to an inaccurate estimation of the SaCM [35, 106]. Techniques to address heterogeneity in clutter has been widely explored [35, 106–130].

The $MN \times 1$ angle-Doppler filter that maximizes SNR is

$$\mathbf{u}_{\mathrm{AD}}(\omega,\theta) = \frac{\mathbf{c}_{\mathrm{st}}(\omega,\theta)}{\mathbf{c}_{\mathrm{st}}^{H}(\omega,\theta)\,\mathbf{c}_{\mathrm{st}}(\omega,\theta)}. \tag{3.12}$$

noting that $\mathbf{c}_{\mathrm{st}}^{H}(\omega,\theta)\,\mathbf{c}_{\mathrm{st}}(\omega,\theta) = MN$. The $MN \times 1$ maximum SINR filter, which is equivalently the STAP filter, uses the cancellation matrix and angle-Doppler filter

$$\mathbf{w}_{\mathrm{AD}}(\omega,\theta,\ell) = \mathbf{R}_{\mathrm{st,canc}}^{-1}(\ell)\,\mathbf{u}_{\mathrm{AD}}(\omega,\theta). \tag{3.13}$$

Applying the filter to the receive data yields

$$\hat{x}_{\mathrm{AD}}[\omega,\theta,\ell] = \mathbf{u}_{\mathrm{AD}}^{H}(\omega,\theta)\,\widehat{\mathbf{z}}_{\mathrm{st}}(\ell) = \mathbf{u}_{\mathrm{AD}}^{H}(\omega,\ell)\,\mathbf{R}_{\mathrm{st,canc}}^{-1}(\ell)\,\mathbf{z}_{\mathrm{st}}(\ell) = \mathbf{w}_{\mathrm{AD}}^{H}(\omega,\theta,\ell)\,\mathbf{z}_{\mathrm{st}}(\ell). \tag{3.14}$$

Windowing is incorporated by replacing $\mathbf{u}_{\mathrm{AD}}(\omega,\theta)$ with

$$\mathbf{u}_{\mathrm{WAD}}(\omega,\theta) = \frac{\mathbf{c}_{\mathrm{st}}(\omega,\theta)\odot\mathbf{b}_{\mathrm{st}}}{(\mathbf{c}_{\mathrm{st}}(\omega,\theta)\odot\mathbf{b}_{\mathrm{st}})^{H}\mathbf{c}_{\mathrm{st}}(\omega,\theta)} \tag{3.15}$$

where $\mathbf{b}_{\mathrm{st}} = \mathbf{b}_{\mathrm{t}} \otimes \mathbf{b}_{\mathrm{s}}$ is a coupling between a $M \times 1$ slow-time taper $\mathbf{b}_{\mathrm{t}}$ and a $N \times 1$ spatial taper $\mathbf{b}_{\mathrm{s}}$. The tapered filtering with cancellation is equivalently expressed as

$$\mathbf{w}_{\mathrm{WAD}}(\omega,\theta,\ell) = \mathbf{R}_{\mathrm{st,canc}}^{-1}(\ell)\,\mathbf{u}_{\mathrm{WAD}}(\omega,\theta). \tag{3.16}$$

The windowed estimate is obtained similar to (3.14). The application of the tapered angle-Doppler filter is

$$\hat{x}_{\mathrm{WAD}}(\omega,\theta,\ell) = \mathbf{u}_{\mathrm{WAD}}^{H}(\omega,\theta)\,\widehat{\mathbf{z}}_{\mathrm{st}}(\ell) = \mathbf{w}_{\mathrm{WAD}}^{H}(\omega,\theta,\ell)\,\mathbf{z}_{\mathrm{st}}(\ell). \tag{3.17}$$

Reduced-rank techniques are employed with STAP to reduce the computational complexity of the matrix inversion [4]. A element-space post-Doppler transformation is considered (see Figure 1.17 in Chapter 1 for more information) [4]. The approach reduces the rank for slow-time in the Doppler spectrum and maintains the full rank in element-space. The approach is considered since the biggest factor to the size of the covariance within this work is the number of pulses. A low number of array elements is being used such that element-space reduction is not needed. Though, the algorithms are generalized to consider any temporal or spatial transformation matrix.

Denote D_{t} as the desired rank in slow-time corresponding to the number of pulses in a sub-CPI. Next, denote D_{s} as the desired rank in element-space corresponding to the number of elements in a sub-array. A $MN \times D_{\mathrm{t}}D_{\mathrm{s}}$ space-time transformation matrix

$$\mathbf{T}_{\mathrm{st}}(\omega,\theta) = \mathbf{T}_{\mathrm{t}}(\omega) \otimes \mathbf{T}_{\mathrm{s}}(\theta) \tag{3.18}$$

is constructed from a $M \times D_{\mathrm{t}}$ temporal transformation matrix $\mathbf{T}_{\mathrm{t}}(\omega)$ and a $N \times D_{\mathrm{s}}$ spatial transformation matrix $\mathbf{T}_{\mathrm{s}}(\theta)$ [4]. The temporal transformation matrix uses an adjacent-bin formulation which considers adjacent steering vectors to the steering vector under test [4, 45]. The matrix is a subset of the bank of slow-time steering vectors. Upon application, the form leverages coherence in slow-time. The temporal transformation matrix is

$$\mathbf{T}_{\mathrm{t}}(\omega) = \frac{1}{\sqrt{L_{\mathrm{D}}}}\left[\begin{array}{ccccc} \mathbf{c}_{\mathrm{t}}(\omega - A_{\mathrm{t}}\Delta\omega) & \cdots & \mathbf{c}_{\mathrm{t}}(\omega) & \cdots & \mathbf{c}_{\mathrm{t}}(\omega + A_{\mathrm{t}}\Delta\omega) \end{array}\right] \tag{3.19}$$

where $A_{\mathrm{t}} = (D_{\mathrm{t}} - 1)/2$ is the surrounding temporal steering vectors on each side of the Doppler frequency of interest [4]. Since reduction in element-space or beamspace is not being performed,

$D_{\mathrm{s}} = N$ and the spatial transformation matrix is an $N \times N$ identity matrix $\mathbf{T}_{\mathrm{s}}(\theta) = \mathbf{I}_{N \times N}$.

The space-time transformation matrix applied to the estimated cancellation matrix produces

$$\tilde{\mathbf{R}}_{\text{st,canc}}(\omega, \theta, \ell) = \mathbf{T}_{\text{st}}^{H}(\omega, \theta)\, \mathbf{R}_{\text{st,canc}}(\ell)\, \mathbf{T}_{\text{st}}(\omega, \theta) \tag{3.20}$$

thus reducing the matrix to $D_{\mathrm{t}} D_{\mathrm{s}} \times D_{\mathrm{t}} D_{\mathrm{s}}$. The downside is that the matrix multiplication needs to be performed for each angle-Doppler bin which has its own computational implications. The matrix is inverted in the lower dimension and mapped back to the full dimension in the following manner

$$\begin{aligned} \mathbf{R}_{\text{rd-st,canc}}(\omega, \theta, \ell) &= \mathbf{T}_{\text{st}}(\omega, \theta)\, \tilde{\mathbf{R}}_{\text{st,canc}}^{-1}(\omega, \theta, \ell)\, \mathbf{T}_{\text{st}}^{H}(\omega, \theta) \\ &= \mathbf{T}_{\text{st}}(\omega, \theta)\, (\mathbf{T}_{\text{st}}^{H}(\omega, \theta)\, \mathbf{R}_{\text{st,canc}}(\ell)\, \mathbf{T}_{\text{st}}(\omega, \theta))^{-1} \mathbf{T}_{\text{st}}^{H}(\omega, \theta) \end{aligned} \tag{3.21}$$

which is $MN \times MN$. The cancellation matrix is then applied to the receive data in a similar to (3.11)

$$\begin{aligned} \widehat{\mathbf{z}}_{\text{rd-st}}(\omega, \theta, \ell) &= \mathbf{R}_{\text{rd-st,canc}}(\omega, \theta, \ell)\, \mathbf{z}_{\text{st}}(\ell). \\ &= \mathbf{T}_{\text{st}}(\omega, \theta)\, (\mathbf{T}_{\text{st}}^{H}(\omega, \theta)\, \mathbf{R}_{\text{st,canc}}(\ell)\, \mathbf{T}_{\text{st}}(\omega, \theta))^{-1} \mathbf{T}_{\text{st}}^{H}(\omega, \theta)\, \mathbf{z}_{\text{st}}(\ell). \end{aligned} \tag{3.22}$$

The application of the matrix transforms the data vector and cancellation matrix into the lower dimension. After the matrix multiple between the reduced vector and matrix, the result is mapped back to the full dimension. An estimate of the angle-Doppler frequency is obtained by applying the angle-Doppler filter shown in (3.12) to the receive data in (3.22)

$$\hat{x}_{\text{RD-AD}}[\omega, \theta, \ell] = \mathbf{u}_{\text{AD}}^{H}(\omega, \theta)\, \widehat{\mathbf{z}}_{\text{rd-st}}(\omega, \theta, \ell) = \mathbf{w}_{\text{RD-AD}}^{H}(\omega, \theta, \ell)\, \mathbf{z}_{\text{st}}(\ell) \tag{3.23}$$

where the reduced dimension STAP filter mapped to the full dimension is equivalently expressed

as

$$\mathbf{w}_{\text{RD-AD}}(\omega,\theta,\ell) = \mathbf{R}_{\text{rd-st,canc}}(\omega,\theta,\ell)\,\mathbf{u}_{\text{AD}}(\omega,\theta). \tag{3.24}$$

The transformation matrices effectively reduces the cancellation matrix, inverts it in the lower dimension, then maps it back to the full dimension. Comparing (3.24) to the filter in (3.13), the estimation stage remains unchanged. A replacement of the matched estimation stage with a mismatch filter, as shown in Chapter 2 for slow-time signals and cancellation, is a viable option for implementation with reduced-rank techniques for STAP. An great example of incorporating a mismatch filter is windowing. The windowed adaptive filter with cancellation is formed using (3.15)

$$\mathbf{w}_{\text{RD-WAD}}(\omega,\theta,\ell) = \mathbf{R}_{\text{rd-st,canc}}(\omega,\theta,\ell)\,\mathbf{u}_{\text{WAD}}(\omega,\theta). \tag{3.25}$$

The application of the filter produces the windowed estimate

$$\hat{x}_{\text{RD-WAD}}[\omega,\theta,\ell] = \mathbf{w}^{H}_{\text{RD-WAD}}(\omega,\theta,\ell)\,\mathbf{z}_{\text{st}}(\ell). \tag{3.26}$$

3.2 Cancellation-Then-Estimation Filtering

STAP maximizes SINR for open-air interference sources. Errors from signal processing such as sidelobes from a matched filter and model mismatch are not consider within the filter derivation. A sequential cancellation-then-estimation filter is derived that maximizes SINR after application of clutter cancellation. Readers are encouraged to review the maximum SNR and SINR filter derivations in Appendix B.

Consider the expanded receive space-time data vector from (3.8). Next, consider an application of arbitrary $MN \times 1$ space-time weight vector $\mathbf{u}(\omega,\theta,\ell)$ applied to the space-time data vector to

obtain an estimate of the angle-Doppler frequency similar to (3.14)

$$\begin{aligned}\hat{x}[\omega,\theta,\ell] &= \mathbf{u}^H(\omega,\theta,\ell)\,\mathbf{z}_{\text{st}}(\ell) \\ &= x_{\text{T}}[\omega,\theta,\ell] + x_{\text{side}}[\omega,\theta,\ell] + x_{\text{clu}}[\omega,\theta,\ell] + \xi[\omega,\theta,\ell] + v[\omega,\theta,\ell]\end{aligned} \tag{3.27}$$

where the desired response is $x_{\text{T}}[\omega,\theta,\ell]$, the remaining components is $x_{\text{side}}[\omega,\theta,\ell]$ which consist of the sidelobe response from movers, the clutter response is $x_{\text{clu}}[\omega,\theta,\ell]$, the error response is $\xi[\omega,\theta,\ell]$, and noise response $v[\omega,\theta,\ell]$. The terms that contribute to the estimate are expanded further.

The desired response component consists of the amplitude and space-time steering vector corresponding to the angle-Doppler bin under test

$$x_{\text{T}}[\omega,\theta,\ell] = x[\omega,\theta,\ell]\,\mathbf{u}^H(\omega,\theta,\ell)\,\mathbf{c}_{\text{st}}(\omega,\theta). \tag{3.28}$$

The ideal weight vector would result in $\mathbf{u}^H(\omega,\theta,\ell)\,\mathbf{c}_{\text{st}}(\omega,\theta) = 1$ to ensure $x_{\text{T}}[\omega,\theta,\ell] = x[\omega,\theta,\ell]$. The resulting desired signal power is

$$P_{\text{r}}(\omega,\theta,\ell) = E\{\left|x[\omega,\theta,\ell]\,\mathbf{u}^H(\omega,\theta,\ell)\,\mathbf{c}_{\text{st}}(\omega,\theta)\right|^2\} = \rho[\omega,\theta,\ell]\left|\mathbf{u}^H(\omega,\theta,\ell)\,\mathbf{c}_{\text{st}}(\omega,\theta)\right|^2 \tag{3.29}$$

where $\rho[\omega,\theta,\ell] = E\{|x[\omega,\theta,\ell]|\}^2$ is the power from the complex scattering in the CUT. Sidelobes from scattering outside the angle-Doppler bin under test will have the response

$$x_{\text{side}}[\omega,\theta,\ell] = \sum_{\substack{\omega_{\text{mov}}\in\Omega_{\text{mov}} \\ \omega_{\text{mov}}\neq\omega}} \sum_{\substack{\theta_{\text{mov}}\in\Theta_{\text{mov}} \\ \theta_{\text{mov}}\neq\theta}} x[\omega_{\text{mov}},\theta_{\text{mov}},\ell]\,\mathbf{u}^H(\omega,\theta,\ell)\,\mathbf{c}_{\text{st}}(\omega_{\text{mov}},\theta_{\text{mov}}) \tag{3.30}$$

where subscript "mov" denotes movers. Recall that the space-time signal produces a multivariate sinc response in the angle-Doppler spectrum due to the time-limitation on the slow-time and element-space signals. From a filter perspective, the sidelobes are a result of phase mismatch between weight vector and steering vector when $\omega \neq \omega_{\text{mov}}$ and $\theta \neq \theta_{\text{mov}}$. The subsequent power

of the sidelobe interfering with the signal is

$$\begin{aligned} P_{\text{side}}(\omega,\theta,\ell) &= \sum_{\substack{\omega_{\text{mov}}\in\Omega_{\text{mov}}\\ \omega_{\text{mov}}\neq\omega}} \sum_{\substack{\theta_{\text{mov}}\in\Theta_{\text{mov}}\\ \theta_{\text{mov}}\neq\theta}} E\{\left|x[\omega_{\text{mov}},\theta_{\text{mov}},\ell]\,\mathbf{u}^H(\omega,\theta,\ell)\,\mathbf{c}_{\text{st}}(\omega_{\text{mov}},\theta_{\text{mov}})\right|^2\} \\ &= \mathbf{u}^H(\omega,\theta,\ell)\,\mathbf{R}_{\text{st,side}}(\ell)\,\mathbf{u}(\omega,\theta,\ell) \end{aligned} \tag{3.31}$$

where the covariance matrix of the contributions from mover sidelobes is

$$\mathbf{R}_{\text{st,side}}(\ell) = \sum_{\substack{\omega_{\text{mov}}\in\Omega_{\text{mov}}\\ \omega_{\text{mov}}\neq\omega}} \sum_{\substack{\theta_{\text{mov}}\in\Theta_{\text{mov}}\\ \theta_{\text{mov}}\neq\theta}} \rho[\omega_{\text{mov}},\theta_{\text{mov}},\ell]\,\mathbf{c}_{\text{st}}(\omega_{\text{mov}},\theta_{\text{mov}})\,\mathbf{c}_{\text{st}}^H(\omega_{\text{mov}},\theta_{\text{mov}}). \tag{3.32}$$

Contributions from clutter has a similar form of the mover sidelobes

$$x_{\text{clu}}[\omega,\theta,\ell] = \sum_{\substack{\omega_{\text{clu}}\in\Omega_{\text{clu}}\\ \omega_{\text{clu}}\neq\omega}} \sum_{\substack{\theta_{\text{clu}}\in\Theta_{\text{clu}}\\ \theta_{\text{clu}}\neq\theta}} x[\omega_{\text{clu}},\theta_{\text{clu}},\ell]\,\mathbf{u}^H(\omega,\theta,\ell)\,\mathbf{c}_{\text{st}}(\omega_{\text{clu}},\theta_{\text{clu}}). \tag{3.33}$$

The associated power of the recieved clutter response is

$$\begin{aligned} P_{\text{clu}}(\omega,\theta,\ell) &= \sum_{\substack{\omega_{\text{clu}}\in\Omega_{\text{clu}}\\ \omega_{\text{clu}}\neq\omega}} \sum_{\substack{\theta_{\text{clu}}\in\Theta_{\text{clu}}\\ \theta_{\text{clu}}\neq\theta}} E\{|x[\omega_{\text{clu}},\theta_{\text{clu}},\ell]\,\mathbf{u}^H(\omega,\theta,\ell)\,\mathbf{c}_{\text{st}}(\omega_{\text{clu}},\theta_{\text{clu}})|^2\} \\ &= \mathbf{u}^H(\omega,\theta,\ell)\,\mathbf{R}_{\text{st,clu}}(\ell)\,\mathbf{u}(\omega,\theta,\ell) \end{aligned} \tag{3.34}$$

where the clutter covariance matrix is

$$\mathbf{R}_{\text{st,clu}}(\ell) = \sum_{\substack{\omega_{\text{clu}}\in\Omega_{\text{clu}}\\ \omega_{\text{clu}}\neq\omega}} \sum_{\substack{\theta_{\text{clu}}\in\Theta_{\text{clu}}\\ \theta_{\text{clu}}\neq\theta}} \rho[\omega_{\text{clu}},\theta_{\text{clu}},\ell]\,\mathbf{c}_{\text{st}}(\omega_{\text{clu}},\theta_{\text{clu}})\,\mathbf{c}_{\text{st}}^H(\omega_{\text{clu}},\theta_{\text{clu}}). \tag{3.35}$$

The model error term is characterized as

$$\xi[\omega,\theta,\ell] = \mathbf{u}^H(\omega,\theta,\ell)\,\mathbf{e}_{\text{st}}(\ell) \tag{3.36}$$

where the associated power is

$$P_{\mathrm{e}}(\omega,\theta,\ell) = E\{|\mathbf{u}^H(\omega,\theta,\ell)\,\mathbf{e}_{\mathrm{st}}(\ell)|^2\} = \mathbf{u}^H(\omega,\theta,\ell)\,\mathbf{R}_{\mathrm{st,err}}(\ell)\mathbf{u}(\omega,\theta,\ell) \tag{3.37}$$

and the subsequent error covariance matrix is

$$\mathbf{R}_{\mathrm{st,err}}(\ell) = \sigma^2_{\mathrm{st,err}}\mathbf{I}_{MN\times MN} \odot \sum_{\omega\in\Omega}\sum_{\theta\in\Theta} \sigma^2[\omega,\theta,\ell]\,\mathbf{c}_{\mathrm{st}}(\omega,\theta)\,\mathbf{c}^H_{\mathrm{st}}(\omega,\theta). \tag{3.38}$$

Lastly, the noise term is

$$v[\omega,\theta,\ell] = \mathbf{u}^H(\omega,\theta,\ell)\,\mathbf{v}_{\mathrm{st}}(\ell) \tag{3.39}$$

with a noise power of

$$P_{\mathrm{v}}(\omega,\theta,\ell) = E\{\left|\mathbf{u}^H(\omega,\theta,\ell)\,\mathbf{v}_{\mathrm{st}}(\ell)\right|^2\} = \mathbf{u}^H(\omega,\theta,\ell)\,\mathbf{R}_{\mathrm{st,v}}\mathbf{u}(\omega,\theta,\ell). \tag{3.40}$$

Using power terms from each response, the resulting SINR is

$$\mathrm{SINR}(\omega,\theta,\ell) = \frac{P_{\mathrm{r}}(\omega,\theta,\ell)}{P_{\mathrm{side}}(\omega,\theta,\ell) + P_{\mathrm{clu}}(\omega,\theta,\ell) + P_{\mathrm{e}}(\omega,\theta,\ell) + P_{\mathrm{v}}(\omega,\theta,\ell)}. \tag{3.41}$$

Applying a cancellation covariance matrix to the receive removes clutter signals and their corresponding sidelobe responses. Cancellation of clutter results in an increase in SINR

$$\begin{aligned}\mathrm{SINR}(\omega,\theta,\ell) &= \frac{P_{\mathrm{r}}(\omega,\theta,\ell)}{P_{\mathrm{side}}(\omega,\theta,\ell) + P_{\mathrm{clu}}(\omega,\theta,\ell) + P_{\mathrm{e}}(\omega,\theta,\ell) + P_{\mathrm{v}}(\omega,\theta,\ell)} \\ &\leq \frac{P_{\mathrm{r}}(\omega,\theta,\ell)}{P_{\mathrm{side}}(\omega,\theta,\ell) + P_{\mathrm{e}}(\omega,\theta,\ell) + P_{\mathrm{v}}(\omega,\theta,\ell)}.\end{aligned} \tag{3.42}$$

Optimal clutter cancellation would result in $P_{\mathrm{clu}}(\omega,\theta,\ell) = 0$ making (3.42) equality. Under this assumption, the weight vector is applied to the cancellation transformed receive data $\widehat{\mathbf{z}}_{\mathrm{st}}(\ell)$ from

(3.11) which contains the remaining interference components

$$\hat{x}[\omega,\theta,\ell] = \mathbf{u}^H(\omega,\theta,\ell)\,\widehat{\mathbf{z}}_{\text{st}}(\ell) = x[\omega,\theta,\ell] + x_{\text{side}}[\omega,\theta,\ell] + \xi[\omega,\theta,\ell] + v[\omega,\theta,\ell] \tag{3.43}$$

Substituting the signal power, adjacent mover sidelobe powers, and noise power in (3.42) (now having equality) results in

$$\text{SINR}(\omega,\theta,\ell) = \frac{P_{\text{r}}(\omega,\theta)}{P_{\text{side}}(\omega,\theta) + P_{\text{e}}(\omega,\theta,\ell) + P_{\text{v}}(\omega,\theta)} = \frac{\rho(\omega,\theta,\ell)\left|\mathbf{u}^H(\omega,\theta,\ell)\,\mathbf{c}_{\text{st}}(\omega,\theta)\right|^2}{\mathbf{u}^H(\omega,\theta,\ell)\,\mathbf{R}_{\text{st,sup}}(\ell)\,\mathbf{u}(\omega,\theta,\ell)} \tag{3.44}$$

where the supplementary covariance matrix is

$$\mathbf{R}_{\text{st,sup}}(\ell) = \mathbf{R}_{\text{st,ms}}(\ell) + \mathbf{R}_{\text{st,err}}(\ell) + \mathbf{R}_{\text{st,v}}. \tag{3.45}$$

The maximum SINR is obtained using a procedure similar to obtaining maximum SINR to formulate STAP (presented in [22])

$$\begin{aligned}
\text{SINR}(\omega,\theta,\ell) &= \frac{\rho(\omega,\theta,\ell)\left|\mathbf{u}^H(\omega,\theta,\ell)\,\mathbf{c}_{\text{st}}(\omega,\theta)\right|^2}{\mathbf{u}^H(\omega,\theta,\ell)\,\mathbf{R}_{\text{st,sup}}(\ell)\,\mathbf{u}(\omega,\theta,\ell)} \\
&= \frac{\rho(\omega,\theta,\ell)\left|\mathbf{u}^H(\omega,\theta,\ell)\,\mathbf{R}_{\text{st,sup}}^{1/2}(\ell)\,\mathbf{R}_{\text{st,sup}}^{-1/2}(\ell)\,\mathbf{c}_{\text{st}}(\omega,\theta)\right|^2}{\mathbf{u}^H(\omega,\theta,\ell)\,\mathbf{R}_{\text{st,sup}}(\ell)\,\mathbf{u}(\omega,\theta,\ell)} \\
&\leq \frac{\rho(\omega,\theta,\ell)\left\|\mathbf{R}_{\text{st,sup}}^{1/2}(\ell)\,\mathbf{u}(\omega,\theta,\ell)\right\|^2\left\|\mathbf{R}_{\text{st,sup}}^{-1/2}(\ell)\,\mathbf{c}_{\text{st}}(\omega,\theta)\right\|^2}{\mathbf{u}^H(\omega,\theta,\ell)\,\mathbf{R}_{\text{st,sup}}(\ell)\,\mathbf{u}(\omega,\theta,\ell)} \\
&= \frac{\rho(\omega,\theta,\ell)\,\mathbf{u}^H(\omega,\theta,\ell)\,\mathbf{R}_{\text{st,sup}}(\ell)\,\mathbf{u}(\omega,\theta,\ell)\,\mathbf{c}_{\text{st}}^H(\omega,\theta)\,\mathbf{R}_{\text{st,sup}}^{-1}(\ell)\,\mathbf{c}_{\text{st}}(\omega,\theta)}{\mathbf{u}^H(\omega,\theta,\ell)\,\mathbf{R}_{\text{st,sup}}(\ell)\,\mathbf{u}(\omega,\theta,\ell)} \\
&= \rho(\omega,\theta,\ell)\,\mathbf{c}_{\text{st}}^H(\omega,\theta)\,\mathbf{R}_{\text{st,sup}}^{-1}(\ell)\,\mathbf{c}_{\text{st}}(\omega,\theta) \\
&= \mathbf{u}_{\text{st,sup}}^H(\omega,\theta)\,\mathbf{c}_{\text{st}}(\omega,\theta).
\end{aligned} \tag{3.46}$$

The resulting optimal filter to maximize the signal after cancellation is

$$\mathbf{u}_{\text{st,opt}}(\omega,\theta,\ell) = \psi \mathbf{R}^{-1}_{\text{st,sup}}(\ell)\,\mathbf{c}_{\text{st}}(\omega,\theta). \tag{3.47}$$

where ψ is a scalar to normalize the response. Applying the optimal filter to the cancellation transformed data yields

$$\begin{aligned}\hat{x}(\omega,\theta,\ell) &= \mathbf{u}^{H}_{\text{st,opt}}(\omega,\theta)\,\widehat{\mathbf{z}}_{\text{st}}(\ell) \\ &= \psi \mathbf{c}^{H}_{\text{st}}(\omega,\theta)\,\mathbf{R}^{-1}_{\text{st,sup}}\mathbf{R}^{-1}_{\text{st,canc}}\mathbf{z}_{\text{st}}(\ell) \\ &= \mathbf{w}^{H}_{\text{st,opt}}(\omega,\theta)\,\mathbf{z}_{\text{st}}(\ell).\end{aligned} \tag{3.48}$$

where the optimal filter combining clutter cancellation and sidelobe suppression is

$$\begin{aligned}\mathbf{w}_{\text{st,opt}}(\omega,\theta,\ell) &= \mathbf{R}^{-1}_{\text{st,canc}}(\ell)\,\mathbf{u}_{\text{st,sup}}(\omega,\theta) \\ &= \psi \mathbf{R}^{-1}_{\text{st,canc}}(\ell)\,\mathbf{R}^{-1}_{\text{st,sup}}(\ell)\,\mathbf{c}_{\text{st}}(\omega,\theta).\end{aligned} \tag{3.49}$$

The space-time clutter covariance matrix is estimated from surrounding range bins. The sidelobes from movers are not captured in this estimation. Actually, steps are taken to avoid the estimation of mover sidelobes via the removal of guard cells and the range cell-under-test to self-cancellation of the desired response. The mismatch estimation approaches in the subsequent sections develop supplementary matrices that account for the sidelobes of scattering in the scene. In a sense, the approaches add sidelobe cancellation to accompany the clutter cancellation in the cancellation-then-estimation procedure. Note that the derivation was void of other unavoidable error including mismatch loss from mismatch filter, covariance estimation loss from the supplementary matrix, covariance estimation loss of the clutter covariance matrix (or the cancellation matrix in general). The SINR is more of an approximation when considering losses. For maximum performance, these errors should be minimized individually prior.

3.3 Least-Squares Space-Time Adaptive Processing

Optimal least-squares approach being considered takes the squared sum of residual error between between the signal model and desired response. The desired response is the mainlobe of a multivariate sinc response. The model is the relationship between the bank of steering vectors and the angle-Doppler filters being applied to the data. The space-time LS cost function is

$$J_{\mathrm{LS}} = \left\| \mathbf{U}^H \mathbf{C}_{\mathrm{st}} - \mathbf{D}_{\mathrm{AD}} \right\|_F^2 \tag{3.50}$$

where $\| \bullet \|_F$ is the Frobenius matrix norm operation, $\mathbf{U}$ is a $MN \times L_{\mathrm{D}} L_{\mathrm{A}}$ matrix of optimal angle-Doppler mismatch filters with each column corresponding to a different angle-Doppler frequency. Define a $L_{\mathrm{D}} L_{\mathrm{A}} \times L_{\mathrm{D}} L_{\mathrm{A}}$ angle-Doppler desired response matrix as

$$\begin{aligned} \mathbf{D}_{\mathrm{AD}} &= \frac{1}{MN} \left(\mathbf{C}_{\mathrm{st}}^H \mathbf{C}_{\mathrm{st}} \right) \odot \mathbf{E}_{\mathrm{AD}} \\ &= \frac{1}{MN} \left(\left(\mathbf{C}_{\mathrm{t}}{}^H \mathbf{C}_{\mathrm{t}} \right) \odot \mathbf{E}_{\mathrm{D}} \right) \otimes \left(\left(\mathbf{C}_{\mathrm{s}}{}^H \mathbf{C}_{\mathrm{s}} \right) \odot \mathbf{E}_{\mathrm{A}} \right) \\ &= \frac{1}{MN} \mathbf{D}_{\mathrm{D}} \otimes \mathbf{D}_{\mathrm{A}} \end{aligned} \tag{3.51}$$

where $\mathbf{E}_{\mathrm{AD}}$ is a $L_{\mathrm{D}} L_{\mathrm{A}} \times L_{\mathrm{D}} L_{\mathrm{A}}$ angle-Doppler banded Toeplitz matrix, $\mathbf{E}_{\mathrm{D}}$ is a $L_{\mathrm{D}} \times L_{\mathrm{D}}$ Doppler banded Toeplitz matrix, $\mathbf{E}_{\mathrm{A}}$ is a $L_{\mathrm{A}} \times L_{\mathrm{A}}$ spatial banded Toeplitz matrix, $\mathbf{D}_{\mathrm{D}}$ is the $L_{\mathrm{D}} \times L_{\mathrm{D}}$ Doppler desired response matrix, and $\mathbf{D}_{\mathrm{A}}$ is the $L_{\mathrm{A}} \times L_{\mathrm{A}}$ spatial desired response matrix. The temporal desired matrix has ones on the $K_{\mathrm{D}} - 1$ diagonals above and below the main diagonal. Similarly, the spatial desired matrix has ones on the $K_{\mathrm{A}} - 1$ diagonals above and below the main diagonal. The off-diagonal terms being zero in the desired response matrix assumes that the steering vectors are orthogonal. The assumption is relevant for a oversampled Doppler and spatial spectrums. Accounting for the oversampling in the banded Toeplitz maintains the nominal resolution of the response. An example of column in $\mathbf{D}_{\mathrm{D}}$ is presented in Figure 3.1 [68]. The columns in $\mathbf{D}_{\mathrm{A}}$ have a similar structure.

A complex gradient vector operator with partial derivatives corresponding to the real and

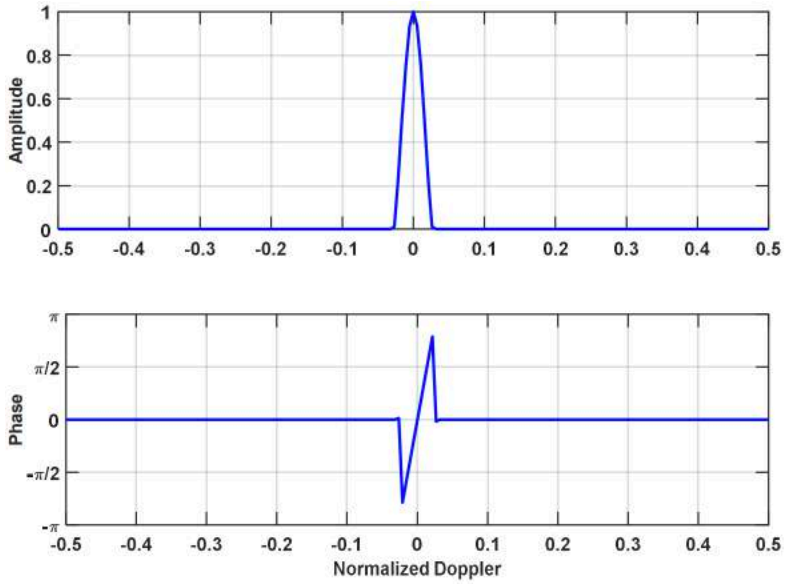

Fig. 3.1: Magnitude and phase of a center column of $\mathbf{D}_{\mathrm{D}}$ used in the least-squares formulation [68]. Columns of $\mathbf{D}_{\mathrm{A}}$ have a similar structure.

imaginary components of the weight vector is applied to minimize the cost function and obtain the optimal solution [92]. The gradient operation was defined in Chapter 2 in (2.14). Application of the $MN \times 1$ gradient vector to the cost function produces

$$\nabla_{\mathbf{u}^*} J_{\mathrm{LS}} = \mathbf{C}_{\mathrm{st}} \mathbf{C}_{\mathrm{st}}^H \mathbf{U}_{\mathrm{LS}} - \mathbf{C}_{\mathrm{st}} \mathbf{D}_{\mathrm{AD}}^H. \tag{3.52}$$

Minimizing the cost function $\nabla_{\mathbf{u}^*} J_{\mathrm{LS}} = 0$ produces the $MN \times L_{\mathrm{D}} L_{\mathrm{A}}$ bank of optimal mismatch angle-Doppler filters

$$\mathbf{U}_{\mathrm{LS}} = \left(\mathbf{C}_{\mathrm{st}} \mathbf{C}_{\mathrm{st}}^H\right)^{-1} \mathbf{C}_{\mathrm{st}} \mathbf{D}_{\mathrm{AD}}^H. \tag{3.53}$$

Notice the LS bank of filters examines the entire 2-D angle-Doppler spectrum. A single spatial frequency and entire Doppler spectrum could be examined using $\mathbf{C}_{\mathrm{st}}(\theta) = \mathbf{C}_{\mathrm{t}} \otimes \mathbf{c}_{\mathrm{s}}(\theta)$ in the LS cost function. However, using the matrix $\mathbf{C}_{\mathrm{st}}(\theta)$ in the cost function would result in the rank-deficient StCM since $\mathbf{C}_{\mathrm{st}}(\theta) \mathbf{C}_{\mathrm{st}}^H(\theta)$ of dimension $MN \times MN$ is rank M. Recall, $\mathbf{C}_{\mathrm{t}}$ is $M \times L_{\mathrm{D}}$ with rank M and $\mathbf{c}_{\mathrm{s}}(\theta)$ is $N \times L_{\mathrm{A}}$ and rank 1. Accordingly, $\mathbf{C}_{\mathrm{st}}(\theta)$ is low-rank compared to

its size of $MN \times L_{\mathrm{D}}$ (alternatively written as $MN \times MK_{\mathrm{D}}$) thereby making $\mathbf{C}_{\mathrm{st}}(\theta)\mathbf{C}_{\mathrm{st}}^{H}(\theta)$ non-invertible. Regularizing the matrix outer product enforces the matrix to be full-rank. Even with regularization, accuracy errors, and spurious responses would still be present when inverting the matrix. The expansion of the spatial spectrum using $\mathbf{C}_{\mathrm{st}}$ has a dimension of $MN \times L_{\mathrm{D}}L_{\mathrm{A}}$ and rank MN. The resulting StCM $\mathbf{C}_{\mathrm{st}}\mathbf{C}_{\mathrm{st}}^{H}$ seen in (3.53) has a size $MN \times MN$, is full rank, and invertible. Regularization is still leveraged to improve the condition number.

A single spatial frequency can still be examined. The estimation stage can be decomposed to

$$\mathbf{u}_{\mathrm{LS}}(\omega,\theta) = \left(\mathbf{C}_{\mathrm{st}}\mathbf{C}_{\mathrm{st}}^{H} + \delta\mathbf{I}_{MN\times MN}\right)^{-1}\left(\dot{\mathbf{c}}_{\mathrm{t}}(\omega)\otimes\mathbf{c}_{\mathrm{s}}(\theta)\right) \tag{3.54}$$

where the following modification to the steering vector,

$$\dot{\mathbf{c}}_{\mathrm{t}}(\omega) = \sum_{k_{\mathrm{D}}=-K_{\mathrm{D}}}^{K_{\mathrm{D}}} \mathbf{c}_{\mathrm{t}}(\omega + k_{\mathrm{D}}\Delta\omega) \tag{3.55}$$

accounts for LS beamspoiling being perform in the desired response matrix and δ is a positive scalar for regularization. An estimate of the angle-Doppler spectrum is obtained by applying the filter to the space-time data vector

$$\hat{x}_{\mathrm{LS}}(\omega,\theta,\ell) = \mathbf{u}_{\mathrm{LS,con}}^{H}(\omega,\theta)\,\widehat{\mathbf{z}}_{\mathrm{st}}(\ell) = \mathbf{w}_{\mathrm{LS,con}}^{H}(\omega,\theta,\ell)\,\mathbf{z}_{\mathrm{st}}(\ell) \tag{3.56}$$

where the filter incorporating the cancellation transform is

$$\mathbf{w}_{\mathrm{LS,con}}(\omega,\theta,\ell) = \mathbf{R}_{\text{rd-st,canc}}(\ell)\,\mathbf{u}_{\mathrm{LS,con}}(\omega,\theta). \tag{3.57}$$

Optimal mismatch processing can be performed off-line since it does not require receive data to form the filter. Alternatively, cancellation is performed on-line since the cancellation matrix is estimated adaptively.

3.4 Reduced-Rank Least-Squares Space-Time Adaptive Processing

Rank reduction of LS mismatch processing optimizes the LS cost function in the reduced dimension by using transformed steering vectors. The filter formation can also be performed off-line. The approach leverages existing rank reduction techniques by transforming the StCM to a reduced rank prior to inversion. The reduced-rank least-squares (RRLS) approach considers a coupling of transformed space-time steering vectors to produce a $D_{\mathrm{t}}D_{\mathrm{s}} \times L_{\mathrm{D}}L_{\mathrm{A}}$ bank of reduced dimension space-time steering vectors

$$\tilde{\mathbf{C}}_{\mathrm{st}}(\omega,\theta) = \mathbf{T}_{\mathrm{t}}^{H}(\omega)\,\mathbf{C}_{\mathrm{t}} \otimes \mathbf{T}_{\mathrm{s}}^{H}(\theta)\,\mathbf{C}_{\mathrm{s}} = \tilde{\mathbf{C}}_{\mathrm{t}}(\omega) \otimes \tilde{\mathbf{C}}_{\mathrm{s}}(\theta) \tag{3.58}$$

where $\tilde{\mathbf{C}}_{\mathrm{t}}(\omega) = \mathbf{T}_{\mathrm{t}}^{H}(\omega)\,\mathbf{C}_{\mathrm{t}}$ is a $D_{\mathrm{t}} \times L_{\mathrm{D}}$ bank of transformed temporal steering vectors and $\tilde{\mathbf{C}}_{\mathrm{s}}(\theta) = \mathbf{T}_{\mathrm{s}}^{H}(\theta)\,\mathbf{C}_{\mathrm{s}}$ is a $D_{\mathrm{s}} \times L_{\mathrm{A}}$ bank of spatial steering vectors. The transformed bank of space-time steering vectors are inserted into the LS cost function

$$\tilde{J}_{\mathrm{LS}}(\omega,\theta) = \left\| \tilde{\mathbf{U}}^{H}(\omega,\theta)\,\tilde{\mathbf{C}}_{\mathrm{st}}(\omega,\theta) - \tilde{\mathbf{D}}_{\mathrm{AD}}(\omega,\theta) \right\|_{F}^{2} \tag{3.59}$$

where the $L_{\mathrm{D}}L_{\mathrm{A}} \times L_{\mathrm{D}}L_{\mathrm{A}}$ space-time desired response matrix is $\tilde{\mathbf{D}}_{\mathrm{AD}}(\omega,\theta) = (\tilde{\mathbf{C}}_{\mathrm{st}}^{H}(\omega,\theta)\,\tilde{\mathbf{C}}_{\mathrm{st}}(\omega,\theta)) \odot \mathbf{E}_{\mathrm{AD}}$. Minimizing the cost function using a $D_{\mathrm{t}}D_{\mathrm{s}} \times 1$ gradient vector results in a $D_{\mathrm{t}}D_{\mathrm{s}} \times L_{\mathrm{D}}L_{\mathrm{A}}$ bank of RRLS filters

$$\begin{aligned} \tilde{\mathbf{U}}_{\mathrm{RRLS}}(\omega,\theta) &= \left(\tilde{\mathbf{C}}_{\mathrm{st}}(\omega,\theta)\,\tilde{\mathbf{C}}_{\mathrm{st}}^{H}(\omega,\theta)\right)^{-1} \tilde{\mathbf{C}}_{\mathrm{st}}(\omega,\theta)\,\tilde{\mathbf{D}}_{\mathrm{AD}}(\omega,\theta) \\ &= \left[\left(\tilde{\mathbf{C}}_{\mathrm{t}}(\omega,\theta)\,\tilde{\mathbf{C}}_{\mathrm{t}}^{H}(\omega,\theta)\right) \otimes \left(\tilde{\mathbf{C}}_{\mathrm{s}}(\omega,\theta)\,\tilde{\mathbf{C}}_{\mathrm{s}}^{H}(\omega,\theta)\right)\right]^{-1} \\ &\quad \times \left(\tilde{\mathbf{C}}_{\mathrm{t}}(\omega,\theta)\,\tilde{\mathbf{D}}_{\mathrm{D}}^{H}(\omega,\theta) \otimes \tilde{\mathbf{C}}_{\mathrm{s}}(\omega,\theta)\,\tilde{\mathbf{D}}_{\mathrm{A}}^{H}(\omega,\theta)\right) \end{aligned} \tag{3.60}$$

corresponding to single Doppler frequency and spatial.

Examining a single angle-Doppler frequency generates $L_{\mathrm{D}}L_{\mathrm{A}}$ number of filters. Obviously, this is far more filters necessary and is also inefficient to generate since only a single angle-Doppler frequency in the bank provides the maximum response. The terms to right of the inverse in (3.60)

are modified to examine RRLS for a single angle-Doppler frequency similar to (3.54). First, $\mathbf{C}_{\mathrm{s}}$ outside of the inverse is replaced by $\mathbf{c}_{\mathrm{s}}(\theta)$. Next, since the oversampling factor of the Doppler spectrum is unchanged, a single column vector in $\tilde{\mathbf{C}}_{\mathrm{t}}(\omega,\theta)\tilde{\mathbf{D}}_{\mathrm{D}}^{H}(\omega,\theta)$ is equivalently expressed as

$$\ddot{\mathbf{c}}_{\mathrm{t}}(\omega)=\sum_{k_{\mathrm{D}}=-K_{\mathrm{D}}}^{K_{\mathrm{D}}}\tilde{\mathbf{c}}_{\mathrm{t}}(\omega+k_{\mathrm{D}}\Delta\omega)=\sum_{k_{\mathrm{D}}=-K_{\mathrm{D}}}^{K_{\mathrm{D}}}\mathbf{T}_{\mathrm{t}}^{H}(\omega)\,\mathbf{c}_{\mathrm{t}}(\omega+k_{\mathrm{D}}\Delta\omega). \tag{3.61}$$

Including these modifications and considering regularization, a $D_{\mathrm{t}}D_{\mathrm{s}}\times 1$ RRLS filter is formed

$$\tilde{\mathbf{u}}_{\mathrm{RRLS}}(\omega,\theta)=\left(\tilde{\mathbf{C}}_{\mathrm{st}}(\omega,\theta)\,\tilde{\mathbf{C}}_{\mathrm{st}}^{H}(\omega,\theta)+\delta\mathbf{I}_{D_{\mathrm{t}}D_{\mathrm{s}}\times D_{\mathrm{t}}D_{\mathrm{s}}}\right)^{-1}\left(\ddot{\mathbf{c}}_{\mathrm{t}}(\omega)\otimes\sum_{k_{\mathrm{D}}=-K_{\mathrm{D}}}^{K_{\mathrm{D}}}\mathbf{T}_{\mathrm{t}}^{H}(\omega)\,\mathbf{c}_{\mathrm{t}}(\omega+k_{\mathrm{D}}\Delta\omega)\right). \tag{3.62}$$

To ensure unity gain when applied to the data vector the RRLS filter is normalized

$$\tilde{\mathbf{u}}_{\mathrm{RRLS,con}}(\omega,\theta)=\frac{\tilde{\mathbf{u}}_{\mathrm{RRLS}}(\omega,\theta)}{\tilde{\mathbf{u}}_{\mathrm{RRLS}}^{H}(\omega,\theta)\,\tilde{\mathbf{c}}_{\mathrm{st}}(\omega,\theta)}. \tag{3.63}$$

The RRLS filter combined with cancellation creates the filter

$$\tilde{\mathbf{w}}_{\mathrm{RRLS,con}}(\omega,\theta,\ell)=\tilde{\mathbf{R}}_{\mathrm{st,canc}}^{-1}(\ell)\,\tilde{\mathbf{u}}_{\mathrm{RRLS,con}}(\omega,\theta). \tag{3.64}$$

The RRLS spectral estimate is obtained by applying the bank of filters to the receive data

$$\hat{x}_{\mathrm{RRLS}}(\omega,\theta,\ell)=\tilde{\mathbf{u}}_{\mathrm{RRLS,con}}^{H}(\omega,\theta)\,\dot{\mathbf{z}}_{\mathrm{st}}(\ell)=\tilde{\mathbf{w}}_{\mathrm{RRLS}}^{H}(\omega,\theta)\,\tilde{\mathbf{z}}_{\mathrm{st}}(\ell). \tag{3.65}$$

3.5 Adaptive Mismatch Angle-Doppler Estimation

In Chapter 2, the implementation of RMMSE in Doppler processing with clutter cancellation was expanded for pulse repetition interval (PRI) staggering with the introduction of a rank reduced formulation for computational improvement. A general form of the mean-square error (MSE) cost function was introduced in (2.15) that incorporated clutter cancellation. The cost function and adaptive filter in Chapter 2 is similar to the form presented in this chapter. The chapters differ in

the steering vectors used. Chapter 2 uses slow-time steering vectors on a stationary platform and this chapter space-time steering vectors on moving platform are considered.

Consider the decomposition of the angle-Doppler estimate at ω and θ from (3.14) into desired estimate and error responses

$$\hat{x}_{\mathrm{AD}}[\omega,\theta,\ell] = g[\omega,\omega,\theta,\theta,\ell]\bar{x}[\omega,\theta,\ell] + \sum_{\gamma\neq\omega}\sum_{\kappa\neq\theta} g[\omega,\gamma,\theta,\kappa,\ell]\bar{x}[\gamma,\kappa,\ell] + \hat{v}[\omega,\theta,\ell] \tag{3.66}$$

where the 2-D frequency response corresponding to the clutter cancellation filter is

$$g\left[\omega_i,\omega_j,\theta_k,\theta_l,\ell\right] = \frac{\mathbf{c}_{\mathrm{st}}^H(\omega_i,\theta_k)\mathbf{R}_{\mathrm{st,canc}}^{-1}(\ell)\mathbf{c}_{\mathrm{st}}(\omega_j,\theta_l)}{MN}. \tag{3.67}$$

The ideal cancellation filter would make the coefficient zero for clutter frequencies and one in other portions of the spectrum. The coefficient is also one when cancellation is not being employed. The cost function considers the residual error between a desired response and its estimate. The desired angle-Doppler response is the illuminated returns of scatterers at a given range, angle, and Doppler after clutter cancellation $d_{\mathrm{opt}} = \bar{x}[\omega,\theta,\ell]\, g[\omega,\omega,\theta,\theta,\ell]$. Using an arbitrary $MN\times 1$ angle-Doppler weight vector, the estimate of the desired response is $d_{\mathrm{est}} = \hat{x}[\omega,\theta,\ell] = \mathbf{u}^H(\omega,\theta,\ell)\,\widehat{\mathbf{z}}_{\mathrm{st}}(\ell)$. The MSE cost function considering the difference between optimal and estimated responses is

$$J_{\mathrm{MSE}}(\omega,\theta,\ell) = E\left\{\left|g[\omega,\omega,\theta,\theta,\ell]\bar{x}[\omega,\theta,\ell] - \mathbf{u}^H(\omega,\theta,\ell)\,\widehat{\mathbf{z}}_{\mathrm{st}}(\ell)\right|^2\right\}. \tag{3.68}$$

Applying a gradient operator to the cost function with respect to $\mathbf{u}^*(\omega,\theta,\ell)$ yields

$$\nabla_{\mathbf{u}^*} J_{\mathrm{MSE}}(\omega,\theta,\ell) = -E\{\widehat{\mathbf{z}}_{\mathrm{st}}(\ell)\widehat{x}^*[\omega,\theta,\ell]\} + E\{\widehat{\mathbf{z}}_{\mathrm{st}}(\ell)\widehat{\mathbf{z}}_{\mathrm{st}}^H(\ell)\}\mathbf{u}(\omega,\theta,\ell). \tag{3.69}$$

Note the dependence on angle, Doppler, and range on the gradient is subsumed for convenience. Finding the minimum of the cost function located at $\nabla_{\mathbf{u}^*} J_{\mathrm{MSE}}(\ell) \stackrel{\Delta}{=} 0$ and solving (3.69) for

$\mathbf{u}(\omega,\theta,\ell)$ produces a $MN \times 1$ minimum mean-square error (MMSE) angle-Doppler filter

$$\mathbf{u}_{\text{MMSE}}(\omega,\theta,\ell) = (E\{\widehat{\mathbf{z}}_{\text{st}}(\ell)\,\widehat{\mathbf{z}}_{\text{st}}^{H}(\ell)\})^{-1} E\{g^{*}[\omega,\omega,\theta,\theta,\ell]\bar{x}^{*}[\omega,\theta,\ell]\,\widehat{\mathbf{z}}(\ell)\}. \tag{3.70}$$

The optimal filter contains a $MN \times MN$ covariance matrix of the space-time data vector $E\{\widehat{\mathbf{z}}_{\text{st}}(\ell)\,\widehat{\mathbf{z}}_{\text{st}}^{H}(\ell)\}$ and a $MN \times 1$ cross-correlation vector between the data vector and angle-Doppler spectrum is $E\{g^{*}[\omega,\omega,\theta,\theta,\ell]\bar{x}^{*}[\omega,\theta,\ell]\,\widehat{\mathbf{z}}(\ell)\}$.

Define the StCM as

$$E\{\widehat{\mathbf{z}}_{\text{st}}(\ell)\,\widehat{\mathbf{z}}_{\text{st}}^{H}(\ell)\} = \mathbf{C}_{\text{st,rem}}\mathbf{P}_{\text{AD,rem}}(\ell)\,\mathbf{C}_{\text{st,rem}}^{H} + \mathbf{R}_{\text{st,err,rem}}(\ell) + \mathbf{R}_{\text{st,v}} \tag{3.71}$$

where $\mathbf{P}_{\text{AD,rem}}(\ell)$ is the $L_{\text{D}}L_{\text{A}} \times L_{\text{D}}L_{\text{A}}$ angle-Doppler power distribution matrix and $\mathbf{R}_{\text{st,err,rem}}(\ell)$ is the $MN \times MN$ space-time error covariance matrix. The model error covariance matrix is a signal-dependent loading term which establishes a dynamic range of the estimates [23]. The noise covariance matrix is a diagonal loading term that reduces the condition number of the matrix to ensure a stable inversion. The StCM inverse is independent of the angle-Doppler frequency and only needs to be performed once per range sample. Practically, the true locations of the clutter are unknown. Recall, that test angle-Doppler frequencies are used to estimate the spectrum. The remaining steering vectors are unknown for an adaptive cancellation filter. The remaining steering vectors $\mathbf{C}_{\text{st,rem}}$ can be approximated and replaced using

$$\mathbf{R}_{\text{st,canc}}^{-1}(\ell)\,\mathbf{C}_{\text{st}} = \mathbf{R}_{\text{st,canc}}^{-1}(\ell)\,[\mathbf{C}_{\text{st,clu}}\ \mathbf{C}_{\text{st,rem}}] \overset{\Delta}{=} [\mathbf{0}_{M \times L_{\text{D,clu}}}\ \mathbf{C}_{\text{st,rem}}] \tag{3.72}$$

since the optimal cancellation matrix is unavailable.

The StCM can incur ill-conditioning errors when inverted if the spatial steering vectors corresponding to the entire spatial spectrum are not considered. Consequently, accounting for multiple spatial steering vectors results in the estimation of multiple beam positions. Processing beams outside of the main beam can be a waste of computational resources. Excluding additional

spatial steering vectors results in the eigenvalues corresponding to the signal-to-noise subspace in the StCM to be less than MN leading to the errors. Including the additional spatial steering vectors makes the signal-to-noise subspace equal to MN thereby maintaining stability. Oversampling in space is not necessary. At a minimum, N evenly spaced beam are required.

Explicitly defined the power distribution matrix to be

$$\mathbf{P}_{\mathrm{AD,rem}}(\ell) \approx \widehat{\mathbf{P}}_{\mathrm{AD}}(\ell) = E\left\{\mathbf{x}_{\mathrm{AD}}(\ell)\mathbf{x}_{\mathrm{AD}}^{H}(\ell)\right\} \odot \mathbf{g}_{\mathrm{AD}}(\ell)\mathbf{g}_{\mathrm{AD}}^{H}(\ell) \odot \mathbf{I}_{L_{\mathrm{D}}L_{\mathrm{A}} \times L_{\mathrm{D}}L_{\mathrm{A}}} \tag{3.73}$$

where the vectorization of the 2-D angle-Doppler power spectrum density of the cancellation is the $L_{\mathrm{D}}L_{\mathrm{A}} \times 1$ vector $\mathbf{g}_{\mathrm{AD}}(\ell)$. The ith element of the vector is $[\mathbf{g}_{\mathrm{AD}}(\ell)]_i = g(\omega_{\iota_{\mathrm{D}}}, \omega_{\iota_{\mathrm{D}}}, \theta_{\iota_{\mathrm{A}}}, \theta_{\iota_{\mathrm{A}}}, \ell)$ for element index $i = \iota_{\mathrm{D}} + \iota_{\mathrm{A}}L_{\mathrm{D}}$, Doppler frequency index $\iota_{\mathrm{D}} = 0, 1, ..., L_{\mathrm{D}} - 1$, spatial frequency index $\iota_{\mathrm{A}} = 0, 1, ..., L_{\mathrm{A}} - 1$, ι_{D}th Doppler frequency $\omega_{\iota_{\mathrm{D}}} = \iota_{\mathrm{D}}\Delta\omega$, Doppler spectrum granularity $\Delta\omega = 1/L_{\mathrm{D}}$, ι_{A}th spatial frequency $\theta_{\iota_{\mathrm{A}}} = \iota_{\mathrm{A}}\Delta\theta$, and spatial spectrum granularity $\Delta\theta = 1/L_{\mathrm{A}}$. The expectation in (3.73) is evaluated under the assumption that the illuminated scatters are statistically IID in Doppler frequency and spatial frequency. Under the assumption diagonal terms within the power distribution matrix would cohere and off-diagonals would de-cohere. Therefore, the power distribution matrix becomes a diagonal matrix with the following terms

$$\widehat{\rho}\left[\omega_i, \omega_j, \theta_k, \theta_l, \ell\right] = \begin{cases} E\left\{\left|\bar{x}\left[\omega_i, \theta_k, \ell\right]\right|^2\right\}\left|g\left[\omega_i, \omega_i, \theta_k, \theta_k \ell\right]\right|^2 & i = j, k = l \\ 0 & i \neq j, k \neq l \end{cases} \tag{3.74}$$

Going forward, the frequencies are subsumed such that $\widehat{\rho}\left[\omega_i, \omega_i, \theta_k, \theta_k, \ell\right]$ is expressed $\widehat{\rho}\left[\omega_i, \theta_k, \ell\right]$.

Define the error covariance matrix to be

$$\begin{aligned} \mathbf{R}_{\mathrm{st,err,rem}}(\ell) &= \sigma_{\mathrm{err}}^2 \mathbf{I}_{MN \times MN} \odot \mathbf{C}_{\mathrm{st,rem}} \mathbf{P}_{\mathrm{AD,rem}}(\ell) \mathbf{C}_{\mathrm{st,rem}}^{H} \\ &\approx \mathbf{R}_{\mathrm{st,err}}(\ell) \\ &= \sigma_{\mathrm{err}}^2 \mathbf{I}_{MN \times MN} \odot \mathbf{R}_{\mathrm{st,canc}}^{-1}(\ell) \mathbf{C}_{\mathrm{st}} \widehat{\mathbf{P}}_{\mathrm{AD}}(\ell) \mathbf{C}_{\mathrm{st}}^{H} \mathbf{R}_{\mathrm{st,canc}}^{-1}(\ell) \end{aligned} \tag{3.75}$$

after incorporating the modifications from (3.72) and (3.73). Substituting the data vector in (3.10)

into the cross-correlation vector in (3.70) forms

$$E\{g^*[\omega,\omega,\theta,\theta,\ell]\,\bar{x}^*[\omega,\theta,\ell]\,\widehat{\mathbf{z}}_{\mathrm{st}}(\ell)\} = \rho[\omega_{\mathrm{rem}},\theta_{\mathrm{rem}},\ell]\,\mathbf{c}_{\mathrm{st}}(\omega_{\mathrm{rem}},\theta_{\mathrm{rem}}) \approx \widehat{\rho}[\omega,\theta,\ell]\,\mathbf{R}^{-1}_{\mathrm{st,canc}}(\ell)\mathbf{c}_{\mathrm{st}}(\omega,\theta) \tag{3.76}$$

where $\rho[\omega_{\mathrm{rem}},\theta_{\mathrm{rem}},\ell] \approx \widehat{\rho}[\omega,\theta,\ell]$ using (3.75). The MMSE angle-Doppler filter in (3.70) is modified by incorporating (3.72) - (3.76) in the filter to produce a structured based MMSE angle-Doppler filter

$$\mathbf{u}_{\mathrm{MMSE}}(\omega,\theta,\ell) = \widehat{\rho}[\omega,\theta,\ell]\,\mathbf{Q}^{-1}_{\mathrm{st}}(\ell)\,\mathbf{R}^{-1}_{\mathrm{st,canc}}(\ell)\mathbf{c}_{\mathrm{st}}(\omega,\theta) \tag{3.77}$$

where the StCM is

$$\begin{aligned}\mathbf{Q}_{\mathrm{st}}(\ell) &= E\{\widehat{\mathbf{z}}_{\mathrm{st}}(\ell)\,\widehat{\mathbf{z}}^H_{\mathrm{st}}(\ell)\} \\ &= \mathbf{R}^{-1}_{\mathrm{st,canc}}(\ell)\,\mathbf{C}_{\mathrm{st}}\widehat{\mathbf{P}}_{\mathrm{AD}}(\ell)\,\mathbf{C}^H_{\mathrm{st}}\mathbf{R}^{-1}_{\mathrm{st,canc}}(\ell) \odot \left(\sigma^2_{\mathrm{err}}\mathbf{I}_{M\times M} + \mathbf{1}_{MN\times MN}\right) + \sigma^2_{\mathrm{v}}\mathbf{I}_{MN\times MN}.\end{aligned} \tag{3.78}$$

A linearly constrained minimum-variance (LCMV) framework [92] is incorporated with MSE cost function to preserve signal loss of low SNR signals and to produce a meaningful noise floor. The formulation is similar to the LCMV MMSE filter presented in the previous chapter. The noise normalization being applied to the cancellation matrix allows for the frequency response to be used as the gain constraint to maintain the distortion at a given angle-Doppler frequency. The constraint is $\mathbf{u}^H(\omega,\theta,\ell)\,\mathbf{R}^{-1}_{\mathrm{st,canc}}(\ell)\mathbf{c}_{\mathrm{st}}(\omega,\theta) = g[\omega,\omega,\theta,\theta,\ell]$. The constraint is angle-Doppler frequency and range dependent and would ideally place a null at clutter frequencies and unity gain at remaining frequencies. The transition regions and inherent estimation loss from the adaptive cancellation place the actual constraint between null and unity gain constraints. An example of the constraint is presented in Figure 3.2 for $\beta = 0$ and $\beta = 1$. Note when cancellation is not being employed, the constraint is a unity gain constraint becomes a is a special case of LCMV known as the minimum variance distortionless response (MVDR). The initial constrained MSE cost function presented in [86, 93] explore the MVDR solution.

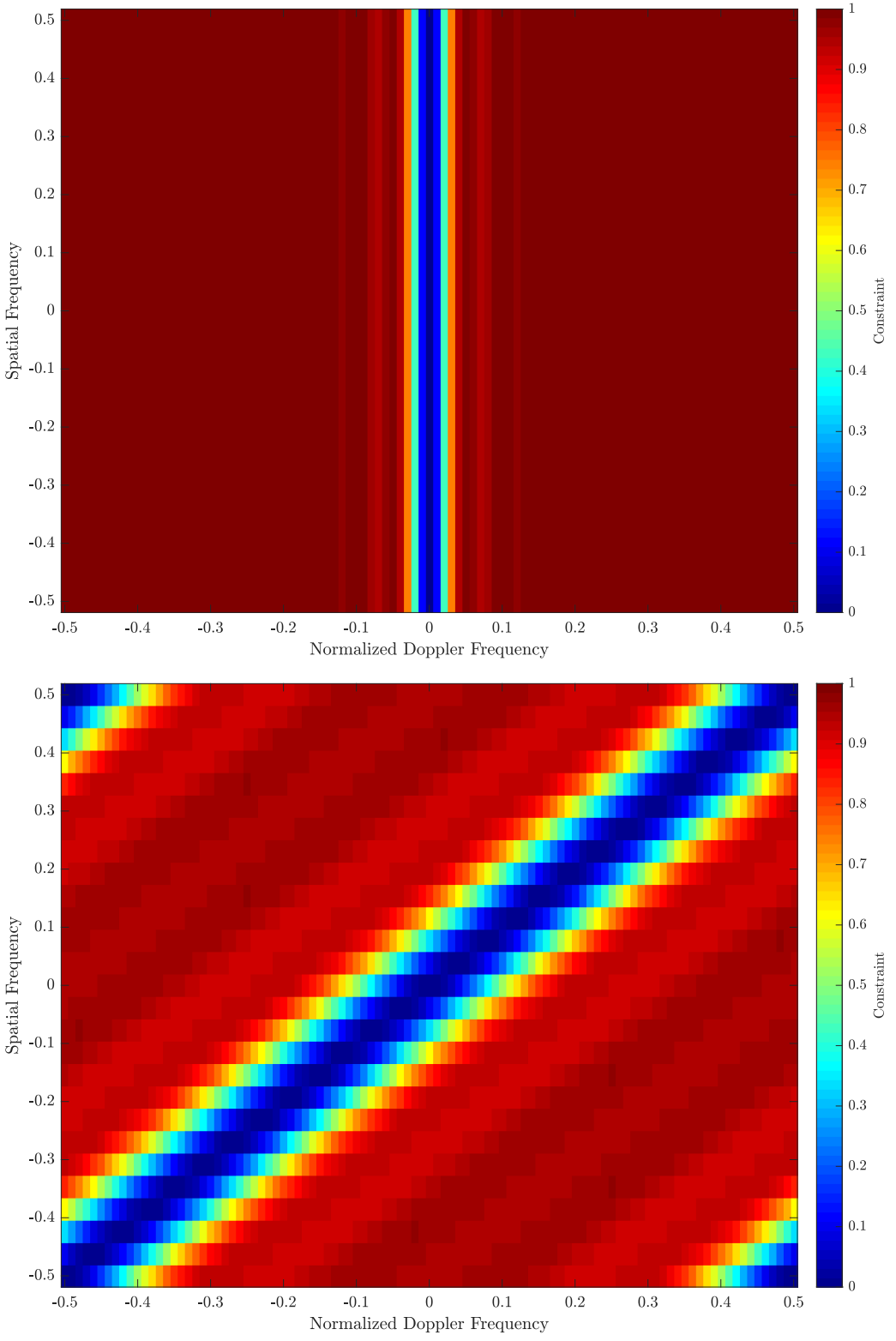

Fig. 3.2: Example of adaptive LCMV constraints using adaptive cancellation for $\beta = 0$ (top) and $\beta = 1$ (bottom)

The constrained MSE cost function is

$$\begin{aligned} J_{\text{MSE}}(\omega,\theta,\ell) = E\{|g[\omega,\omega,\theta,\theta,\ell]\bar{x}[\omega,\theta,\ell] - \mathbf{u}^H(\omega,\theta,\ell)\,\widehat{\mathbf{z}}_{\text{st}}(\ell)|^2\} \\ + \text{Re}\{\lambda_{\text{L}}^*\left(\mathbf{u}^H(\omega,\theta,\ell)\,\mathbf{R}_{\text{st,canc}}^{-1}(\ell)\mathbf{c}_{\text{st}}(\omega,\theta) - g[\omega,\omega,\theta,\theta,\ell]\right)\}. \end{aligned} \tag{3.79}$$

Minimizing the cost function with respect to the filter and incorporating assumptions for the expectations yields the gain constrained MMSE filter

$$\begin{aligned} \mathbf{u}_{\text{MMSE,con}}(\omega,\theta,\ell) &= \left(E\{\widehat{\mathbf{z}}_{\text{st}}(\ell)\widehat{\mathbf{z}}_{\text{st}}^H(\ell)\}\right)^{-1}\left(E\{g^*[\omega,\omega,\theta,\theta,\ell]\bar{x}^*[\omega,\theta,\ell]\widehat{\mathbf{z}}_{\text{st}}(\ell)\} - \frac{\lambda_{\text{L}}}{2}\mathbf{R}_{\text{st,canc}}^{-1}(\ell)\mathbf{c}_{\text{st}}(\omega,\theta)\right) \\ &= \left(\widehat{\rho}[\omega,\theta,\ell] - \frac{\lambda_{\text{L}}}{2}\right)\mathbf{Q}_{\text{st}}^{-1}(\ell)\mathbf{R}_{\text{st,canc}}^{-1}(\ell)\mathbf{c}_{\text{st}}(\omega,\theta). \end{aligned} \tag{3.80}$$

Following a similar procedure from the previous chapter (using (2.33) - (2.35)), the constrained MMSE filter can be show to be

$$\mathbf{u}_{\text{MMSE,con}}(\omega,\theta,\ell) = \frac{g[\omega,\omega,\theta,\theta,\ell]\mathbf{Q}_{\text{st}}^{-1}(\ell)\mathbf{R}_{\text{st,canc}}^{-1}(\ell)\mathbf{c}_{\text{st}}(\omega,\theta)}{\mathbf{c}_{\text{st}}^H(\omega,\theta)\mathbf{R}_{\text{st,canc}}^{-1}(\ell)\mathbf{Q}_{\text{st}}^{-1}(\ell)\mathbf{R}_{\text{st,canc}}^{-1}(\ell)\mathbf{c}_{\text{st}}(\omega,\theta)}. \tag{3.81}$$

The application of the filter produces the following angle-Doppler response

$$\begin{aligned} \hat{x}_{\text{MMSE,con}}[\omega,\theta,\ell] &= \mathbf{u}_{\text{MMSE,con}}^H(\omega,\theta,\ell)\,\widehat{\mathbf{z}}_{\text{st}}(\ell) \\ &= \frac{g^*[\omega,\omega,\theta,\theta,\ell]\mathbf{c}_{\text{st}}^H(\omega,\theta)\mathbf{R}_{\text{st,canc}}^{-1}(\ell)\mathbf{Q}_{\text{st}}^{-1}(\ell)\mathbf{R}_{\text{st,canc}}^{-1}(\ell)\mathbf{z}_{\text{st}}(\ell)}{\mathbf{c}_{\text{st}}^H(\omega,\theta)\mathbf{R}_{\text{st,canc}}^{-1}(\ell)\mathbf{Q}_{\text{st}}^{-1}(\ell)\mathbf{R}_{\text{st,canc}}^{-1}(\ell)\mathbf{c}_{\text{st}}(\omega,\theta)}. \end{aligned} \tag{3.82}$$

Oversampling in the Doppler is often implemented to overcome Doppler straddling that may diminish RMMSE performance by inducing a mismatch loss. RMMSE generates a super resolution effect that makes the algorithm susceptible to mismatch loss from angle-Doppler straddling of scatterers. Oversampling the signal beyond the nominal resolution has long been a method to address straddling in range, Doppler, and space. RMMSE has been shown to benefit from beamspoiling which is a method to maintain the nominal resolution [94]. Beamspoling for

angle-Doppler signals with RMMSE is

$$\mathbf{u}_{\text{MMSE,beam}}(\omega,\theta,\ell) = \frac{\sqrt{K_{\text{D}}K_{\text{A}}}\sum\limits_{\omega_k=-\Omega_K}^{\Omega_K}\sum\limits_{\theta_k=-\Theta_K}^{\Theta_K}\mathbf{u}_{\text{MMSE,con}}(\omega+\omega_k,\theta+\theta_k,\ell)\,\mathbf{c}_{\text{st}}^{H}(\omega+\omega_k,\theta+\theta_k)\,\mathbf{c}_{\text{st}}(\omega,\theta)}{\sum\limits_{\omega_k=-\Omega_k}^{\Omega_K}\sum\limits_{k_{\text{A}}=-\Theta_K}^{\Theta_K}\mathbf{c}_{\text{st}}^{H}(\omega+\omega_k,\theta+\theta_k)\,\mathbf{c}_{\text{st}}(\omega,\theta)} \tag{3.83}$$

where $\omega_k = k_{\text{D}}\Delta\omega$, $\Omega_K = K_{\text{D}}\Delta\omega$, $\theta_k = k_{\text{A}}\Delta\theta$, and $\Theta_K = K_{\text{A}}\Delta\theta$. The beamspoiling form in (3.83) accounts for oversampling after filter formation and was first introduced in the previous chapter for Doppler signals. The first inclusion of beamspoiling for MMSE was in [94]. The beamspoiling method presented in [94] differs in its implementation since it operates on fast-time signals. The application of the filter produces the following angle-Doppler response

$$\hat{x}_{\text{MMSE,beam}}[\omega,\theta,\ell] = \mathbf{u}_{\text{MMSE,beam}}^{H}(\omega,\theta,\ell)\,\widehat{\mathbf{z}}_{\text{st}}(\ell)\,. \tag{3.84}$$

Setting K_{A} to one would minimize the number of beams necessary. Increasing K_{A} beyond one would be favorable to RMMSE performance since it would take into account straddling in space. That would mean more beams would need to be estimated. Which would also lead to an increase in the number of angle-Doppler filters that need to be examined. There is a trade-off there that must be taken into consideration. If straddling in space is not a concern, then K_{A} should be kept at one.

Adaptive mismatch angle-Doppler estimation (AMADE) is an iterative procedure that leverages RMMSE for angle-Doppler signals. When combined with adaptive clutter cancellation, AMADE becomes a subset of the baseline supplementary cancellation (BaSC) filter presented in [34]. BaSC performs a "hard" cancellation by performing linear transformation on the receive data prior to adaptive estimation. AMADE procedure initializes by applying the STAP filter to the receive data to form the initial angle-Doppler estimate

$$\hat{\mathbf{x}}_{\text{AMADE},0}(\ell) = \mathbf{U}_{\text{AD}}^{H}\hat{\mathbf{R}}_{\text{st,canc}}^{-1}(\ell)\,\mathbf{z}_{\text{st}}(\ell) \tag{3.85}$$

using an estimate of the cancellation matrix. The first iteration begins by forming the ith angle-Doppler power distribution matrix using a previous angle-Doppler estimate

$$\hat{\mathbf{P}}_{\text{AMADE},i}(\ell) = \hat{\mathbf{x}}_{\text{AMADE},i-1}(\ell)\,\hat{\mathbf{x}}^{H}_{\text{AMADE},i-1}(\ell) \odot \mathbf{I}_{L_{\text{D}}L_{\text{A}} \times L_{\text{D}}L_{\text{A}}}. \tag{3.86}$$

The vectorized angle-Doppler spectrum of the cancellation, $\mathbf{g}_{\text{AD}}(\ell)$, presented in (3.73) is subsumed into (3.86) due to the cancellation in the previous estimate (shown in (3.85) and later in (3.90)). After, the StCM is formed

$$\hat{\mathbf{Q}}_{\text{AMADE},i}(\ell) = \hat{\mathbf{R}}^{-1}_{\text{st,canc}}(\ell)\,\mathbf{C}_{\text{st}}\hat{\mathbf{P}}_{\text{AMADE},i}(\ell)\,\mathbf{C}^{H}_{\text{st}}\hat{\mathbf{R}}^{-1}_{\text{st,canc}}(\ell) \odot \left(\mathbf{1}_{MN\times MN} + \sigma^2_{\text{err}}\mathbf{I}_{MN\times MN}\right) + \sigma^2_{\text{v}}\mathbf{I}_{MN\times MN}. \tag{3.87}$$

The StCM estimate is leveraged to form the ith constrained AMADE filter

$$\hat{\mathbf{u}}_{\text{AMADE,con},i}(\omega,\theta,\ell) = \frac{\hat{g}[\omega,\omega,\theta,\theta,\ell]\hat{\mathbf{Q}}^{-1}_{\text{AMADE},i}(\ell)\,\hat{\mathbf{R}}^{-1}_{\text{st,canc}}(\ell)\,\mathbf{c}_{\text{st}}(\omega,\theta)}{\mathbf{c}^{H}_{\text{st}}(\omega,\theta)\,\hat{\mathbf{R}}^{-1}_{\text{st,canc}}(\ell)\,\hat{\mathbf{Q}}^{-1}_{\text{AMADE},i}(\ell)\,\hat{\mathbf{R}}^{-1}_{\text{st,canc}}(\ell)\,\mathbf{c}_{\text{t}}(\omega,\theta)} \tag{3.88}$$

where $\hat{g}[\omega,\omega,\theta,\theta,\ell]$ is formed using (3.67) and the estimated cancellation matrix. After all the filters have been formed, beamspoiling is performed

$$\hat{\mathbf{u}}_{\text{AMADE,beam}}(\omega,\theta,\ell) = \frac{\sqrt{K_{\text{D}}K_{\text{A}}}\sum\limits_{\omega_k=-\Omega_K}^{\Omega_K}\sum\limits_{\theta_k=-\Theta_K}^{\Theta_K}\hat{\mathbf{u}}_{\text{AMADE,con}}(\omega+\omega_k,\theta+\theta_k,\ell)\,\mathbf{c}^{H}_{\text{st}}(\omega+\omega_k,\theta+\theta_k)\,\mathbf{c}_{\text{st}}(\omega,\theta)}{\sum\limits_{\omega_k=-\Omega_k}^{\Omega_K}\sum\limits_{k_{\text{A}}=-\Theta_K}^{\Theta_K}\mathbf{c}^{H}_{\text{st}}(\omega+\omega_k,\theta+\theta_k)\,\mathbf{c}_{\text{st}}(\omega,\theta)} \tag{3.89}$$

A $MN \times L_{\text{D}}L_{\text{A}}$ bank of beamspoiled filters is generated using filters formed from (3.89) and subsequently applied to the space-time receive data to obtain the updated estimate of the spectrum

$$\hat{\mathbf{x}}_{\text{AMADE},i}(\ell) = \hat{\mathbf{U}}^{H}_{\text{AMADE,beam},i}(\ell)\,\hat{\mathbf{R}}^{-1}_{\text{st,canc}}(\ell)\,\mathbf{z}_{\text{st}}(\ell). \tag{3.90}$$

The procedure returns to (3.86) and concludes after a user-defined number of iterations.

Examples of AMADE using the gain constraint and beamspoiling is presented in Figures 3.3

to 3.6 for a single mover in clutter for 20 pulses and 5 elements after 10 iterations. In Figure 3.3, presents the approach without cancellation. A mover is placed at boresight spatially with a normalized Doppler of 0.3 for $\beta = 1$. AMADE is shown to resolve scattering and suppress sidelobes. The unconstrained and constrained solutions generates a super resolution response with the latter providing a more robust solution. Beamspoiling deviates from the super resolution and generates a response to the nominal resolution. However, doing beamspoiling adds a single sidelobe on each side of the scattering mainlobe. In Fig. 3.4, similar responses are shown with clutter cancellation. AMADE with cancellation displays the moving scatterer only.

For analysis purposes, the Doppler and spatial spectrum were oversampled by a factor of five each in Figures 3.3 and 3.4. Examples of these same scenarios are presented for a Doppler oversampling of five and spatial spectrum not being oversampled without and with cancellation in Figs 3.5 and 3.6, respectively. Comparing Fig. 3.3 to Fig. 3.5 shows AMADE sidelobe suppression benefits from spatial oversampling without cancellation. Comparing Fig. 3.5 to Fig. 3.6 shows AMADE is much better in mover resolution when incorporated with clutter cancellation. The results are on par with the oversampling seen in Fig. 3.4.

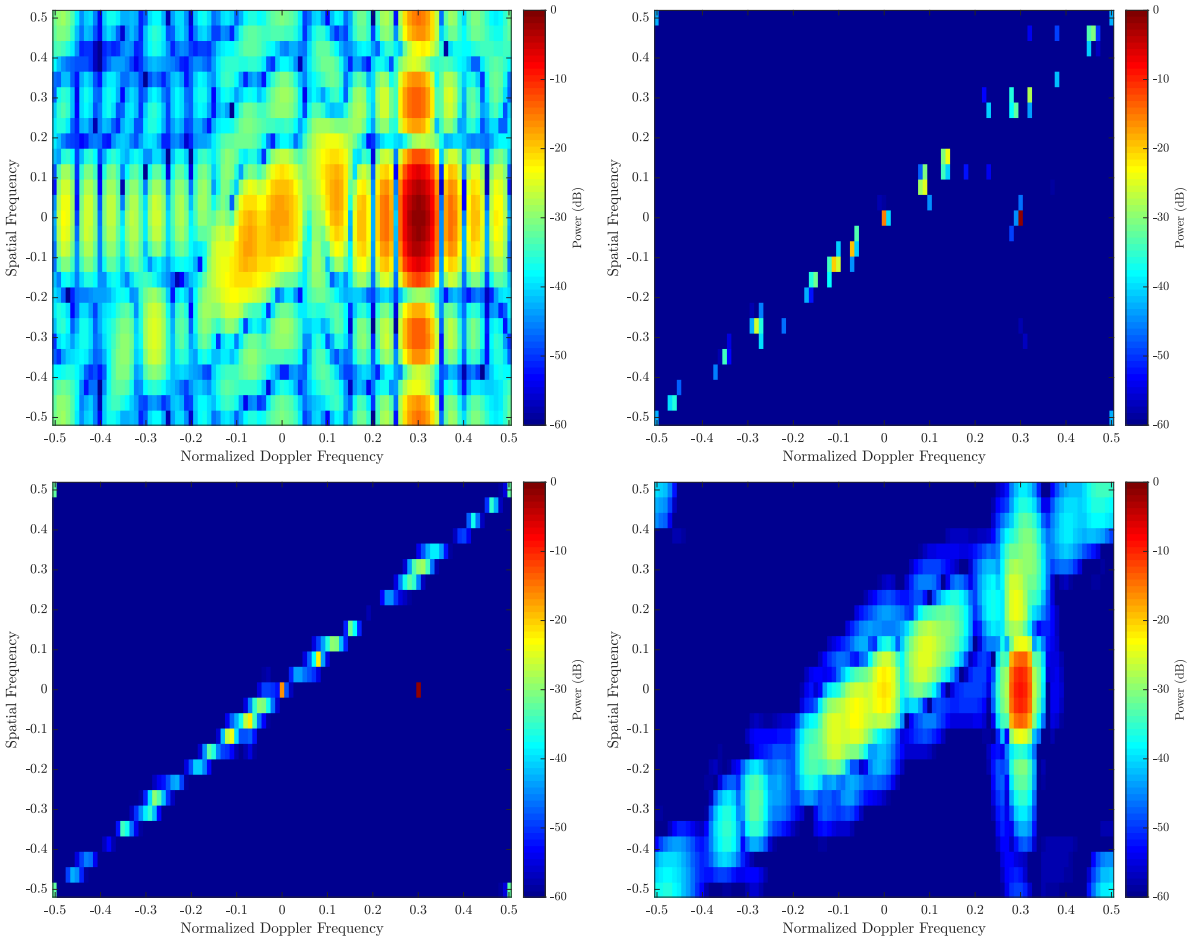

Fig. 3.3: Normalized angle-Doppler response without cancellation for standard angle-Doppler processing (top left), unconstrained AMADE (top right), constrained AMADE (bottom left), and beamspoiled & constrained AMADE (bottom right)

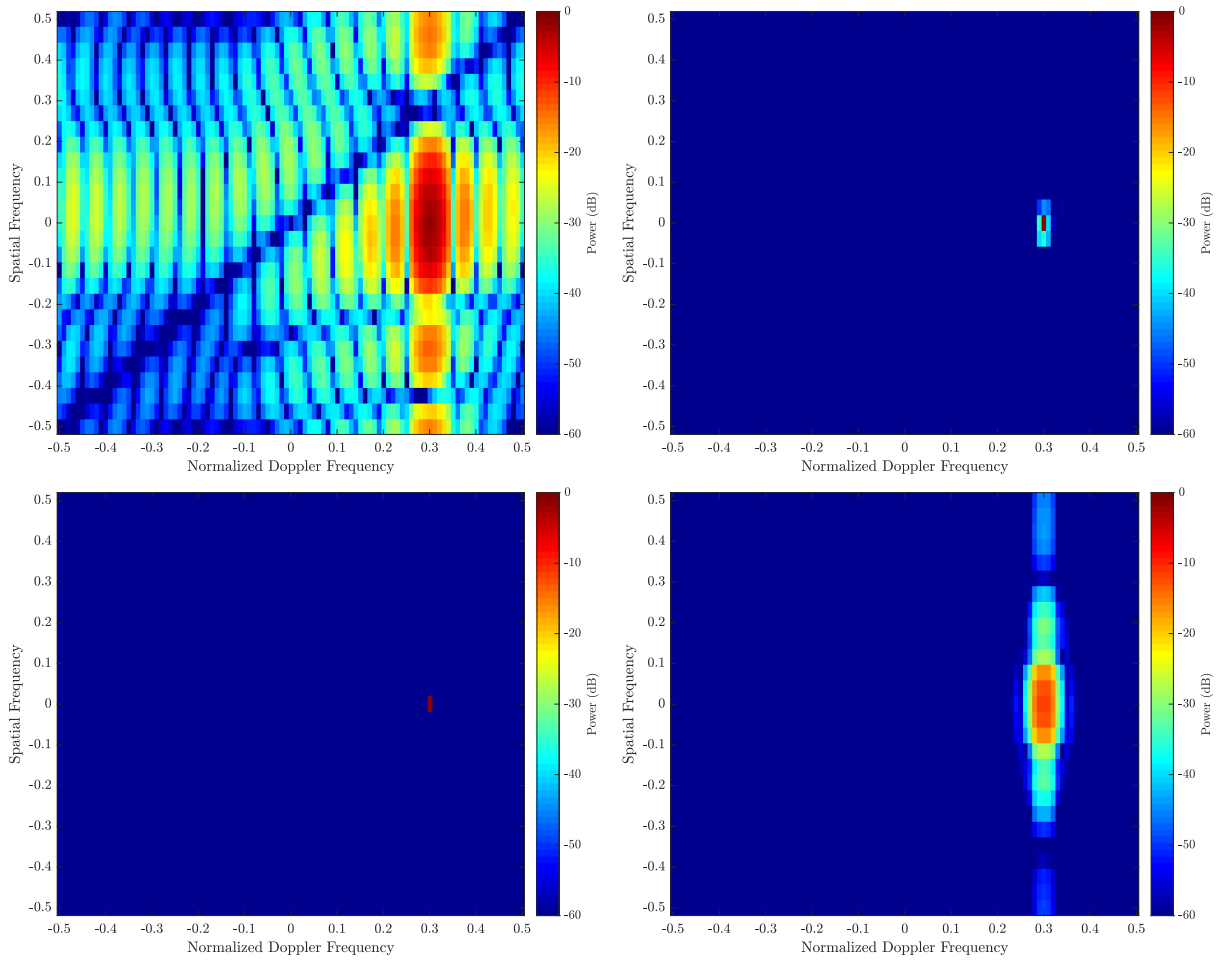

Fig. 3.4: Normalized angle-Doppler response with cancellation for STAP (top left), unconstrained AMADE (top right), constrained AMADE (bottom left), and beamspoiled & constrained AMADE (bottom right)

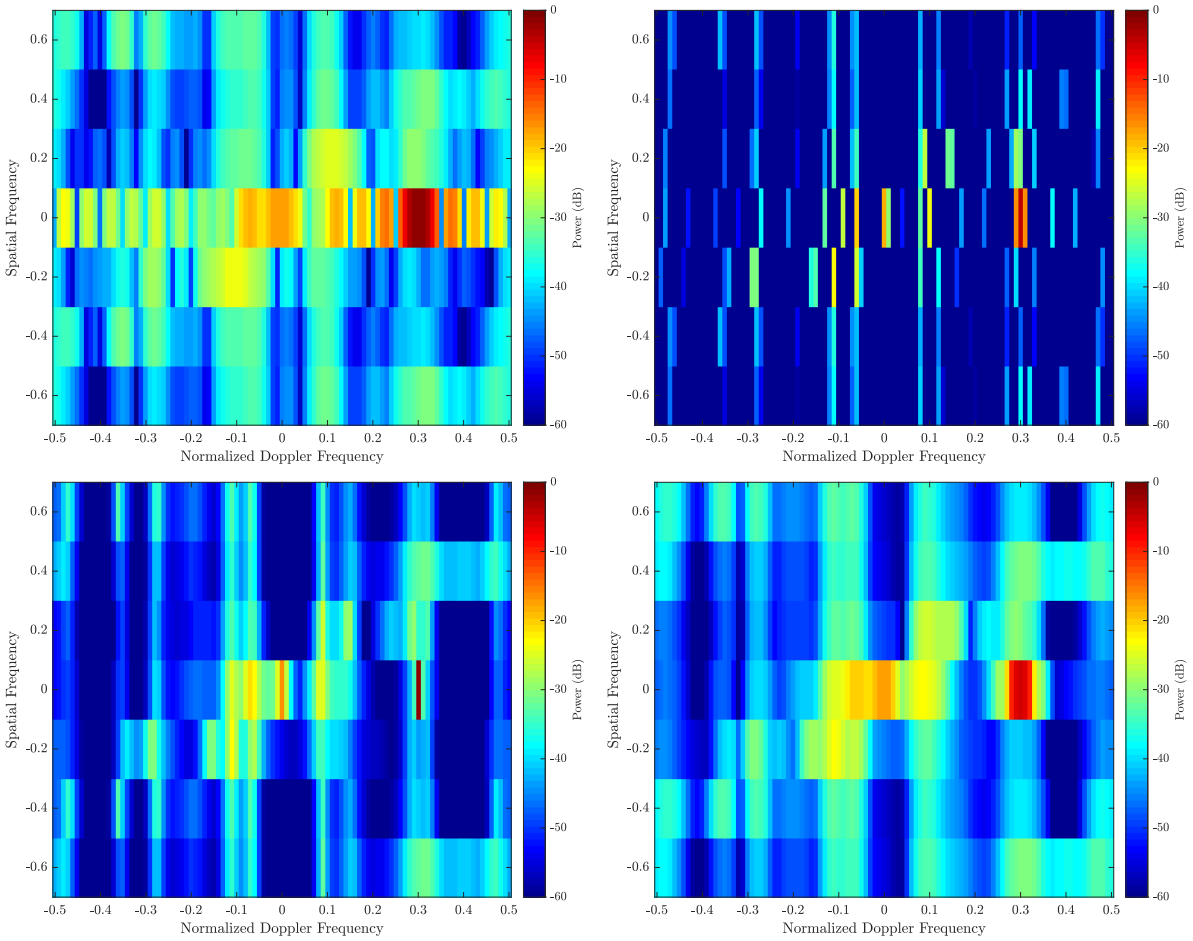

Fig. 3.5: Normalized angle-Doppler response without cancellation for standard angle-Doppler processing (top left), unconstrained AMADE (top right), constrained AMADE (bottom left), and beamspoiled & constrained AMADE (bottom right)

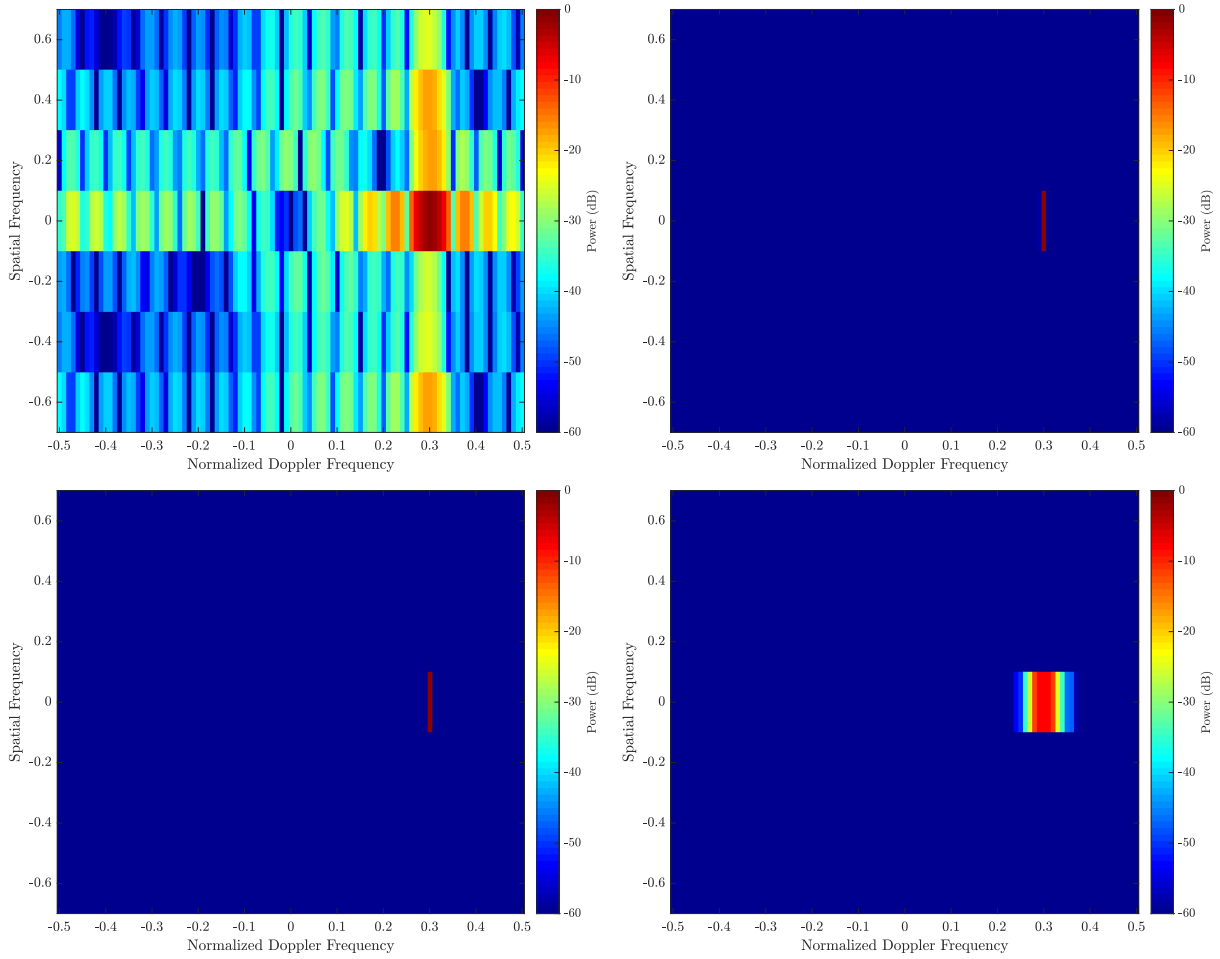

Fig. 3.6: Normalized angle-Doppler response with cancellation for STAP (top left), unconstrained AMADE (top right), constrained AMADE (bottom left), and beamspoiled & constrained AMADE (bottom right)

3.6 Partial Adaptive Mismatch Angle-Doppler Estimation

Incorporating an adaptive angle-Doppler estimation using AMADE, which has its own matrix inversion, adds to the computational complexity of STAP. A reduce-rank version of AMADE known as partial adaptive mismatch angle-Doppler estimation (PAMADE) is considered to reduce the computational complexity of the adaptive estimator. PAMADE will use the *same* transformation matrices used to reduce the clutter cancellation covariance matrix in STAP. PAMADE leverages the reduced-rank formulation for RMMSE introduced in the previous chapter for Doppler processing and expends the formulation for angle-Doppler processing. The previous chapter explored full-rank and reduced-rank adaptive estimation while maintaining full-rank cancellation. PAMADE introduces the combination of adaptive estimation and adaptive cancellation in their reduce-rank forms to reduce computation, suppress clutter, and suppress sidelobes.

Consider the $MN \times D_{\mathrm{t}}D_{\mathrm{s}}$ space-time transformation matrix $\mathbf{T}_{\mathrm{st}}(\omega,\theta)$ presented in (3.18). The relationship between the $MN \times 1$ full rank weight vector $\mathbf{u}(\omega,\theta,\ell)$ and $D_{\mathrm{t}}D_{\mathrm{s}} \times 1$ reduced-rank weight vector $\tilde{\mathbf{u}}(\omega,\theta,\ell)$ is

$$\mathbf{u}(\omega,\theta,\ell) = \mathbf{T}_{\mathrm{st}}(\omega,\theta)\,\tilde{\mathbf{u}}(\omega,\theta,\ell) \tag{3.91}$$

[4]. The estimate of the desired response considers the $MN \times 1$ post cancellation receive data vector from (3.22) and the reduced-rank weight vector $d_{\mathrm{est}} = \hat{x}[\omega,\theta,\ell] = \tilde{\mathbf{u}}^H(\omega,\theta,\ell)\,\mathbf{T}^H(\omega,\omega,\theta)\,\widehat{\mathbf{z}}_{\text{rd-st}}(\omega,\theta,\ell)$. The desired response remains the same from the previous section. The space-time reduced-rank MSE cost function is

$$\begin{aligned}\tilde{J}_{\mathrm{MSE}}(\omega,\theta,\ell) &= E\left\{\left|g[\omega,\omega,\theta,\theta,\ell]\,\bar{x}[\omega,\theta,\ell] - \left(\mathbf{T}_{\mathrm{st}}(\omega,\theta)\,\tilde{\mathbf{u}}(\omega,\theta,\ell)\right)^H \widehat{\mathbf{z}}_{\text{rd-st}}(\omega,\theta,\ell)\right|^2\right\} \\ &= E\left\{\left|g[\omega,\omega,\theta,\theta,\ell]\,\bar{x}[\omega,\theta,\ell] - \tilde{\mathbf{u}}^H(\omega,\theta,\ell)\,\tilde{\mathbf{z}}_{\text{rd-st}}(\omega,\theta,\ell)\right|^2\right\}.\end{aligned} \tag{3.92}$$

The $D_{\mathrm{t}}D_{\mathrm{s}} \times 1$ space-time data vector is transformed twice, once for clutter cancellation and once

for rank reduction

$$\tilde{\mathbf{z}}_{\text{rd-st}}(\omega,\theta,\ell) = \mathbf{T}_{\text{st}}^{H}(\omega,\theta)\,\widehat{\mathbf{z}}_{\text{rd-st}}(\omega,\theta,\ell) = \mathbf{T}_{\text{st}}^{H}(\omega,\theta)\,\mathbf{R}_{\text{rd-st,canc}}(\omega,\theta,\ell)\mathbf{z}_{\text{st}}(\ell) \tag{3.93}$$

where $\mathbf{R}_{\text{rd-st,canc}}(\omega,\theta,\ell)$ is formed using (3.23). Recall, $\mathbf{R}_{\text{rd-st,canc}}(\omega,\theta,\ell)$ is a $MN \times MN$ matrix that contains matrix inversion of a $D_{\text{t}}D_{\text{s}} \times D_{\text{t}}D_{\text{s}}$ cancellation matrix mapped back to the full dimension. The $D_{\text{t}}D_{\text{s}} \times 1$ reduced dimension MMSE (RD-MMSE) angle-Doppler filter

$$\tilde{\mathbf{u}}_{\text{RD-MMSE}}(\omega,\theta,\ell) = \left(E\left\{\tilde{\mathbf{z}}_{\text{rd-st}}(\omega,\theta,\ell)\tilde{\mathbf{z}}_{\text{rd-st}}^{H}(\omega,\theta,\ell)\right\}\right)^{-1} E\{g^{*}[\omega,\omega,\theta,\theta,\ell]\bar{x}^{*}[\omega,\theta,\ell]\,\tilde{\mathbf{z}}_{\text{rd-st}}(\omega,\theta,\ell)\} \tag{3.94}$$

is formed from applying the gradient operation with respect to the reduced rank filter, minimizing the cost function such that $\nabla_{\tilde{\mathbf{u}}^{*}}\tilde{J}_{\text{MSE}}(\omega,\theta,\ell) = 0$, and solving for $\tilde{\mathbf{u}}(\omega,\theta,\ell)$. When the filter is mapped back to full dimension using (3.91), the filter is compactly expressed as

$$\begin{aligned}\mathbf{u}_{\text{RD-MMSE}}(\omega,\theta,\ell) &= \mathbf{T}_{\text{st}}(\omega,\theta)\,\tilde{\mathbf{u}}_{\text{RD-MMSE}}(\omega,\theta,\ell) \\ &= \widehat{\rho}\,[\omega,\theta,\ell]\,\mathbf{Q}_{\text{rd-st}}(\omega,\theta,\ell)\,\mathbf{R}_{\text{rd-st,canc}}(\omega,\theta,\ell)\mathbf{c}_{\text{st}}(\omega,\theta)\end{aligned} \tag{3.95}$$

where the $MN \times MN$ StCM inverted in a lower dimension then mapped to full dimension is

$$\mathbf{Q}_{\text{rd-st}}(\omega,\theta,\ell) = \mathbf{T}_{\text{st}}(\omega,\theta)\,\tilde{\mathbf{Q}}_{\text{st}}^{-1}(\omega,\theta,\ell)\,\mathbf{T}_{\text{st}}^{H}(\omega,\theta) \tag{3.96}$$

and the $D_{\text{t}}D_{\text{s}} \times D_{\text{t}}D_{\text{s}}$ auto-covariance matrix of the recieved data matrix

$$\begin{aligned}\tilde{\mathbf{Q}}_{\text{st}}(\omega,\theta,\ell) &= E\{\tilde{\mathbf{z}}_{\text{rd-st}}(\omega,\theta,\ell)\tilde{\mathbf{z}}_{\text{rd-st}}^{H}(\omega,\theta,\ell)\} \\ &= \mathbf{T}_{\text{st}}^{H}(\omega,\theta)\,\mathbf{R}_{\text{rd-st,canc}}(\omega,\theta,\ell)\,\mathbf{C}_{\text{st}}\widehat{\mathbf{P}}_{\text{AD}}(\ell)\,\mathbf{C}_{\text{st}}^{H}\mathbf{R}_{\text{rd-st,canc}}(\omega,\theta,\ell)\,\mathbf{T}_{\text{st}}(\omega,\theta) \\ &\quad \odot\left(\sigma_{\text{err}}^{2}\mathbf{I}_{D_{\text{t}}D_{\text{s}}\times D_{\text{t}}D_{\text{s}}} + \mathbf{1}_{D_{\text{t}}D_{\text{s}}\times D_{\text{t}}D_{\text{s}}}\right) + \sigma_{\text{v}}^{2}\mathbf{I}_{D_{\text{t}}D_{\text{s}}\times D_{\text{t}}D_{\text{s}}}.\end{aligned} \tag{3.97}$$

Similar assumptions from the previous section regarding statistically independence are made for

the expectation to obtain the matrix. The cross-correlation vector in (3.94) is

$$\begin{aligned} E\{g^*[\omega,\omega,\theta,\theta,\ell]\,\bar{x}^*[\omega,\theta,\ell]\,\widehat{\mathbf{z}}_{\text{rd-st}}(\omega,\theta,\ell)\} &= \rho[\omega_{\text{rem}},\theta_{\text{rem}},\ell]\,\mathbf{c}_{\text{st}}(\omega_{\text{rem}},\theta_{\text{rem}}) \\ &\approx \widehat{\rho}[\omega,\theta,\ell]\,\mathbf{R}_{\text{rd-st,canc}}(\omega,\theta,\ell)\mathbf{c}_{\text{st}}(\omega,\theta) \end{aligned} \tag{3.98}$$

and obtained using similar assumptions from the previous section. An estimate is obtained by applying the filter to the post cancellation receive data

$$\begin{aligned} \hat{x}_{\text{RD-MMSE}}(\omega,\theta,\ell) &= \mathbf{u}^H_{\text{RD-MMSE}}(\omega,\theta,\ell)\,\widehat{\mathbf{z}}_{\text{st}}(\ell) \\ &= \mathbf{w}^H_{\text{RD-MMSE}}(\omega,\theta,\ell)\,\mathbf{z}_{\text{st}}(\ell) \\ &= \widehat{\rho}[\omega,\theta,\ell]\mathbf{c}^H_{\text{st}}(\omega,\theta)\mathbf{Q}_{\text{rd-st}}(\omega,\theta,\ell)\,\mathbf{R}_{\text{rd-st,canc}}(\omega,\theta,\ell)\,\mathbf{z}(\ell) \end{aligned} \tag{3.99}$$

where the RD-MMSE filter in space-time is

$$\begin{aligned} \mathbf{w}_{\text{RD-MMSE}}(\omega,\theta,\ell) &= \mathbf{R}_{\text{rd-st,canc}}(\omega,\theta,\ell)\,\mathbf{u}_{\text{RD-MMSE}}(\omega,\theta,\ell) \\ &= \widehat{\rho}[\omega,\theta,\ell]\,\mathbf{R}_{\text{rd-st,canc}}(\omega,\theta,\ell)\,\mathbf{Q}_{\text{rd-st}}(\omega,\theta,\ell)\,\mathbf{R}_{\text{rd-st,canc}}(\omega,\theta,\ell)\,\mathbf{c}_{\text{st}}(\omega,\theta). \end{aligned} \tag{3.100}$$

The RD-MMSE filter overall structure is similar to MMSE filter.

RD-MMSE filter in (3.100) reduces and inverts the covariance matrices corresponding to cancellation and estimation individually then maps the matrices back to the full dimension prior to their matrix multiplication. Since the matrices corresponding to estimation and cancellation are reduced, inverted, and mapped individually, they do not necessary have to use the same transformation. In Chapter 1, and as Ward pointed out in [4], options for reduction of STAP can be in element-space or beamspace for spatial spectrum and pre-Doppler or post-Doppler for Doppler spectrum. The combination leads to four possibilities to reduce cancellation covariance matrix (See Fig 1.17 for a depiction of the four possibilities). Each possibility has its own computational and performance benefits [4]. Reduction of the StCM in the RD-MMSE filter has the same four possibilities. Accordingly, there is a multiplicative increase to 16 possibilities when

combining adaptive cancellation and estimation. More research is needed that explores each reduction.

Element-space post-Doppler is used for both estimation and cancellation matrix reduction in this chapter. Based on the structure of the element-space post-Doppler transformation matrix selected for this chapter, the transformation maps full dimension space-time samples to a reduced dimension space-frequency bins (which is subset of the Doppler spectrum over all elements). The basis vectors for the approach maintains the sampled complex sinusoid of different spatial frequencies and changes the slow-time samples to Doppler frequency-shifted sinc functions localized about the mainlobe width. The portion of the sinc response mainlobe and potential sidelobes captured is D_{t}.

RD-MMSE approach has a similar constrained and beamspoling solutions to the MMSE proposed in the previous chapter. The constrained reduced-rank MSE cost function is

$$\begin{aligned}\tilde{J}_{\mathrm{MSE}}(\omega,\theta,\ell) = E\left\{\left|g[\omega,\omega,\theta,\theta,\ell]\bar{x}[\omega,\theta,\ell] - \tilde{\mathbf{u}}^H(\omega,\theta,\ell)\tilde{\mathbf{z}}_{\text{rd-st}}(\omega,\theta,\ell)\right|^2\right\} \\ + \mathrm{Re}\{\lambda_{\mathrm{L}}^*(\tilde{\mathbf{u}}^H(\omega,\theta,\ell)\mathbf{T}_{\mathrm{st}}^H(\omega,\theta)\mathbf{R}_{\text{rd-st,canc}}(\omega,\theta,\ell)\mathbf{c}_{\mathrm{st}}(\omega,\theta) - g[\omega,\omega,\theta,\theta,\ell])\}\end{aligned} \tag{3.101}$$

using the data vector from (3.93). The constrained filter is straightforward to obtained by solving the Lagrange multiplier using a similar approach shown in (2.31) - (2.35) from the previous chapter. Performing the procedure and mapping to full dimension produces the filter

$$\mathbf{u}_{\text{RD-MMSE,con}}(\omega,\theta,\ell) = \frac{g[\omega,\omega,\theta,\theta,\ell]\mathbf{Q}_{\text{rd-st}}(\omega,\theta,\ell)\mathbf{R}_{\text{rd-st,canc}}(\omega,\theta,\ell)\mathbf{c}_{\mathrm{st}}(\omega,\theta)}{\mathbf{c}_{\mathrm{st}}^H(\omega,\theta)\mathbf{R}_{\text{rd-st,canc}}(\omega,\theta,\ell)\mathbf{Q}_{\text{rd-st}}(\omega,\theta,\ell)\mathbf{R}_{\text{rd-st,canc}}(\ell)\mathbf{c}_{\mathrm{st}}(\omega,\theta)}. \tag{3.102}$$

Beamspoiling is obtained using (3.84)

$$\mathbf{u}_{\text{RD-MMSE,beam}}(\omega,\theta,\ell) = \frac{\sqrt{K_{\mathrm{D}}K_{\mathrm{A}}}\sum\limits_{\omega_k=-\Omega_K}^{\Omega_K}\sum\limits_{\theta_k=-\Theta_K}^{\Theta_K}\mathbf{u}_{\text{RD-MMSE,con}}(\omega+\omega_k,\theta+\theta_k,\ell)\,\mathbf{c}_{\mathrm{st}}^H(\omega+\omega_k,\theta+\theta_k)\,\mathbf{c}_{\mathrm{st}}(\omega,\theta)}{\sum\limits_{\omega_k=-\Omega_k}^{\Omega_K}\sum\limits_{k_{\mathrm{A}}=-\Theta_K}^{\Theta_K}\mathbf{c}_{\mathrm{st}}^H(\omega+\omega_k,\theta+\theta_k)\,\mathbf{c}_{\mathrm{st}}(\omega,\theta)}. \tag{3.103}$$

The application of the filter produces the following angle-Doppler response

$$\hat{x}_{\text{RD-MMSE,beam}}\left[\omega,\theta,\ell\right] = \mathbf{u}^{H}_{\text{RD-MMSE,beam}}\left(\omega,\theta,\ell\right)\widehat{\mathbf{z}}_{\text{rd-st}}\left(\omega,\theta,\ell\right). \tag{3.104}$$

The PAMADE procedure follows closely to the AMADE. PAMADE procedure initializes by applying the partial adaptive STAP filter to the receive data to form the initial $L_{\text{D}}L_{\text{A}} \times 1$ angle-Doppler estimate corresponding to ω and θ under test

$$\hat{\mathbf{r}}_{\text{PAMADE},0}\left(\omega,\theta,\ell\right) = \mathbf{U}^{H}_{\text{AD}}\hat{\mathbf{R}}_{\text{rd-st,canc}}\left(\omega,\theta,\ell\right)\mathbf{z}_{\text{st}}\left(\ell\right) \tag{3.105}$$

where clutter cancellation uses an estimation of the cancellation matrix within (3.20). The first iteration begins by forming the *i*th angle-Doppler power distribution matrix using a previous angle-Doppler estimate

$$\hat{\mathbf{P}}_{\text{PAMADE},i}\left(\omega,\theta,\ell\right) = \hat{\mathbf{r}}_{\text{PAMADE},i-1}\left(\omega,\theta,\ell\right)\hat{\mathbf{r}}^{H}_{\text{PAMADE},i-1}\left(\omega,\theta,\ell\right) \odot \mathbf{I}_{L_{\text{D}}L_{\text{A}}\times L_{\text{D}}L_{\text{A}}}. \tag{3.106}$$

Next, the reduced-rank StCM is formed using the current estimate of the power distribution matrix

$$\begin{aligned}\tilde{\mathbf{Q}}_{\text{PAMADE},i}\left(\omega,\theta,\ell\right) = {} & \mathbf{T}^{H}_{\text{st}}\left(\omega,\theta\right)\hat{\mathbf{R}}_{\text{rd-st,canc}}\left(\omega,\theta,\ell\right)\mathbf{C}_{\text{st}}\hat{\mathbf{P}}_{\text{PAMADE},i}\left(\omega,\theta,\ell\right)\mathbf{C}^{H}_{\text{st}}\hat{\mathbf{R}}_{\text{rd-st,canc}}\left(\omega,\theta,\ell\right)\mathbf{T}_{\text{st}}\left(\omega,\theta\right) \\ & \odot\left(\sigma^{2}_{\text{err}}\mathbf{I}_{D_{\text{t}}D_{\text{s}}\times D_{\text{t}}D_{\text{s}}} + \mathbf{1}_{D_{\text{t}}D_{\text{s}}\times D_{\text{t}}D_{\text{s}}}\right) + \sigma^{2}_{\text{v}}\mathbf{I}_{D_{\text{t}}D_{\text{s}}\times D_{\text{t}}D_{\text{s}}}.\end{aligned} \tag{3.107}$$

The matrix is then mapped to the full dimension for filter formation

$$\hat{\mathbf{Q}}_{\text{PAMADE},i}\left(\omega,\theta,\ell\right) = \mathbf{T}_{\text{st}}\left(\omega,\theta\right)\tilde{\mathbf{Q}}^{-1}_{\text{PAMADE},i}\left(\omega,\theta,\ell\right)\mathbf{T}^{H}_{\text{st}}\left(\omega,\theta\right). \tag{3.108}$$

The estimated PAMADE filter is formed

$$\hat{\mathbf{u}}_{\text{PAMADE,con},i}(\omega,\theta,\ell) = \frac{\hat{g}[\omega,\omega,\theta,\theta,\ell]\hat{\mathbf{Q}}_{\text{PAMADE},i}(\omega,\theta,\ell)\hat{\mathbf{R}}_{\text{rd-st,canc}}(\omega,\theta,\ell)\mathbf{c}_{\text{st}}(\omega,\theta)}{\mathbf{c}_{\text{st}}^{H}(\omega,\theta)\hat{\mathbf{R}}_{\text{rd-st,canc}}(\omega,\theta,\ell)\hat{\mathbf{Q}}_{\text{PAMADE},i}(\omega,\theta,\ell)\hat{\mathbf{R}}_{\text{rd-st,canc}}(\ell)\mathbf{c}_{\text{st}}(\omega,\theta)} \tag{3.109}$$

where $\hat{g}[\omega,\omega,\theta,\theta,\ell]$ is formed using (3.67) and the estimated cancellation matrix. Filters are then formed for the extent of the oversampling beyond the current angle-Doppler under test. After all the filters have been formed, beamspoiling is performed

$$\hat{\mathbf{u}}_{\text{PAMADE,beam}}(\omega,\theta,\ell) = \frac{\sqrt{K_{\text{D}}K_{\text{A}}}\sum\limits_{\omega_k=-\Omega_K}^{\Omega_K}\sum\limits_{\theta_k=-\Theta_K}^{\Theta_K}\hat{\mathbf{u}}_{\text{PAMADE,con}}(\omega+\omega_k,\theta+\theta_k,\ell)\,\mathbf{c}_{\text{st}}^{H}(\omega+\omega_k,\theta+\theta_k)\,\mathbf{c}_{\text{st}}(\omega,\theta)}{\sum\limits_{\omega_k=-\Omega_k}^{\Omega_K}\sum\limits_{k_{\text{A}}=-\Theta_K}^{\Theta_K}\mathbf{c}_{\text{st}}^{H}(\omega+\omega_k,\theta+\theta_k)\,\mathbf{c}_{\text{st}}(\omega,\theta)}. \tag{3.110}$$

The $MN\times 1$ filter is subsequently applied to the space-time receive data to obtain the updated estimate of the angle-Doppler frequency

$$\hat{x}_{\text{PAMADE},i}(\omega,\theta,\ell) = \hat{\mathbf{u}}_{\text{PAMADE,beam},i}^{H}(\omega,\theta,\ell)\,\hat{\mathbf{R}}_{\text{rd-st,canc}}(\omega,\theta,\ell)\,\mathbf{z}_{\text{st}}(\ell). \tag{3.111}$$

The procedure is performed for each angle-Doppler frequency to produce a filter that is populated into a $MN\times L_{\text{D}}L_{\text{A}}$ filter bank. Once each filter in the bank has been formed, the updated angle-Doppler estimate is formed

$$\hat{\mathbf{r}}_{\text{PAMADE},i}(\omega,\theta,\ell) = \mathbf{U}_{\text{AD}}^{H}\hat{\mathbf{R}}_{\text{rd-st,canc}}(\omega,\theta,\ell)\,\mathbf{z}_{\text{st}}(\ell). \tag{3.112}$$

The procedure returns to (3.106) and concludes after a user-defined number of iterations. The estimation portion of the angle-Doppler techniques operate per range gate and, therefore, the number of range gates is not a leading factor in estimation performance. However, the number of range gates do drive computation time. Cancellation is driven by number of range gates for adequate training of the estimation of the cancellation covariance matrix.

3.7 Simulation Results

The proposed approaches are examined using the average sidelobe response (ASR), average loss factor (ALF), and total residual sidelobe response (TRSR) metrics. ASR examines the sidelobe structure of the responses following estimation. ALF examines the inherent mismatch loss and minimum detectable Doppler (MDD) when sequential estimation- then-cancellation is performed. Lastly, TRSR examines the aggregate suppression of the sidelobes. The metrics are examined using Monte Carlo simulations for 1000 trials. Details about movers and clutter parameters are specified under each analysis. Movers are fixed for each trial. New instantiations of clutter and noise are generated each trial.

For each metric, a LFM waveform with a $B\tau = 150$ is implemented. The radar datacube consist of $M = 32$ pulses in a CPI, $N = 5$ antenna elements in a ULA, and $L = 300$ range samples. The platform motion, which is characterized by the interelement spacing transvered in a PRI, is set to $\beta = 1$. The Doppler and spatial spectrums are oversampled by $K_{\mathrm{D}} = 5$ and $K_{\mathrm{A}} = 5$, respectively. Tapering is performed in slow-time only using a Taylor window with -50 dB peak sidelobe and five nearly constant sidelobes. AMADE and PAMADE perform 10 adaptive iterations. Rank reduction will vary from the maximum reduction of $D_{\mathrm{t}} = 3$ to the minimum reduction of $D_{\mathrm{t}} = 31$. A high SNR of 70 dB after pulse compression gain is set to show the sidelobe suppression limitations relative to the noise floor. Practical implementation of the approaches are presented in Section 3.8 within the experimental results.

3.7.1 Average sidelobe response

Average sidelobe response considers the average power spectral density of the angle-Doppler spectrum. The signal vector consist of a single point scatterer at zero-Doppler $\omega_{\mathrm{mov}} = 0$ and boresight $\theta_{\mathrm{mov}} = 0$ with unit amplitude $\bar{x}[\omega_{\mathrm{mov}}, \theta_{\mathrm{mov}}, \ell] = 1$ following pulse compression

$$\mathbf{z}_{\mathrm{st}}(\ell) = \bar{x}[\omega_{\mathrm{mov}}, \theta_{\mathrm{mov}}, \ell]\, \mathbf{c}_{\mathrm{st}}(\omega_{\mathrm{mov}}, \theta_{\mathrm{mov}}) + \mathbf{v}_{\mathrm{st}}(\ell). \tag{3.113}$$

The ASR is the expectation of the estimate of the power spectrum over Monte Carlo trials

$$\mathrm{ASR}_p(\omega,\theta,\ell) = E\left\{\left|\mathbf{u}_p^H(\omega,\theta)\,\mathbf{z}_{\mathrm{t}}(\ell)\right|^2\right\} \tag{3.114}$$

where $p \in$ [ADP, WADP, LS, RRLS, AMADE, PAMADE] denote standard angle-Doppler processing, windowed angle-Doppler processing, RRLS, AMADE, and PAMADE, respectively. The responses are peak-normalized for a one-to-one comparison. The mismatch loss that occurs with the response is presented in the next subsection.

The analysis begins with the spatial CUT of ASR at boresight for the full dimension techniques in Figure 3.7 and their respective angle-Doppler responses in Fig. 3.8. The standard angle-Doppler response produces the well-known sinc-like response in Doppler with a known peak sidelobe of approximately -13 dB. Tapering is able to suppress the sidelobes below the -50 dB (set for the windowing function) while having the well-known unfavorable widening of the mainlobe. Note there exist other windowing functions (such as Tukey, Blackmon, Hamming, or Hanning) that provide different sidelobe responses. Each have some form of mainlobe widening. LS provides a middle ground between windowing and standard angle-Doppler processing. LS provides a modest improvement with a peak sidelobe of -19.75 dB while maintaining the nominal resolution. LS would be a favorable approach if maintaining the nominal resolution with a non-adaptive filter is desired. AMADE suppresses the sidelobes to the noise floor while maintaining resolution. The approaches angle-Doppler response are consistent with the Doppler CUT. Tapering is performed in Doppler only so the mainlobe and sidelobe structure are unaffected spatially. Although, windowing is applicable spatially. The AMADE shows a less suppression performance in the spatial sidelobes which is caused by the incorporation of beamspoiling. Overall, The full dimension results show that optimal and adaptive mismatch approaches are applicable with space-time signals.

Figure 3.9 shows a spatial CUT of ASR at boresight comparing LS and different reductions of RRLS. The angle-Doppler responses are presented in Fig. 3.10. Minimizing the LS cost function in the reduce dimension subspace provides a robust response comparable to the full dimension LS

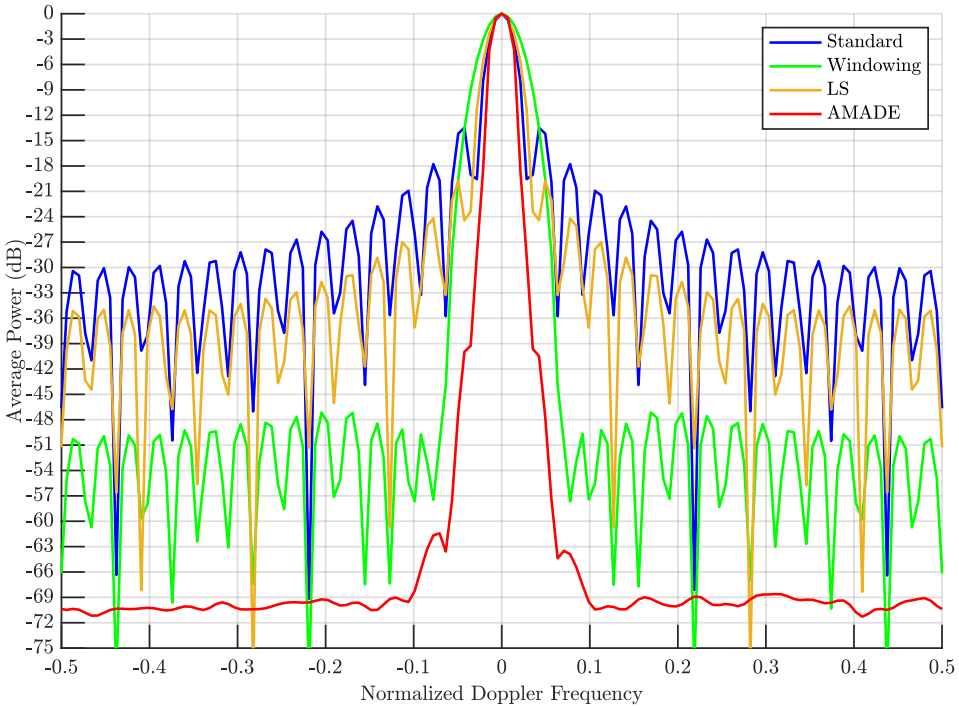

Fig. 3.7: Average sidelobe response at boresight for full dimension angle-Doppler processing techniques

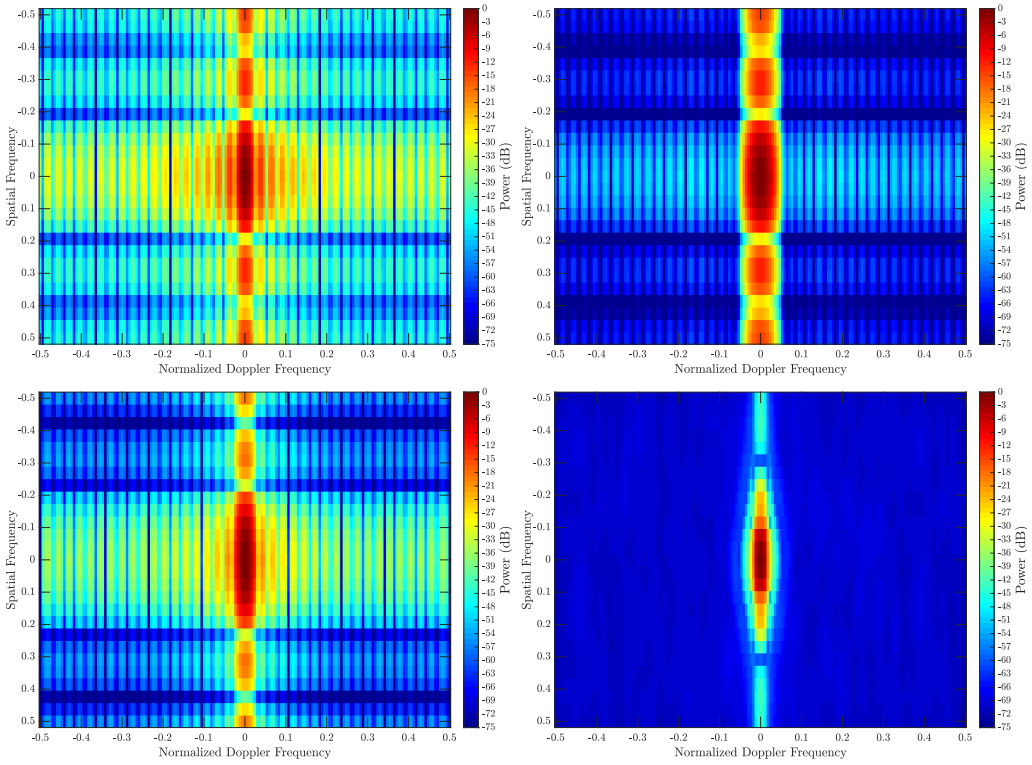

Fig. 3.8: Angle-Doppler responses for angle-Doppler processing (top left), windowed angle-Doppler processing (top right), least-squares (bottom left), and AMADE (bottom right)

approach. At the lowest rank reduction for $D_t = 3$, the peak sidelobe is -15 dB. At amounts $D_t = 7$ and $D_t = 11$, the reduce dimension approaches effectively match the full dimension performance. The performance loss as the reduction increases is effectively negligible. Lastly, Fig. 3.11 presents the full and partial adaptive mismatch estimation for various reduction amounts. The angle-Doppler responses for full and partial adaptive adaptation are shown in Fig. 3.12. The response provides a robust sidelobe suppression in compassion to the full rank approach. At $D_t = 3$, the performance begins to degrade compared to AMADE. Compared to standard angle-Doppler processing, PAMADE at $D_t = 3$ provides a significant improvement in the sidelobe albeit not as good as when $D_t \geq 7$.

The robust performance of RRLS and PAMADE at low rank reduction reinforces the notion that a small number of degrees-of-freedom are necessary to obtain robust solution due to the sinc-like structure in angle-Doppler. The reduce rank approaches are optimized in the Doppler spectrum and element-space. Unlike the full rank approaches which are optimized in slow-time and element-space. When the reduction is below the oversampling factor, the performance of the reduce rank approaches diminish since only a fraction of the Doppler mainlobe is captured for processing. Note this approach was tested in the element-space post-Doppler rank reduction approach and should be taken into consideration for other reduction approaches. Additionally, the partial adaptive approaches are robust in their suppression capabilities in comparison to the full rank counterparts.

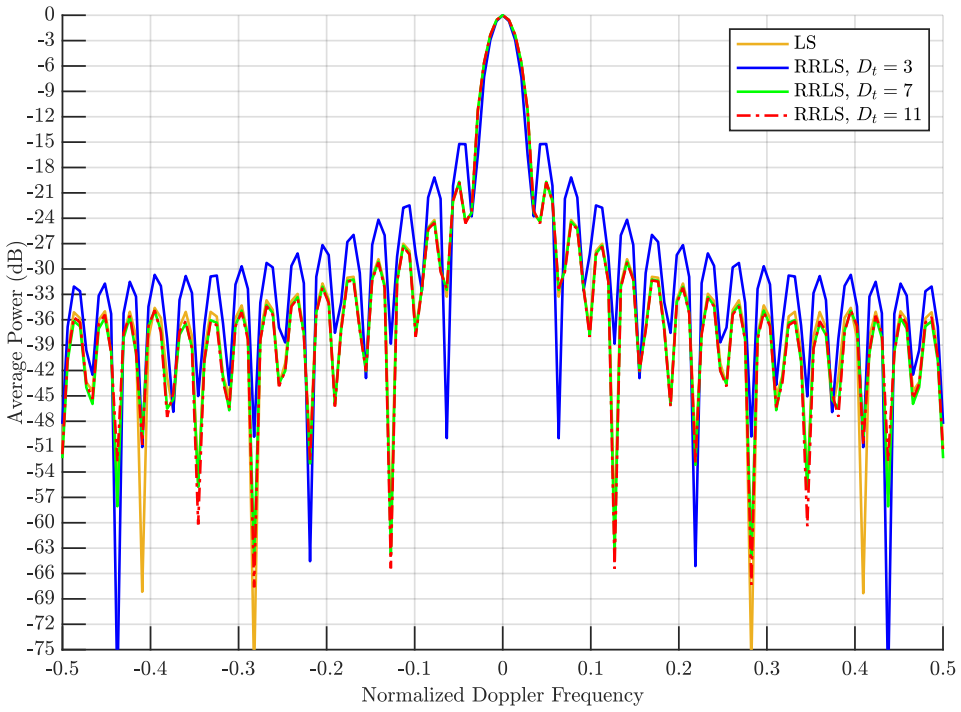

Fig. 3.9: Average sidelobe response at boresight for full and reduce rank LS techniques

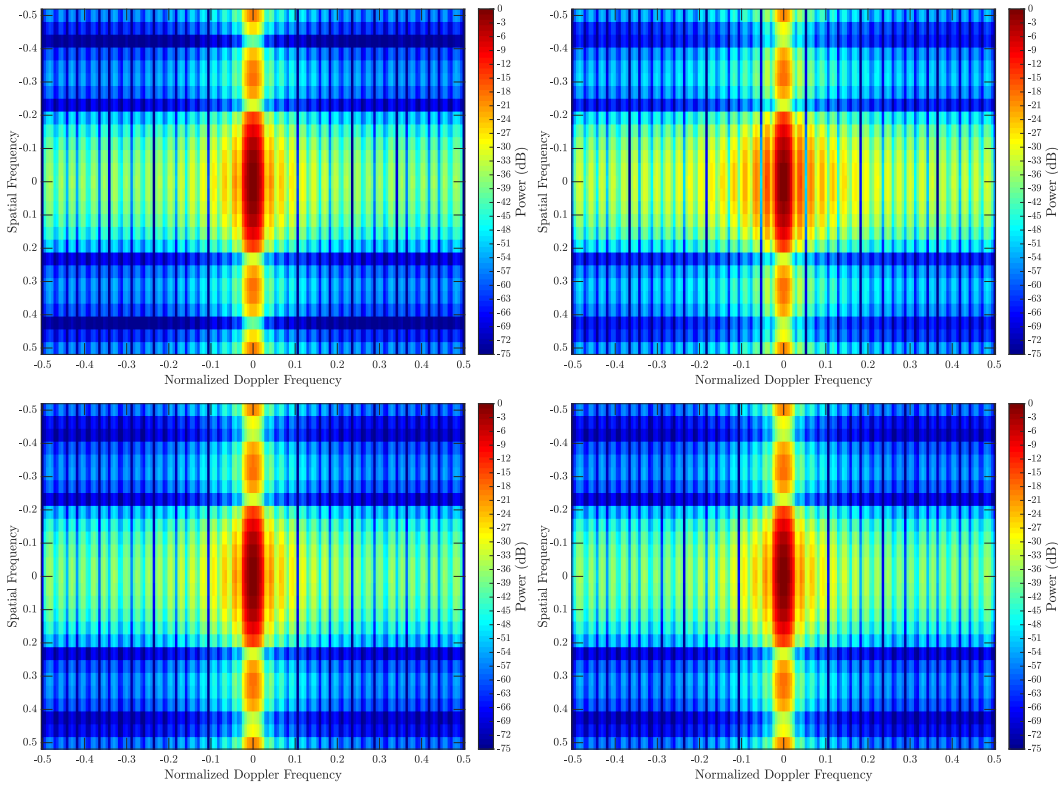

Fig. 3.10: Average sidelobe response at boresight for full rank LS (top left) and reduce rank LS techniques at $D_{\mathrm{t}} = 3$ (top right), $D_{\mathrm{t}} = 7$ (bottom left), $D_{\mathrm{t}} = 11$ (bottom left)

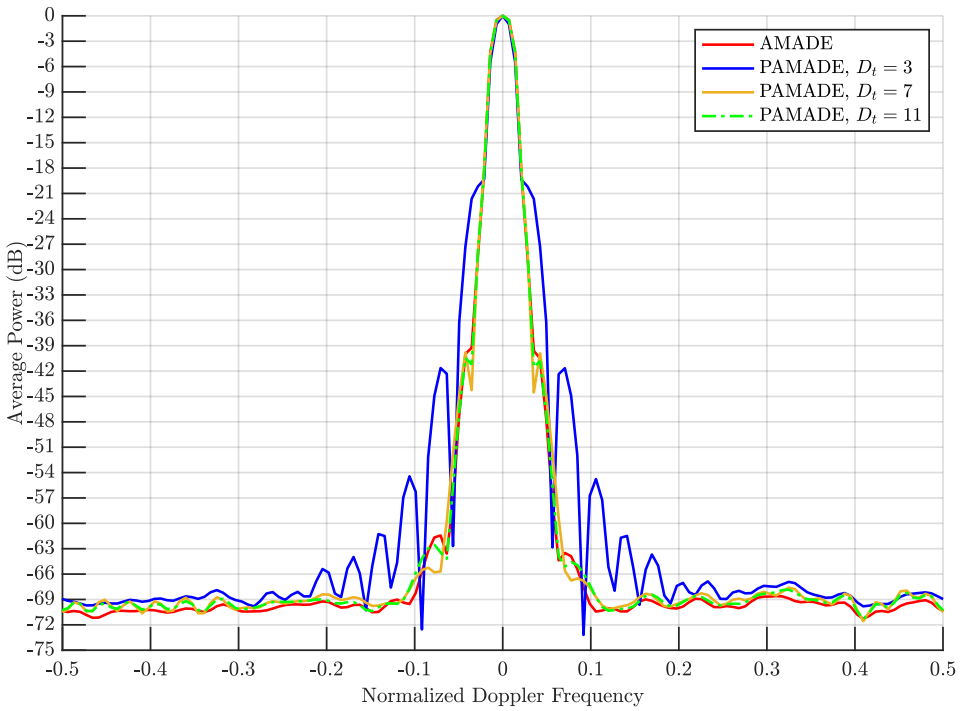

Fig. 3.11: Average sidelobe response at boresight for AMADE and PAMADE techniques

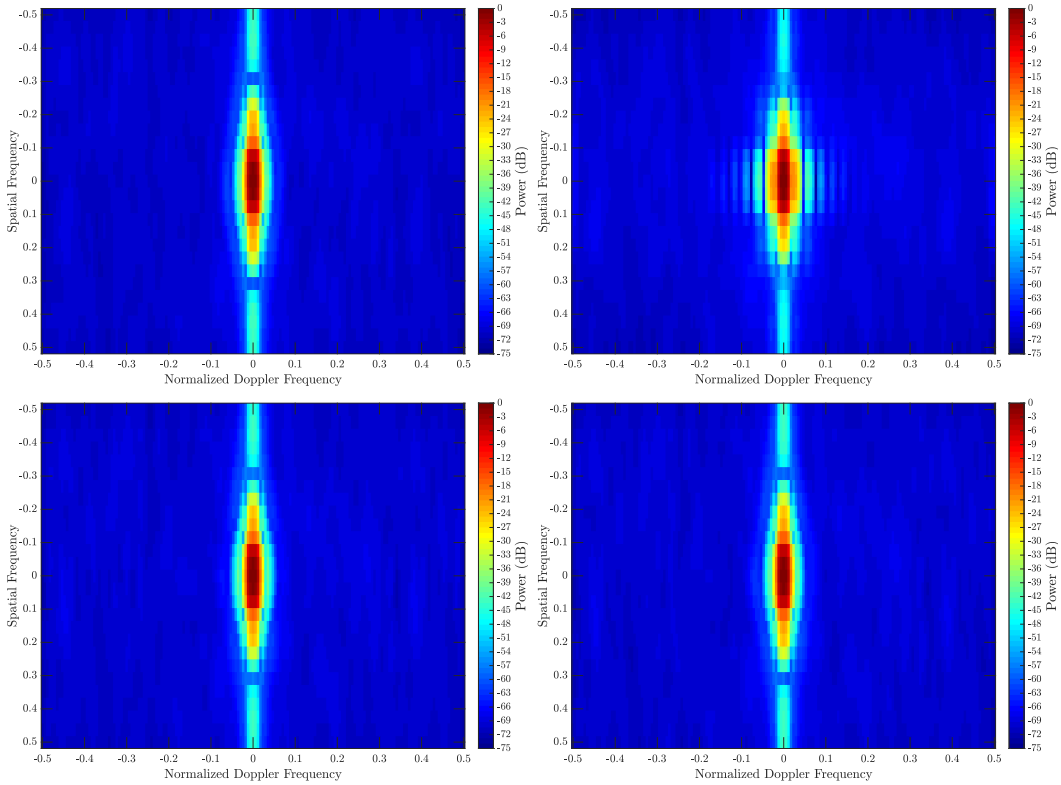

Fig. 3.12: Average sidelobe response at boresight for AMADE (top left) and PAMADE at $D_{\mathrm{t}} = 3$ (top right), $D_{\mathrm{t}} = 7$ (bottom left), $D_{\mathrm{t}} = 11$ (bottom left)

3.7.2 Average Loss Factor

The SNR-normalized SINR metric from [32] and used within the previous chapter is implemented for ALF. The loss factor for angle-Doppler processing considers the following signal model

$$\mathbf{z}_{\text{st}}(\ell) = \sum_{\omega_{\text{clu}}} \sum_{\theta_{\text{clu}}} \bar{x}(\omega_{\text{clu}}, \theta_{\text{clu}}, \ell)\, \mathbf{c}_{\text{st}}(\omega_{\text{clu}}, \theta_{\text{clu}}) + \mathbf{v}_{\text{st}}(\ell). \tag{3.115}$$

Homogeneous clutter is generated using multiple point scatterers based on statistically independent clutter patches (see 1.11). One hundred clutter scatterers are uniformly distributed over a normalized Doppler and shifted spatially based on relationship $\omega = \beta\theta$. The average clutter-to-noise (CNR) set to 70 dB. For clutter cancellation, the space-time data vectors samples used to generate the clutter in the range sample bin is preserved for formation of the optimal cancellation matrix. The optimal cancellation matrix provides a bound on performance since full knowledge of the clutter in the range CUT is known. Standard, windowed, optimal, and adaptive angle-Doppler processing are examined under optimal clutter cancellation.

The loss factor is the ratio of SINR to SNR

$$\eta_p(\omega, \theta, \ell) = \frac{\text{SINR}_p(\omega, \theta, \ell)}{\text{SNR}_p(\omega, \theta, \ell)} = \frac{\sigma_{\text{v}}^2 \left\| \mathbf{R}_{\text{st,canc}}^{-1}(\ell)\, \mathbf{u}_p(\omega, \theta, \ell) \right\|^2}{\mathbf{u}_p^H(\omega, \theta, \ell)\, \mathbf{R}_{\text{t,canc}}^{-1}(\ell)\, \mathbf{u}_p(\omega, \theta, \ell)}. \tag{3.116}$$

The ALF is the expectation over Monte Carlo trials

$$\text{ALF}_p(\omega, \theta, \ell) = E\left\{ \eta_p(\omega, \theta, \ell) \right\}. \tag{3.117}$$

Outside the clutter notch, a ALF response less than 0 dB shows the mismatch loss incurred by the estimation approach. Inside the clutter notch, the ALF presents the MDD. MDD describes the closet Doppler frequency to zero that can be attained before a predetermined SINR loss γ_{MDD} in

the clutter notch. The MDD using ALF is

$$\text{MDD}_p(\theta,\ell) = \frac{1}{2}\left(\underset{\omega_U}{\text{argmin}}\{|\text{ALF}_p(\omega_U,\theta,\ell) - \gamma_{\text{MDD}}|^2\} - \underset{\omega_L}{\text{argmin}}\{|\text{ALF}_p(\omega_L,\theta,\ell) - \gamma_{\text{MDD}}|^2\}\right). \tag{3.118}$$

where defines $\omega_L \in \Omega_L$ for the set of normalized Doppler frequencies from -0.5 to 0, $\omega_L \in \Omega_U$ for a set of frequencies from 0 to 0.5, and γ_{MDD} is a predetermined SINR loss attributed to clutter cancellation. For the following results, the spatial frequency is set to boresight. For visual depiction of MDD see Figure 2.16 from the previous chapter.

In Figure 3.13, the loss factor is presented for the full dimension approaches. AMADE incurs minor mismatch loss from the optimal SINR presented in the blue trace. LS incurs an approximately 1 dB loss from the optimal SINR. AMADE and LS each incur a dip in the spectrum at ± 0.5. This is due to the examination region being from ± 0.5. To avoid this response, examining the response beyond ± 0.5 such that the filter wraps around the aliased regions. AMADE and LS maintain the MDD at -3 dB.

Figures 3.14 and 3.15 present ALF for RRLS and PAMADE, respectively. At the highest rank reduction amounts, the approaches incur minor loss from the the full rank approaches. As the reduces decreases, more mismatch loss is incurred. For RRLS, the results hit a limit of approximately -1.5 dB (excluding the edge effect). The reduce rank of the optimal and adaptive

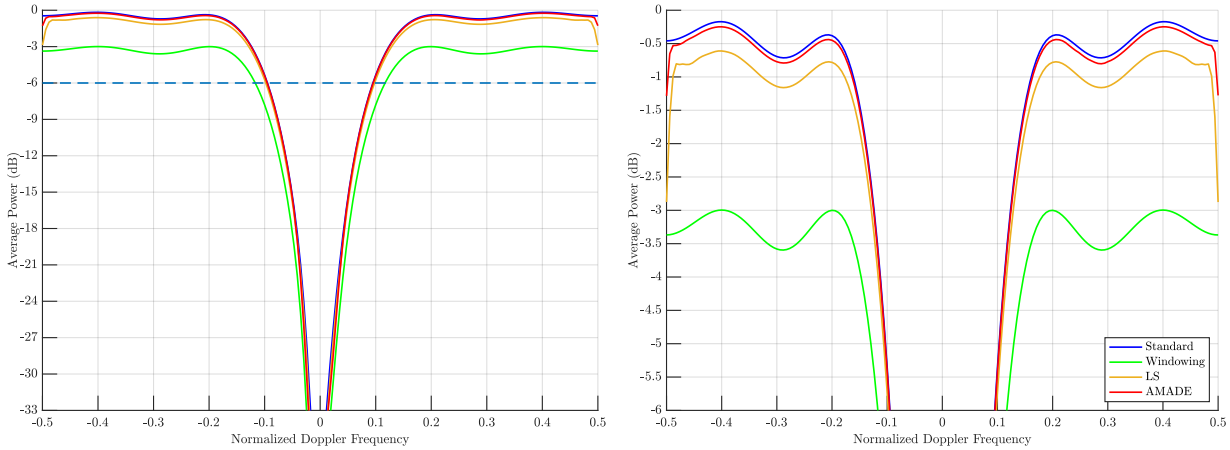

Fig. 3.13: Average loss factor at boresight for full dimension angle-Doppler processing techniques; Zoomed out (left) and zoomed in above -6 dB (right)

approaches are able to maintain the MDD. Overall, the optimal and adaptive approaches have a minor effect on the performance of cancellation.

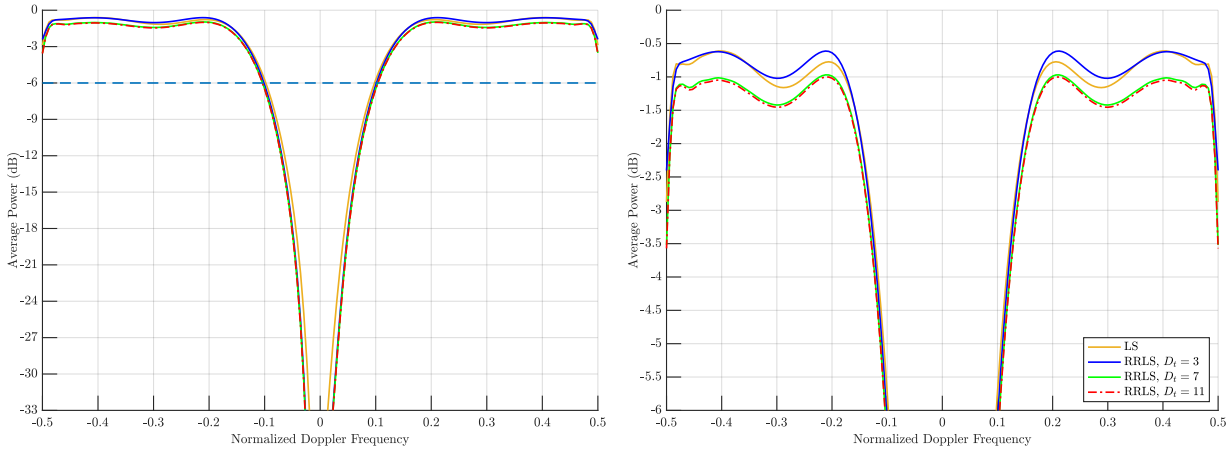

Fig. 3.14: Average loss factor at boresight for full and reduce rank LS techniques; Zoomed out (left) and zoomed in above -6 dB (right)

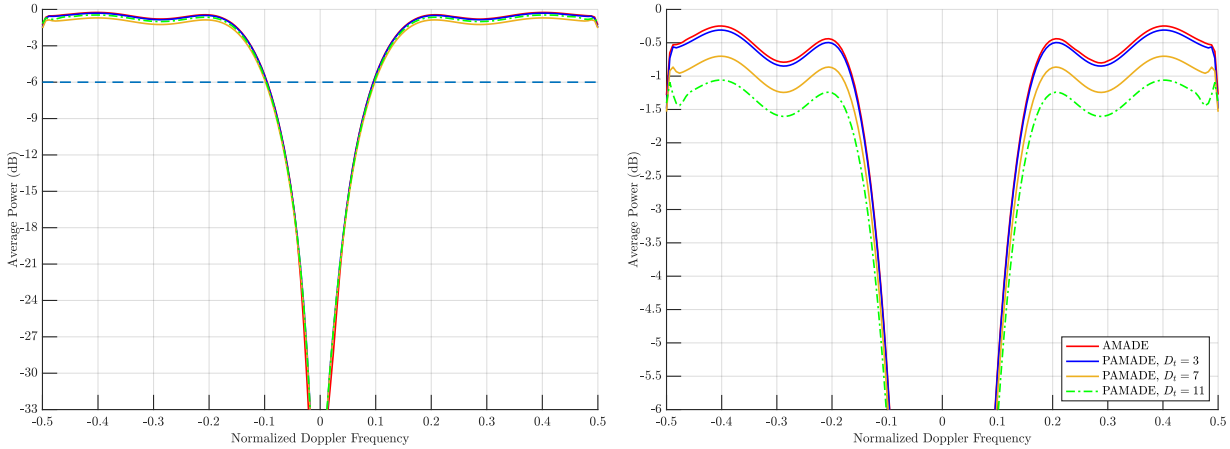

Fig. 3.15: Average loss factor at boresight for AMADE and PAMADE techniques; Zoomed out (left) and zoomed in above -6 dB (right)

3.7.3 Total Residual Sidelobe Response

The last analysis examines the aggregate sidelobe power after angle-Doppler processing. The analysis considers a receive signal model containing a single mover in clutter

$$\mathbf{z}_{\text{st}}(\ell) = \begin{cases} \bar{x}[\omega_{\text{mov}}, \theta_{\text{mov}}, \ell_{\text{mov}}]\, \mathbf{c}_{\text{st}}(\omega_{\text{mov}}, \theta_{\text{mov}}) + \sum\limits_{\omega_{\text{clu}} \in \Omega_{\text{clu}}} \bar{x}[\omega_{\text{clu}}, \theta_{\text{clut}}, \ell_{\text{clu}}]\, \mathbf{c}_{\text{st}}(\omega_{\text{clu}}, \theta_{\text{clu}}) + \mathbf{v}_{\text{st}}(\ell) & \text{for } \ell_{\text{mov}} = \ell \\ \sum\limits_{\omega_{\text{clu}} \in \Omega_{\text{clu}}} \bar{x}[\omega_{\text{clu}}, \theta_{\text{clu}}, \ell_{\text{clu}}]\, \mathbf{c}_{\text{st}}(\omega_{\text{clu}}, \theta_{\text{clut}}) + \mathbf{v}_{\text{st}}(\ell) & \text{otherwise,} \end{cases} \tag{3.119}$$

The target is place in the center range bin in the radar datacube with a $\omega_{\text{mov}} = 0.8$ at boresight with SNR = 70 dB. The clutter is generated similar to the previous section by using homogeneous clutter patches uniformly distribution over a normalized Doppler bandwidth of 0.0001 centered at zero Doppler and an average CNR of 50 dB. Clutter cancellation considers optimal cancellation. The TRSR metric without cancellation is

$$\text{TRSR}_p(\ell) = \frac{\sum\limits_{\omega \in \Omega} \sum\limits_{\theta \in \Theta} \left| \mathbf{u}_p^H(\omega, \theta)\, \mathbf{z}_{\text{st}}(\ell) \right|^2}{\max\limits_{\theta} \left\{ \max\limits_{\omega} \left\{ \left| \mathbf{u}_{\text{DP}}^H(\omega, \theta)\, \mathbf{z}_{\text{st}}(\ell) \right|^2 \right\} \right\}} \tag{3.120}$$

where $p \in$ [ADP, WADP, LS, RRLS, AMADE, PAMADE] to denote the different processing techniques. When cancellation is performed, $\mathbf{z}_{\text{st}}(\ell)$ is replaced by $\widehat{\mathbf{z}}_{\text{st}}(\ell)$. The set Ω and Θ omits frequencies corresponding to the nominal angle-Doppler mainlobe resolution of the mover and clutter angle-Doppler bandwidth. Tables 3.1 presents the TRSR for the full and reduced dimension approaches without clutter cancellation. The results differ from the previous chapter since aliased portions of the Doppler spectrum were examined. The RRLS have a fractional difference from full rank LS as the reduction amount differs. For PAMADE, the suppression performance decreases by a little under 4 dB as the rank decreases. When cancellation is introduced, as shown in Table 3.2, the approaches improve in their suppression benefits.

Table 3.1: Total Residual Sidelobe Response for various angle-Doppler processing approaches without clutter cancellation in dB

Approach	Full rank	Reduced Rank							
		$D_t = 3$	$D_t = 7$	$D_t = 11$	$D_t = 15$	$D_t = 19$	$D_t = 23$	$D_t = 27$	$D_t = 31$
Standard	-13.50								
Window	-12.16								
Optimal (LS / RRLS)	-13.54	-13.22	-13.19	-13.18	-13.18	-13.18	-13.18	-13.18	-13.18
Adaptive (AMADE / PAMADE)	-32.47	-26.35	-29.98	-30.65	-31.06	-31.46	-31.72	-31.92	-32.02

Table 3.2: Total Residual Sidelobe Response for various angle-Doppler processing approaches with clutter cancellation in dB

Approach	Full rank	Reduced Rank							
		$D_t = 3$	$D_t = 7$	$D_t = 11$	$D_t = 15$	$D_t = 19$	$D_t = 23$	$D_t = 27$	$D_t = 31$
Standard	-26.15								
Window	-24.62								
Optimal (LS / RRLS)	-30.07	-26.68	-29.85	-30.01	-29.97	-29.97	-29.94	-29.94	-29.90
Adaptive (AMADE / PAMADE)	-61.54	-55.64	-59.66	-59.32	-59.37	-59.40	-59.31	-59.21	-59.22

3.8 Airborne Open-Air Experimental Results

The matched and mismatch processing algorithms are examined using the GOTCHA airborne radar dataset from the Synthetic Aperture Radar (SAR) Based GMTI in Urban Environment Challenge by Air Force Research Laboratory Layered Sensing Exploitation Division (AFRL/RYA) [5]. SAR uses the motion of a radar to generate high resolution images. Each pulse transmission is at a different spatial location. By accounting for time delays in the flight path, each pulse can be considered as propagating from a different "antenna element" thereby creating the synthetic aperture [131]. Incorporating multiple receive antennas for SAR enables the simultaneous implementation of SAR and GMTI. The latter of which is most pertinent to the proposed algorithms. The authors in [5] outlined five potential research areas related to detection, geolocation, and tracking for the challenge. The first four research areas address SAR related challenges. The final challenge was to "go out and do great things with the data...". With that in mind, the dataset is leveraged as a proof-of-concept for sequential cancellation-then-estimation using mismatch estimation in GMTI radars.

The airborne radar operated at X-band with a PRF of 2.1 kHz. Mounted on the platform were

three phase centers (used as array elements) which collected radar reflections over hundreds of thousands of pulses. SAR uses thousands of pulses to obtain the high-quality images. Only a fraction of the pulses is needed for GMTI. The number of range gates available for processing is 384 range gates. The range gates were segmented to focused on scatterers. The final radar datacube used for analysis is $L = 200$ range samples, $M = 32$ pulses in a CPI, and $N = 3$ phase centers in an array.

The processing techniques are presented using range-Doppler maps at multiple receive beam positions. The number of degree-of-freedom for angle-Doppler processing is $MN = 96$. The Doppler spectrum is oversampled by a factor of $K_{\mathrm{D}} = 5$ for a total of $L_{\mathrm{D}} = 161$ Doppler frequencies in the spectrum. The spatial spectrum is not oversampled making $K_{\mathrm{A}} = 1$. Three beam positions are examined: $\theta = -1/3, 0, 1/3$. The spatial steering vectors are formed assuming equidistant phase centers since the distance between the phase centers were unavailable. Figure 3.16 presents the beampatterns for the receive beamformers used. The different beams were selected such that each receive beam mainlobe is the spatial null of the others. The noise power after pulse compression was measured to approximately -95 dB. The noise power was determined by examining a region of the range-Doppler map from the STAP results shown later where targets were not localized. AMADE and PAMADE used an error power equal to the noise power and concluded their procedures after 10 iterations. The diagonal loading for the LS and RRLS approaches were set to the noise power. RRLS and PAMADE were reduced the processing by 84% to $D_{\mathrm{t}} = 5$ such that the number of degree-of-freedom for angle-Doppler processing became $D_{\mathrm{t}}N = 15$. A taper is implemented in slow-time only using a Taylor window with -50 dB peak sidelobe and five nearly constant sidelobes.

The SaCM for adaptive cancellation omitted the range CUT and 5 guard cells on each side of the CUT prior to collecting training samples. The first 12 range samples after guard cells are used for covariance estimation for a total of $L_{\mathrm{p}} = .25MN = 24$ training samples which is low sample support. When less than 12 samples are available on any side of a CUT, an asymmetric number of samples are used on each side of the CUT such that the number of training samples is maintained.

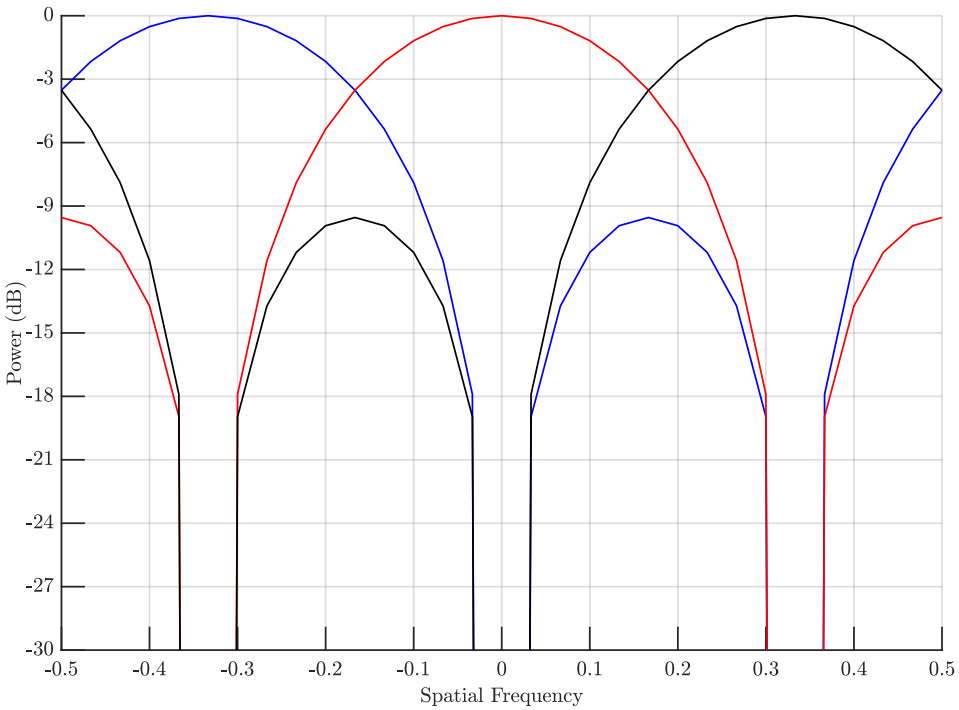

Fig. 3.16: Beampattern of the three receive beams at $\theta = -1/3$ (blue), $\theta = 0$ (red), and $\theta = 1/3$ (black)

The analysis begins with the range-Doppler map of angle-Doppler processing in Figure 3.17. There are characteristics within the data that each receive beam presents. At $\theta = -1/3$, a mover is present at approximately the 20th range bin and $\omega = -0.35$ that subsides in the other beams. Similarly, at $\theta = 0$, multiple movers are present between range bins 140 to 180 at $\omega = 0.3$ that subsides in the other beams. Each beam has a clutter ridge shifted from zero-Doppler to approximately $\omega = 0.1$ with the final beam at $\theta = 1/3$ having the strongest clutter response. The Doppler sidelobes from clutter and movers is present throughout the dataset. In some cases, such as range bin 180, the sidelobe spread is high for all the Doppler frequencies. Implementing STAP on the data, as shown in Fig. 3.18, the clutter ridge within each beam is removed. What remains within the dataset is Doppler sidelobes from movers within the scene and residue including the high sidelobe responses matched processing cannot diminish.

The mismatch approaches will be presented after clutter cancellation only. STAP using a Taylor window is presented in Fig. 3.19. As expected, tapering does well with reducing Doppler sidelobes

in comparison to matched processing at the expense of a widening mainlobe. The dynamic range of the dataset does allow for tapering to suppress the Doppler sidelobes to the noise floor. Figure 3.20 presents the results for combined cancellation and LS. Optimal mismatch processing provides a middle ground between windowing and tapering for sidelobe suppression while maintaining resolution. Although the sidelobes have not been reduced to the noise floor completely, some reduction in the sidelobes provides a finer range-Doppler which would be benefit for detection processing. Maintaining the resolution while providing modest sidelobes suppression is a key attribute of optimal mismatch processing. Optimal mismatch processing sidelobe suppression is limited by the unity gain normalization in the filter. Varying the oversampling factor or the diagonal loading did not provide an increase in performance suppression.

In Figure 3.21, AMADE applied to the measured data. The resolution benefits of AMADE for the movers is prevalent. Additionally, AMADE provides significant visibility improvement by reducing the sidelobe response to the noise floor. There is an inherent signal loss when implementing AMADE that is attributed to two causes. First, since sidelobes are optimally removed from a given range bin, the energy being contributed there reduces leading a reduction in the perceived signal strength. Overall, this signal reduction peaks at the truth target signal power. Second, the beamspoiling approach causes a signal loss due to the combining of filters. This

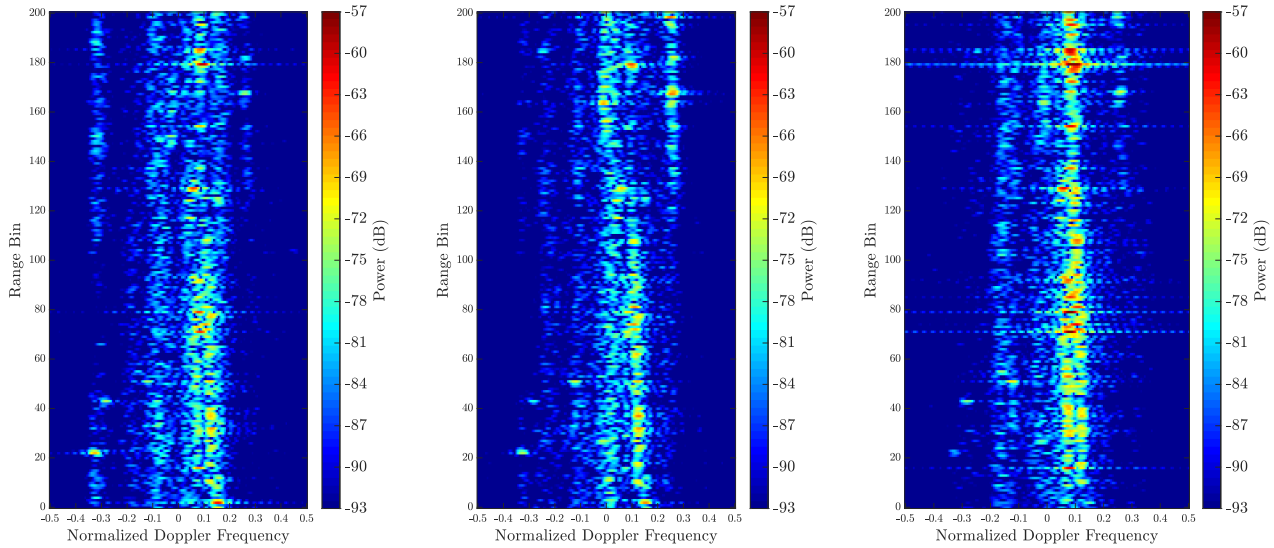

Fig. 3.17: Angle-Doppler processing at $\theta = -1/3$ (left), $\theta = 0$ (middle), and $\theta = 1/3$ (right)

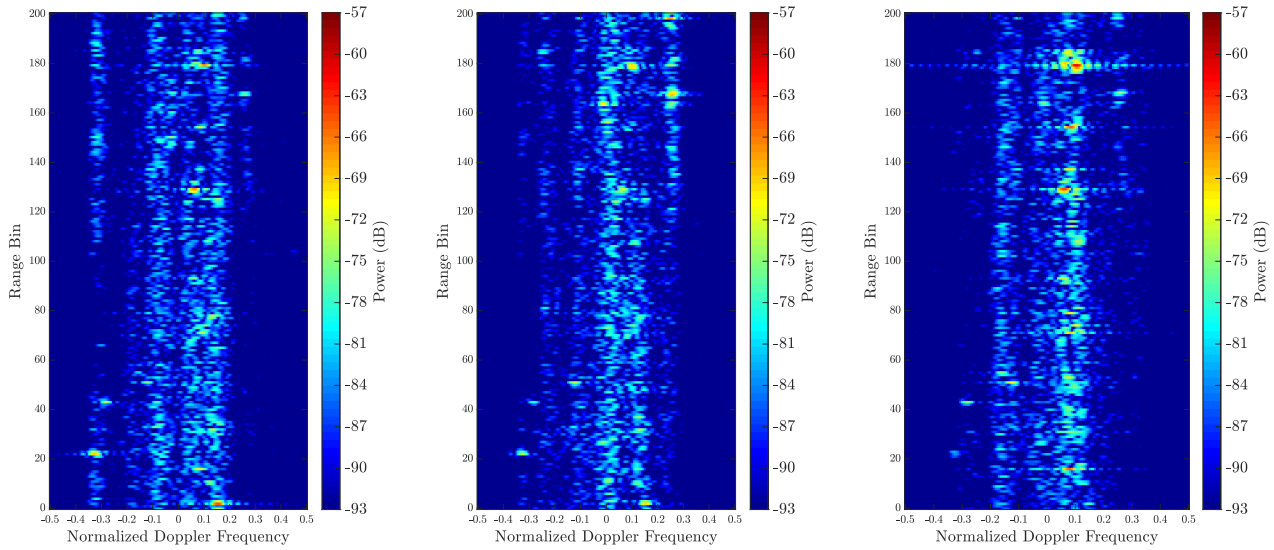

Fig. 3.18: Space-time adaptive processing at $\theta = -1/3$ (left), $\theta = 0$ (middle), and $\theta = 1/3$ (right)

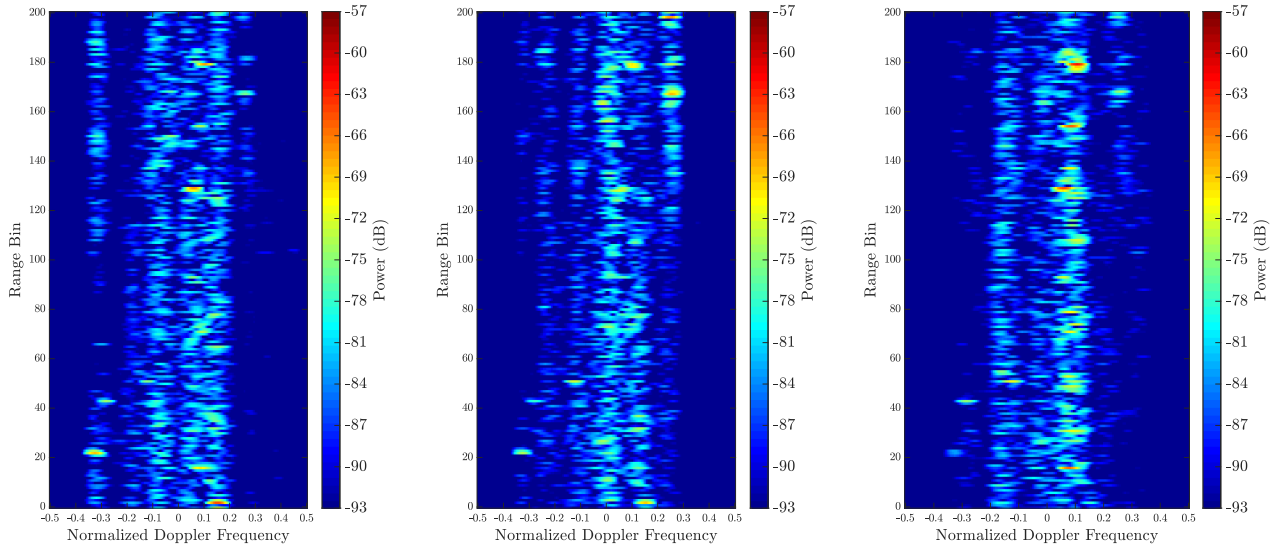

Fig. 3.19: Windowed space-time adaptive processing at $\theta = -1/3$ (left), $\theta = 0$ (middle), and $\theta = 1/3$ (right)

affect can be detrimental to high SNR signals. Implementing a partial constraint from [93] with the adaptive constraints with the approach can alleviate some of the loss observed. The potential detection benefit in the sensitivity gain from sidelobe suppression and maintaining nominal resolution can justify the use of beamspoiling.

The analysis continues to the reduced dimension results. In Figure 3.22, STAP using a reduce dimension cancellation matrix is presented. Comparing the result to the full rank approach in

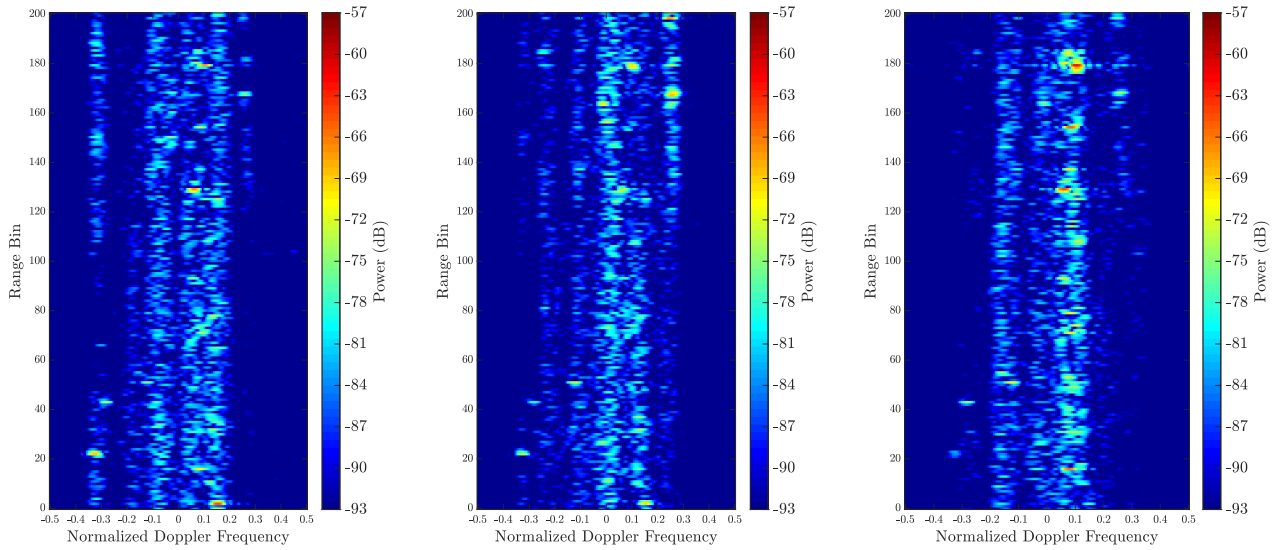

Fig. 3.20: Least-squares optimal mismatch angle-Doppler estimation with adaptive cancellation at $\theta = -1/3$ (left), $\theta = 0$ (middle), and $\theta = 1/3$ (right)

Fig. 3.20, the cancellation performance is fairly consistent. Figs 3.24 and 3.25 showing RRLS and PAMADE, respectively, are also consistent with the full rank counterparts in Figures 3.20 and 3.21. The response is expected as simulation results showed that RRLS and PAMADE can provide robust sidelobe suppression with significant covariance reduction. Therefore, the consideration of implementing RRLS and PAMADE becomes dependent on the processor used to implement estimation and inversion of the StCM and SaCM. The practical implementation of the reduced dimension filters shows their applicability to be significantly reduced while maintaining sidelobe suppression performance.

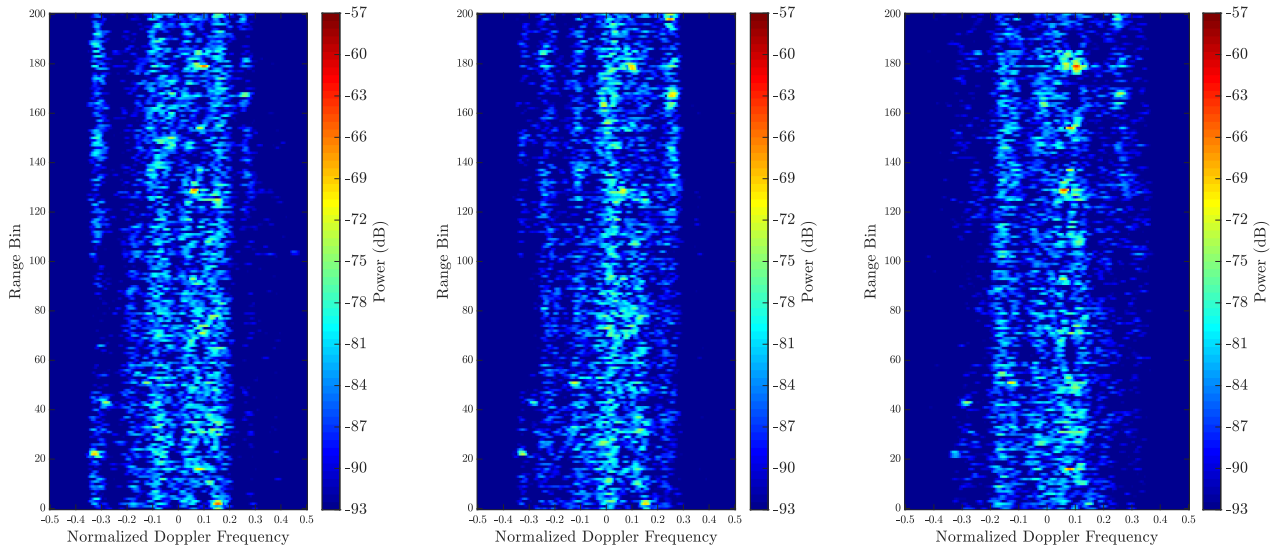

Fig. 3.21: Adaptive mismatch angle-Doppler estimation with adaptive cancellation at $\theta = -1/3$ (left), $\theta = 0$ (middle), and $\theta = 1/3$ (right)

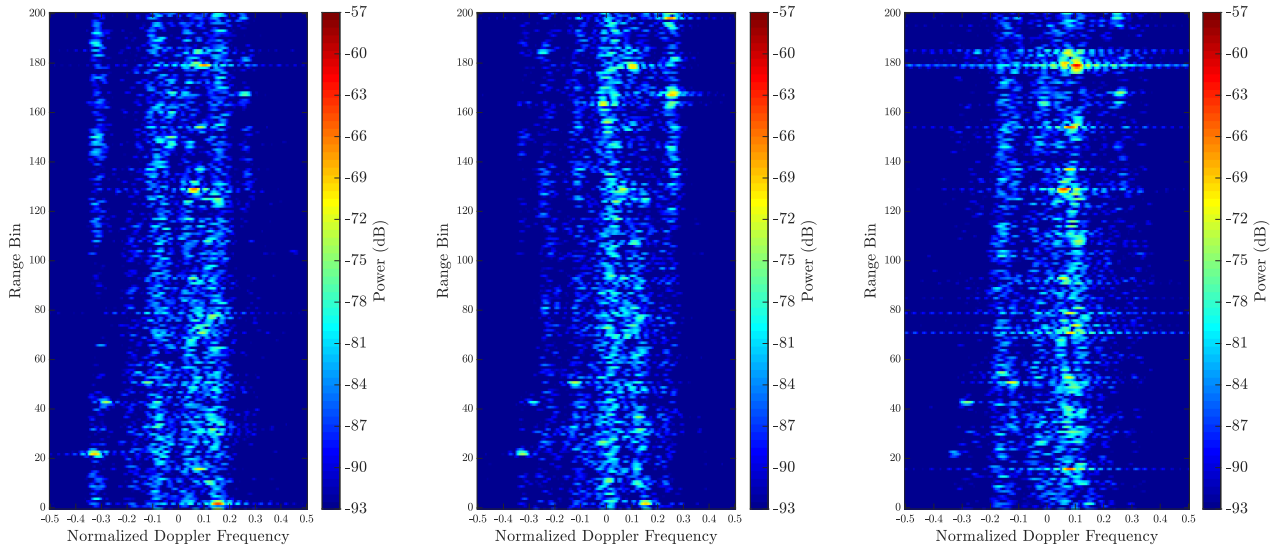

Fig. 3.22: Reduce dimension space-time adaptive processing at $\theta = -1/3$ (left), $\theta = 0$ (middle), and $\theta = 1/3$ (right)

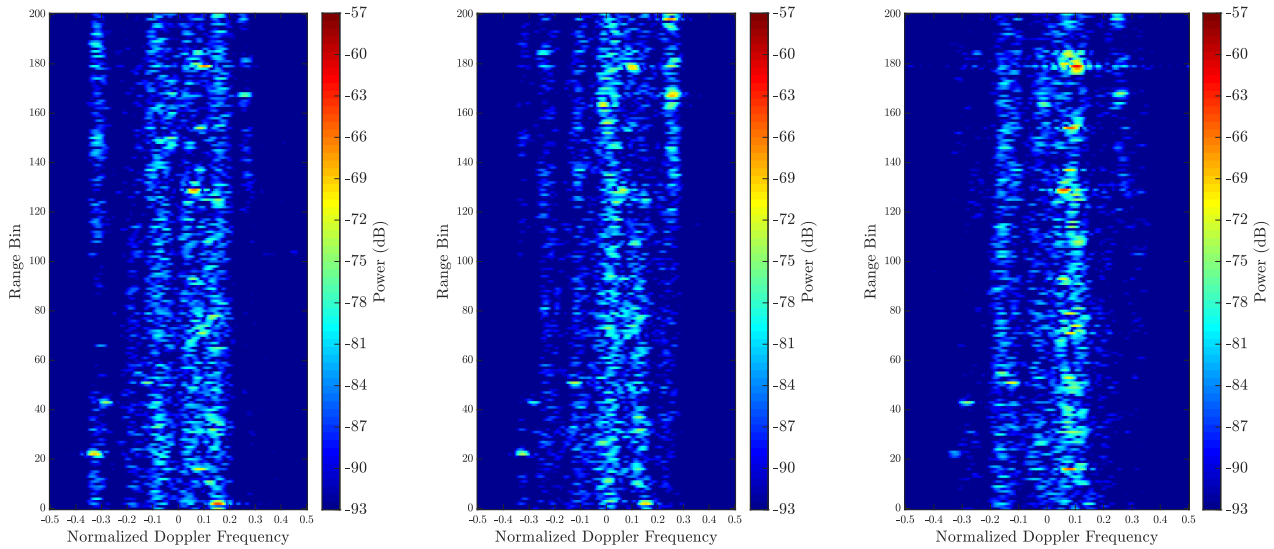

Fig. 3.23: Reduce rank least-squares optimal mismatch angle-Doppler estimation with adaptive cancellation at $\theta = -1/3$ (left), $\theta = 0$ (middle), and $\theta = 1/3$ (right)

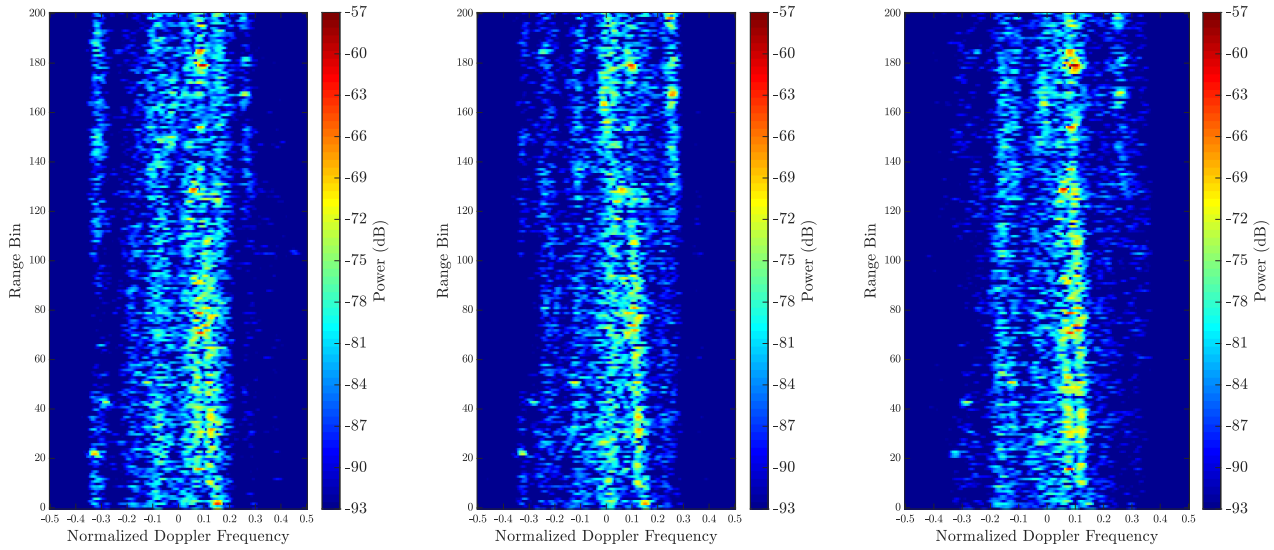

Fig. 3.24: Reduce adaptive mismatch angle-Doppler estimation with adaptive cancellation with adaptive cancellation at $\theta = -1/3$ (left), $\theta = 0$ (middle), and $\theta = 1/3$ (right)

Chapter 4

Adaptive Pulse Compression for Radar and Wireless Communication Coexistence

The dawn of the third millennium saw a boom in wireless communication technologies. The proliferation of communications generated an exponential demand in products such as smartphones, smart watches, tablets, and laptops. Recent technological advancements, such as the introduction of the internet-of-things where almost every device in modern homes have a wireless connection to the internet, have only accelerated consumer demand in wireless technologies. As the use of wireless devices rapidly increases, additional radio frequencies (RFs) must be made available on the electromagnetic (EM) spectrum. However, the EM spectrum is a finite, limited resource. Radar systems risk frequency reallocation on the EM spectrum to accommodate the growing commercial demand. Radar transmit and receive hardware are designed to operate efficiently within a finite RF bandwidth. Reallocation would require hardware modifications which can be potentially costly financially. An emerging solution to spectral congestion is spectrum sharing between radar and communications.

Wireless communications and radars fundamentally have different functions. Wireless communication systems exchange information between users over a wireless channel. Radars illuminates the environment, collects the illuminated reflections, and subsequently extracts physical information from the radar scene. When these services overlap in RF, mutual interference occurs which reduces their performance. Figure 4.1 diagrams the radar and communication mutual interference model. Reports of mutual interference between radar and communication systems date back to the middle 1950s when radar systems overpowered a

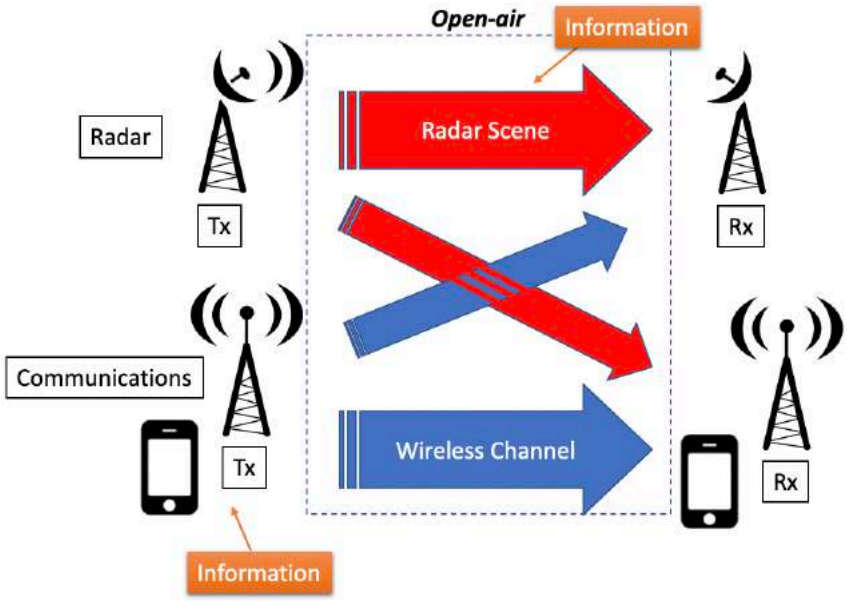

Fig. 4.1: Radar and communication mutual interference diagram

communication system designed by Bell Telephone Laboratories [132]. In early 2022, the Federal Aviation Administration (FAA) addressed serious concerns to aviation safety due in part to the deployment of Fifth Generation (5G) mobile communications interfering with air traffic control radars [133]. The Federal Communications Commission (FCC) and National Telecommunications and Information Administration (NTIA) regulate commercial and federal usage of radio spectrum, respectively, to ensure services have the spectral resources to perform their functions [134]. Mutual interference has always been addressed by designating RF bands for services to minimize frequency overlap. However, RF mutual interference remains an ongoing concern.

Through the years, multiple presidential memorandums have been enacted to dedicate resources, develop initiatives, and direct government agencies to address spectrum congestion and technological advancement within the US [135–137]. Initiatives were introduced by the FCC in the 2010 *National Broadband Plan* [138] to better allocate and manage the spectrum. A recommendation made within the report suggested 300 MHz be made available between 225 MHz and 3.7 GHz for mobile use over the course of 10 years. In that time span, a November 2015

spectrum auction for 1.7 GHz and 2.1 GHz spectra generated a record-breaking $45 billion in bids, which was set for advance wireless architectures like Fourth Generation (4G) technology [139]. In July 2019, FCC chairman released a report informing of an auction to open up the 2.5 GHz band for 5G technologies [140]. President's Council of Advisors on Science and Technology (PCAST) proposed that 1 GHz of federally held spectrum be made available for shared spectrum for use by private and public users [141]. Within the same report, PCAST suggested new technologies should enable multiple users to "share spectrum without mutual interference." Policy changes to accommodate the emerging technology to perform radar cognition and facilitate spectrum sharing were investigated in [142, 143].

Spectrum sharing can be addressed in fast-time delay, RF, spatial angle, slow-time Doppler, and polarization to name of few [144]. An overview of challenges facing spectrum sharing were examined within [145–147]. Spectrum sharing can be divided into three categories: co-design, cooperation, and coexistence [141, 143, 148]. Co-design is the development of new RF systems that consider radar and communication systems jointly in the hardware and software design stages [149]. Others propose the development of systems level architecture to incorporate multi-systems [150]. Cooperation considers multiple RF systems are able to share properties about their signal transmission such that a impacted RF receiver can mitigate the interference [141, 143]. Coexistence considers radar and communication systems operate in the same RF band without knowledge of the communication signal [141, 143]. The proposed approach in this chapter will address spectrum sharing via coexistence.

Coexistence is addressed under three architectures: coexistence via cognition, functional coexistence, and coexistence in spectral overlap [151]. In a seminal paper on radar cognition [152], one of three characteristics necessary to fulfill cognition is "intelligent signal processing which builds on learning through interaction of the radar with the surrounding environment." A recent paper on cognition highlighted practical limitations of implementation radar cognition [153]. Coexistence via cognition has been proposed under techniques that sense the environment and occupied frequencies and either avoid the interference or nullifies the interference in receive

processing [154–163]. Functional coexistence consist of dual-function radar communication which include radar waveforms containing embedded communications [151, 164–170]. In [171], a modification to communication symbols was proposed to facilitate operation of radar and communications overlapping in spectrum. Performance bounds of radar and communication coexistence were explored in [172].

In this chapter, spectrum sharing is addressed for coexistence in spectral overlap using digital receive beamforming and mismatch pulse compression. Digital beamforming exploits the spatial separability between radar and communication signal by determining the direction-of-arrival (DOA) of the signals onto a receive phased array. Pulse compression is a fundamental filtering operation to determine the range of the scattering. A standard beamformer for receive beamforming and match filter for pulse compression maximize signal-to-noise ratio (SNR) in their domain. These maximum SNR filters are ineffective in regaining sensitivity lost from the presence of wireless communications in the receive measurement. An adaptive pulse compression (APC) procedure after beamforming is proposed to regain sensitivity.

Adaptive pulse compression is a re-iterative minimum mean-square error (RMMSE) procedure in fast-time. The formulation mitigates range sidelobes for an enhanced pulse compression response prior to detection processing. APC was initially proposed for phase-coded waveforms [71, 72] and later for practical implementation of frequency modulation (FM) waveforms [94]. Multi-static APC (MAPC) addresses shared spectrum of multiple radars by performing mutual interference and sidelobe suppression together [173–175]. MAPC considered the implementation of a beamformer to maximize coherent gain in the spatial direction of its transmission prior to adaptive filtering for each radar. The beamforming stage also provides separability from mutual interference. A key consideration of MAPC is that the transmit waveform of the radars are known. The APC formulation being proposed for radar and communication coexistence considers any knowledge of the communication signal unavailable.

Adaptive pulse compression belongs to a family of RMMSE algorithms that not only have been implemented in fast-time but also in element-space [23, 93], slow-time [34, 176], space-time

(presented in the Chapter 3), time-range [19], and space-range [20]. RMMSE has been implemented for applications such as pulse agile waveforms [19, 20], stretch processing [77], fast-time Doppler [78–80], mutual coupling [81], brain imaging [82], and PRI-staggered radar (presented in the Chapter 2). RMMSE was also expanded to be combine with adaptive cancellation for optimal removal of clutter (a typical interference source in slow-time) in techniques known as baseline supplementary cancellation (BaSC) and baseline supplementary loading (BaSL) [34]. BaSC is a sequential estimation-then-cancellation procedure and BaSL is a joint cancellation and estimation procedure. Each approach incorporated an adaptive cancellation matrix that characterize the interference in the measurement.

The proposed approach facilitates coexistence by combining RMMSE with beamforming and adaptive cancellation. The approach considers the collection of radar and communication signals simultaneously on a phased array to obtain an element-space fast-time measurement. In receive processing, multiple receive beamformers are applied to the single element-space fast-time measurement to form multiple beamspace fast-time estimates. Beams are formed in the DOA of radar and each communication signal impinging onto receive array. Next, an adaptive cancellation matrix is formed from the beamspace fast-time estimates of the communication signals. The cancellation matrix is then used within the APC filter and applied to the beamspace fast-time estimate of the radar for simultaneous estimation the radar returns, mitigation range sidelobes, and cancellation the communication signal.

APC is designed to perform a matrix inversion per range sample which can be computationally expensive. Multiple methods have been proposed to address the computational complexity of APC [83–85, 88, 89]. Each seek to reduce the covariance matrix dimensional but not the number of matrices that need to be performed for a group of range samples. Block APC (BAPC) is introduced to reduce the processing to a single matrix inverse for multiple range samples.

The chapter begins with an overview of the wireless communication architecture. After, a joint radar and communication signal model is presented. The model is followed by the presentation of APC and BAPC procedures. The approaches are examined via a synthetic dataset formed from

free-space measurements of radar and communication signals. A long-term evolution (LTE) signal is examined as the mutual interference signal to the radar. LTE will provide a benchmark for performance since 5G systems leverage 4G architectures [141]. Conclusions and future work are presented in Chapter 5.

4.1 Wireless Communication Systems

Wireless communication systems transfer data between two points over an open-air medium. The information in the data can be voice, audio, video, data files, etc. [177]. For wireless communications, generational technology standards are defined to maximize the exchange of information and to ensure multiple companies are operating under the same criterion. LTE is the 4G standard developed by the 3rd-Generation Partnership Project (3GPP). LTE is designed to provide higher date rates, lower latency, and packet-optimized radio-access technology over previous generations [178]. The system attributes of LTE are presented in Table 4.1 [178–180].

Table 4.1: LTE system attributes

Parameter	Attribute	
Bandwidth	1.25-20 MHz	
Channel Spacing	15 kHz	
OFDM Symbol Period	66.7 μs	
Resource Block	12 Subcarriers	
Radio Frame	10ms	
Modulation	QPSK, 16-QAM, 64-QAM	
Multiple Access	Downlink:	OFDMA
	Uplink:	SC-FDMA
Duplexing	FDD, TDD, half-duplex FDD	
MIMO	Downlink:	2×2, 4×2, 4×4
	Uplink:	1×2, 1×4

A general flow diagram of a wireless communication system is presented in Figure 4.3. First, a serial bit data stream is formed. The data stream encounters a data source encoder to increase the amount of information per bit and reduce the amount of data needed to be transmitted. The result is a reduction in transmission time and/or bandwidth requirements [181]. Encryption of the

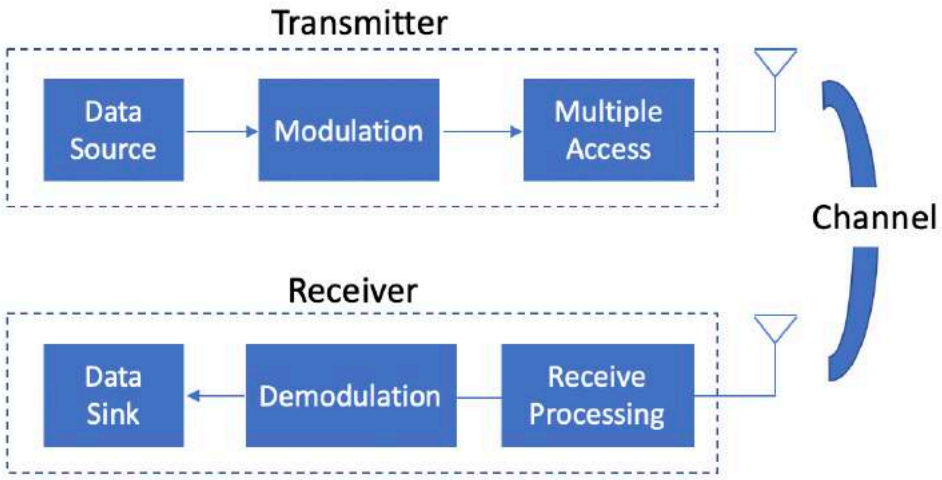

Fig. 4.2: Communication transmit/receive flow diagram

data stream will likewise occur at this stage. The data will next flow through a channel encoder to add redundancy combat against errors in open-air transmission along the channel [181]. Next, the data stream undergoes modulation such that the digital information can be made into an analog waveform [177]. LTE uses quadrature phase-shift keying (QPSK) and quadrature amplitude modulation (QAM) modulation schemes. Examples of the modulation schemes are depcited in Figure 4.4. QPSK and 4-QAM constellations are equivalent. The difference is the coordinate system the modulation procedure occurs [177]. QPSK uses a polar coordinate system that maintains a constant amplitude for all modulation symbols. A phase shift is then performed to obtained to modulation symbol. QAM on the other hand operates in a Cartesian coordinate system and is performed by varying the in-phase and quadrature (IQ) components. 4-QAM, 16-QAM, and 64-QAM constellations have symbol rates of 2, 4 and 6 bits per symbol, respectively. The symbol modulation selection changes in LTE depending on channel characteristics.

Continuing through the transmit chain, multiple access allows for multiple users to access the base station simultaneously [179, 181]. LTE leverages orthogonal frequency division multiple access (OFDMA) for downlink (base station to cellular device) and single-carrier frequency division multiple access (SC-FDMA) for uplink (cellular device to base station). SC-FDMA

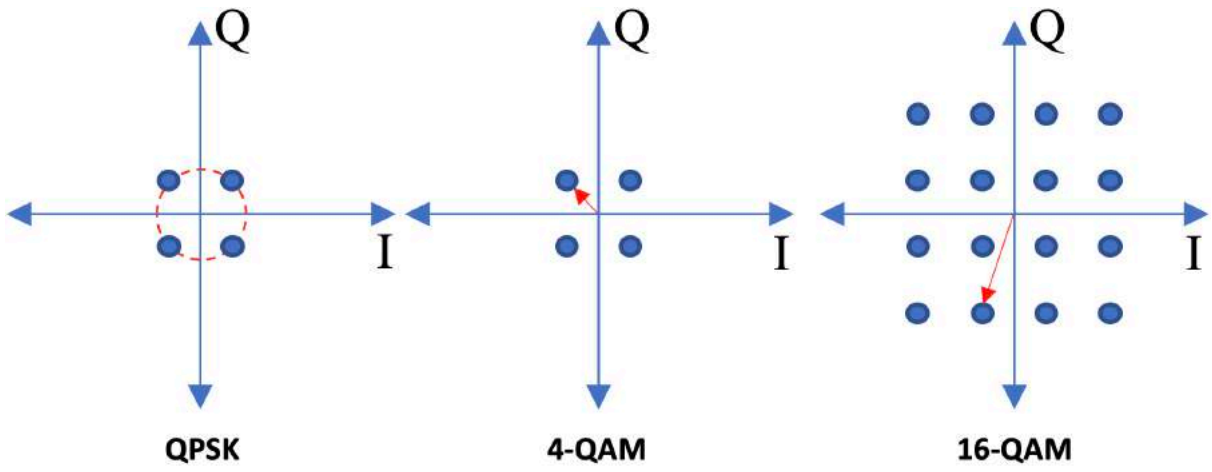

Fig. 4.3: Examples of PSK and QAM Constellations

incorporates a form of time-division multiple access (TDMA). Duplexing also occurs at this stage which allows for simultaneous uplink and downlink to the base station [181]. Frequency-division duplexing (FDD) separates uplink and downlink in frequency. Time-division duplexing (TDD) separates them in time. Wideband communication systems must also combat frequency-selective fading in which the transfer function of the channel varies with time. In flat-fading, the channel properties are constant across frequency [181].

A signal communication waveform generated from the multiple access scheme into the channel. One-way propagation occurs from the transmitter to the receiver. Several different types of fading can affect the channel. Small-scale fading occurs due to multipath reflections of the signal. The different arrival times of the signal causes inter-symbol interference (ISI). ISI is addressed using a cyclic prefix that creates redundancy [179]. Large-scale fading occurs due to a mobile device traveling into a shadowed area. The signal varies over the course of a longer time period in comparison to small-scale fading [181].

Similar phenomena in radar and wireless communication systems are described using different nomenclature. From a pulse-Doppler radar perspective, the communication signal is a pulse agile random continuous-wave (CW) noise waveform. Depending on the modulation, such as phase-shift keying (PSK), the signal can be a frequency modulated CW (FMCW) waveform.

Otherwise, amplitude modulation in communication makes the signal CW. The communication signal is expected to be transmitting for the full duration of a radar PRI. The "communication signal pulse" duration and PRI are thereby the same length (meaning the duty cycle is 100%) with each PRI containing a different segment of the "CW communication waveform." A pulse agile transmission has a different waveform pulse-to-pulse which, in this case, the communication waveform has.

From a communication perspective, a pulse-Doppler radar transmission can be viewed as a broadcast communication signal from a base-station with PSK modulation and TDMA transmit schemes. Wireless communication is inherently a broadcast system in its transmission. However, the voice and data transfer on the broadcast is point-to-point or multi-cast. Typical pulse-Doppler radar does not provide data to individual users. Although, a budding topic in radar is co-operation and co-design of radar waveforms that contain data to send to a user. The "radar broadcast signal" strives for constant modulus amplitude and frequency modulation. Also, the constant toggling of the radar transmission to create a pulse train separates the transmission in time similar to TDMA.

Another interesting connection between radar and communication systems is channel sounding in wireless communications. Wireless communication sounds the channel to determine the impulse response of the channel which describes the multipath components [181]. Channel sounding is performed by transmitting a known signal into the environment, compressing the reflected signal on receive, and examining the compressed response response. This may sound familiar since it is exactly what a radar does.

4.2 Radar and Communications Signal Model

Consider a wireless communication signal transmitting waveform $s_{\mathrm{c}}(t)$ into an open-air environment

$$s_{\mathrm{c}}(t) = A_{\mathrm{c}}(t)\, e^{j\Phi_{\mathrm{c}}(t)} \tag{4.1}$$

where $A_{\mathrm{c}}(t)$ is a time varying amplitude and $\Phi_{\mathrm{c}}(t)$ is a time-varying phase. For example, a OFDM waveform with a duration T_{c}, channel spacing $f_{\mathrm{c}} = 1/T_{\mathrm{c}}$, and RF bandwidth $B_{\mathrm{c}} = N_{\mathrm{c}} f_{\mathrm{c}}$ for N_{c} subcarriers has an initial waveform (prior to adding the cyclic prefix) of

$$\dot{s}_{\mathrm{c}}(t) = \sum_{n_{\mathrm{c}}=0}^{N_{\mathrm{c}}-1} a[n_{\mathrm{c}}]\, e^{j2\pi f_{\mathrm{c}} n_{\mathrm{c}} t} \tag{4.2}$$

where $a[n_{\mathrm{c}}]$ is a complex modulation symbol transmitted on each subcarrier [179]. Based on the constellation, the amplitude and phase of a transmission will vary. Adding the cyclic prefix with duration T_{pre} to the beginning of the signal produces the following waveform

$$s_{\mathrm{c}}(t) = \begin{cases} \dot{s}_{\mathrm{c}}(t + T_{\mathrm{c}} - T_{\mathrm{pre}}) & 0 \leq t \leq T_{\mathrm{pre}} \\ \dot{s}_{\mathrm{c}}(t - T_{\mathrm{pre}}) & T_{\mathrm{pre}} < t \leq T_{\mathrm{c}} + T_{\mathrm{pre}}. \end{cases} \tag{4.3}$$

The waveform travels along a wireless channel to RF receivers in the environment. Denote the wireless channel from the communication transmitter to the radar receiver as $x_{\mathrm{c}}(t)$. The channel can be direct from line-of-sight and indirect from multipath reflections. The communication signal interaction with the channel at the radar receive antenna is

$$y_{\mathrm{c}}(t) = s_{\mathrm{c}}(t) * x_{\mathrm{c}}(t). \tag{4.4}$$

Next, consider a radar transmitting a pulse waveform

$$s_{\mathrm{r}}(t) = A_{\mathrm{r}}(t)\, e^{j\Phi_{\mathrm{r}}(t)} \tag{4.5}$$

also with time-varying amplitude and phase. Recall from Chapter 1 that the baseband representation of an chirp waveform has an constant modulus amplitude of $A_{\mathrm{r}}(t) = 1$ and phase $\Phi_{\mathrm{r}}(t) = \pi(B_{\mathrm{r}}/\tau_{\mathrm{r}})t^2$ for a 3 dB bandwidth B_{r} and pulse duration τ_{r}. The radar receive fast-time

signal is obtained from the illumination of scatterers in the radar scene is

$$y_{\mathrm{r}}(t) = s_{\mathrm{r}}(t) * x_{\mathrm{r}}(t) \tag{4.6}$$

where $x_{\mathrm{r}}(t)$ is the range profile defined over $0 \leq t \leq T_{\mathrm{r}}$ for PRI T_{r}.

Consider the receive aperture being a N-element uniform linear array (ULA) with elements spaced $\lambda_{\mathrm{RF}}/2$. A monostatic radar transmission is considered such that the receive array is co-located with the radar transmit array. Collecting radar reflections and the communication signals at the nth element for a single PRI produces the following element-space fast-time collection

$$y(n,t) = y_{\mathrm{r}}(t)\, e^{jn\theta_{\mathrm{r,look}}} + \sum_{q=0}^{Q-1} y_{\mathrm{c},q}(t)\, e^{jn\theta_{\mathrm{c},q,\mathrm{look}}} + v(n,t) \tag{4.7}$$

where $\theta_{\mathrm{r,look}}$ is the spatial frequency corresponding to the look direction of the radar transmitter, $\theta_{\mathrm{c},q,\mathrm{look}}$ is the spatial frequency corresponding to the DOA of the qth communication transmission, Q is the total number of communication signals impinging onto the radar receiver, and $v(n,t)$ represents thermal noise. The collected signal is amplified, down-converted to baseband, and discretized for receive processing. Following discretization, the element-space fast-time measurement is

$$y[n,\ell] = y_{\mathrm{r}}[\ell]\, e^{jn\theta_{\mathrm{r,look}}} + \sum_{q=0}^{Q-1} y_{\mathrm{c},q}[\ell]\, e^{jn\theta_{\mathrm{c},q,\mathrm{look}}} + \xi[n,\ell] + v[n,\ell] \tag{4.8}$$

where $\xi[n,\ell]$ accounts for model mismatch.

Mutual interference depends on a various parameters such as transmit powers, frequency overlap, temporal overlap, spatial location, direction-of-arrival of signals to name a few. Other factors include the antennas, transmission lines, propagation phenomena, receivers, and filters [182]. The radar and communication transmissions in this work share two properties that result in mutual interference: RF bandwidth and temporal duration. The carrier frequencies of the transmissions may differ. However, the radar 3 dB bandwidth is assumed to be fully or partially

overlapped with the communication occupied bandwidth. There are two possible temporal relationships between the radar and communication transmission that must be accounted for: full collection of a single symbol and partial collection of multiple symbols [144]. When the PRI is greater than the symbol duration, the communication symbol is fully captured. However, a portion of the next symbol would be collected. In the opposite case of the symbol duration being greater then the PRI, only a portion of the signal symbol is captured. Lastly, if the communication transmission is powered off during a PRI, a portion of the symbol is captured.

To facilitate radar coexistence with communications, some form of diversity is necessary to provide a sense of orthogonality for separation of the systems. No two signals are truly orthogonal. Rather, the signals can have low correlation between each other. Digital beamforming is used to provide that separability by exploiting the DOA of the signals impinging on the radar array. Consider the orientation of the element-space fast-time measurement in (4.8) into a $N \times 1$ element-space measurement vector as a function of fast-time

$$\mathbf{y}_{\mathrm{s}}(\ell) = y_{\mathrm{r}}[\ell]\,\mathbf{c}_{\mathrm{s}}(\theta_{\mathrm{r,look}}) + \sum_{q=0}^{Q-1} y_{\mathrm{c},q}[\ell]\,\mathbf{c}_{\mathrm{s}}(\theta_{\mathrm{c},q,\mathrm{look}}) + \mathbf{e}_{\mathrm{s}}(\ell) + \mathbf{v}_{\mathrm{s}}(\ell) \tag{4.9}$$

where $\mathbf{c}_{\mathrm{s}}(\theta) = \begin{bmatrix} 1 & e^{j\theta} & \cdots & e^{j(N-1)\theta} \end{bmatrix}^T$ is the $N \times 1$ spatial steering vector for a spatial frequency θ, $\mathbf{e}_{\mathrm{s}}(\ell)$ is a $N \times 1$ model error vector, and $\mathbf{v}_{\mathrm{s}}(\ell)$ is a $N \times 1$ noise vector. Receive beamforming is employed on the vector using the maximum SNR beamformer which is

$$\mathbf{u}_{\mathrm{BF}}(\theta) = \frac{\mathbf{c}_{\mathrm{s}}(\theta)}{N}. \tag{4.10}$$

A beamformer is generated for the radar returns and each communication signal for a total of $Q+1$ beamformers. Each beamformer is electronically steered in the DOA of its respective signal to maximize coherent gain in that direction. Applying the beamformer corresponding to the radar returns to the receive data vector produces the following beamspace fast-time response of the radar

transmission

$$\widehat{y}\left[\ell,\hat{\theta}_{\mathrm{r}}\right]=\mathbf{u}_{\mathrm{BF}}^{H}\left(\hat{\theta}_{\mathrm{r}}\right)\mathbf{y}_{\mathrm{s}}\left(\ell\right)=y\left[\ell\right]+\sum_{q=0}^{Q-1}y_{\mathrm{c},q}\left[\ell\right]\alpha(\hat{\theta}_{\mathrm{r}},\theta_{\mathrm{c},q,\mathrm{look}})+v[\ell,\hat{\theta}_{\mathrm{r}}]+\xi[\ell,\hat{\theta}_{\mathrm{r}}] \tag{4.11}$$

where $\alpha(\theta_i,\theta_k)=\mathbf{u}_{\mathrm{BF}}^{H}\left(\theta_i\right)\mathbf{c}_{\mathrm{s}}\left(\theta_k\right)$ denotes the complex amplitude resulting from the inner product between a beamformer and a steering vector, $v[\ell,\hat{\theta}_{\mathrm{r}}]=\mathbf{u}_{\mathrm{BF}}^{H}\left(\theta_{\mathrm{r}}\right)\mathbf{v}_{\mathrm{s}}(\ell)$ is filtered noise, and $\xi[\ell,\hat{\theta}_{\mathrm{r}}]=\mathbf{u}_{\mathrm{BF}}^{H}\left(\theta_{\mathrm{r}}\right)\mathbf{e}_{\mathrm{s}}(\ell)$ is filtered error. Similarly applying the beamformer corresponding to the qth communication signal produces the following beamspace fast-time response

$$\begin{aligned}\widehat{y}\left[\ell,\hat{\theta}_{\mathrm{c},q}\right]=\mathbf{u}_{\mathrm{BF}}^{H}\left(\hat{\theta}_{\mathrm{c},q}\right)\mathbf{y}_{\mathrm{s}}\left(\ell\right)=y_{\mathrm{c},q}\left[\ell\right]+y_{\mathrm{r}}\left[\ell\right]\alpha(\hat{\theta}_{\mathrm{c},q},\theta_{\mathrm{r,look}})+\sum_{q\neq k}y_{k}\left[\ell\right]\alpha(\hat{\theta}_{\mathrm{c},q},\theta_{k,\mathrm{look}})+v[\ell,\hat{\theta}_{\mathrm{c},q}]\\+\xi[\ell,\hat{\theta}_{\mathrm{c},q}]\end{aligned} \tag{4.12}$$

where the filtered noise and error have similar forms as (4.11).

Effectively, the beamformer for one signal imposes a complex amplitude, or in other words a destructive coherence, on the other signals providing the necessary separation. The receive beamformer beampattern dictates the complex amplitude that is applied. The DOA of the communication signals in the null of the beamformer beampattern is best for radar estimation. The worst case is the communication signal is in a main or peak sidelobe of the beamformer beampattern. When a communication transmit beam lies in the radar recieve beamformer mainbeam, the complex amplitude approaches one thereby reducing the spatial separability. Physically, this implies that the radar transmit and receive beams are pointing in the vicinity of the communication receive beam. Knowledge of the signal DOAs are required. Since the transmit look direction of the radar is known, its corresponding beamformer is steered in that direction $\hat{\theta}_{\mathrm{r}}=\theta_{\mathrm{r,look}}$. The DOA of the qth communication signal, $\hat{\theta}_{\mathrm{c},q}$, is unknown but assumed to be readily attainable via traditional receive beamforming and a detector or the application of a direction finding algorithm [23, 54–59]. The number of communication signals and the number of array elements can not be ignored in their role in receive beamforming. The spatial

degrees-of-freedom are limited by the number of array elements. The radiation and array patterns are dictated by the antenna type and element spacing [183].

Following beamforming, pulse compression is employed to obtain the range delay of scatterers in the scene. Define the total number of fast-time samples in the PRI as $L_{\mathrm{r}} = f_{\mathrm{s}} T_{\mathrm{r}}$. The receiver sampling frequency is oversampled relative to the 3 dB bandwidth $f_{\mathrm{s}} = K_{\mathrm{r}} B_{\mathrm{r}}$ where K_{r} denotes the oversampling factor. The range profile can be examined over a segment of the PRI. Define L_{start} as the first sample and L_{stop} as the last sample in the interval that is to be examined in a observation window. The number of fast-time samples after segmentation is $L = L_{\mathrm{stop}} - L_{\mathrm{start}}$. The $L \times 1$ fast-time measurement vector after segmentation is

$$\widehat{\mathbf{y}}_{\mathrm{f}}(\ell, \theta) = \left[\begin{array}{cccc} \widehat{y}\,[\ell, \theta] & \widehat{y}\,[\ell+1, \theta] & \cdots & \widehat{y}\,[\ell+L-1, \theta] \end{array} \right]^T \tag{4.13}$$

where the interval begins at $\ell = L_{\mathrm{start}}$. The beamspace fast-time estimate from (4.11) and (4.12) from can be structurally represented as

$$\begin{aligned} \widehat{\mathbf{y}}_{\mathrm{f}}\left(\ell, \hat{\theta}_{\mathrm{r}}\right) &= \mathbf{S}_{\mathrm{r}} \mathbf{x}_{\mathrm{r}}(\ell) + \sum_{q=0}^{Q-1} \alpha(\hat{\theta}_{\mathrm{r}}, \theta_{\mathrm{c},q,\mathrm{look}}) \mathbf{y}_{\mathrm{c},q}(\ell) + \mathbf{v}_{\mathrm{r}}(\ell) + \mathbf{e}_{\mathrm{r}}(\ell) \\ \widehat{\mathbf{y}}_{\mathrm{f}}\left(\ell, \hat{\theta}_{\mathrm{c},q}\right) &= \mathbf{y}_{\mathrm{c},q}(\ell) + \alpha(\hat{\theta}_{\mathrm{c},q}, \theta_{\mathrm{r,look}}) \mathbf{y}_{\mathrm{r}}(\ell) + \sum_{q \neq k} \alpha(\hat{\theta}_{\mathrm{c},q}, \theta_{k,\mathrm{look}}) \mathbf{y}_{k}(\ell) + \mathbf{v}_{\mathrm{c},q}(\ell) + \mathbf{e}_{\mathrm{c},q}(\ell) \end{aligned} \tag{4.14}$$

where $\mathbf{S}_{\mathrm{r}}$ is a $L \times K$ waveform convolution matrix of the radar waveform, $\mathbf{x}_{\mathrm{r}}(\ell) = \left[\begin{array}{cccc} x[\ell] & \cdots & x[\ell+1] & \cdots \quad x[\ell+K-1] \end{array} \right]^T$ is a $K \times 1$ range delay vector for $K = L + L_{\mathrm{s}} - 1$ range delay samples, $\mathbf{v}_{\mathrm{r}}(\ell) = \left[\begin{array}{cccc} v_{\mathrm{r}}[\ell] & \cdots & v[\ell+1] & \cdots \quad v_{\mathrm{r}}[\ell+L-1] \end{array} \right]^T$ is a $L \times 1$ noise vector after beamforming, $\mathbf{e}_{\mathrm{r}}(\ell) = \left[\begin{array}{cccc} \xi_{\mathrm{r}}[\ell] & \cdots & \xi[\ell+1] & \cdots \quad \xi_{\mathrm{r}}[\ell+L-1] \end{array} \right]^T$ is a $L \times 1$ error vector after beamforming, $\mathbf{v}_{\mathrm{c},q}(\ell)$ is the noise vector from the qth communication signal beamformer (structured similar to $\mathbf{v}_{\mathrm{r}}(\ell)$), and $\mathbf{e}_{\mathrm{c},q}(\ell)$ is the error vector from the qth communication signal beamformer (structured similar to $\mathbf{e}_{\mathrm{r}}(\ell)$). Each column in the waveform matrix is a time-delayed

shift of the discretized radar waveform

$$\mathbf{s}_{\mathrm{r}} = \left[\begin{array}{cccc} s_{\mathrm{r}}[0] & s_{\mathrm{r}}[1] & \cdots & s_{\mathrm{r}}[L_{\mathrm{s}}-1] \end{array} \right]^T \tag{4.15}$$

where $L_{\mathrm{s}} = f_{\mathrm{s}}\tau_{\mathrm{r}} = K_{\mathrm{r}}B_{\mathrm{r}}\tau_{\mathrm{r}}$ is the number of samples in the waveform. For notation convenience, denote the columns of the convolution matrix as

$$\mathbf{S}_{\mathrm{r}} = \left[\begin{array}{cccc} \mathbf{s}_{\mathrm{r},0} & \mathbf{s}_{\mathrm{r},1} & \cdots & \mathbf{s}_{\mathrm{r},K-1} \end{array} \right] \tag{4.16}$$

where the kth column is

$$\mathbf{s}_{\mathrm{r},k} = \begin{cases} \left[\begin{array}{cccc} s_{\mathrm{r}}[L_{\mathrm{s}}-k] & \cdots & s_{\mathrm{r}}[L_{\mathrm{s}}] & \mathbf{0}_{1\times(L-k+1)} \end{array} \right]^T & 0 \le k \le L_{\mathrm{s}} \\ \left[\begin{array}{ccc} \mathbf{0}_{1\times(L_{\mathrm{s}}-k)} & \mathbf{s}_{\mathrm{r}} & \mathbf{0}_{1\times(L-k+))} \end{array} \right]^T & L_{\mathrm{s}} < k \le L-K \\ \left[\begin{array}{cccc} \mathbf{0}_{1\times k} & s_{\mathrm{r}}[0] & \cdots & s_{\mathrm{r}}[k-(L-K)] \end{array} \right]^T & L-K < k \le K. \end{cases} \tag{4.17}$$

Discrete pulse compression is employed using a match filter

$$\mathbf{u}_{\mathrm{MF},k} = \frac{1}{L_{\mathrm{s}}}\mathbf{s}_{\mathrm{r},k}. \tag{4.18}$$

The pulse compression response from the application of the match filter to beamspace fast-time receive data produces the beamspace range response

$$\hat{x}\left[\ell+k, \hat{\theta}_{\mathrm{r}}\right] = \mathbf{u}_{\mathrm{MF},k}^H \widehat{\mathbf{y}}_{\mathrm{f}}\left(\ell, \hat{\theta}_{\mathrm{r}}\right) \tag{4.19}$$

for $k = 0, 1, \cdots, K-1$. A $L \times K$ match filter bank can form from the convolution matrix,

$$\mathbf{U}_{\mathrm{MF}} = \frac{1}{L_{\mathrm{s}}}\mathbf{S}_{\mathrm{r}} = \left[\begin{array}{cccc} \mathbf{u}_{\mathrm{MF},0} & \mathbf{u}_{\mathrm{MF},1} & \cdots & \mathbf{u}_{\mathrm{MF},K-1} \end{array} \right]. \tag{4.20}$$

Application of the match filter bank to the radar beamspace fast-time data vector is

$$\hat{\mathbf{x}}_{\mathrm{MF}}\left(\ell,\hat{\theta}_{\mathrm{r}}\right)=\mathbf{U}_{\mathrm{MF}}^{H}\widehat{\mathbf{y}}_{\mathrm{f}}\left(\ell,\hat{\theta}_{\mathrm{r}}\right). \tag{4.21}$$

to form a $K\times 1$ estimate of the range profile. Pulse compression produces convolution tails. Scatterer responses may occur in these eclipsed regions [184]. The aggregate cross-correlation between the radar and communication signals sets the new "noise floor". A robust estimate of the range profile relies on the radar match filter to have a low cross-correlation to communication signal. To achieve this, the pulse compression filters must estimate of the radar range profile and suppress the communication signals simultaneously. In the case of radar and communication, a high correlation exists that prevents the match filters producing a robust estimate. Additionally when using a LFM, which has a sinc response after pulse compression, range sidelobes must be accounted for to unmask scattering obscured by the sidelobes.

4.3 Adaptive Pulse Compression

The estimate of a beamspace range sample can be decomposed into the following

$$\begin{aligned}\hat{x}_{\mathrm{r}}\left[\ell+k,\hat{\theta}_{\mathrm{r}}\right]=x_{\mathrm{r}}\left[\ell+k\right]+\sum_{i\neq k}x_{\mathrm{r}}\left[\ell+i\right]\mathbf{u}_{\mathrm{MF},k}^{H}\mathbf{s}_{\mathrm{r},i}+\sum_{q=0}^{Q-1}\alpha(\hat{\theta}_{\mathrm{r}},\theta_{\mathrm{c},q,\mathrm{look}})\mathbf{u}_{\mathrm{MF},k}^{H}\mathbf{y}_{\mathrm{c},q}\left(\ell\right)+\mathbf{u}_{\mathrm{MF},k}^{H}\mathbf{v}_{\mathrm{r}}\left(\ell\right)\\+\mathbf{u}_{\mathrm{MF},k}^{H}\mathbf{e}_{\mathrm{r}}\left(\ell\right)\end{aligned} \tag{4.22}$$

where the desired response is $d_{\mathrm{opt}}=x_{\mathrm{r}}\left[\ell+k\right]$ and the remaining error responses consist of range sidelobes, mutual interference, thermal noise, and model mismatch error for $i,k=0,1,\cdots,K-1$. An estimate of the desired response is obtained for each range sample by applying a weight vector to the beamspace fast-time snapshot starting at ℓ i.e., $d_{\mathrm{est}}=\hat{x}_{\mathrm{r}}\left[\ell+k,\hat{\theta}_{\mathrm{r}}\right]=\mathbf{u}^{H}(\ell+k)\widehat{\mathbf{y}}_{\mathrm{f}}\left(\ell+k,\hat{\theta}_{\mathrm{r}}\right)$. Since the filter and data vector each shift with k, the variable is subsumed for the rest of the section. Using the relationship between the desired and estimated responses $d_{\mathrm{est}}=d_{\mathrm{opt}}+d_{\mathrm{err}}$ and solving

for error d_{err}, a MSE cost function for the ℓth sample is obtained [71, 72]

$$J_{\text{MSE}} = E\left\{\left|x_{\text{r}}[\ell] - \mathbf{u}^H(\ell)\widehat{\mathbf{y}}_{\text{f}}\left(\ell,\hat{\theta}_{\text{r}}\right)\right|^2\right\}. \tag{4.23}$$

A complex gradient vector operator with partial derivatives corresponding to the real and imaginary components of the weight vector is applied to minimize the cost function and obtain the optimal solution [92]. Consider an arbitrary $K\times 1$ vector $\mathbf{a} = [\ a_0 \quad a_1 \quad \cdots \quad a_{K-1}\ ]^T$ where the real and imaginary components of ith element is $a_i = p_i + jq_i$. The partial derivatives with respect to a_i using Wirtinger derivatives is $\frac{\partial}{\partial a_i^*} = \frac{1}{2}\left(\frac{\partial}{\partial p_i} + j\frac{\partial}{\partial q_i}\right)$. The corresponding $K\times 1$ gradient vector operations with respect to $\mathbf{a}^*$ is $\nabla_{\mathbf{a}^*} = [\ \frac{\partial}{\partial a_0^*} \quad \frac{\partial}{\partial a_1^*} \quad \cdots \quad \frac{\partial}{\partial a_{K-1}^*}\ ]^T$ [92].

Applying the gradient with respect to the conjugate of the weight vector, setting to $\nabla_{\mathbf{u}^*} J_{\text{MSE}} = 0$, and solving for $\mathbf{u}(\ell)$ yields the $K\times 1$ MMSE pulse compression filter

$$\mathbf{u}_{\text{MMSE}}(\ell) = \left(E\left\{\widehat{\mathbf{y}}_{\text{f}}(\ell,\hat{\theta}_{\text{r}})\widehat{\mathbf{y}}_{\text{f}}^H(\ell,\hat{\theta}_{\text{r}})\right\}\right)^{-1} E\left\{x_{\text{r}}^*[\ell]\widehat{\mathbf{y}}_{\text{f}}(\ell,\hat{\theta}_{\text{r}})\right\} \tag{4.24}$$

following a similar procedure presented in [86]. The autocovariance matrix denoted as $\mathbf{Q}_{\text{r}}(\ell) = E\{\widehat{\mathbf{y}}_{\text{f}}(\ell,\hat{\theta}_{\text{r}})\widehat{\mathbf{y}}_{\text{f}}^H(\ell,\hat{\theta}_{\text{r}})\}$ is expanded by substituting the fast-time data from (4.14) into the matrix. The result of the expansion is

$$\begin{aligned}\mathbf{Q}_{\text{r}}(\ell) &= \mathbf{S}_{\text{r}}\mathbf{P}_{\text{r}}(\ell)\mathbf{S}_{\text{r}}^H + \sum_{q=0}^{Q-1}\mathbf{R}_{\text{c},q}(\ell) + \mathbf{R}_{\text{r,err}}(\ell) + \mathbf{R}_{\text{r,v}} \\ &= \mathbf{S}_{\text{r}}\mathbf{P}_{\text{r}}(\ell)\mathbf{S}_{\text{r}}^H \odot \left(\frac{\sigma_{\text{err}}^2}{N}\mathbf{I}_{L\times L} + \mathbf{1}_{L\times L}\right) + \sum_{q=0}^{Q-1}|\alpha(\hat{\theta}_{\text{r}},\theta_{\text{c},q,\text{look}})|^2 E\{\mathbf{y}_{\text{c},q}(\ell)\mathbf{y}_{\text{c},q}^H(\ell)\} + \frac{\sigma_{\text{v}}^2}{N}\mathbf{I}_{L\times L}\end{aligned} \tag{4.25}$$

where $\mathbf{P}_{\text{r}}(\ell) = E\{\mathbf{x}_{\text{r}}(\ell)\mathbf{x}_{\text{r}}^H(\ell)\} = \mathbf{x}_{\text{r}}(\ell)\mathbf{x}_{\text{r}}^H(\ell)\odot\mathbf{I}_{K\times K}$ is a $K\times K$ power distribution matrix from radar reflections, $\mathbf{R}_{\text{c},q}(\ell) = |\alpha(\hat{\theta}_{\text{r}},\theta_{\text{c},q,\text{look}})|^2 E\{\mathbf{y}_{\text{c},q}(\ell)\mathbf{y}_{\text{c},q}^H(\ell)\}$ is the $L\times L$ interference covariance matrix for the qth communication signal, $\mathbf{R}_{\text{r,err}}(\ell) = (\sigma_{\text{err}}^2/N)\mathbf{I}_{L\times L}\odot\mathbf{S}_{\text{r}}\mathbf{P}_{\text{r}}(\ell)\mathbf{S}_{\text{r}}^H$ is a $L\times L$ error covariance matrix with error power σ_{err}^2, and $\mathbf{R}_{\text{r,v}} = (\sigma_{\text{v}}^2/N)\mathbf{I}_{L\times L}$ is a $L\times L$ noise covariance matrix with noise

power σ_{v}^2. The noise and error powers are scaled by N due to the coherent gain beamforming provides. As seen from previous chapters, the elements in $\mathbf{x}_{\mathrm{r}}(\ell)$ are assumed to be statistically independent of each other [72] making the distribution matrix a diagonal matrix with the power of the filter response along the diagonal. For fast-time signals, this is the pulse compression response. Substituting (4.14) into the cross-correlation vector in (4.23) expands to

$$E\left\{x_{\mathrm{r}}^{*}[\ell]\widehat{\mathbf{y}}_{\mathrm{f}}(\ell,\hat{\theta}_{\mathrm{r}})\right\}=\rho_{\mathrm{r}}[\ell]\mathbf{s}_{\mathrm{r}} \tag{4.26}$$

where $\rho_{\mathrm{r}}[\ell]=E\{|x_{\mathrm{r}}[\ell]|^2\}$. Using (4.25) and (4.26), the MMSE filter is

$$\mathbf{u}_{\mathrm{MMSE}}(\ell)=\rho_{\mathrm{r}}[\ell]\mathbf{Q}_{\mathrm{r}}^{-1}(\ell)\mathbf{s}_{\mathrm{r}}. \tag{4.27}$$

The autocovariance matrix contains a structure covariance matrix (StCM) of the radar collection since the transmit waveform is known. The Q interference matrices are unknown but can be adaptively estimated using a sample covariance matrix (SaCM). The presence of the interference covariance matrix provides the cancellation of the communication signals. Therefore, the aggregate of the interference covariance matrices is akin to a cancellation matrix

$$\mathbf{R}_{\mathrm{canc}}(\ell)=\sum_{q=0}^{Q-1}\mathbf{R}_{\mathrm{c},q}(\ell). \tag{4.28}$$

APC is an re-iterative procedure using the MMSE pulse compression filter. Each successive iteration updates the pulse compression response. The MMSE pulse compression filter requires knowledge of the radar transmit waveform, range profile, communication signals, error power, and noise power. The radar transmit waveform is known. The noise power is obtained via analysis of the radar receiver noise figure. The error power is determined via an empirical analysis following receive processing. The radar range profile and communication signals are unknown a priori. Beamspace fast-time estimates of the communication signals are used in its place. The range profile is adaptively estimated using APC. Utilizing the StCM from APC with a cancellation matrix

makes the formulation a subset of baseline supplementary loading (BaSL) [34]. BaSL performs a "soft" cancellation by jointly performing the estimation and cancellation stages.

The $L \times L$ cancellation matrix is estimated using beamspace fast-time estimates of the communication signals

$$\hat{\mathbf{R}}_{\text{canc}}(\ell) = \sum_{q=0}^{Q-1} \widehat{\mathbf{y}}_{\text{f}}\left(\ell, \hat{\theta}_{\text{c},q}\right) \widehat{\mathbf{y}}_{\text{f}}^{H}\left(\ell, \hat{\theta}_{\text{c},q}\right) \tag{4.29}$$

which contains errors from the radar and other sources. In order satisfy the Reed, Mallett, and Brennan rule [36], approximately $2L$ homogeneous beamspace snapshots of the communication signal would be necessary in order to be within 3 dB of the optimal matrix. Reaching that number of snapshots is dependent on the number of receive beams used. The rank will most often be Q but only occurs if each communication signal is separated spatially. The rank can be at most N which is also the number of spatial degrees-of-freedom. The matrix has low sample support since $Q \leq L$. The benefit of APC is that only a single snapshot of each communication signal is required to remove each.

Considerations have been taken for practical implementation of APC. APC can suppress sidelobes to an impractical floor response that is ineffective for detection processing [86] . A gain constraint is employed with APC to suppress the sidelobes to the original noise floor [86]. Consider the MSE cost function such that the filter has unity gain $\mathbf{u}^{H}(\ell)\mathbf{s}_{\text{r}} = 1$

$$J_{\text{MSE}} = E\left\{\left|x_{\text{r}}[\ell] - \mathbf{u}^{H}(\ell)\widehat{\mathbf{y}}_{\text{f}}\left(\ell, \hat{\theta}_{\text{r}}\right)\right|^{2}\right\} + \text{Re}\{\lambda_{\text{L}}^{*}(\mathbf{u}^{H}(\ell)\mathbf{s}_{\text{r}} - 1)\} \tag{4.30}$$

where λ_{L} is a Lagrange multiplier. Minimizing the cost function and determining the unity gain constraint produces the constrained MMSE pulse compression filter

$$\mathbf{u}_{\text{MMSE,con}}(\ell) = \frac{\mathbf{Q}_{\text{r}}^{-1}(\ell)\mathbf{s}_{\text{r}}}{\mathbf{s}_{\text{r}}^{H}\mathbf{Q}_{\text{r}}^{-1}(\ell)\mathbf{s}_{\text{r}}} \tag{4.31}$$

[86]. The constrained solution has shown to suffer a performance loss against low SNR signals. The unity gain constraint can be modified to a partial gain constraint which provides a trade-space

between a noise floor and practical performance of low SNR signals [93]. For the purposes of testing APC for coexistence, the gain constrained solution is implemented. Superresolution results in a mismatch loss when range straddling is present [94]. Beamspoiling for APC is performed by setting K_{r} columns, corresponding to the oversampling factor, on each side of the center column in $\mathbf{S}_{\mathrm{r}}$ to zeros.

$$\mathbf{s}_{\mathrm{r},K/2+k_{\mathrm{r}}} = \mathbf{0}_{L\times 1} \tag{4.32}$$

for $|k_{\mathrm{r}}| = 1,2,\cdots,K_{\mathrm{r}}$. The result is the null-to-null range resolution remains nominal. APC can also collapse the range window in the eclipsed regions in successive adaptive iterations [184]. A pulse compression repair is employed to preserve the response in the eclipsed regions [94, 184]. Pulse eclipsing repair [184] is not addressed within this work although the approach is applicable due to the structure of the APC formulation.

The presentation of APC in fast-time follows [94]. The major difference in the procedure is the incorporation of the cancellation matrix. The procedure begins with the estimation of the beamspace fast-time data using (4.14). Next, the procedure is initialized by the using the match filter estimate of the range profile from (4.21)

$$\hat{\mathbf{x}}_{\mathrm{APC},0}(\ell,\hat{\theta}_{\mathrm{r}}) = \hat{\mathbf{x}}_{\mathrm{MF}}(\ell,\hat{\theta}_{\mathrm{r}}). \tag{4.33}$$

The ith iteration of the procedure begins by forming the power distribution matrix using the previous estimate of the range profile

$$\mathbf{P}_{\mathrm{APC},i}(\ell,\hat{\theta}_{\mathrm{r}}) = \mathbf{x}_{\mathrm{APC},i-1}(\ell,\hat{\theta}_{\mathrm{r}})\mathbf{x}^{H}_{\mathrm{APC},i-1}(\ell,\hat{\theta}_{\mathrm{r}}) \odot \mathbf{I}_{K\times K}. \tag{4.34}$$

The fast-time covariance matrix is formed using the updated power distribution matrix and Q beamformed fast-time estimates of the communication signals

$$\mathbf{Q}_{\mathrm{APC},i}(\ell,\hat{\theta}_{\mathrm{r}}) = \mathbf{S}_{\mathrm{r}}\mathbf{P}_{\mathrm{APC},i}(\ell,\hat{\theta}_{\mathrm{r}})\mathbf{S}_{\mathrm{r}}^{H} \odot \left(\frac{\sigma^2_{\mathrm{err}}}{N}\mathbf{I}_{L\times L} + \mathbf{1}_{L\times L}\right) + \hat{\mathbf{R}}_{\mathrm{canc}}(\ell) + \frac{\sigma^2_{\mathrm{v}}}{N}\mathbf{I}_{L\times L}. \tag{4.35}$$

The kth APC filter for the ith iteration is formed using updated fast-time covariance matrix

$$\mathbf{u}_{\text{APC,con},i}(\ell,\hat{\theta}_{\text{r}}) = \frac{\mathbf{Q}^{-1}_{\text{APC},i}(\ell,\hat{\theta}_{\text{r}})\mathbf{s}_{\text{r}}}{\mathbf{s}^{H}_{\text{r}}\mathbf{Q}^{-1}_{\text{APC},i}(\ell,\hat{\theta}_{\text{r}})\mathbf{s}_{\text{r}}} \tag{4.36}$$

and applied to the receive data to form its corresponding range estimate

$$\hat{x}_{\text{APC},i}(\ell,\hat{\theta}_{\text{r}}) = \mathbf{u}^{H}_{\text{APC,con},i}(\ell,\hat{\theta}_{\text{r}})\widehat{\mathbf{y}}_{\text{f}}\left(\ell,\hat{\theta}_{\text{r}}\right). \tag{4.37}$$

Steps (4.33) - (4.37) are then repeated for each ℓth range sample. Next, a $K \times 1$ vector of the range estimates is formed

$$\mathbf{x}_{\text{APC},i}(\ell,\hat{\theta}_{\text{r}}) = \left[\ x_{\text{APC},i}(\ell,\hat{\theta}_{\text{r}}) \quad x_{\text{APC}}(\ell+1,\hat{\theta}_{\text{r}}) \quad \cdots \quad x_{\text{APC},i}(\ell+K-1,\hat{\theta}_{\text{r}})\ \right]^{T}. \tag{4.38}$$

and used in the replacement of (4.33) and iterated through. The APC approach presented only requires prior knowledge of the communication signal DOA of instead its frequency or temporal structure.

4.4 Block Adaptive Pulse Compression

The downside of APC is the requirement of a covariance matrix to be formed and inverted per range sample. APC implements of $L \times L$ matrix inversions per sample per iteration. The amount of matrix inverses can be computationally costly. There exist other APC approaches such as fast APC [83–85], match filter APC [89], gradient descent APC [88] that focus on reducing covariance size. A approach is presented that reduces the filter to a single StCM for a block of data. BAPC uses a single $L \times L$ matrix per iteration for L snapshots. The block approach is structured similarly to RMMSE for spectral estimation called re-iterative superresolution (RISR) [23]. The RISR approach takes a single StCM for a bank of filters. The RISR has been extensively examined in previous chapters. Although the processing is in a different domain, the same principles and performance characteristics of the RISR carry over into BAPC algorithm.

Consider the estimate of the range sample from (4.22). An alternate estimate from APC considers a weight vector corresponding to the the time-shifted delays with the discrete convolution matrix $d_{\text{est}} = \hat{x}_{\text{r}}[\ell+k] = \mathbf{u}_{\text{r},k}^H \widehat{\mathbf{y}}_{\text{f}}\left(\ell, \hat{\boldsymbol{\theta}}_{\text{r}}\right)$ for $k = 0, 1, \cdots, K-1$ samples. The corresponding MSE cost function for the kth sample in the data vector is

$$J_{\text{MSE}} = E\left\{\left|x_{\text{r}}[\ell+k] - \mathbf{u}_{\text{r},k}^H \widehat{\mathbf{y}}_{\text{f}}\left(\ell, \hat{\boldsymbol{\theta}}_{\text{r}}\right)\right|^2\right\}. \tag{4.39}$$

In this context, ℓ is the starting point. Applying the gradient with respect to the conjugate of the weight vector, setting to $\nabla_{\mathbf{u}_{\text{r},k}^*} J_{\text{MSE}} = 0$, and solving for $\mathbf{u}_{\text{r},k}$ yields the $K \times 1$ MMSE pulse compression filter

$$\mathbf{u}_{\text{MMSE},k} = \left(E\left\{\widehat{\mathbf{y}}_{\text{f}}(\ell, \hat{\boldsymbol{\theta}}_{\text{r}}) \widehat{\mathbf{y}}_{\text{f}}^H(\ell, \hat{\boldsymbol{\theta}}_{\text{r}})\right\}\right)^{-1} E\left\{x_{\text{r}}^*(\ell+k) \widehat{\mathbf{y}}_{\text{f}}(\ell, \hat{\boldsymbol{\theta}}_{\text{r}})\right\}. \tag{4.40}$$

In this case, multiple estimates are formed from a single data vector. Using (4.14), the expectations can be expanded. The autocovariance matrix $\mathbf{Q} = E\{\widehat{\mathbf{y}}_{\text{r}}(\ell) \widehat{\mathbf{y}}_{\text{r}}^H(\ell)\}$ is equivalent to (4.25). Note, that in the case the matrix is independent of k. Therefore, each kth MMSE pulse compression filter has the same autocovariance matrix. The expectation of the cross-covariance vector in (4.40) is

$$E\left\{x_{\text{r}}^*(\ell+k) \mathbf{y}_{\text{f}}(\ell, \hat{\boldsymbol{\theta}}_{\text{r}})\right\} = \rho[\ell+k] \mathbf{s}_{\text{r},k}. \tag{4.41}$$

when substituting (4.14) into the vector. Substituting the expectations from (4.25) and (4.41) into the MMSE pulse compression filter from (4.40) produces the following MMSE filter

$$\mathbf{u}_{\text{MMSE},k} = \rho_{\text{r}}[\ell+k] \mathbf{Q}_{\text{r}}^{-1}(\ell) \mathbf{s}_{\text{r},k}. \tag{4.42}$$

The MMSE filter in (4.42) and the previous MMSE filter in (4.27) differ in vectors and matrices change with k. In (4.27) the power distribution matrix $\mathbf{P}(\ell)$, subsumed in $\mathbf{Q}(\ell)$, changes each snapshot. Every delay shift in the snapshot performs a delay shift along the diagonal of $\mathbf{P}(\ell)$. The

result is a new covariance is estimated and inverted each range sample. In (4.42), $\mathbf{Q}(\ell)$ is the same while $\mathbf{s}_{\mathrm{r},k}(\ell)$ its corresponding power are shifted. Therefore, a similar covariance is used for block of range samples.

A filter bank is formed for K filters using (4.42)

$$\mathbf{U}_{\mathrm{MMSE}} = \mathbf{Q}_{\mathrm{r}}^{-1}(\ell)\mathbf{P}_{\mathrm{r}}(\ell)\mathbf{S}_{\mathrm{r}}. \tag{4.43}$$

Application of the filter bank to the receive data produces the MMSE estimate of the range profile

$$\hat{\mathbf{x}}_{\mathrm{MMSE}}\left(\ell,\hat{\theta}_{\mathrm{r}}\right) = \mathbf{U}_{\mathrm{MMSE}}^{H}\widehat{\mathbf{y}}_{\mathrm{f}}\left(\ell,\hat{\theta}_{\mathrm{r}}\right). \tag{4.44}$$

The basis vector in the convolution matrix being discrete time-shifted sinc functions which make the approach suboptimal. Portions of convolution are zero-filled due to the time shift. The zero-filled vectors causes a loss in fidelity since a portion of the waveform is used. Although the adaptive degree-of-freedom remains the same, the vector norm decreases. This leads to a lost in robustness.

Techniques for the unity gain constraint and beamspoiling are considered here for practical implementation of BAPC. The gain constrained solution is similar to APC. The constrained MSE cost function is

$$J_{\mathrm{MSE}} = E\left\{\left|x_{\mathrm{r}}\left[\ell+k\right] - \mathbf{u}_{\mathrm{r},k}^{H}\widehat{\mathbf{y}}_{\mathrm{f}}\left(\ell,\hat{\theta}_{\mathrm{r}}\right)\right|^{2}\right\} + \mathrm{Re}\{\lambda^{*}(\mathbf{u}_{\mathrm{r},k}^{H}\mathbf{s}_{\mathrm{r},k}-1)\}. \tag{4.45}$$

where $\mathbf{u}_{\mathrm{r},k}^{H}\mathbf{s}_{\mathrm{r},k} = 1$ is the unity gain constraint. The resulting filter solution is

$$\mathbf{u}_{\mathrm{MMSE,con},k} = \frac{\mathbf{Q}_{\mathrm{r}}^{-1}(\ell)\mathbf{s}_{\mathrm{r},k}}{\mathbf{s}_{\mathrm{r},k}^{H}\mathbf{Q}_{\mathrm{r}}^{-1}(\ell)\mathbf{s}_{\mathrm{r},k}} \tag{4.46}$$

The beamspoiling approaches considers the adjacent bin approaches presented in the previous

chapters

$$\mathbf{u}_{\text{MMSE,beam},k} = \frac{\sqrt{K_r}\sum_{k_\text{r}=-K_\text{r}}^{K_\text{r}} \mathbf{u}_{\text{MMSE,con},k+K_\text{r}} \mathbf{s}_{\text{r},k+K_\text{r}}^H \mathbf{s}_{\text{r},k}}{\sum_{k_\text{r}=-K_\text{r}}^{K_\text{r}} \mathbf{s}_{\text{r},k+K_\text{r}}^H \mathbf{s}_{\text{r},k}}. \tag{4.47}$$

A $L \times K$ filter bank is formed from the beamspoiled filters

$$\mathbf{U}_{\text{MMSE}} = [\ \mathbf{u}_{\text{MMSE},0} \quad \mathbf{u}_{\text{MMSE},1} \quad \cdots \quad \mathbf{u}_{\text{MMSE},K-1}.\ ]. \tag{4.48}$$

Pulse eclipsing needs to be investigated more for BAPC. The approaches presented in [94, 184] are not applicable due to the StCM remaining consistent for a block of pulses. Additionally, the eclipse regions need to be discarded such that the consecutive blocks can be combined to form a single range profile. Approaches must consider the overlapping of these blocks. For now, only the observation region of the filter response is examined.

The BAPC produces follows APC closely. For operation within BAPC the number of samples must be $L \geq f_\text{s}\tau_\text{r}$ The beamformer is obtained and applied to the receive data. The BAPC is initialized by the using the match filter estimate of the range profile

$$\hat{\mathbf{x}}_{\text{BAPC},0}(\ell, \hat{\theta}_\text{r}) = \hat{\mathbf{x}}_{\text{MF}}(\ell, \hat{\theta}_\text{r}). \tag{4.49}$$

The *i*th iteration of the procedure begins by forming the power distribution matrix using the previous estimate of the range profile

$$\mathbf{P}_{\text{BAPC},i}(\ell, \hat{\theta}_\text{r}) = \mathbf{x}_{\text{BAPC},i-1}(\ell, \hat{\theta}_\text{r}) \mathbf{x}_{\text{BAPC},i-1}^H(\ell, \hat{\theta}_\text{r}) \odot \mathbf{I}_{K\times K}. \tag{4.50}$$

The fast-time covariance matrix is formed using the updated power distribution matrix and Q beamformed fast-time estimates of the communication signals obtained

$$\mathbf{Q}_{\text{BAPC},i}(\ell, \hat{\theta}_\text{r}) = \mathbf{S}_\text{r} \mathbf{P}_{\text{BAPC},i}(\ell, \hat{\theta}_\text{r}) \mathbf{S}_\text{r}^H \odot \left(\frac{\sigma_\text{err}^2}{N} \mathbf{I}_{L\times L} + \mathbf{1}_{L\times L} \right) + \hat{\mathbf{R}}_\text{canc}(\ell) + \frac{\sigma_\text{v}^2}{N} \mathbf{I}_{L\times L}. \tag{4.51}$$

The kth BAPC filter is formed using updated fast-time covariance matrix

$$\mathbf{u}_{\mathrm{BAPC,con},k,i} = \frac{\mathbf{Q}^{-1}_{\mathrm{BAPC},i}(\ell)\mathbf{s}_{\mathrm{r},k}}{\mathbf{s}^{H}_{\mathrm{r},k}\mathbf{Q}^{-1}_{\mathrm{BAPC},i}(\ell)\mathbf{s}_{\mathrm{r},k}} \tag{4.52}$$

then is beamspoiled to maintain nominal resolution

$$\mathbf{u}_{\mathrm{BAPC,beam},k} = \frac{\sum\limits_{k_{\mathrm{r}}=-K_{\mathrm{r}}}^{K_{\mathrm{r}}} \mathbf{u}_{\mathrm{BAPC,con},k+K_{\mathrm{r}}}\mathbf{s}^{H}_{\mathrm{r},k+K_{\mathrm{r}}}\mathbf{s}_{\mathrm{r},k}}{\sum\limits_{k_{\mathrm{r}}=-K_{\mathrm{r}}}^{K_{\mathrm{r}}} \mathbf{s}^{H}_{\mathrm{r},k+K_{\mathrm{r}}}\mathbf{s}_{\mathrm{r},k}}. \tag{4.53}$$

Next, a $L \times K$ filter bank is formed from the filters

$$\mathbf{U}_{\mathrm{BAPC,beam},i} = \left[\begin{array}{cccc} \mathbf{u}_{\mathrm{BAPC,beam},0,i} & \mathbf{u}_{\mathrm{BAPC,beam},1,i} & \cdots & \mathbf{u}_{\mathrm{BAPC,beam},K-1,i} \end{array}\right] \tag{4.54}$$

and applied to the measurement vector for an updated estimate of the range profile.

$$\hat{\mathbf{x}}_{\mathrm{BAPC},i}\left(\ell,\hat{\theta}_{\mathrm{r}}\right) = \mathbf{U}^{H}_{\mathrm{BAPC,beam},i}\widehat{\mathbf{y}}_{\mathrm{f}}\left(\ell,\hat{\theta}_{\mathrm{r}}\right). \tag{4.55}$$

The procedure returns to (4.50) for a set number of iterations. If the same covariance size and number of iterations are performed for APC and BAPC, the latter would reduce the computation by the number of range bins being examined.

4.5 Synthetic Results using Ground-Based Open-Air Measurements

Open-air experimental testing was performed at the University of Kansas to examine APC and BAPC for radar and communication coexistence. The experiment consisted of two open-air collections are performed: one for the radar and another for the wireless communication. A synthetic beamspace fast-time dataset is generated off-line by synthetically imposing a linear array onto the collections then combining thereafter. The synthetic dataset allows for control of the receive powers and DOAs while maintaining open-air and hardware effects. The subsections

Fig. 4.4: Radar hardware instrumentation setup (left) and annotated field of view (right, courtesy of Google Maps) for measured results. The radar and intersection are depicted with a yellow star and yellow ellipse, respectively

below include details of the data formation and the performance analyses.

4.5.1 Data formation

The radar collection is the same uniform PRI collection from Chapter 2. There are more details on the fast-time aspects since this chapter focuses on fast-time signals in contrast to Chapter 2 which focused on slow-time signals. The radar is a monostatic, ground based, pulse-Doppler radar operating at a carrier frequency of 3.55 GHz. For reference, Figure 4.4 presents the experimentation set-up and scene field of view for the radar system (and is the same as Fig. 2.30). A LFM waveform with a 3 dB bandwidth of B_{r} = 50 MHz and pulse duration of τ_{r} = 3 μs is generated using an arbitrary waveform generator. The PRI was set to 20 μs for a longer unambiguous range. The transmit and receive antennas are mechanically steered towards a busy intersection approximately 1100 m from the radar. The radar has simultaneous transmit and receive capabilities. Therefore, the direct path is captured in the receive antenna. The radar scene included forestry and buildings in addition to moving vehicles. On receive, the collected signal is sent through a bandpass filter, passed through a low-noise amplifier, and passed through a real-time spectrum analyzer where the collected signal is downconverted to baseband then

undergoes IQ sampling and quantization for later off-line processing. The receiver sampling rate is f_s = 200 MHz. The receiver noise power was measured to be approximately -65 dBm.

In a separate experiment, a 4G LTE signal was transmitted from a nearby location in the direction of the radar receive antenna. Figure 4.5 depicts the experimentation set-up and scene field of view for the wireless communication system. The communication signal was generated using a Agilent/Keysight vector signal generator. To mimic a deployed LTE signal, a built-in LTE software package by Keysight was implemented that consisted of different physical broadcast channels, synchronization channels, and constellations. The LTE signal had a bandwidth of 20 MHz is upconverted to a center frequency of 3.55 GHz. The communication transmit antenna was mechanically steered to have a direct line-of-sight to the radar receiver. The receiver then collects the communication transmission and obtains the baseband signal the same way as the radar. Note the communication transmitter and the radar receiver did not have phase synchronization. Decoding the communication bit stream was not of interest.

Denote the following subscripts: "open" denotes a phenomenon occurring during open-air propagation, "col" denotes a collection obtained at radar receiver, and "syn" denotes a synthetic parameter added off-line. The collection of the radar and communication signals at the radar receiver can be modeled as

$$\begin{aligned} y_{\mathrm{r,col}}[\ell] &= y_{\mathrm{r,open}}[\ell] + v_{\mathrm{r,col}}[\ell] \\ y_{\mathrm{c,col}}[\ell] &= y_{\mathrm{c,open}}[\ell] + v_{\mathrm{c,col}}[\ell] \end{aligned} \tag{4.56}$$

where $y_{\mathrm{r,open}}[\ell]$ represents the radar waveform interaction with the open air environment (see (4.6)), $y_{\mathrm{c,open}}[\ell]$ represents the communication signal interaction with the open air environment (see (4.4)), and $v_{\mathrm{r,col}}[\ell]$ and $v_{\mathrm{c,col}}[\ell]$ represent the thermal noise at the receiver for each collection. Figure 4.6 and 4.7 present the radar and communication open-air collections in fast-time and frequency for one PRI.

The communication transmission operates for the duration of the PRI. The communication bandwidth partially overlaps 40% of the radar bandwidth. A synthetic signal amplification and

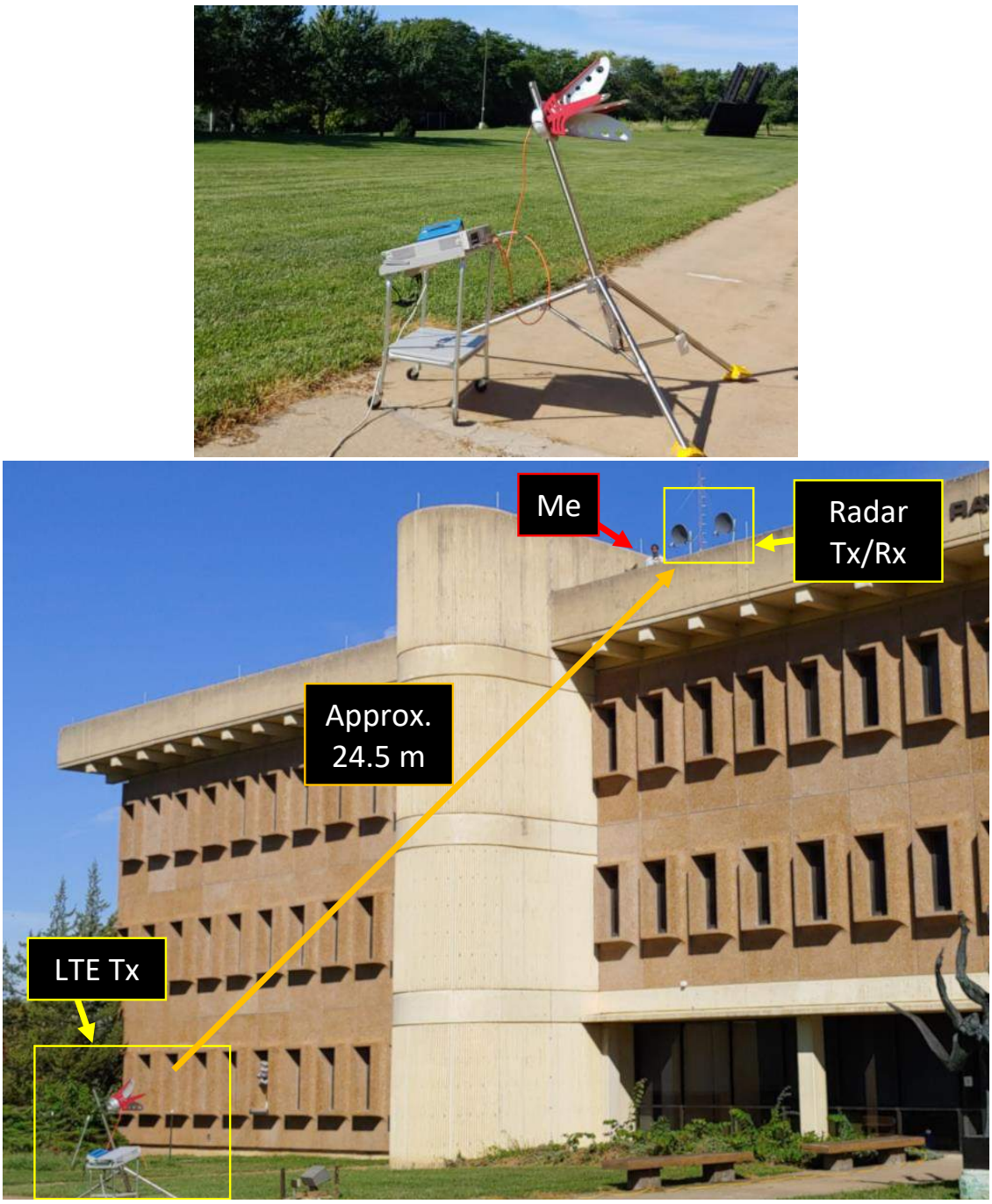

Fig. 4.5: Wireless communications hardware instrumentation setup (top) and annotated field of view (bottom) for measured results

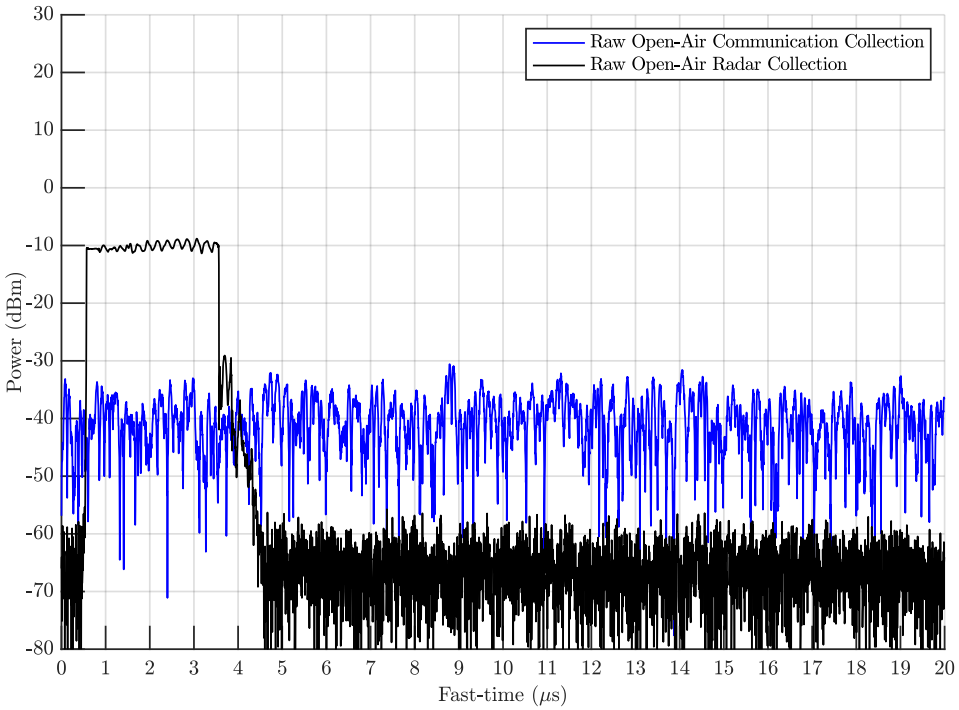

Fig. 4.6: Fast-time signal of the radar (black) and communication (blue) open-air collections for one PRI

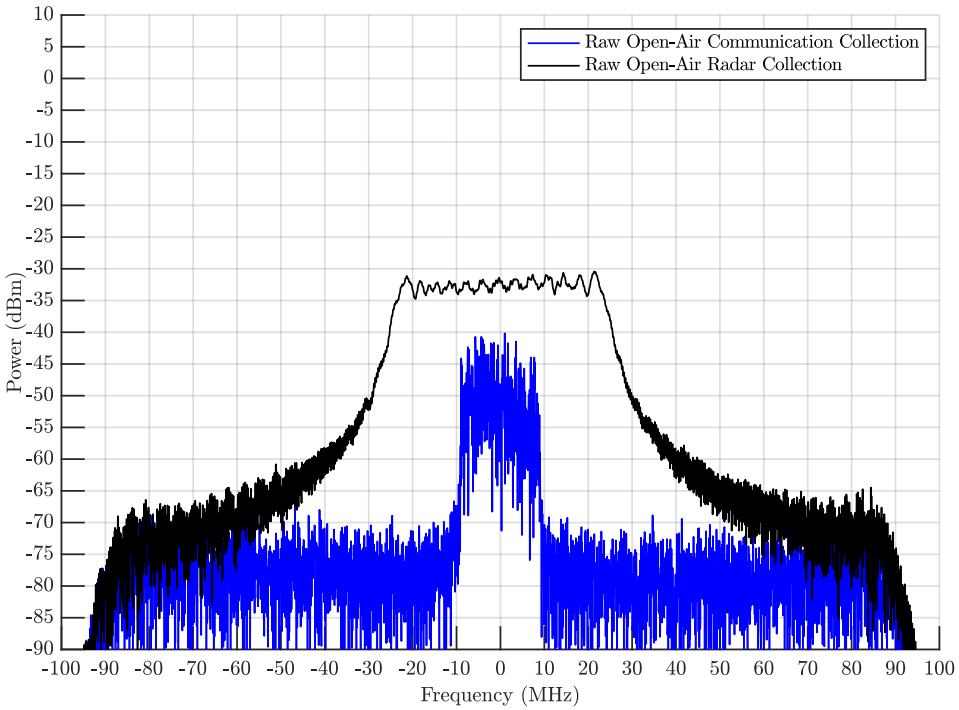

Fig. 4.7: Baseband spectrum of the radar (black) and communication (blue) open-air collections for one PRI

synthetic ULA (assumed to have $\lambda_{\mathrm{RF}}/2$ element spacing) with a corresponding synthetic look direction is added to each collection. The combination of the separate synthetic data collection is

$$\begin{aligned} y_{\mathrm{syn}}[n,\ell] &= \sqrt{P_{\mathrm{r,syn}}}y_{\mathrm{r,col}}[\ell]\,e^{jn\theta_{\mathrm{r,look,syn}}} + \sqrt{P_{\mathrm{c,syn}}}y_{\mathrm{c,col}}[\ell]\,e^{jn\theta_{\mathrm{c,look,syn}}} + \sqrt{P_{\mathrm{v,syn}}}v_{\mathrm{syn}}[n,\ell] \\ &= \sqrt{P_{\mathrm{r,syn}}}y_{\mathrm{r,open}}[\ell]\,e^{jn\theta_{\mathrm{r,look,syn}}} + \sqrt{P_{\mathrm{c,syn}}}y_{\mathrm{c,open}}[\ell]\,e^{jn\theta_{\mathrm{c,look,syn}}} \\ &\quad + \sqrt{P_{\mathrm{r,syn}}}v_{\mathrm{r,col}}[\ell]\,e^{jn\theta_{\mathrm{r,look,syn}}} + \sqrt{P_{\mathrm{c,syn}}}v_{\mathrm{c,col}}[\ell]\,e^{jn\theta_{\mathrm{c,look,syn}}} \end{aligned} \tag{4.57}$$

At this stage, the data is now in the form of an element-space fast-time samples.

Processing from element-space fast-time to beamspace fast-time is performed using (4.8) - (4.14). First, the data is formed into an element-space data vector

$$\begin{aligned} \mathbf{y}_{\mathrm{s,syn}}(\ell) &= \sqrt{P_{\mathrm{r,syn}}}y_{\mathrm{r,open}}[\ell]\,\mathbf{c}_{\mathrm{s}}(\theta_{\mathrm{r,look,syn}}) + \sqrt{P_{\mathrm{c,syn}}}y_{\mathrm{c,open}}[\ell]\,\mathbf{c}_{\mathrm{s}}(\theta_{\mathrm{c,look,syn}}) \\ &\quad + \sqrt{P_{\mathrm{r,syn}}}v_{\mathrm{r,col}}[\ell]\,\mathbf{c}_{\mathrm{s}}(\theta_{\mathrm{r,look,syn}}) + \sqrt{P_{\mathrm{c,syn}}}v_{\mathrm{c,col}}[\ell]\,\mathbf{c}_{\mathrm{s}}(\theta_{\mathrm{c,look,syn}}). \end{aligned} \tag{4.58}$$

Next, beamformers are applied to the synthetic data to obtain the beamspace radar and communication estimates

$$\begin{aligned} \widehat{y}_{\mathrm{syn}}[\ell,\hat{\theta}_{\mathrm{r}}] &= \mathbf{u}_{\mathrm{BF}}^{H}(\hat{\theta}_{\mathrm{r}})\,\mathbf{y}_{\mathrm{s,syn}}(\ell) \\ &= \sqrt{P_{\mathrm{r,syn}}}y_{\mathrm{r,open}}[\ell] + \sqrt{P_{\mathrm{c,syn}}}y_{\mathrm{c,open}}[\ell]\,\alpha(\hat{\theta}_{\mathrm{r}},\theta_{\mathrm{c,look,syn}}) \\ &\quad + \sqrt{P_{\mathrm{r,syn}}}v_{\mathrm{r,col}}[\ell] + \sqrt{P_{\mathrm{c,syn}}}v_{\mathrm{c,col}}[\ell]\,\alpha(\hat{\theta}_{\mathrm{r}},\theta_{\mathrm{c,look,syn}}) \\ \widehat{y}_{\mathrm{syn}}[\ell,\hat{\theta}_{\mathrm{c}}] &= \mathbf{u}_{\mathrm{BF}}^{H}(\hat{\theta}_{\mathrm{c}})\,\mathbf{y}_{\mathrm{s,syn}}(\ell) \\ &= \sqrt{P_{\mathrm{c,syn}}}y_{\mathrm{c,open}}[\ell] + \sqrt{P_{\mathrm{r,syn}}}y_{\mathrm{r,open}}[\ell]\,\alpha(\hat{\theta}_{\mathrm{c}},\theta_{\mathrm{r,look,syn}}) \\ &\quad + \sqrt{P_{\mathrm{c,syn}}}v_{\mathrm{c,col}}[\ell] + \sqrt{P_{\mathrm{r,syn}}}v_{\mathrm{r,col}}[\ell]\,\alpha(\hat{\theta}_{\mathrm{c}},\theta_{\mathrm{r,look,syn}}). \end{aligned} \tag{4.59}$$

The synthetic powers are set to $10\log_{10}(P_{\mathrm{c,syn}}) = NB\tau$ and $10\log_{10}(P_{\mathrm{r,syn}}) = 0$. The communication power is set to counteract any gains from beamforming and pulse compression which ensures the radar response stays below the communication signal after coherent processing. This also ensures the improvement observed is accredited to adaptive algorithms

instead of coherent gain. Taking these parameters into consideration, the fast-time signal becomes

$$\begin{aligned}\widehat{\mathbf{y}}_{\mathrm{f,syn}}\left(\ell,\hat{\theta}_{\mathrm{r}}\right) &= \mathbf{y}_{\mathrm{r,open}}\left(\ell\right)+\sqrt{P_{\mathrm{c,syn}}}\alpha(\hat{\theta}_{\mathrm{r}},\theta_{\mathrm{c,look,syn}})\mathbf{y}_{\mathrm{c,open}}\left(\ell\right)\\ &\quad+\mathbf{v}_{\mathrm{r,col}}\left(\ell\right)+\sqrt{P_{\mathrm{c,syn}}}\alpha(\hat{\theta}_{\mathrm{r}},\theta_{\mathrm{c,look,syn}})\mathbf{v}_{\mathrm{c,col}}\left(\ell\right)\\ \widehat{\mathbf{y}}_{\mathrm{f,syn}}\left(\ell,\hat{\theta}_{\mathrm{c}}\right) &= \sqrt{P_{\mathrm{c,syn}}}\mathbf{y}_{\mathrm{c,open}}\left(\ell\right)+\alpha(\hat{\theta}_{\mathrm{c}},\theta_{\mathrm{r,look,syn}})\mathbf{y}_{\mathrm{r,open}}\left(\ell\right)\\ &\quad+\sqrt{P_{\mathrm{c,syn}}}\mathbf{v}_{\mathrm{c,col}}\left(\ell\right)+\alpha(\hat{\theta}_{\mathrm{c}},\theta_{\mathrm{r,look,syn}})\mathbf{v}_{\mathrm{r,col}}\left(\ell\right),\end{aligned} \tag{4.60}$$

which is used to determine the efficacy of the adaptive algorithms.. The cancellation matrix used within APC and BAPC is

$$\hat{\mathbf{R}}_{\mathrm{canc}}(\ell,\hat{\theta}_{\mathrm{c}})=\widehat{\mathbf{y}}_{\mathrm{f,syn}}\left(\ell,\hat{\theta}_{\mathrm{c}}\right)\widehat{\mathbf{y}}_{\mathrm{f,syn}}^{H}\left(\ell,\hat{\theta}_{\mathrm{c}}\right). \tag{4.61}$$

Within the radar synthetic estimation, the radar portion is unaffected while the communication signal and its corresponding noise are synthetically amplified and scaled by a complex amplitude. Within the radar synthetic estimation, the communication portion is again synthetically amplified while the radar portion is synthetically scaled by a complex amplitude. Some analyses consider the case where communication is not present using the top equation in (4.56)

$$\mathbf{y}_{\mathrm{f,col}}(\ell)=\mathbf{y}_{\mathrm{r,open}}\left(\ell\right)+\mathbf{v}_{\mathrm{r,col}}\left(\ell\right) \tag{4.62}$$

which is similar the top equation in (4.60) without the communication contribution.

4.5.2 Range Performance

The pulse compression responses for the synthetic data is presented. A single PRI and a single collection of the communication of the same duration are combined. The size of the fast-time interval being examined is set to the minimum value of $L=f_{\mathrm{s}}\tau_{\mathrm{r}}=600$ samples. For block size to be consistent within BAPC, the first 1800 samples of the PRI are processed which corresponds to the first 1350 m. Therefore, 3 blocks are processed for BAPC at starting sample marks of

points 0, 600, and 1200. The phased array had $N = 10$ elements. The spatial frequencies were set to $\hat{\theta}_{\mathrm{r}} = \theta_{\mathrm{r,look,syn}} = 0$ and $\hat{\theta}_{\mathrm{c}} = \theta_{\mathrm{c,look,syn}} = 3/2N$ such that the parameters have errorless DOA estimation and the communication signal is in the peak sidelobe of the radar receive beampattern. APC and BAPC procedures conclude after 10 iterations.

Figure 4.8 presents a comparison between match filtering and adaptive approaches with and without interference. The top figure shows the range to 1100 m and the bottom presents a zoomed in version up to 200 m. The high-power pulse compression response seen for APC and BAPC is due to the direct path between the transmit and receive antennas. The horizontal axis is shifted based on the direct path range. The match filter response, denoted as MF in the figures throughout the analyses, succumbs to the interference from the communication signal. APC and BAPC are both able to remove the interference and get an estimation of the range profile. APC provides the most robust solution of the lower SNR results. BAPC fidelity diminishes in its estimation for the lower SNR signals as seen between 200-400 m. Otherwise, APC and BAPC interference suppression overlap. They differ in their estimation resolution performance. For example, APC is able to have a better notch depth at approximately 45m and can also discern two closely spaced scatterers at 70 m. BAPC detection performance diminishes due to the resolution loss. However, BAPC does provide the computation improvement and similar interference suppression.

APC and match filter response without interference is presented in Figure 4.9. The match filter response without interference presents a familiar aggregate of range-delayed sinc responses from using a LFM. APC is able to obtain the same response with or without the interference present. BAPC and match filter response comparison is presented in Fig. 4.10. BAPC has similar results to APC. Each are able to unmask targets that were previously obscured by the direct path range sidelobes seen at 70 m, 80 m, and 90 m. Lastly, Figure 4.11 presents a comparison of APC with and without the inclusion of the SaCM within the filter. The inclusion of the communication SaCM is required for APC to obtain a robust solution. Without an estimate of the communication signal, APC returns to the match filter response. The response for BAPC without the SaCM is omitted since it is similar to APC without the SaCM. The results shows that the SaCM implemented with

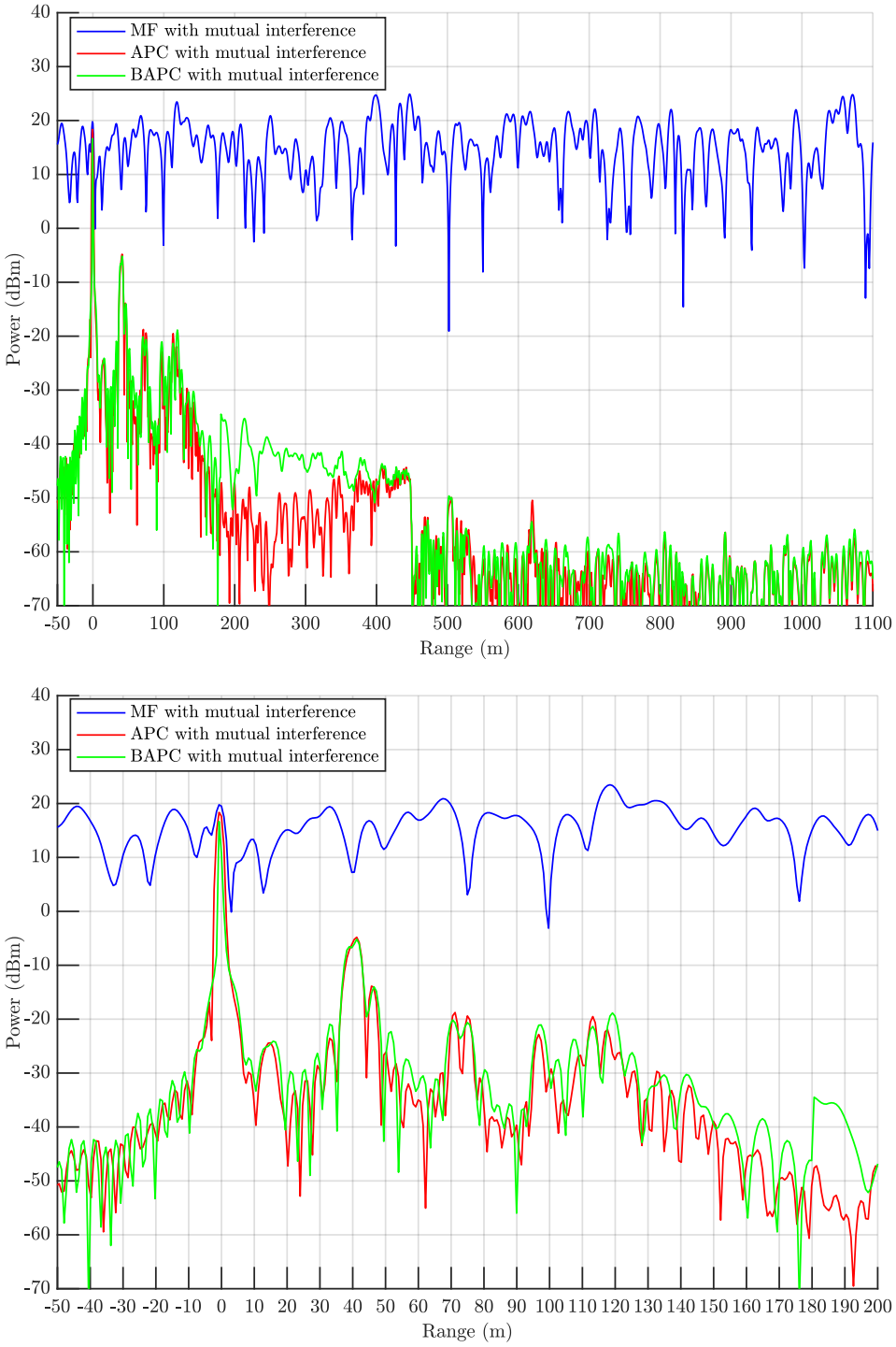

Fig. 4.8: Pulse compression response using a match filter (blue), APC (red), and BAPC (green) adaptive filter with and without interference at zero-Doppler; Zoomed in depiction at the bottom

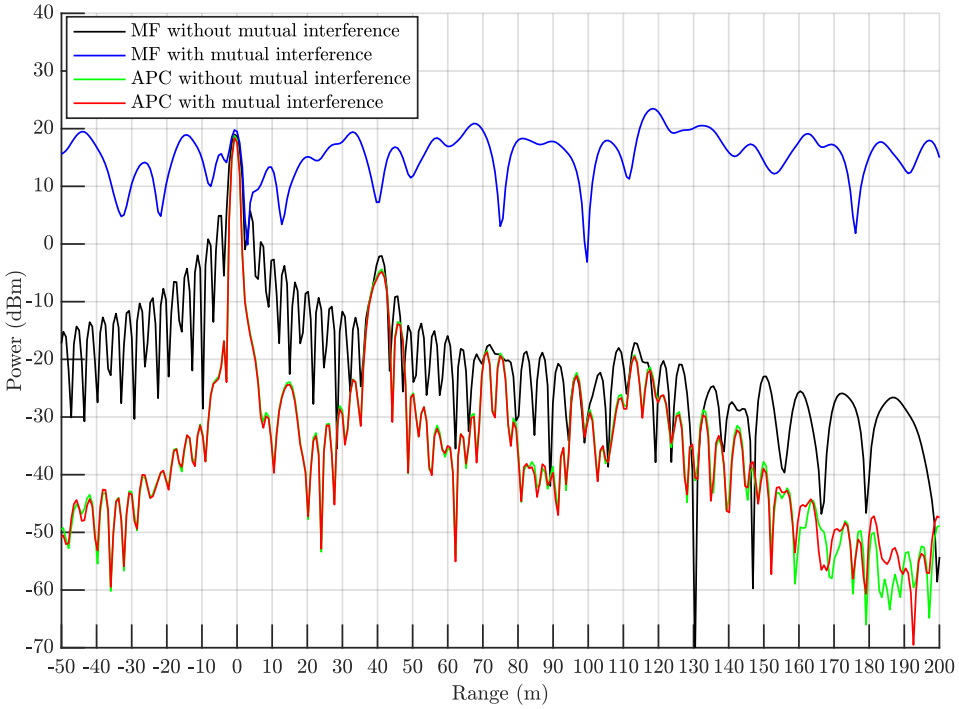

Fig. 4.9: Match filter and APC response with and without interference at zero-Doppler

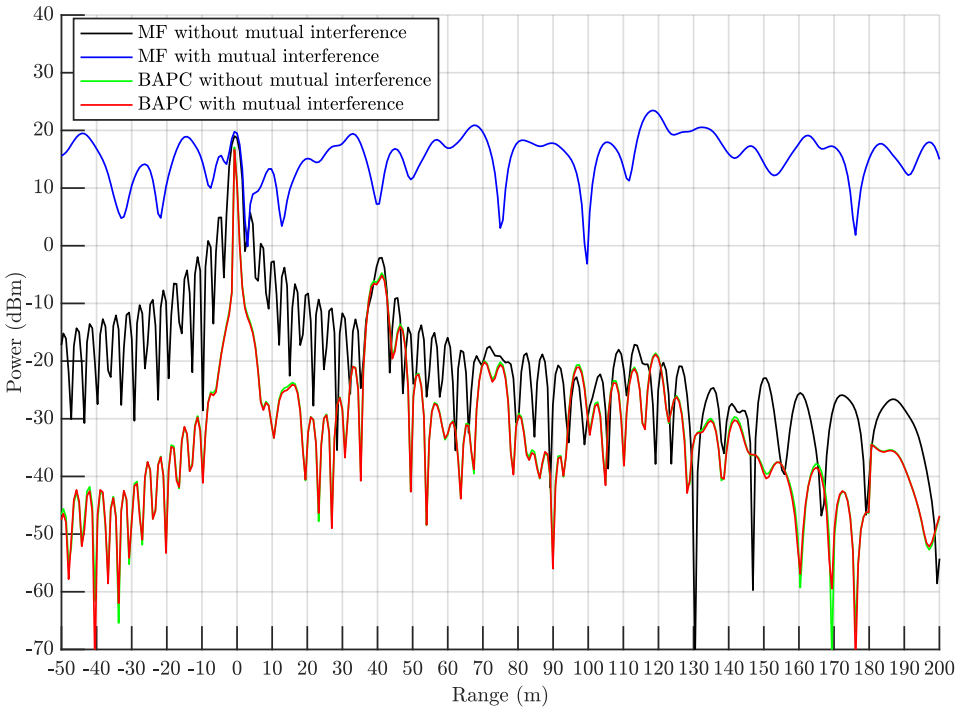

Fig. 4.10: Match filter and BAPC response with and without interference at zero-Doppler

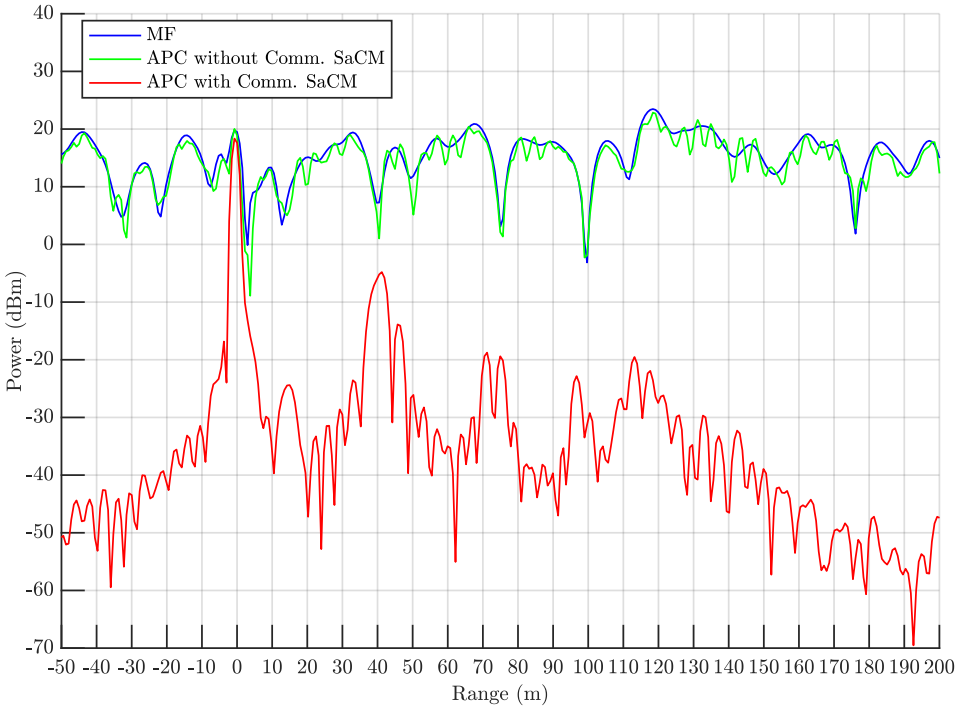

Fig. 4.11: APC response with and without SaCM

the solution for cancellation is critical to mitigate the interference.

4.5.3 Angle Estimation Error

A Monte Carlo analysis is conducted to address the ramifications from beamforming and inaccurate DOA estimation. The communication signal is segmented into 1000 segments with each having 1800 samples. A different communication segment is used each trial. The radar PRI examined remains the same for all the trials. The results are presented for BAPC only since APC presents similar performance behavior.

The first analysis addresses the loss of BAPC suffers as angle separation between radar DOA and communication DOA varies. The analysis assumes errorless DOA estimation of the communication signal $\hat{\theta}_{\mathrm{c}} = \theta_{\mathrm{c,look,syn}}$ and varies $\hat{\theta}_{\mathrm{c}}$ to determine how performance degrades with spatial frequency separation from $\hat{\theta}_{\mathrm{r}}$. The transmit and receive beams for the radar were steered to boresight $\hat{\theta}_{\mathrm{r}} = \theta_{\mathrm{r,look,syn}} = 0$. An initial analysis of the loss factor presented that BAPC suffers from self-cancellation loss when the communication is in the mainbeam of the radar beampattern.

A loss factor based on the cancellation loss was developed that considers the ratio of BAPC with and without interference present

$$LF_1\left[\ell,\hat{\theta}_c\right]=\left|\frac{\mathbf{u}^H_{\text{BAPC,syn}}(\ell,\hat{\theta}_c)\widehat{\mathbf{y}}_{\text{f,syn}}\left(\ell,\hat{\theta}_r;\theta_{\text{r,look,syn}}\right)}{\mathbf{u}^H_{\text{BAPC,col}}(\ell)\mathbf{y}_{\text{f,col}}\left(\ell\right)}\right|^2 \tag{4.63}$$

where $\mathbf{u}_{\text{BAPC,syn}}(\ell,\hat{\theta}_c)$ is the filter generated for synthetic data and $\mathbf{u}_{\text{BAPC,col}}(\ell)$ is the filter generated for collected data. The dependence of $\hat{\theta}_c$ on the BAPC filter is due to the dependence on $\hat{\mathbf{R}}_{\text{canc}}(\ell,\hat{\theta}_c)$ subsumed into the filter. The loss factor effectively would take the power ratio between the red and green trace in Figure 4.9 as $\hat{\theta}_c$ varies. The loss factor is examined at the direct path response.

Figure 4.12 presents the performance loss for BAPC for different array sizes. BAPC is most effective against communication signals within its sidelobes. As the radar begins to transit and receive in the direction of the communication signal, BAPC effectiveness diminishes. This is

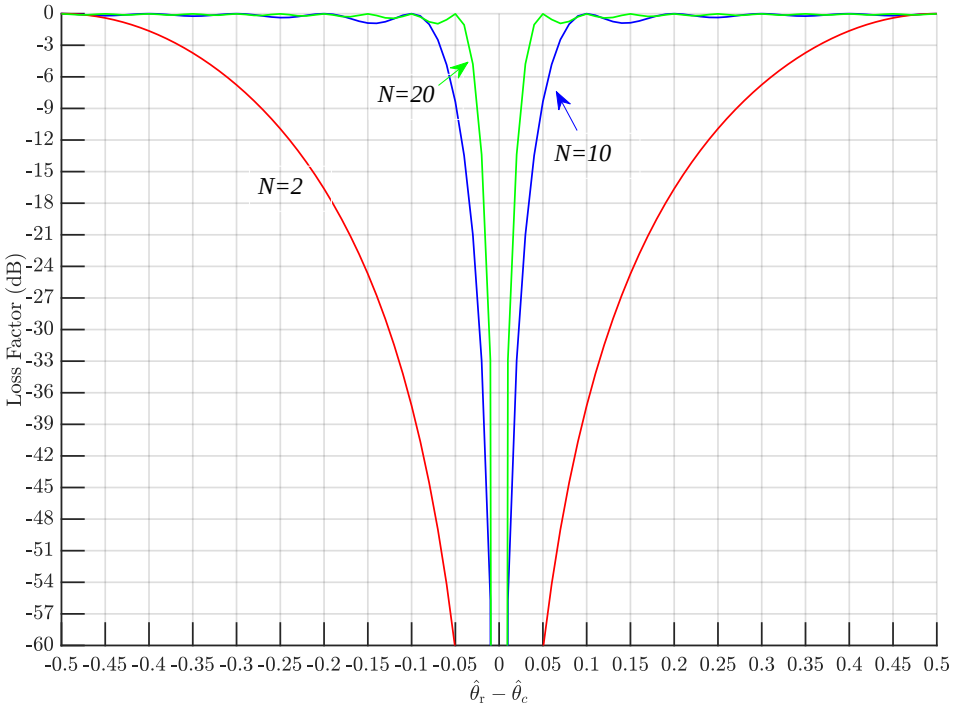

Fig. 4.12: BAPC performance loss by spatial frequency separation of radar and communication signal

due to the radar and communication beamspace fast-time estimate becoming less separated. This means that $\widehat{\mathbf{y}}_{\text{f,syn}}\left(\ell,\hat{\theta}_{\text{c}}\right)$ is approaching equality with $\widehat{\mathbf{y}}_{\text{f,syn}}\left(\ell,\hat{\theta}_{\text{r}}\right)$. When equality is reached, self-cancellation on the radar estimate begins to occur. As the number of array elements increase, the effective of the mainlobe deceases. This is to be expected since the 3 dB beamwidth decreases with increasing N. The ripple that is seen is due to the sidelobe peaks. APC and BAPC performs best when the communication signal outside the mainbeam. If communication signal is in the receive beamformer mainbeam of the radar, self-cancellation loss can occur.

A second analysis examines the communication DOA estimation error tolerance. Consider an estimation error θ_{err} such that

$$\hat{\theta}_{\text{c}} = \theta_{\text{c,look,syn}} + \theta_{\text{err}}. \tag{4.64}$$

The radar DOA look direction and radar DOA estimate are fix in the direction of boresight. The communication DOA look direction is fixed in the first peak sidelobe of the radar beamformer beampattern at $\theta_{\text{c,look,syn}} = 3/2N$. The error is examined for $\pm 1/N$ at $N = 20$. The error is θ_{err} which varies $\hat{\theta}_{\text{c}}$ as a well. An preliminary examined of the error tolerance showed that an estimation loss from the match filter response occurs. A loss factor based on the estimation loss is considered that takes the ratio of the match filter and BAPC response with interference present

$$LF_2\left[\ell,\hat{\theta}_{\text{c}}\right] = \left|\frac{\mathbf{u}_{\text{MF},\ell}^H \widehat{\mathbf{y}}_{\text{f,syn}}\left(\ell,\hat{\theta}_{\text{r}}\right)}{\mathbf{u}_{\text{BAPC,syn}}^H(\ell,\hat{\theta}_{\text{c}})\mathbf{y}_{\text{f,syn}}\left(\ell,\hat{\theta}_{\text{r}}\right)}\right|^2. \tag{4.65}$$

The loss factor would take the power ratio between the blue and green trace in Figure 4.11 as $\hat{\theta}_{\text{c}}$ varies.

Figure 4.13 present the error tolerance for BAPC. The estimation loss is examined over the beamwidth of the communication beamformer beampattern. As the error increases towards the first null on each side of the beampattern, the cancellation matrix $\hat{\mathbf{R}}_{\text{canc}}(\ell)$ approaches $\mathbf{0}_{K\times K}$ effectively making the cancellation ineffective. Therefore, APC and BAPC performs similar to the green trace in Fig. 4.11 where the cancellation matrix. The response from DOA estimation error is consistent over N meaning the error tolerance increases with decreasing number of array elements. APC

and BAPC performs best when the communication DOA estimate is within half the null-to-null beamwidth. If the estimated DOA of the communication is greater than the null-to-null beamwidth of the beamformer, a estimation loss occurs making the adaptive approaches ineffective.

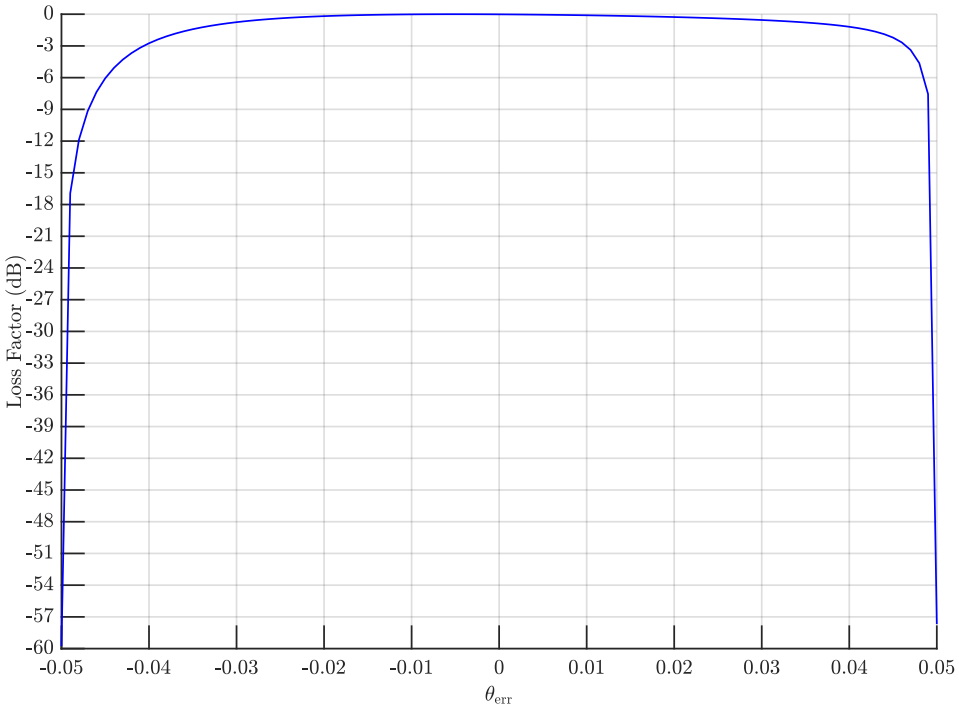

Fig. 4.13: BAPC performance loss by communication DOA estimation error

Chapter 5

Conclusions and Future Work

Conclusions and future work to the topics are highlighted below. Throughout this work, mismatch processing is combined with interference cancellation for enhanced signal estimation in the presence of interference. Additionally, computing challenges that come with the proposed mismatch approaches are addressed via sub-optimal approaches. Sections 5.1, 5.2, and 5.3 address Chapters 2, 3, and 4 respectively.

5.1 Adaptive Mismatch Doppler Processing for Uniform and Staggered Pulse Repetition Interval Radar

Adaptive mismatch Doppler processing (AMMDP), a form of re-iterative minimum mean-square error (RMMSE), is proposed for spectral estimation for uniform and random staggered pulse repetition interval (PRI) staggering. To address the computationally pitfalls of adaptive filter generation, partial adaptive mismatch Doppler processing (PAMMDP) was introduced. Non-uniform sampling increases the correlation of frequencies in the Doppler spectrum thereby increasing the sidelobe response and decreasing aliasing. By accounting for the non-uniform sampling within the temporal steering vector, AMMDP was shown to be provide robustness to uniform and staggered PRI transmissions. PAMMDP was robust to uniform PRI transmissions and provided a trade-space between performance and computation as function of the reduced-rank of the filter for random staggered PRI transmissions. AMMDP and PAMMDP were shown to improve in estimation performance when integrated with adaptive clutter cancellation. The techniques were experimentally demonstrated on open-air experimental data. A major caveat

of AMADE and PAMADE is beamspoiling which increases the computation. The results presented focus on stationary radar in slow-time and were a baseline to the use of RMMSE in space-time (spatial/slow-time) for airborne sidelooking radar in Chapter 3.

Future work includes exploring different transformation matrices for rank reduction. The transformation matrices leveraged are well known to be useful. Proven matrices were necessary to show the efficacy of the proposed PAMMDP formulation. Modifying the form of the Doppler transformation matrix may improve estimation and cancellation abilities. Another path for future work is exploring different cancellation matrices. Using adaptive cancellation for clutter cancellation of stationary radar is not necessary but rather a more robust approach to explore over non-adaptive techniques. The exploration of adaptive filter is a precursor to using MMSE for airborne GMTI where adaptive filtering is essentially required for adequate clutter cancellation.

5.2 Optimal and Adaptive Mismatch Angle-Doppler Processing for Airborne Radar

Optimal and adaptive forms of mismatch processing for angle-Doppler estimation was combined with adaptive clutter cancellation using traditional space-time adaptive processing (STAP) approaches for side-looking airborne radar. Optimal mismatch processing uses a least-squares (LS) cost function. Adaptive mismatch processing, named adaptive mismatch angle-Doppler estimation (AMADE), uses RMMSE. The computational cost of the estimation approaches were addressed via the introduction of reduced-rank approaches for each algorithm. The reduced-rank mismatch processing approaches named reduced-rank least-squares (RRLS) and partially adaptive mismatch angle-Doppler estimation (PAMADE), respectively, were combined with well-known reduced-rank STAP approaches. LS shown a lack of robustness and provided minimal sidelobe suppression. RRLS benefited from rank-reduction but overall had a similar response to LS. AMADE and PAMADE provide robust angle-Doppler sidelobe suppress. PAMADE had minimal performance loss as the covariance matrix reduction increased. AMADE

and PAMADE performance significantly improves when combined with adaptive cancellation. A major caveat of AMADE and PAMADE is beamspoiling which increases the computation. The approaches were experimentally demonstrated using open-air synthetic aperture radar (SAR) ground moving target indication (GMTI) experimental dataset from the Air Force Research Laboratory called GOTCHA. The experimental demonstration confirmed their applicability to data.

Future work includes explore different configurations and structures of transformation matrices to reduce rank and different. Also consider that the work from this chapter align close with the previous chapter. They differ in the steering vectors being used (slow-time and space-time respectively). The future work from the previous chapter effectively relates to this chapter as well.

5.3 Adaptive Mismatch Processing for Radar and Communication Coexistence

Radar and communication cohabitation in the radio spectrum is addressed via the application of receive digital beamforming of element-space signals and adaptive filtering of fast-time signals. Adaptive pulse compression (APC) using RMMSE is proposed for simultaneous estimation of the radar range profile and removal of the interfering communication. Additionally, a suboptimal computationally efficient version of APC called block APC (BAPC) is also proposed. Each approach was applied to synthetically combined radar and communication data separately capture from open-air experiments. Beamforming was leveraged to separate the signals by their direction-of-arrival onto receive phased array. Doing so provide separate estimates of the radar and communication signals. The radar estimate assisted with the estimation while the communication signal assisted with the cancellation. APC and BAPC were shown to be effective in mitigating a 4G long-term evolution (LTE) wireless communication signal and estimating the range profile. Each estimate was leveraged within the APC and BAPC. APC provides a robust

response while BAPC suffers a performance loss for low SNR signals. However, BAPC is able to reduce computation by the number of range bins being examined. Both approaches can suffer a estimation loss if the direction-to-arrival estimate of the communication has a error beyond a half-beamwidth and a self-cancellation loss if the communication transmit signal is in in the mainbeam of the radar.

Future work should entail implementing the proposed techniques on collected data instead of synthetic data. A natural progression for future work is incorporating adaptive digital beamformers prior to performing adaptive pulse compression. A sidelobe canceller in the direction of the competing signal will provide better estimates of the radar and communication collections. Any residual interference within the radar signal from the communication signal may be mitigated by APC or BAPC.

Appendix A

Derivation of Maximum Signal-to-Noise Ratio and Signal-to-Interference-Plus-Noise Ratio Filters

Radars, and radio frequency (RF) devices, operate in a noise-limited environment due to active components within the RF receiver (primarily during signal amplification) producing and subsequently contributing a noisy signal to the recieved RF signal. The ratio of the relative powers of the signal and noise known as the signal-to-noise ratio (SNR) is a key metric to analyzing radar signal processing performance. As such, a higher SNR provides better radar detection performance due to higher dynamic range and sensitivity. However, there are limitations to SNR performance since signal power is driven by amplification from the RF transmitter and losses from open-air propagation and lossy RF hardware components. In radar receive processing, passing the receive signal through a maximum signal-to-noise (SNR) filter provides the maximum likelihood estimate (MLE) of the signal in a noise-limited environment. The filter maximizes the signal strength by exploiting the coherence from a known transmitted signal.

Radars often operate in scenes that are interference-limited due to signals captured during the open-air propagation of the transmit signal. One example is clutter reflections. The interference dominates the noise. The interference raises the "noise floor" and causing a loss in radar sensitivity and dynamic range. The power of the noise floor becomes an a aggregate of the noise and interference powers. The ratio of signal and aggregate of interfering sources known as the signal-to-interference-plus-noise ratio (SINR) becomes the driving factor for radar performance. The metric likewise has practical limitations. Passing the receive signal through a maximum signal-to-interference-plus-noise ratio (SINR) filter maximizes the signal strength via signal

coherence and performs interference cancellation in a sequential manner.

Throughout this work, noise- and interference-limited environments are explored in various radar signal domains (fast-time, slow-time, and element-space signals). As such, the reader should have awareness of the maximum SNR and SINR filters. Below are generalized versions of the maximum SNR and SINR filter as derived in [22]. A maximum SNR and SINR filter can be developed with proper manipulation of the signal model to fit the RF signal domain of interest under similar statistical assumptions.

Consider a discretized signal oriented into a $K \times 1$ data snapshot $\mathbf{z}(t)$ containing a signal $\mathbf{s}(t)$, interference $\mathbf{i}(t)$, and noise $\mathbf{n}(t)$

$$\mathbf{z}(t) = x(t)\mathbf{s}(t) + \mathbf{i}(t) + \mathbf{n}(t). \tag{A.1}$$

where the vector $\mathbf{z}(t) = [\ z(t) \quad \cdots \quad z(t+1) \quad \cdots \quad z(t+K-1)\ ]^T$ is formed using samples of the signal and $x(t)$ is a complex amplitude. Note, $\mathbf{s}(t)$, $\mathbf{i}(t)$, and $\mathbf{n}(t)$ are formed similarly to $\mathbf{z}(t)$. In context to radar signals, the transmitted signal is deterministic and known at the receiver. The complex amplitude, interference, and noise are unknown stochastic processes. Therefore, their statistics are examined.

The first and second order moments of the signals are of the most interest. The first moment is captured in the mean of the signal. The second moment is captured in the autocovariance (or covariance for short) of the signal. The formal definition of covariance matrix is

$$\mathbf{R}(t) = E\left\{\mathbf{a}(t)\mathbf{a}^H(t)\right\} - E\left\{\mathbf{a}(t)\right\}\left(E\left\{\mathbf{a}(t)\right\}\right)^H \tag{A.2}$$

where $(\bullet)^H$ denotes conjugate transposition, $E\{\bullet\}$ is the expectation operator, and $\mathbf{a}(t)$ is an arbitrary $K \times 1$ vector [22]. The vector outer product consists of the variance/auto-correlation of a single element on the main diagonal and co-variance/cross-correlation of different elements on the off-diagonal terms [22]. The covariance matrix is symmetric, positive definite Hermitian matrix. Having the covariance matrix be full rank is ideal but not always the case.

The stochastic processes are considered to be wide-sense stationary and ergodic. The signal is stationary in the wide sense when the mean is constant, $E\{\mathbf{a}(t)\} = \mu_{\mathbf{a}}(t)$, and the covariance matrix depends on delay $E\{\mathbf{a}(t)\mathbf{a}^H(t+\tau)\} = \mathbf{R}(\tau)$ [11]. Ergodicity stems from the signal mean and variance maintaining a constant as a function of time. Therefore, $\lim_{t\to\infty} E\{\mu_{\mathbf{a}}(t)\} = \mu_{\mathbf{a}}$ and $\lim_{t\to\infty} \text{var}\{\mu_{\mathbf{a}}(t)\} = 0$ for signal mean and likewise $\lim_{t\to\infty} E\{\mathbf{R}(t)\} = \mathbf{R}$ and $\lim_{t\to\infty} \text{var}\{\mathbf{R}(t)\} = 0$ for signal variance where $\text{var}\{\bullet\}$ is the variance operation [11]. All in all, the signal mean and covariance are fixed over time. In radar, the signals are considered to have zero-mean making (B.2)

$$\mathbf{R}(t) = E\left\{\mathbf{a}(t)\mathbf{a}^H(t)\right\}. \tag{A.3}$$

Consider a filter $\mathbf{w}(t)$ is formed for estimation of $x(t)$ via application to the receive data $\mathbf{z}(t)$

$$\hat{x}(t) = \mathbf{w}^H(t)\mathbf{z}(t) = x(t)\mathbf{w}^H(t)\mathbf{s}(t) + \mathbf{w}^H(t)\mathbf{i}(t) + \mathbf{w}^H(t)\mathbf{n}(t) \tag{A.4}$$

where accent $\hat{\bullet}$ represents an estimate. The power of each component after filter application is determined for later use in SNR and SINR. The signal power is

$$P_{\text{s}}(t) = E\left\{\left|x(t)\mathbf{w}^H(t)\mathbf{s}(t)\right|^2\right\} = E\left\{\left|x(t)\right|^2\right\}\left|\mathbf{w}^H(t)\mathbf{s}(t)\right|^2 = \sigma_{\text{s}}^2(t)\left|\mathbf{w}^H(t)\mathbf{s}(t)\right|^2. \tag{A.5}$$

The interference power is

$$P_{\text{i}}(t) = E\left\{\left|\mathbf{w}^H(t)\mathbf{i}(t)\right|^2\right\} = \mathbf{w}^H(t)E\left\{\mathbf{i}(t)\mathbf{i}^H(t)\right\}\mathbf{w}(t) = \mathbf{w}^H(t)\mathbf{R}_{\text{i}}(t)\mathbf{w}(t). \tag{A.6}$$

The distribution of the interference component may or may not be independent or identically distributed. With that being said, $\mathbf{R}_{\text{i}}(t) = E\left\{\mathbf{i}(t)\mathbf{i}^H(t)\right\}$ is maintained for generality. The noise power is

$$P_{\text{n}}(t) = E\left\{\left|\mathbf{w}^H(t)\mathbf{n}(t)\right|^2\right\} = \mathbf{w}^H(t)E\left\{\mathbf{n}(t)\mathbf{n}^H(t)\right\}\mathbf{w}(t) = \mathbf{w}^H(t)\mathbf{R}_{\text{n}}(t)\mathbf{w}(t). \tag{A.7}$$

The elements in the noise are considered statistically independent and have the same Gaussian distribution. The noise has a mean vector $\mathbf{0}_{K\times 1}$ and covariance matrix $\mathbf{R}_{\mathrm{n}}(t) = \sigma_{\mathrm{n}}^2\mathbf{I}_{K\times K}$ with variance/noise power σ_{n}^2.

SNR is the ratio of (A.5) and (A.7)

$$\mathrm{SNR}(t) = \frac{P_{\mathrm{s}}(t)}{P_{\mathrm{n}}(t)} = \frac{\sigma_{\mathrm{s}}^2(t)\left|\mathbf{w}^H(t)\mathbf{s}(t)\right|^2}{\sigma_{\mathrm{n}}^2\mathbf{w}^H(t)\mathbf{R}_{\mathrm{n}}(t)\mathbf{w}(t)}. \tag{A.8}$$

Expanding (A.8) using the Cauchy-Schwarz inequality $|\mathbf{a}^H\mathbf{b}|^2 \leq \|\mathbf{a}\|^2\|\mathbf{b}\|^2$, where $\|\bullet\|$ denotes the norm operator, SNR is maximized such that

$$\begin{aligned}
\frac{\sigma_{\mathrm{s}}^2(t)\left|\mathbf{w}^H(t)\mathbf{s}(t)\right|^2}{\mathbf{w}^H(t)\mathbf{R}_{\mathrm{n}}(t)\mathbf{w}(t)} &\leq \frac{\sigma_{\mathrm{s}}^2(t)\|\mathbf{w}(t)\|^2\|\mathbf{s}(t)\|^2}{\mathbf{w}^H(t)\left(\sigma_{\mathrm{n}}^2\mathbf{I}_{K\times K}\right)\mathbf{w}(t)} \\
&= \frac{\sigma_{\mathrm{s}}^2(t)\mathbf{w}^H(t)\mathbf{w}(t)\mathbf{s}^H(t)\mathbf{s}(t)}{\sigma_{\mathrm{n}}^2\mathbf{w}^H(t)\mathbf{w}(t)} \\
&= \frac{\sigma_{\mathrm{s}}^2(t)\mathbf{s}^H(t)\mathbf{s}(t)}{\sigma_{\mathrm{n}}^2} \\
&= \frac{\sigma_{\mathrm{s}}^2(t)\mathbf{w}^H(t)\mathbf{s}(t)}{\sigma_{\mathrm{n}}^2}
\end{aligned} \tag{A.9}$$

Therefore, optimal maximum SNR filter is obtained by setting the filter to

$$\mathbf{w}_{\mathrm{SNR}}(t) = \frac{1}{\mathbf{s}^H(t)\mathbf{s}(t)}\mathbf{s}(t). \tag{A.10}$$

such that (A.9) equates to maximum SNR value of

$$\mathrm{SNR}_{\max}(t) = \sigma_{\mathrm{s}}^2(t)/\sigma_{\mathrm{n}}^2 \tag{A.11}$$

The maximum SNR filter is a bandpass finite impulse response (FIR) filter that matches the frequency extent of the signal.

SINR is define as the ratio between the signal power and summation of the interference and

noise powers. The powers definitions from (A.4-A.6) are leveraged within this ratio such that

$$\begin{aligned}
\mathrm{SINR}(t) &= \frac{P_{\mathrm{s}}(t)}{P_{\mathrm{i}}(t)+P_{\mathrm{n}}(t)} \\
&= \frac{\sigma_{\mathrm{s}}^2(t)\left|\mathbf{w}^H(t)\mathbf{s}(t)\right|^2}{\mathbf{w}^H(t)\mathbf{R}_{\mathrm{i}}(t)\mathbf{w}(\mathbf{t})+\mathbf{w}^H(t)\mathbf{R}_{\mathrm{n}}(t)\mathbf{w}(t)} \\
&= \frac{\sigma_{\mathrm{s}}^2(t)\left|\mathbf{w}^H(t)\mathbf{s}(t)\right|^2}{\mathbf{w}^H(t)\left(\mathbf{R}_{\mathrm{i}}(t)+\mathbf{R}_{\mathrm{n}}(t)\right)\mathbf{w}(t)} \\
&= \frac{\sigma_{\mathrm{s}}^2(t)\left|\mathbf{w}^H(t)\mathbf{s}(t)\right|^2}{\mathbf{w}^H(t)\mathbf{R}_{\mathrm{opt}}(t)\mathbf{w}(t)}
\end{aligned} \tag{A.12}$$

where $\mathbf{R}_{\mathrm{opt}}(t)$ optimal interference covariance matrix defined as

$$\mathbf{R}_{\mathrm{opt}}(t) = \mathbf{R}_{\mathrm{i}}(t)+\mathbf{R}_{\mathrm{n}}(t) = \mathbf{R}_{\mathrm{i}}(t)+\sigma_{\mathrm{n}}^2\mathbf{I}_{K\times K} \tag{A.13}$$

Before going forward, by definition of a matrix inverse, the relationship $\mathbf{R}_{\mathrm{opt}}^{1/2}(t)\mathbf{R}_{\mathrm{opt}}^{-1/2}(t) = \mathbf{I}_{K\times K}$ is true. Utilizing the Cauchy-Schwarz inequality, SINR becomes

$$\begin{aligned}
\frac{\sigma_{\mathrm{s}}^2(t)\left|\mathbf{w}^H(t)\mathbf{s}(t)\right|^2}{\mathbf{w}^H(t)\mathbf{R}_{\mathrm{opt}}\mathbf{w}(t)} &= \frac{\sigma_{\mathrm{s}}^2(t)\left|\mathbf{w}^H(t)\mathbf{R}_{\mathrm{opt}}^{1/2}(t)\mathbf{R}_{\mathrm{opt}}^{-1/2}(t)\mathbf{s}(t)\right|^2}{\mathbf{w}^H(t)\mathbf{R}_{\mathrm{opt}}(t)\mathbf{w}(t)} \\
&\leq \frac{\sigma_{\mathrm{s}}^2(t)\left\|\mathbf{R}_{\mathrm{opt}}^{1/2}(t)\mathbf{w}(t)\right\|^2\left\|\mathbf{R}_{\mathrm{opt}}^{-1/2}(t)\mathbf{s}(t)\right\|^2}{\mathbf{w}^H(t)\mathbf{R}_{\mathrm{opt}}(t)\mathbf{w}(t)} \\
&= \frac{\sigma_{\mathrm{s}}^2(t)\mathbf{w}^H(t)\mathbf{R}_{\mathrm{opt}}(t)\mathbf{w}(t)\mathbf{s}^H(t)\mathbf{R}_{\mathrm{opt}}^{-1}\mathbf{s}(t)}{\mathbf{w}^H(t)\mathbf{R}_{\mathrm{opt}}(t)\mathbf{w}(t)} \\
&= \sigma_{\mathrm{s}}^2(t)\mathbf{s}^H(t)\mathbf{R}_{\mathrm{opt}}^{-1}(t)\mathbf{s}(t) \\
&= \psi\sigma_{\mathrm{s}}^2(t)
\end{aligned} \tag{A.14}$$

[22] such that $\psi = \|\mathbf{R}_{\mathrm{opt}}^{-1/2}(t)\mathbf{s}(t)\|^2$ which is residual mismatch. The optimal maximum SINR filter is

$$\mathbf{w}_{\mathrm{SINR}}(t) = \frac{1}{\psi}\mathbf{R}_{\mathrm{opt}}^{-1}(t)\mathbf{s}(t) \tag{A.15}$$

which sequentially attenuates the interference sources and estimates x. The maximum SINR filter

is sequential bandstop (notch) FIR filter that matches the frequency extent of the interference and a bandpass FIR filter that matches the frequency extent of the signal. The obvious difference between SNR and SINR filters is the inclusion of the optimal covariance matrix which performs the bandstop filtering operation. Where the SNR filter is simply a estimation procedure, the SINR filter is a sequential cancellation-then-estimation procedure.

Appendix B

List of Acronyms, Mathematical Notations, and Operators

B.1 Acronyms

Acronym	Description
3GPP	3rd-Generation Partnership Project
4G	Fourth generation
5G	Fifth generation
ADC	Analog-to-digital conversion
ALF	Average loss factor
AMADE	Adaptive mismatch angle-Doppler estimation
AMMDP	Adaptive mismatch Doppler processing
APC	Adaptive pulse compression
ASR	Average sidelobe response
AWGN	Additive white Gaussian noise
BAPC	Block adaptive pulse compression
BaSC	Baseline supplementary cancellation
BaSL	Baseline supplementary loading
CFAR	Constant false alarm rate
CNR	Clutter-to-noise ratio
CPI	Coherent processing interval
CUT	Cell-under-test

Acronym	Description
CW	Continuous wave
DFT	Discrete Fourier transform
DOA	Direction-of-arrival
DPCA	Displace phase center antenna
EM	Electromagnetic
EMI	Electromagnetic interference
ESPRIT	Estimation of signal parameters via rotational invariance technique
FAA	Federal Aviation Administration
FAPC	Fast adaptive pulse compression
FCC	Federal Communications Commission
FDD	Frequency-division duplexing
FIR	Finite impulse response
FM	Frequency modulation
FMCW	Frequency modulation continuous wave
FT	Fourier transform
GMTI	Ground moving target indication
HPA	High power amplifier
ICM	Internal clutter motion
IID	Independent and identically distributed
IIR	infinite impulse response
IQ	in-phase and quadrature
ISI	inter-symbol interference
LCM	Least common multiple
LCMV	Linear constrained minimum variance
LFM	Linear frequency modulation

Acronym	Description
LNA	Low-noise amplifier
LS	Least-squares
LTE	Long term evolution
MAPC	Multi-static adaptive pulse compression
MDD	Minimum detectable Doppler
MF-RMMSE	Match filter re-iterative minimum mean-square error
MIMO	Multi-input multiple-output
MLE	Maximum likelihood estimate
MMSE	Minimum mean-square error
MSE	Mean-square error
MTI	Moving target indication
MUSIC	Multiple-signal characterization method
MVDR	Minimum variance distortionless response
NTIA	National Telecommunications and Information Administration
OFDM	Orthogonal frequency division multiplexing
OFDMA	Orthogonal frequency division multiple access
PAMADE	Partial adaptive mismatch angle-Doppler estimation
PAMMDP	Partial Adaptive mismatch Doppler processing
PCAST	President's Council of Advisors on Science and Technology
PD	Pulse-Doppler
PRF	Pulse repetition frequency
PRI	Pulse repetition interval
PSK	Phase-shift keying
QAM	Quadrature amplitude modulation
QPSK	Quadrature phase-shift keying

Acronym	Description
RCS	Radar cross section
RD-RMMSE	Reduced dimension re-iterative minimum mean-square error
RD-RISR	Reduced dimension re-iterative superresolution
RF	Radio frequency
RIAA	Real-valued iterative adaptive approach
RISR	Re-iterative superresolution
RMB	Reed, Mallett, and Brennan
RMMSE	Re-iterative minimum mean-square error
RRLS	Reduced rank least-squares
SaCM	Sample covariance matrix
SAR	Synthetic aperture radar
SC-FDMA	Single-carrier frequency division multiple access
SIMO	Single-input multiple-output
SINR	Signal-to-interference-plus-noise ratio
SIR	Signal-to-interference ratio
SLAR	Side-looking airborne radar
SNR	Signal-to-noise ratio
SRAP	Space-range adaptive processing
STAP	Space-time adaptive processing
StCM	Structure covariance matrix
TDD	Time-division duplexing
TDMA	Time-division multiple access
TRAP	Time-range adaptive processing
TRSR	Total residual sidelobe response
ULA	Uniform linear array

B.2 Mathematical Notations and Operations

Notation	Description
a	Scalar quantity
A	Scalar quantity or set (when explicitly defined)
$\mathbf{a}$	Column vector quantity
$\mathbf{A}$	Matrix quantity
$a(x)$	Continuous function dependent on variable t. In the case where it is a combination of continuous and discrete, this notation supersedes.
$a[\ell]$	Discrete scalar dependent on variable ℓ
$a(x,y)$	Continuous function dependent on discrete scalar variable x and continuous variable y
$\mathbf{a}(\ell)$	Discrete vector dependent variable ℓ
$\mathbf{A}(\ell)$	Discrete matrix dependent on variable ℓ
$\bullet^*$	Complex conjugation operation of a quantity (superscript)
$\bullet^T$	Transposition operation of a quantity (superscript)
$\bullet^H$	Conjugate (Hermitian) transposition operation of a quantity (superscript)
$\mathrm{Re}\{\bullet\}$	Real component of a complex-valued quantity
$\mathrm{Im}\{\bullet\}$	Imaginary component of a complex-valued quantity
$E\{\bullet\}$	Expected value operation of a quantity
$\mathrm{var}\{\bullet\}$	variance of a quantity
$\lvert a\rvert$	Absolute value operation of a scalar
$\langle a(x), b(x)\rangle$	Continuous-time inner product of functions $a(x)$ and $b(x)$
$a(x) * b(x)$	Convolution operation of functions $a(x)$ and $b(x)$
$\underset{x}{\mathrm{argmin}}\{a(x)\}$	Argument minimum operation of $a(x)$ with respect to x
$\nabla_b a(x)$	Gradient operation of function $a(x)$ with respect to b
$\lVert\mathbf{a}\rVert$	Euclidean norm operation of a vector

Notation	Description
$\|\mathbf{A}\|$	Euclidean norm operation of a matrix
$\|\mathbf{A}\|_F$	Frobenius norm operation of a matrix
$\mathrm{Tr}\{\mathbf{A}\}$	Trace operation of a matrix
$\mathrm{rank}\{\mathbf{A}\}$	Rank of a matrix
$\mathbf{A} \odot \mathbf{B}$	Element-wise (Hadamard) product operation of matrices **A** and **B**
$\mathbf{A} \otimes \mathbf{B}$	Kronecker product operation of matrices **A** and **B**
$\mathbf{0}_{N\times 1}$	A vector containing only the number of dimension $N \times 1$ (in this example only 0)
$\mathbf{I}_{N\times N}$	Identity matrix of dimension $N \times N$
$\mathfrak{c}\{\bullet\}$	Cardinality of a set
$\mathrm{LCM}\{\bullet\}$	Least common multiple of scalar quantities
$\mathrm{vec}\{\bullet\}$	Vectorization of a matrix quantity
$\lfloor \bullet \rfloor$	Rounding real scalar to the next integer closet to $-\infty$
$O\{\bullet\}$	Computational cost of a algorithm

References

[1] F. T. Ulaby and D. G. Long, *Microwave Radar and Radiometric Remote Sensing*. Norwood, MA, USA: Artech House, 2015.

[2] J. A. Scheer and W. A. Holm, "Introduction and radar overview," in *Principles of Modern Radar: Basic Principles*, M. A. Richards, J. A. Scheer, and W. A. Holm, Eds. Raleigh, NC, USA: SciTech Publishing, Inc., 2010, vol. 1, ch. 1, pp. 3–57.

[3] N. C. Currie, "Characteristics of clutter," in *Principles of Modern Radar: Basic Principles*, M. A. Richards, J. A. Scheer, and W. A. Holm, Eds. Raleigh, NC, USA: SciTech Publishing, Inc., 2010, vol. 1, ch. 5, pp. 165 – 210.

[4] J. Ward, "Space-time adaptive processing for airborne radar," Lincoln Laboratory, Massachusetts Institute of Technology, Cambridge, MA, USA, Tech. Rep. ESC-TR-94-109, 1994.

[5] S. M. Scarborough, C. H. C. Jr., L. Gorham, M. J. Minardi, U. K. Majumder, M. G. Judge, E. Zelnio, M. Bryant, H. Nichols, and D. Page, "A challenge problem for SAR-based GMTI in urban environments," in *SPIE Defense, Security, and Sensing*, Orlando, FL, USA, Apr. 2009, pp. 143–152.

[6] W. K. Saunders and V. Gregers-Hansen, "MTI radar," in *Radar Handbook*, 2nd ed., M. Skolnik, Ed. New York, NY, USA: McGraw-Hill Companies, 1990, ch. 15.

[7] R. Klemm, *Principles of Space-time Adaptive Processing*. London, EN, United Kingdom: The Institution of Electrical Engineers, 2002.

[8] B. Keel, "Fundamentals of pulse compression waveforms," in *Principles of Modern Radar:*

Basic Principles, M. A. Richards, J. A. Scheer, and W. A. Holm, Eds. Raleigh, NC, USA: SciTech Publishing, Inc., 2010, vol. 1, ch. 20, pp. 773–830.

[9] N. Levanon and E. Mozeson, *Radar Signals*. Hoboken, NJ, USA: Wiley, 2004.

[10] D. M. Pozar, *Microwave Engineering*, 4th ed. Hoboken, NJ, USA: Wiley, 2012.

[11] K. Shanmugam, *Random Signals*, 1st ed. Hoboken, NJ, USA: Wiley, 1998.

[12] E. C. Farnett and G. H. Stevens, "Pulse compression radar," in *Radar Handbook*, 2nd ed., M. Skolnik, Ed. New York, NY, USA: McGraw-Hill Companies, 1990, ch. 10.

[13] S. D. Blunt and E. L. Mokole, "Overview of radar waveform diversity," *IEEE Aerospace & Electronic Systems Mag.*, vol. 31, no. 11, pp. 2–42, Nov. 2016.

[14] J. A. Scheer, "The radar range equation," in *Principles of Modern Radar: Basic Principles*, M. A. Richards, J. A. Scheer, and W. A. Holm, Eds. Raleigh, NC, USA: SciTech Publishing, Inc., 2010, vol. 1, ch. 2, pp. 59–85.

[15] B. M. Keel, "Constant false alarm rate detectors," in *Principles of Modern Radar: Basic Principles*, M. A. Richards, J. A. Scheer, and W. A. Holm, Eds. Raleigh, NC, USA: SciTech Publishing, Inc., 2010, vol. 1, ch. 16, pp. 589–623.

[16] H. Friis, "A note on a simple transmission formula," *Proc. of the IRE*, vol. 34, no. 5, pp. 254–256, May 1946.

[17] C. D. Bailey, "Radar antennas," in *Principles of Modern Radar: Basic Principles*, M. A. Richards, J. A. Scheer, and W. A. Holm, Eds. Raleigh, NC, USA: SciTech Publishing, Inc., 2010, vol. 1, ch. 9, pp. 309–345.

[18] W. K. Saunders, "CW and FM radar," in *Radar Handbook*, 2nd ed., M. Skolnik, Ed. New York, NY, USA: McGraw-Hill Companies, 1990, ch. 14.

[19] T. Higgins, S. D. Blunt, and A. K. Shackelford, "Time-range adaptive processing for pulse agile radar," in *Int. Waveform Diversity & Design Conf.*, Niagara Falls, ON, Canada, Aug. 2010, pp. 115–120.

[20] T. Higgins, S. D. Blunt, and A. K. Shackelford, "Space-range adaptive processing for waveform-diverse radar imaging," in *IEEE Radar Conf.*, Washington, DC, USA, May 2010, pp. 321–326.

[21] M. A. Richards, "Doppler phenomenology and data acquisition," in *Principles of Modern Radar: Basic Principles*, M. A. Richards, J. A. Scheer, and W. A. Holm, Eds. Raleigh, NC, USA: SciTech Publishing, Inc., 2010, vol. 1, ch. 8, pp. 273–305.

[22] W. L. Melvin, "Clutter suppression using space-time adaptive processing," in *Principles of Modern Radar: Advanced Technique*, W. L. Melvin and J. A. Scheer, Eds. Raleigh, NC, USA: SciTech Publishing, Inc., 2013, vol. 2, ch. 10, pp. 453–497.

[23] S. D. Blunt, T. Chan, and K. Gerlach, "Robust DOA estimation: The reiterative superresolution (RISR) algorithm," *IEEE Trans. on Aerospace & Electronic Systems*, vol. 47, no. 1, pp. 332–346, Jan. 2011.

[24] M. A. Richards, "Doppler processing," in *Principles of Modern Radar: Basic Principles*, M. A. Richards, J. A. Scheer, and W. A. Holm, Eds. Raleigh, NC, USA: SciTech Publishing, Inc., 2010, vol. 1, ch. 17, pp. 625–676.

[25] C. Schleher, D, *MTI and Pulse Doppler Radar with MATLAB*. Norwood, MA, USA: Artech House, 2010.

[26] S. Bagchi and S. K. Mitra, "The nonuniform discrete Fourier transform and its applications in filter design. I. 1-D," *IEEE Trans. on Circuits & Systems II: Analog & Digital Signal Processing*, vol. 43, no. 6, pp. 422–433, Jun. 1996.

[27] H. L. V. Trees, *Optimum Array processing*. New York, NY, USA: Wiley, 2002.

[28] M. A. Richards, "Digital signal processing fundamentals for radar," in *Principles of Modern Radar: Basic Principles*, M. A. Richards, J. A. Scheer, and W. A. Holm, Eds. Raleigh, NC, USA: SciTech Publishing, Inc., 2010, vol. 1, ch. 14, pp. 495–542.

[29] L. A. Harnett, "Post pulse compression & partially adaptive multi-waveform space-time adaptive processing for heterogeneous clutter," Master's thesis, University of Kansas, 2018.

[30] L. Brennan and F. Staudaher, "Subclutter visibility demonstration," Adaptive Sensors Incorporated, Tech. Rep. RL-TR-92-21, 1992.

[31] R. Brawer and M. Pirovino, "The linear algebra of the pascal matrix," *Linear Algebra and its Applications*, vol. 174, pp. 13–23, 1992.

[32] W. L. Melvin, "A STAP overview," *IEEE Aerospace & Electronic Systems Mag.*, vol. 19, no. 1, pp. 19–35, Jan. 2004.

[33] J. R. Guerci, *Space-time adaptive processing for radar*, 2nd ed. Norwood, MA, USA: Artech House, 2015.

[34] C. C. Jones, L. A. Harnett, C. A. Mohr, S. D. Blunt, and C. T. Allen, "Structure-based adaptive radar processing for joint clutter cancellation and moving target estimation," in *IEEE Int. Radar Conf.*, Washington, DC, USA, Jun. 2020, pp. 413–418.

[35] W. L. Melvin, "Space-time adaptive radar performance in heterogeneous clutter," *IEEE Trans. on Aerospace & Electronic Systems*, vol. 36, no. 2, pp. 621–633, Apr. 2000.

[36] I. S. Reed, J. D. Mallett, and L. E. Brennan, "Rapid convergence rate in adaptive arrays," *IEEE Trans. on Aerospace & Electronic Systems*, vol. AES-10, no. 6, pp. 853–863, Nov. 1974.

[37] D. Aalfs, "Adaptive receive beamforming," in *Principles of Modern Radar: Advanced Technique*, W. L. Melvin and J. A. Scheer, Eds. Raleigh, NC, USA: SciTech Publishing, Inc., 2013, vol. 2, ch. 9, pp. 401–452.

[38] C. Peckham, A. Haimovich, T. Ayoub, J. Goldstein, and I. Reid, "Reduced-rank STAP performance analysis," *IEEE Trans. on Aerospace & Electronic Systems*, vol. 36, no. 2, pp. 664–676, Apr. 2000.

[39] J. Guerci, J. Goldstein, and I. Reed, "Optimal and adaptive reduced-rank STAP," *IEEE Trans. on Aerospace & Electronic Systems*, vol. 36, no. 2, pp. 647–663, Apr. 2000.

[40] I. Kirsteins and D. Tufts, "Adaptive detection using low rank approximation to a data matrix," *IEEE Trans. on Aerospace & Electronic Systems*, vol. 30, no. 1, pp. 55–67, Jan. 1994.

[41] A. Haimovich, "The eigencanceler: adaptive radar by eigenanalysis methods," *IEEE Trans. on Aerospace & Electronic Systems*, vol. 32, no. 2, pp. 532–542, Apr. 1996.

[42] L. Chang and C.-C. Yeh, "Performance of DMI and eigenspace-based beamformers," *IEEE Trans. on Antennas & Propagation*, vol. 40, no. 11, pp. 1336–1347, Nov. 1992.

[43] R. Kumaresan and D. W. Tufts, "Data-adaptive principal component signal processing," in *IEEE Conf. on Decision & Control including the Symp. on Adaptive Processes*, Dec. 1980, pp. 949–954.

[44] D. Tufts, R. Kumaresan, and I. Kirsteins, "Data adaptive signal estimation by singular value decomposition of a data matrix," *Proc. of the IEEE*, vol. 70, no. 6, pp. 684–685, Jun. 1982.

[45] R. C. DiPietro, "Extended factored space-time processing for airborne radar systems," in *Asilomar Conf. on Signals, Systems & Computers*, Pacific Grove, CA, USA, Oct. 1992, pp. 425–430 vol.1.

[46] R. J. McAulay, "The effect of staggered PRF's on MTI signal detection," *IEEE Trans. on Aerospace & Electronic Systems*, vol. AES-9, no. 4, pp. 615–618, Jul. 1973.

[47] R. Pribic, "Doppler processing on irregular PRT," in *IEEE Int. Radar Conf.*, Edinburgh, SC, United Kingdom, Oct. 2002, pp. 295–299.

[48] T. T. Taylor, "Design of line-source antennas for narrow beamwidth and low side lobes," *Trans. of the IRE Professional Group on Antennas & Propagation*, vol. 3, no. 1, pp. 16–28, Jan. 1955.

[49] S. Ferraz-Mello, "Estimation of periods from unequally spaced observations," *The Astronomical Journal*, vol. 86, p. 619, Apr. 1981.

[50] J. D. Scargle, "Studies in astronomical time series analysis. ii. statistical aspects of spectral analysis of unevenly spaced data." *The Astronomical Journal*, vol. 263, pp. 835–853, Dec. 1982.

[51] P. Vaníček, "Approximate spectral analysis by least-squares fit. successive spectral analysis," *Astrophysics & Space Science*, vol. 4, no. 4, pp. 387–391, Aug. 1969.

[52] ——, "Further development and properties of the spectral analysis by least-squares," *Astrophysics & Space Science*, vol. 12, no. 1, pp. 10–33, Jul. 1971.

[53] N. R. Lomb, "Least-squares frequency analysis of unequally spaced data," *Astrophysics & Space Science*, vol. 39, no. 2, pp. 447–462, Feb. 1976.

[54] P. Stoica and N. Sandgren, "Spectral analysis of irregularly-sampled data: Paralleling the regularly-sampled data approaches," *Digital Signal Processing*, vol. 16, no. 6, pp. 712–34, Nov. 2006.

[55] T. A. Garcia-Calva, D. Morinigo-Sotelo, and R. de Jesus Romero-Troncoso, "Non-uniform time resampling for diagnosing broken rotor bars in inverter-fed induction motors," in *IEEE Trans. on Industrial Electronics*, vol. 64, no. 3, Mar. 2017, pp. 2306–2315.

[56] C. Wijenayake, A. Antonir, G. Keller, and A. Ignjatović, "An adaptive denoising algorithm for improving frequency estimation and tracking," in *IEEE Trans. on Circuits and Systems II: Express Briefs*, vol. 67, no. 1, Jan. 2020, pp. 172–176.

[57] M. Rubsamen and A. B. Gershman, "Direction-of-arrival estimation for nonuniform sensor arrays: From manifold separation to Fourier domain music methods," in *IEEE Trans. on Signal Processing*, vol. 57, no. 2, Feb. 2009, pp. 588–599.

[58] S. Mulleti and C. S. Seelamantula, "Periodic non-uniform sampling for FRI signals," in *Int. Conf. on Acoustics, Speech, & Signal Processing*, Brisbane, QLD, Australia, Apr. 2015, pp. 5942–5946.

[59] J. Steinwandt, F. Roemer, and M. Haardt, "Performance analysis of ESPRIT-type algorithms for co-array structures," in *IEEE Int. Workshop on Computational Advances in Multi-Sensor Adaptive Processing*, Curacao, Dec. 2017, pp. 1–5.

[60] P. Stoica, J. Li, and H. He, "Spectral analysis of nonuniformly sampled data: A new approach versus the periodogram," in *IEEE Trans. on Signal Processing*, vol. 57, no. 3, Mar. 2009, pp. 848–58.

[61] G. Glentis and A. Jakobsson, "Efficient implementation of iterative adaptive approach spectral estimation techniques," in *IEEE Trans. on Signal Processing*, vol. 59, no. 9, Sep. 2011, pp. 4154–4167.

[62] J. Karlsson, W. R. abd L. Xu, G. Glentis, and J. Li, "Fast missing-data IAA with application to notched spectrum SAR," in *IEEE Trans. on Aerospace & Electronic Systems*, vol. 50, no. 2, Apr. 2014, pp. 959–971.

[63] ——, "Fast missing-data IAA by low rank completion," in *IEEE Int. Conf. on Acoustics, Speech & Signal Processing*, Vancouver, BC, Canada, May 2013, pp. 6215–6219.

[64] R. Roy and O. Lowenschuss, "Design of MTI detection filters with nonuniform interpulse periods," *IEEE Trans. on Circuit Theory*, vol. 17, no. 4, pp. 604–612, Nov. 1970.

[65] R. Benjamin, "Form of Doppler processing for radars of random p.r.i. and r.f." *Electronics Letters*, vol. 15, no. 24, p. 782, Feb. 1979.

[66] L. Vergara-Dominguez, "Analysis of the digital MTI filter with random PRI," *IEE Proc. F - Radar & Signal Processing*, vol. 140, no. 2, pp. 129–137, Apr. 1993.

[67] A. J. Zejak, E. Zentner, and P. B. Rapajic, "Doppler optimised mismatched filters," *Electronics Letters*, vol. 27, no. 7, pp. 558–560, Mar. 1991.

[68] L. A. Harnett and S. D. Blunt, "Least-squares optimal mismatched Doppler processing," in *IEEE Radar Conf.*, Boston, MA, USA, Apr. 2019, pp. 1–5.

[69] S. Yuen and H. Subbaram, "A new super-resolution spectral estimation technique using staggered PRFs," in *Int. Conf. on Acoustics, Speech, & Signal Processing*, Tampa, FL, USA, Apr. 1985, pp. 1360–1363.

[70] D. P. Scholnik, "Range-ambiguous clutter suppression with pulse-diverse waveforms," in *IEEE Radar Conf.*, Kansas City, MO, USA, May 2011, pp. 336–341.

[71] S. D. Blunt and K. Gerlach, "A novel pulse compression scheme based on minimum mean-square error reiteration," in *IEEE Int. Conf. on Radar*. Adelaide, Australia: IEEE, Sep. 2003, pp. 349–353.

[72] S. D. Blunt and K. Gerlach, "Adaptive pulse compression via MMSE estimation," *IEEE Trans. on Aerospace & Electronic Systems*, vol. 42, no. 2, pp. 572–584, Apr. 2006.

[73] C. C. Jones, Z. E. Gannon, D. DePardo, J. W. Owen, S. D. Blunt, C. T. Allen, and B. Kirk, "Development & experimental assessment of robust direction finding and self-calibration," in *IEEE Radar Conf.*, New York City, NY, USA, Mar. 2022.

[74] C. C. Jones, Z. E. Gannon, S. D. Blunt, C. T. Allen, and A. F. Martone, "An adaptive spectrogram estimator to enhance signal characterization," in *IEEE Radar Conf.*, New York City, NY, USA, Mar. 2022.

[75] H. F. Alqadah and D. P. Scholnik, "A reiterative superresolution approach for direction of

arrival estimation with sparse arrays," in *IEEE Radar Conf.*, Oklahoma City, OK, USA, Jun. 2018, pp. 0559–0563.

[76] H. F. Alqadah, D. P. Scholnik, and J. D. Graaf, "Nonlinear array processing via a nested array: Theory and experimental evaluation," in *IEEE Radar Conf.*, Washington, DC, USA, Apr. 2020, pp. 572–577.

[77] L. A. Harnett, D. Hemmingsen, P. M. McCormick, S. D. Blunt, C. Allen, A. Martone, K. Sherbondy, and D. Wikner, "Optimal and adaptive mismatch filtering for stretch processing," in *IEEE Radar Conf.*, Oklahoma City, OK, USA, Apr. 2018, pp. 0682–0686.

[78] S. D. Blunt, A. Shackelford, and K. Gerlach, "Doppler compensated adaptive pulse compression," in *Intl. Waveform Diversity and Design Conf.*, Lihue, HI, USA, Jan. 2006, pp. 1–5.

[79] S. D. Blunt, K. J. Smith, and K. Gerlach, "Doppler-compensated adaptive pulse compression," in *IEEE Radar Conf.*, Verona, NY, USA, Apr. 2006, p. 6.

[80] S. D. Blunt, A. Shackelford, K. Gerlach, and K. Smith, "Doppler compensation & single pulse imaging via adaptive pulse compression," *IEEE Trans. on Aerospace and Electronic Systems*, vol. 45, no. 2, pp. 647–659, Apr. 2009.

[81] B. D. Cordill, S. A. Seguin, and S. D. Blunt, "Mutual coupling calibration using the reiterative superresolution (RISR) algorithm," in *IEEE Radar Conf.*, Cincinnati, OH, USA, May 2014, pp. 1278–1282.

[82] M. Popescu, S. D. Blunt, and T. Chan, "Magnetoencephalography source localization using the source affine image reconstruction (SAFFIRE) algorithm," *IEEE Trans. on Biomedical Engineering*, vol. 57, no. 7, pp. 1652–1662, Jul. 2010.

[83] S. D. Blunt and T. Higgins, "Achieving real-time efficiency for adaptive radar pulse compression," in *IEEE Radar Conf.*, Boston, MA, USA, Apr. 2007, pp. 116–121.

[84] S. D. Blunt and T. Higgins, "Dimensionality reduction techniques for efficient adaptive radar pulse compression," *IEEE Trans. on Aerospace and Electronic Systems*, vol. 46, no. 1, pp. 349–362, Jan. 2010.

[85] S. D. Blunt and T. Higgins, "Dimensionality reduction techniques for efficient adaptive pulse compression," in *IEEE Trans. on Aerospace & Electronic Systems*, vol. 46, no. 1, Jan. 2010, pp. 349–362.

[86] T. Higgins, S. D. Blunt, and K. Gerlach, "Gain-constrained adaptive pulse compression via an MVDR framework," in *IEEE Radar Conf.*, Pasadena, CA, USA, May 2009, pp. 1–6.

[87] T. Higgins, "Waveform diversity and range-coupled adaptive radar signal processing," Ph.D. dissertation, University of Kansas, 2011.

[88] P. M. McCormick, S. D. Blunt, and T. Higgins, "A gradient descent implementation of adaptive pulse compression," in *IEEE Radar Conf.*, Philadelphia, PA, USA, May 2016, pp. 1–5.

[89] Z. Li, Y. Zhang, S. Wang, L. Li, and M. Mclinden, "Fast adaptive pulse compression based on matched filter outputs," *IEEE Trans. on Aerospace & Electronic Systems*, vol. 51, no. 1, pp. 548–564, Jan. 2015.

[90] D. Xiaofang, M. Ke, C. Baixiao, and Y. Minglei, "Direction of arrival estimation for monostatic mimo radar using reduced-dimension RISR algorithm," in *Int. Symp. on Antennas, Propagation & EM Theory*, Oct. 2016, pp. 607–611.

[91] L. A. Harnett, B. Ravenscroft, S. D. Blunt, and C. T. Allen, "Experimental evaluation of adaptive doppler estimation for PRI-staggered radar," in *IEEE Radar Conf.*, New York City, NY, USA, Mar. 2022.

[92] S. S. Haykin, *Adaptive Filter Theory*. Upper Saddle River, NJ, USA: Pearson Education, Inc., 2014.

[93] E. Hornberger, S. D. Blunt, and T. Higgins, "Partially constrained adaptive beamforming for super-resolution at low SNR," in *IEEE Int. Workshop on Computational Advances in Multi-Sensor Adaptive Processing*, Cancun, Mexico, Dec. 2015, pp. 129–132.

[94] D. Henke, P. McCormick, S. D. Blunt, and T. Higgins, "Practical aspects of optimal mismatch filtering and adaptive pulse compression for FM waveforms," in *IEEE Radar Conf.*, Arlington, VA, USA, May 2015, pp. 1149–1155.

[95] P. Parker, "Performance of the space-time AR filter in non-homogeneous clutter [airborne radar STAP]," in *IEEE Int. Radar Conf.*, Sep. 2003, pp. 67–70.

[96] R. Blum, W. Melvin, and M. Wicks, "An analysis of adaptive DPCA," in *IEEE Radar Conf.*, May 1996, pp. 303–308.

[97] J. Goldstein, I. Reed, P. Zulch, and W. Melvin, "A multistage STAP CFAR detection technique," in *IEEE Radar Conf.*, May 1998, pp. 111–116.

[98] J. Goldstein, I. Reed, and L. Scharf, "A multistage representation of the Wiener filter based on orthogonal projections," *IEEE Trans. on Information Theory*, vol. 44, no. 7, pp. 2943–2959, Nov. 1998.

[99] B. Himed and J. Michels, "Performance analysis of the multi-stage Wiener filter," in *IEEE Int. Radar Conf.*, May 2000, pp. 729–734.

[100] M. Weippert, J. Hiemstra, J. Goldstein, and D. Garren, "Efficient implementation of the multistage Wiener filter for multiple beam applications," in *IEEE Int. Symp. on Phased Array Systems & Technology*, Oct. 2003, pp. 152–157.

[101] M. Weippert, J. Hiemstra, J. Goldstein, V. Sabio, M. Zoltowski, and I. Reed, "Signal-dependent reduced-rank multibeam processing [radar SIGPRO]," in *IEEE Int. Radar Conf.*, Sep. 2003, pp. 51–56.

[102] J. Li, G. Liu, N. Jiang, and P. Stoica, "Moving target feature extraction for airborne high-range resolution phased-array radar," *IEEE Trans. on Signal Processing*, vol. 49, no. 2, pp. 277–289, Feb. 2001.

[103] J. Li, X. Zhu, P. Stoica, and M. Rangaswamy, "High resolution angle-Doppler imaging for MTI radar," *IEEE Trans. on Aerospace & Electronic Systems*, vol. 46, no. 3, pp. 1544–1556, Jul. 2010.

[104] M. H. Ackroyd and F. Ghani, "Optimum mismatched filters for sidelobe suppression," *IEEE Trans. on Aerospace & Electronic Systems*, vol. AES-9, no. 2, pp. 214–218, Mar. 1973.

[105] S. D. Blunt, M. Cook, J. Jakabosky, J. D. Graaf, and E. Perrins, "Polyphase-coded FM (PCFM) radar waveforms, part I: implementation," *IEEE Trans. on Aerospace & Electronic Systems*, vol. 50, no. 3, pp. 2218–2229, Jul. 2014.

[106] Y.-L. Wang, J.-W. Chen, Z. Bao, and Y.-N. Peng, "Robust space-time adaptive processing for airborne radar in nonhomogeneous clutter environments," *IEEE Trans. on Aerospace & Electronic Systems*, vol. 39, no. 1, pp. 70–81, Jan. 2003.

[107] J. R. Guerci, "Theory and application of covariance matrix tapers for robust adaptive beamforming," *IEEE Trans. on Signal Processing*, vol. 47, no. 4, pp. 977–985, Apr. 1999.

[108] D. J. Rabideau and A. O. Steinhardt, "Improved adaptive clutter cancellation through data-adaptive training," *IEEE Trans. on Aerospace & Electronic Systems*, vol. 35, no. 3, pp. 879–891, Jul. 1999.

[109] S. M. Kogon and M. A. Zatman, "STAP adaptive weight training using phase and power selection criteria," in *Asilomar Conf. on Signals, Systems & Computers*, vol. 1, Pacific Grove, CA, USA, Nov. 2001, pp. 98–102 vol.1.

[110] T. M. Selee, K. F. Bing, and W. L. Melvin, "STAP application in mountainous terrain:

Challenges and strategies," in *IEEE Radar Conf.*, Atlanta, GA, USA, May 2012, pp. 0824–0829.

[111] J. R. Roman, M. Rangaswamy, D. W. Davis, Q. Zhang, B. Himed, and J. H. Michels, "Parametric adaptive matched filter for airborne radar applications," *IEEE Trans. on Aerospace & Electronic Systems*, vol. 36, no. 2, pp. 677–692, Apr. 2000.

[112] R. S. Adve, T. B. Hale, and M. C. Wicks, "Practical joint domain localised adaptive processing in homogeneous and nonhomogeneous environments. Part 2: Nonhomogeneous environments," *IEE Proc. - Radar, Sonar & Navigation*, vol. 147, no. 2, pp. 66–74, Apr. 2000.

[113] T. K. Sarkar, H. Wang, S. Park, R. Adve, J. Koh, K. Kim, Y. Zhang, M. C. Wicks, and R. D. Brown, "A deterministic least-squares approach to space-time adaptive processing (STAP)," *IEEE Trans. on Antennas & Propagation*, vol. 49, no. 1, pp. 91–103, Jan. 2001.

[114] G. A. Fabrizio and M. D. Turley, "An advanced STAP implementation for surveillance radar systems," in *IEEE Workshop on Statistical Signal Processing*, Singapore, Aug. 2001, pp. 134–137.

[115] K. Gerlach, "Outlier resistant adaptive matched filtering," *IEEE Trans. on Aerospace & Electronic Systems*, vol. 38, no. 3, pp. 885–901, Jul. 2002.

[116] Y.-L. Wang, J.-W. Chen, Z. Bao, and Y.-N. Peng, "Robust space-time adaptive processing for airborne radar in nonhomogeneous clutter environments," *IEEE Trans. on Aerospace & Electronic Systems*, vol. 39, no. 1, pp. 70–81, Jan. 2003.

[117] M. L. Picciolo and K. Gerlach, "Median cascaded canceller for robust adaptive array processing," *IEEE Trans. on Aerospace & Electronic Systems*, vol. 39, no. 3, pp. 883–900, Jul. 2003.

[118] K. Gerlach, S. D. Blunt, and M. L. Picciolo, "Robust adaptive matched filtering using the FRACTA algorithm," *IEEE Trans. on Aerospace & Electronic Systems*, vol. 40, no. 3, pp. 929–945, Jul. 2004.

[119] S. D. Blunt and K. Gerlach, "Efficient robust AMF using the FRACTA algorithm," *IEEE Trans. on Aerospace & Electronic Systems*, vol. 41, no. 2, pp. 537–548, Apr. 2005.

[120] W. L. Melvin and J. R. Guerci, "Knowledge-aided signal processing: a new paradigm for radar and other advanced sensors," *IEEE Trans. on Aerospace & Electronic Systems*, vol. 42, no. 3, pp. 983–996, Jul. 2006.

[121] W. L. Melvin and G. A. Showman, "An approach to knowledge-aided covariance estimation," *IEEE Trans. on Aerospace & Electronic Systems*, vol. 42, no. 3, pp. 1021–1042, Jul. 2006.

[122] S. D. Blunt, K. Gerlach, and M. Rangaswamy, "STAP using knowledge-aided covariance estimation and the FRACTA algorithm," *IEEE Trans. on Aerospace & Electronic Systems*, vol. 42, no. 3, pp. 1043–1057, Jul. 2006.

[123] F. Gini and M. Rangaswamy, *Knowledge Based Radar Detection, Tracking, and Classification,*. Hoboken, NJ, USA: Wiley, 2008.

[124] E. Aboutanios and B. Mulgrew, "Hybrid detection approach for STAP in heterogeneous clutter," *IEEE Trans. on Aerospace & Electronic Systems*, vol. 46, no. 3, pp. 1021–1033, Jul. 2010.

[125] O. Besson and S. Bidon, "Adaptive processing with signal contaminated training samples," *IEEE Trans. on Signal Processing*, vol. 61, no. 17, pp. 4318–4329, Sep. 2013.

[126] A. K. Shackelford, K. Gerlach, and S. D. Blunt, "Partially adaptive STAP using the FRACTA algorithm," *IEEE Trans. on Aerospace & Electronic Systems*, vol. 45, no. 1, pp. 58–69, Jan. 2009.

[127] S. D. Blunt, J. Metcalf, J. Jakabosky, J. Stiles, and B. Himed, "Multi-waveform space-time adaptive processing," *IEEE Trans. on Aerospace & Electronic Systems*, vol. 53, no. 1, pp. 385–404, Feb. 2017.

[128] S. D. Blunt, J. Jakabosky, J. Metcalf, J. Stiles, and B. Himed, "Multi-waveform STAP," in *IEEE Radar Conf.*, Ottawa. ON, Canada, Apr. 2013, pp. 1–6.

[129] S. D. Blunt, J. Metcalf, J. Jakabosky, and B. Himed, "SINR analysis of multi-waveform STAP," in *IEEE Int. Radar Conf.*, Lille, France, Oct. 2014, pp. 1–6.

[130] L. A. Harnett, J. G. Metcalf, and S. D. Blunt, "Post pulse compression and partially adaptive multi-waveform STAP," *IET Radar, Sonar & Navigation*, vol. 13, no. 10, pp. 1678–1688, Oct. 2019.

[131] L. J. Cutrona, "Synthetic aperture radar," in *Radar Handbook*, 2nd ed., M. Skolnik, Ed. New York, NY, USA: McGraw-Hill Companies, 1990, ch. 21.

[132] R. D. Campbell, "Radar interference to microwave communication services," *Electrical Engineering*, vol. 77, no. 10, pp. 916–921, Oct. 1958.

[133] Federal Communication Commission, "5G and aviation safety," Federal Communication Commission, Washington, DC, USA, Tech. Rep., 2022. [Online]. Available: https://www.faa.gov/5g

[134] ——, "FCC online table of frequency allocations," Federal Communication Commission, Washington, DC, USA, Tech. Rep., 2021. [Online]. Available: https://www.fcc.gov/engineering-technology/policy-and-rules-division/general/radio-spectrum-allocation

[135] B. Obama, "Presidential Memorandum: Unleashing the Wireless Broadband Revolution," Official Memorandum, The White House, Washington, DC, USA, Jun. 2010.

[136] ——, "Presidential Memorandum – Expanding America's Leadership in Wireless Innovation," Official Memorandum, The White House, Washington, DC, USA, Jun. 2013.

[137] D. Trump, "Presidential Memorandum on Developing a Sustainable Spectrum Strategy for America's Future," Official Memorandum, The White House, Washington, DC, USA, Oct. 2018.

[138] United States Federal Communications Commission, *National Broadband Plan*, 2010 (accessed November 10, 2019), https://www.fcc.gov/general/national-broadband-plan/.

[139] ——, *Auction 97: Advanced Wireless Services (AWS-3)*, 2015 (accessed November 25, 2019), fcc.gov/auction/97.

[140] A. Pai, "A giant leap for 5G," FCC.gov. https://www.fcc.gov/news-events/blog/2019/06/18/giant-leap-5g, (accessed Jul. 28 2019).

[141] A. R. Chiriyath, B. Paul, and D. W. Bliss, "Radar-communications convergence: Coexistence, cooperation, and co-design," *IEEE Trans. on Cognitive Communications & Networking*, vol. 3, no. 1, pp. 1–12, Mar. 2017.

[142] J. Peha, "Emerging technology and spectrum policy reform," in *International Telecommunications Union (ITU) Workshop on Market Mechanisms for Spectrum Management*. Geneva, Switzerland: ITU, Jan. 2007, p. 12.

[143] ——, "Sharing spectrum through spectrum policy reform and cognitive radio," *Proc. of the IEEE*, vol. 97, no. 4, pp. 708–719, Apr. 2009.

[144] S. D. Blunt and E. S. Perrins, "The case for spectrum access," in *Radar and Communication Spectrum Sharing*, S. D. Blunt and E. S. Perrins, Eds. London, EN, United Kingdom: SciTech Publishing, 2018, ch. 1, pp. 3–26.

[145] S. Bhattarai, J.-M. Park, B. Gao, K. Bian, and W. Lehr, "An overview of dynamic spectrum sharing: Ongoing initiatives, challenges, and a roadmap for future research," *IEEE Trans. on Cognitive Communications & Networking*, vol. 2, no. 2, pp. 110–128, Jun. 2016.

[146] H. Griffiths, L. Cohen, S. Watts, E. Mokole, C. Baker, M. Wicks, and S. Blunt, "Radar spectrum engineering and management: Technical and regulatory issues," *Proc. of the IEEE*, vol. 103, no. 1, pp. 85–102, Jan. 2015.

[147] H. Griffiths, S. Blunt, L. Cohen, and L. Savy, "Challenge problems in spectrum engineering and waveform diversity,," in *IEEE Radar Conf.* Ottawa, Canada: IEEE, May 2013, pp. 1–5.

[148] J. Peha, "Approaches to spectrum sharing," *IEEE Communications Mag.*, vol. 43, no. 2, pp. 10–12, Feb. 2005.

[149] B. Paul, A. R. Chiriyath, and D. W. Bliss, "Survey of RF communications and sensing convergence research," *IEEE Access*, vol. 5, pp. 252–270, Dec. 2017.

[150] A. Herschfelt, A. Chiriyath, D. W. Bliss, C. D. Richmond, U. Mitra, and S. D. Blunt, "Vehicular RF convergence: Simultaneous radar, communications, and PNT for urban air mobility and automotive applications," in *IEEE Radar Conf.* Florence, Italy: IEEE, Sep. 2020, pp. 1–6.

[151] L. Zheng, M. Lops, Y. C. Eldar, and X. Wang, "Radar and communication coexistence: An overview: A review of recent methods," *IEEE Signal Processing Mag.*, vol. 36, no. 5, pp. 85–99, Sep. 2019.

[152] S. Haykin, "Cognitive radar: a way of the future," *IEEE Signal Processing Mag.*, vol. 23, no. 1, pp. 30–40, Jan. 2006.

[153] M. S. Greco, F. Gini, P. Stinco, and K. Bell, "Cognitive radars: On the road to reality: Progress thus far and possibilities for the future," *IEEE Signal Processing Mag.*, vol. 35, no. 4, pp. 112–125, Jul. 2018.

[154] F. Gini, M. S. Greco, and P. Stinco, "Spectrum sensing and sharing for cognitive radars," *IET Radar, Sonar & Navigation*, vol. 10, no. 3, pp. 595–602, Mar. 2016.

[155] J. W. Owen, B. Ravenscroft, B. H. Kirk, S. D. Blunt, C. T. Allen, A. F. Martone, K. D. Sherbondy, and R. M. Narayanan, "Experimental demonstration of cognitive spectrum sensing & notching for radar," in *IEEE Radar Conf.* Oklahoma City, OK, USA: IEEE, Apr. 2018, pp. 0957–0962.

[156] A. F. Martone, K. I. Ranney, K. Sherbondy, K. A. Gallagher, and S. D. Blunt, "Spectrum allocation for noncooperative radar coexistence," *IEEE Trans. on Aerospace & Electronic Systems*, vol. 54, no. 1, pp. 90–105, Feb. 2018.

[157] B. Ravenscroft, J. W. Owen, J. Jakabosky, S. D. Blunt, A. F. Martone, and K. D. Sherbondy, "Experimental demonstration and analysis of cognitive spectrum sensing & notching," *IET Radar, Sonar & Navigation*, vol. 12, no. 12, pp. 1466–1475, Dec. 2018.

[158] B. Ravenscroft, J. W. Owen, B. H. Kirk, S. D. Blunt, A. F. Martone, K. D. Sherbondy, and R. M. Narayanan, "Experimental assessment of joint range-Doppler processing to address clutter modulation from dynamic radar spectrum sharing," in *IEEE Int. Radar Conf.* Washington, DC, USA: IEEE, Apr. 2020, pp. 448–453.

[159] J. W. Owen, C. A. Mohr, B. H. Kirk, S. D. Blunt, A. F. Martone, and K. D. Sherbondy, "Demonstration of real-time cognitive radar using spectrally-notched random FM waveforms," in *IEEE Int. Radar Conf.* Washington, DC, USA: IEEE, Apr. 2020, pp. 123–128.

[160] A. F. Martone, K. D. Sherbondy, J. A. Kovarskiy, B. H. Kirk, C. E. Thornton, J. W. Owen, B. Ravenscroft, A. Egbert, A. Goad, A. Dockendorf, R. M. Buehrer, R. M. Narayanan, S. D. Blunt, and C. Baylis, "Metacognition for radar coexistence," in *IEEE Int. Radar Conf.* Washington, DC, USA: IEEE, Apr. 2020, pp. 55–60.

[161] A. Dockendorf, A. Egbert, A. Goad, C. Calabrese, B. Adkins, B. Ravenscroft, J. Owen, C. Baylis, S. Blunt, A. Martone, K. Gallagher, and R. J. Marks, "Impedance tuning with

notched waveforms for spectrum sharing in cognitive radar," in *IEEE Int. Radar Conf.* Washington, DC, USA: IEEE, Apr. 2020, pp. 135–140.

[162] A. Martone, J. Kovarskiy, C. Thornton, B. Kirk, J. Owen., B. Ravenscroft, A. Egbert, A. Goad, R. Buehrer, R. Narayanan, S. Blunt, C. Baylis, and K. Sherbondy, "Closing the loop on cognitive radar for spectrum sharing," *IEEE Aerospace & Electronic Systems Magazine*, vol. 36, no. 9, pp. 44–55, Sep. 2021.

[163] J. Owen, C. Mohr, B. Ravenscroft, S. Blunt, B. Kirk, and A. Martone, "Real-time experimental demonstration and evaluation of open-air sense-and-notch radar," in *IEEE Radar Conf.*, New York City, NY, USA, Mar. 2022.

[164] A. Aubry, A. De Maio, M. Piezzo, and A. Farina, "Radar waveform design in a spectrally crowded environment via nonconvex quadratic optimization," *IEEE Trans. on Aerospace & Electronic Systems*, vol. 50, no. 2, pp. 1138–1152, Apr. 2014.

[165] A. Hassanien, M. G. Amin, E. Aboutanios, and B. Himed, "Dual-function radar communication systems: A solution to the spectrum congestion problem," *IEEE Signal Processing Mag.*, vol. 36, no. 5, pp. 115–126, Sep. 2019.

[166] P. M. McCormick, C. Sahin, S. D. Blunt, and J. G. Metcalf, "FMCW implementation of phase-attached radar-communications (PARC)," in *IEEE Radar Conf.* Boston, MA, USA: IEEE, Apr. 2019, pp. 1–6.

[167] B. Ravenscroft, P. M. McCormick, S. Blunt, E. S. Perrins, C. Sahin, and J. G. Metcalf, "Experimental assessment of tandem-hopped radar and communications (THoRaCs)," in *IEEE Int. Radar Conf.* Toulon, France: IEEE, Sep. 2019, pp. 1–6.

[168] K. V. Mishra, M. Bhavani Shankar, V. Koivunen, B. Ottersten, and S. A. Vorobyov, "Toward millimeter-wave joint radar communications: A signal processing perspective," *IEEE Signal Processing Mag.*, vol. 36, no. 5, pp. 100–114, Sep. 2019.

[169] B. Paul, A. R. Chiriyath, and D. W. Bliss, "Joint communications and radar performance bounds under continuous waveform optimization: The waveform awakens," in *IEEE Radar Conf.* Philadelphia, PA, USA: IEEE, May 2016, pp. 1–6.

[170] A. Hassanien, M. G. Amin, Y. D. Zhang, and F. Ahmad, "Signaling strategies for dual-function radar communications: an overview," *IEEE Aerospace & Electronic Systems Mag.*, vol. 31, no. 10, pp. 36–45, Oct. 2016.

[171] J. G. Metcalf, C. Sahin, and S. D. Blunt, "Impact of adjacent/overlapping communication waveform design within a radar spectrum sharing context," in *IEEE Int. Radar Conf.* Washington, DC, USA: IEEE, Apr. 2020, pp. 472–477.

[172] A. R. Chiriyath, B. Paul, G. M. Jacyna, and D. W. Bliss, "Inner bounds on performance of radar and communications co-existence," *IEEE Trans. on Signal Processing*, vol. 64, no. 2, pp. 464–474, Jan. 2016.

[173] S. D. Blunt and K. Gerlach, "Multistatic adaptive pulse compression," *IEEE Trans. on Aerospace & Electronic Systems*, vol. 42, no. 3, pp. 891–903, Jul. 2006.

[174] K. Gerlach, A. K. Shackelford, and S. D. Blunt, "Combined multistatic adaptive pulse compression and adaptive beamforming for shared-spectrum radar," *IEEE Journal of Selected Topics in Signal Processing*, vol. 1, no. 1, pp. 137–146, Jun. 2007.

[175] P. McCormick, T. Higgins, S. Blunt, and M. Rangaswamy, "Adaptive receive processing of spatially-modulated physical radar emissions," *IEEE Journal of Selected Topics in Signal Processing*, vol. 9, no. 8, pp. 1415–1426, Dec. 2015.

[176] J. Ward and A. O. Steinhardt, "Multiwindow post-Doppler space-time adaptive processing," in *IEEE Workshop on Statistical Signal & Array Processing*, Jun. 1994, pp. 461–464.

[177] U. Madhow, *Fundamentals of Digital Communication*. New York, NY, USA: Cambrigde University Press, 2008.

[178] Third Generation Partnership Project, "Requirements for evolved UTRA (E-UTRA) and evolved UTRAN (E-UTRAN)," European Telecommunications Standards Institute, Sophia Antipolis Cedex, France, Tech. Rep. 3GPP TR 25.913 version 7.3.0 Release 7, 2013.

[179] F. Khan, *LTE for 4G Mobile Broadband*. New York, NY, USA: Cambrige University Press, 2009.

[180] Third Generation Partnership Project, "Evolved universal terrestrial radio access (E-UTRA): LTE physical layer general description," European Telecommunications Standards Institute, Sophia Antipolis Cedex, France, Tech. Rep. 3GPP TS 36.201 V15.2.0 Release 15, 2019.

[181] A. F. Molisch, *Wireless Communications*, 2nd ed. Hoboken, NJ, USA: Wiley, 2011.

[182] O. M. Salati, "Recent developments in RF interference," *IRE Trans. on Radio Frequency Interference*, vol. RFI-4, no. 2, pp. 24–33, May 1962.

[183] T. C. Cheston and J. Frank, "Phased array radar antennas," in *Radar Handbook*, 2nd ed., M. Skolnik, Ed. New York, NY, USA: McGraw-Hill Companies, 1990, ch. 7.

[184] S. D. Blunt, K. Gerlach, and E. L. Mokole, "Pulse compression eclipsing-repair," in *IEEE Radar Conf.*, Rome, ITA, May 2008, pp. 1–5.